Search for Sterile Neutrinos with MINOS and MINOS+

DISSERTATION

Presented to the Faculty of the Graduate School of

the University of Cincinnati

in Partial Fulfillment

of the Requirements

for the Degree of

DOCTOR OF PHILOSOPHY

in the Department of Physics

of the College of Arts and Sciences

by

Jacob Todd, M.S., M.Ed., B.A.

UNIVERSITY OF CINCINNATI

August 2018

Committee Chair: Alexandre Sousa

Search for Sterile Neutrinos with MINOS and MINOS+

Publication No. _____

Jacob Todd, Ph.D.
University of Cincinnati, 2018

Supervisor: Alexandre Sousa

MINOS+, a three year extension of the successful MINOS experiment, is a long-baseline neutrino experiment consisting of a beam originating at the NuMI beam facility, which is sampled 1 km downstream from in the 1 kt Near Detector at Fermilab, and again at 735 km downstream in the 5.4 kt Far Detector in the Soudan Underground Laboratory. Comparison of measurements taken at the Near and Far Detectors allows MINOS+ to probe with great precision the atmospheric domain of neutrino oscillations. Through observation of both neutral-current and charged-current weak interactions, MINOS+ is sensitive to both the muon neutrino survival and muon neutrino disappearance along its long baseline, which not only permits the high-precision measurement of Δm^2_{32} and θ_{23} in the standard three-flavor neutrino oscillations model but also allows for searches for anomalous oscillation behaviors. Here we show that observation of the anomalous disappearance of muon neutrinos can be interpreted in the context of oscillations in a phenomenological model containing three active neutrino flavor eigenstates and one sterile neutrino eigenstate.

Using this type of model, we demonstrate that the MINOS+ experiment, in combination with data collected during the MINOS era, achieves world-leading sensitivity to the sterile neutrino eigenstate over seven orders of magnitude in the mass-splitting Δm^2_{41}.

Copyright

by

Jacob Todd

2018

To Tina, Robert, Helen, Estel, and Ned

Requiem aeternam dona eis, Domine. Et lux perpetua luceat eis.

Fidelium animae, per misericordiam Dei, requiescant in pace.

Acknowledgments

Though the body of work represented by this dissertation is the result of the efforts of many, I believe I owe a few people a particular expression of gratitude.

I must first acknowledge and thank my advisor Alex Sousa. He showed constant interest and encouragement in my work and provided consistant support in the face of many challenges. I am forever thankful to him for the many oppurtunities experienced and successes achieved in the past four years.

In the MINOS+ collaboration, Adam Aurisano has been an impeccable discussion partner in tackling new frontiers in our field, and I have learned a great deal from our time working together. I would like to give special thanks to Leigh Whitehead for showing confidence and lending encouragement to my efforts when my own confidence was lacking. Jenny Thomas and Karol Lang have always demanded work of the highest quality, and I thank them for the inspiration to do what I may never have thought possible. Ashley Timmons and Junting Huang provided a warm welcome at my first visit to Fermilab, and by their efforts paved the way forward for what I have been able to accomplish. I would also like to thank Simon De Rijck, Rui Chen, and Tom Carroll, for their many insightful conversations and hard work behind the scenes that made all of our analyses possible.

At the University of Cincinnati, Rohana Wijewardhana welcomed me into the Ph.D. program with open arms, ensured that I was intellectually prepared for the future, and planted the quantum mechanics seeds that would sprout into my interest in neutrino physics. Mike Sokoloff introduced me to the landscape of particle physics and has been my advocate in both personal and career development. Matteo Lotito has been a great friend and has taught me many things ranging from superconformal filed theory to long-distance running to authentic Italian ragù, for which I offer my deepest gratitude.

I thank my parents, Pam and Gary, for every sacrifice they have made to make my life and career possible. No amount of words could ever repay the debt I owe. I thank my wife Emma for her constant love and support even when it seemed all my time was consumed by work. Last, but by no means least, I thank Zoë for letting me borrow some time from the first six months of her life in the hope that I can make the rest that much more special.

Table of Contents

Abstract **ii**

Acknowledgments **vi**

List of Figures **xiii**

List of Tables **xxxvi**

Chapter 1. Neutrino Physics **1**

1.1 Origins 1
1.1.1 Neutrino Discovery 3
1.1.2 Neutrino Flavors 4
1.1.3 Neutrino Properties 8
1.2 Neutrino Oscillations 10
1.2.1 Solar Neutrino Problem 10
1.2.2 Atmospheric Neutrino Problem 14
1.2.3 Neutrino Oscillation Formalism 18
1.2.4 Observation of Oscillations 25
1.2.5 Three-Flavor Formalism 31
1.2.6 Era of Precision 33
1.3 Anomalous Results 40
1.3.1 LSND 40
1.3.2 MiniBooNE 43
1.3.3 Reactor Antineutrino Anomaly 47
1.3.4 Gallium Anomaly 48
1.3.5 Null Results 50
1.4 Sterile Neutrinos 53
1.4.1 Properties 53
1.4.2 Oscillations in a 3+1 Flavor Model 54

Chapter 2. MINOS and MINOS+ Experiments **59**
2.1 MINOS and MINOS+ 59
2.1.1 MINOS 60
2.1.2 MINOS+ 65
2.1.3 NuMI Beam 67
2.1.4 NuMI Target Design 71
2.2 The MINOS/MINOS+ Detectors 72
2.2.1 Scintillator Strips 74
2.2.2 Instrumentation 75
2.2.3 Far Detector 76
2.2.4 Near Detector 80
2.2.5 Calibration Detector 81
2.2.6 Light Injection System 82
2.2.7 Electronics Trigger 83
2.3 Detecting Neutrino Interactions 84
2.3.1 Interaction Types and Cross sections 84
2.3.2 Event Topologies 87

Chapter 3. Calibration and Reconstruction **89**
3.1 Calibration 89
3.1.1 Drift and Gains Calibration 90
3.1.2 Linearity Calibration 94
3.1.3 Strip-to-Strip Calibration 95
3.1.4 Attenuation Calibration 98
3.1.5 Inter-detector Calibration 101
3.1.6 Absolute Energy Scale Calibration 103
3.2 Simulation 104
3.2.1 NuMI Beam Simulation 105
3.2.2 Selecting Flux Model 106
3.2.3 MINOS Detector Simulation 108
3.3 Event Reconstruction 110
3.3.1 Digitization and Slicing 110

3.3.2 Track Reconstruction 111
3.3.3 Shower Reconstruction 113
3.3.4 kNN Estimation of Shower Energy 114
3.3.5 Event Building 117

Chapter 4. Event Selection 118
4.1 Common Preselection 118
4.2 NC Selection 122
4.2.1 NC Fiducial Volume Cuts 122
4.2.2 NC Cleaning Cuts 126
4.2.3 NC Selection Cuts 131
4.3 CC Selection 133
4.3.1 CC Fiducial Volume Cuts 133
4.3.2 CC Selection Algorithm 136
4.3.3 The roID Selector 137
4.3.4 The jmID Selector 143
4.4 Efficiency and Purity of Selection 145

Chapter 5. Systematic Uncertainties 150
5.1 Methodology 150
5.2 Acceptance 152
5.3 Backgrounds 155
5.4 Energy Scale 159
5.5 Hadron production 164
5.6 Beam optics 174
5.7 Cross Sections 180
5.8 Normalization 186
5.9 Neutral Current Cleaning 191
5.10 Combined Systematic Uncertainties 194

Chapter 6. Search Methodology **200**
6.1 Phenomenology of Sterile Neutrino Oscillations 200
6.1.1 Atmospheric Oscillations Parameters 202
6.1.2 The Sterile Mass-Splitting Δm^2_{41} 205
6.1.3 The Sterile Mixing Angle θ_{24} 209
6.1.4 The Sterile Mixing Angle θ_{34} 214
6.2 Motivation for a Two-Detector Fit 216
6.3 Simultaneous Two-Detector Fit 223
6.3.1 Fit Strategy 224
6.3.2 Near Detector Oscillations 227
6.3.3 Conditional Multivariate Gaussian Distributions 228
6.4 Asimov Sensitivities 234
6.4.1 Shape vs. Normalization 237
6.4.2 Insufficiency of Asimov Sensitivity 241

Chapter 7. Results of the Sterile Neutrino Oscillations Search **247**
7.1 Reconstructed Energy Data Spectra 248
7.1.1 Consistency with Standard Oscillations 248
7.2 The χ^2 Surfaces 252
7.2.1 Best Fit Reconstructed Energy Spectra 255
7.2.2 Degeneracies 260
7.2.3 Systematic effects 261
7.2.4 Decomposition of the χ^2 Contributions 264
7.3 Statistical Interpretation 272
7.3.1 Fluctuated Data 272
7.3.2 Feldman-Cousins Unified Approach 274
7.3.3 Fluctuated Sensitivity Band 282
7.3.4 CL_s Method 283
7.4 MINOS/MINOS+ and Daya Bay/Bugey-3 285
7.5 Projection to Probability Space 288

Chapter 8. Summary and Future Work **292**

Bibliography **297**

Index **328**

Vita **329**

List of Figures

1.1 The cross section for hadron production in the approximate energy range of the Z^0 boson resonance as measured by the LEP Electroweak Working Group. The curves are plotted for hypotheses of two (red), three (green), and four (red) light, active neutrino flavors. The best agreement is found for a model with three neutrinos. Figure reproduced from Ref. [29]. 7

1.2 Plotted are the predicted solar neutrino energy spectra as computed from the Standard Solar Model. Figure reproduced from Ref. [48] 13

1.3 Plotted are the allowed regions for atmospheric neutrino mixing parameters in a two-flavor oscillations framework using data from Kamiokande-II [57] and IMB [59]. Figure reproduced from Ref. [61] 17

1.4 Plotted is the transition probability for $\nu_\alpha \to \nu_\beta$ oscillations using a two-flavor oscillations framework with mass-splitting $\Delta m^2 = 2.37 \times 10^{-3}$ eV^2 and mixing angle $\theta = 0.69$ as a function of L/E. The proximity of the mixing angle to $\pi/4$ results in near-maximal mixing, which is demonstrated by the large oscillations in the transition probability. 26

1.5 The $(\nu_\mu + \nu_\tau)$ solar neutrino flux versus the ν_e solar neutrino flux from ^8B neutrinos as measured by the SNO and Super-K experiments. The blue, red and green bands give the allowed solar neutrino flux as measured by SNO in the independent CC, NC and ES channels, respectively. The black band is the allowed ES channel flux measurement from Super-K [73]. The dashed lines define the allowed region of the total solar neutrino flux in the relevant energy range as predicted by the SSM [53]. The non-zero, favored region for the $(\nu_\mu + \nu_\tau$ component of the NC events is indicated by the solid elipses and gives strong evidence for neutrino oscillations. Figure reproduced from Ref. [71]. . . 29

1.6 The best-fit oscillation parameters in a three-flavor model to global neutrino oscillations data available as of November 2017. The first column gives the best-fit parameters for the normal mass ordering while the second column gives the best fit parameters for inverted mass ordering, which is disfavored at $\sim 2\sigma(\Delta\chi^2 = 4.14)$. The third column shows the result when minimizing with respect to the mass ordering. Table reproduced from Ref. [114]. 38

1.7 The total excess of $\nu_\mu \to \nu_e$ appearance events observed by LSND as a function of L/E. The data are shown by the black points, and the best fit is shown for background sources given by the red and green histograms and an oscillation signal shown by the blue histogram. The figure is taken from Ref. [120]. . . 40

1.8 The allowed region in a two-flavor oscillations parameter space as derived from the ν_e excess observed by LSND. The yellow and blue shaded regions show the 90% and 99% confidence intervals respectively. Exclusion limits from a selection of experiments obtaining null results are also shown by the red lines for comparison. The figure is taken from Ref. [120]. 41

1.9 The total excess of $\nu_\mu(\bar{\nu}_\mu) \to \nu_e(\bar{\nu}_e)$ appearance events observed by MiniBooNE as a function of visible energy. The data are shown by the black points, which are observed above the level of estimated backgrounds (shaded histograms) in the low energy region. The figure is taken from Ref. [125]. 44

1.10 The allowed region in a two-flavor oscillations parameter space as derived from the $\nu_e(\bar{\nu}_e$ excess observed by MiniBooNE. The colored lines show the MiniBooNE results at the listed confidence levels. The identical LSND allowed regions as shown in Fig. 1.8 are plotted as the shaded regions. Exclusion limits from the null results observed by KARMEN2 and ICARUS are also plotted for comparison. The figure is taken from Ref. [125]. . . 45

1.11 A plot illustrating the reactor electron antineutrino anomaly. Under the assumption of standard three flavor oscillations, the data points shown in the plot measured at a menagerie of nuclear reactor neutrino experiments should agree with the red line. However, solutions such as the blue line, which is not a fit but is for illustration purposes, could describe the data given the overall average rate deficit observed with respect to the standard three-flavor prediction. The figure is taken from Ref. [134]. 47

1.12 Plot summarizing the Gallium anomaly. The ratios of expected to calculated electron neutrino events are shown for the GALLEX [139] [140] and SAGE [141] along with the combined average from all of the plotted measurements (red-hatched band). Figure reproduced from Ref. [142]. 49

1.13 (a) Excluded regions (shaded) at a 95% CL of the neutrino oscillations parameter space (Δm^2_{41}, $\sin^2 2\theta_{24}$) for a fourth mass eigenstate corresponding to the existence of a sterile neutrino. The limits shown are from MINOS [155], IceCube [156], the forecast of the Fermilab Short-Baseline Nuetrino (SBN) program [157], and three scenarios from the Planck experiment detailed in [154]. (b) The excluded regions from the top panel mapped into the parameter space ($m^{sterile}_{eff}$,ΔN_{eff}) which are those relevant to neutrino oscillations in the fit to the power spectrum of the CMB. Differences between the Planck scenarios are negligible in the CMB parameter space. Figure reproduced from Ref. [154]. 52

2.1 A map indicating the locations of the MINOS and MINOS+ ND and FD. The ND is located at Fermilab at a baseline of 1.04 km from the target while the FD is located in the Soudan Underground Laboratory at a baseline of 735 km. Figure is reproduced from Ref. [166]. 61

2.2 The cumulative and per-week POT data exposure for the full period of MINOS and MINOS+ running. MINOS and MINOS+ collected beam data from approximately 25×10^{20} POT over a total of 13 years of running. Figure is taken from Ref. [167]. . 62

2.3 The selection of spectra plots show the samples used in the standard three-flavor MINOS and MINOS+ analysis. The top four spectra show the MINOS beam data. The lower plots show the atmospheric neutrino data obtained by both MINOS and MINOS+. The atmospheric data is plotted as a function of zenith angle and are differentiated by contained-vertex muons, non-fiducial muons, and reconstructed energy of the neutrinos. Observed data are shown as points and are compared to the unoscillated (grey) and best fit oscillated spectra(red), while cosmic ray and NC background are shown in solid grey and blue, respectively. Figure reproduced from Ref. [169]. 63

2.4 Plot showing the results of the combined three flavor analysis in terms of contours in (Δm^2_{32}, $sin^2\theta_{23}$), with the T2K results for comparison. Figure reproduced from Ref. [169]. 64

2.5 Plotted is the NuMI neutrino beam simulated reconstructed energy spectrum for the MINOS+ medium-energy configuration as the red line, the NOνA spectrum (using the same energy as the MINOS+ spectrum but at a 14 mrad offset from the beam axis, along which MINOS+ is located) as the blue shaded histogram, and the MINOS low-energy beam configuration as the shaded golden histogram. Figure reproduced from Ref. [171]. 66

2.6 Shown is a schematic drawing of the components of NuMI Beam. The beam is initiated at the left with Main Injector protons bombarding the target. Then moving rightward through the diagram, showering hadrons are focused in the electromagnetic horns and allowed to decay in the decay pipe or pass throug the hadron monitor into the absorber. Muons produced from hadronic decays pass on to muon monitors and terminate in the rock, while the neutrinos from these decays proceed on to the MINOS/MINOS+ detectors. This drawing was reproduced from Ref. [165]. 69

2.7 Diagram illustrating the focusing properties of the NuMI horns. In the horn current orientation shown positively charged hadron parents are focused while negatively charged parents are defocused. The relative position of the target with respect to the first horn generally controls the position of the energy peak. The horns are separated by a distance of 10 m and the vertical scale in the diagram is four times as large as the horizontal scale. Figure reproduced from [93]. 69

2.8 The predicted neutrino (black) and antineutrino (red) flux at the MINOS ND for configuration of the NuMI beam in neutrino optimized (left) and antineutrino optimized mode (right). The figure is reproduced from Ref. [175]. 70

2.9 The decomposition of the combined MINOS and MINOS+ ν_μ-mode neutrino beams by hadron parent (left) and beam neutrino flavor (right) as a function of the true neutrino energy. In this configuration, the beam is dominated by π^+ and K^+ parents for low- and high-energy neutrinos, respectively. 71

2.10 A schematic of the design of the NuMI graphite fin target and the canister house the target assembly. Figure is reproduced from Ref. [176]. 72

2.11 Diagram of the scintillator strip assembly used to intstrument the MINOS and MINOS+ detector planes. Scintillaton light from ionizing particles is internally relfected in the strip until it is collected by the WLS fiber. Reemission occurs isotropically so that only those photons emitted in the direction of the fiber are transmitted to the PMT assembly at the strip end. The diagram is taken from Ref. [177]. 73

2.12 Diagram of the readout assembly for the scintillator strips. The scintillation light colleced and transmitted by the WLS fiber is guided through a clear optical fiber to a single PMT pixel. The diagram is taken from Ref. [177]. 75

2.13 A schematic diagram (left) and photograph (right) of the end view of the second of two FD supermodules viewed toward the target. The labeled components in the diagram are: (A) the final FD steel plane, (B) the cosmic ray veto shield, (C) the exit point of the magnetic coil from the supermodule, and (D) one of the electronics racks situated along the sides of the detector. Other elements of the diagram are non-detector machinery or fixed structures within the FD cavern. Figure reproduced from Ref. [177]. 77

2.14 Diagram showing the orientation of the U and V orientation of scintillator strips for the FD planes. The planes alternate between U and V views in order to provide stereo readout of the position of detector hits. Figure reproduced from Ref. [177]. 77

2.15 A schematic diagram (left) and photograph (right) of the end view of the ND viewed in the direction of the NuMI beam. The labeled components in the diagram are: (A) the first ND steel plane, (B) the exit of the magnetic coil from the front face of the ND, (C) one of the electronics racks situated along the sides of the detector. The position of the (A) label also indicates the center of the beam spot on the ND. Figure reproduced from Ref. [177]. 79

2.16 A schematic of the four configurations of plane instrumentation used in the ND. The configurations are the partial U-view (upper left), the partial V-view (upper right), the full U-view (lower left), and the full V-view (lower right). The U and V view planes are alternated in the detector in order to give a stereo readout of particle track position in the detector. The partially instrumentation on the upper plane diagrams is situated to the left of the magnetic coil in order to cover the beam spot location. Diagrams are reproduced from Ref. [177]. . . . 79

2.17 A schematic model of a single subsection of the MINOS CalDet, consisting of 12 planes with alternating vertical and horizontal scintillator strip orientation. The diagram shows the readout modules on both sides of each plane, which were used to simultaneously readout signals using both FD and ND electronics. Figure reproduced from Ref. [180]. 81

2.18 The per nucleon total CC cross section for neutrinos (upper) and antineutrinos (lower) divided by and plotted as a function of the neutrino energy. The contributions from quasi-elastic (QE), resonant (RES), and deep inelastic scattering (DIS) interactions to each total cross sections are shown by various broken line styles. A selection of experimental scattering data is also plotted in order to compare with the theoretical calculations. Figure reproduced from Ref. [181]. 85

2.19 Simulated MC event topologies in the MINOS detectors for ν_μ-CC (left), ν_e-CC (center), and NC (right) interactions. Feynman diagrams describing the reactions are shown below the event displays. Figure reproduced from Ref. [183]. 87

3.1 Schematic of the calibration chain used in MINOS and MINOS+ to convert electronic signals into units of enegy. Diagram reproduced from Ref. [184]. 91

3.2 Time dependent variation in the ND (green) and FD (blue) response used in the drift and gains calibration. The drift (top) shows the daily changes in detector response normalized to the first day of data. The PMT gains (middle) show the changes in number of ADC per photoelectron averaged over three day intervals. The relative light level (bottom) is the ratio of the drift to gains. The figure is reproduced form Ref. [185]. 92

3.3 Plots showing the response of the ND (lower) and FD (upper) at different stages of the calibration procedure. Left: The raw ADC distribution. Center: Detector response after the linearity, drift, and strip-to-strip calibrations have been implemented. Right: The final post-calibration detector response after correcting fiber attenuation. Plots are shown for the V planes and similar effects are observed in the U planes. Figure taken from Ref. [187] 96

3.4 The light output observed from cosmic ray muon data (blue points) compared with the module mapper fit result (black line) for a sample ND detector strip. Figure reproduced from Ref. [177]. 98

3.5 The stopping power of copper on muons as computed by the Bethe-Bloch equation as a funtion of the muon momemtum. The relevant region in MINOS and MINOS+ is near the point of minimum ionization. Figure taken from Ref. [30]. 99

3.6 Plot of the energy loss per scintillator plane along muon tracks (upper) and the mean energy loss as a function of distance for stopping muons in the FD as a function of momentum (lower). The track window used for the inter-detector calibration is shown in the upper plot, while the lower plot shows the strong agreement between the analytical Bethe-Bloch prediciton, MC simulation, and the observed FD data. Figure reproduced from Ref. [185]. 100

3.7 Plotted are the calorimetric energy response data for pions (upper) and electrons (lower) with momenta 0.6 GeV/c (red), 1.6 GeV/C (blue), and 3.0 GeV/c (green), compared with MC simulation (black). Figure reproduced from Ref. [177]. 103

3.8 The ND reconstructed energy spectrum for focused neutrinos (left) and defocused antineutrinos (right). The spectra are plotted prior to the SKZP beam fit (blue) and after the beam fit (red). Figure taken from Ref. [167]. 106

3.9 A simulated reconstructed event display for a ν_μ-CC event in the MINOS FD. The red points indicate hits reconstructed as part of a track, which follows closely the MC true μ^- indicated by the blue line. Long muon tracks of this form are an identifying feature of the CC events. Figure reproduced from Ref. [204]. . 112

3.10 A simulated reconstructed event display for an NC event in the MINOS FD. In this event, all of the energy deposits given by the green, blue, and black circles are identified as elements of a shower feature, indicated by the yellow circles. The absence of reconstructed tracks is indicative of an NC event. Figure reproduced from Ref. [204]. 113

3.11 The ratio of the kNN shower energy to the simulated true shower energy as a function of true shower energy before and after energy corrections. A 14th order polynomial function is used in three iterations to fit and correct the kNN shower energy to improve agreement with the true shower energy. Figure taken from Ref. [187]. 114

3.12 The fractional improvement in the energy resolution due to using the kNN shower energy estimation as opposed to the calorimetric shower energy as a function of the true shower energy. Improvement along the y-axis is defined as the fractional reduction of the deviation between the mean kNN shower energy and the true shower energy. Figure reproduced from Ref. [187]. . . 115

4.1 Fiducial volume events in the MINOS/MINOS+ FD as a function of the time elapsed between the most recent beam spill and the time of the first event hit. Rejection of cosmic muon contamination is achieved by accepting only those events occuring within the $10\mu s$ window indicated by the red lines. The blue distribution represents those events passing the remainder of the preselection cuts. Figure reproduced from Ref. [175]. . . . 119

4.2 The locations of the NC-selected event vertices (black circles) in the XY-plane of the ND. The large number of events overlap significantly, which prevents resolution of the individual vertex locations. The black region therefore represents the cross sectional face of the fiducial volume. Figure reproduced from Ref. [187]. 123

4.3 The vertex positions along the Z-axis, the direction of the beam, for NC-selected events in the ND. The data and MC simulation have good agreement over the length of the detector. This distribution includes all MINOS neutrino data and the first two years of MINOS+ data. 123

4.4 The locations of the NC-selected event vertices (black circles) in the XY-plane of the FD. The events roughly indicate the cross sectional area of the fiducial volume. Figure reproduced from Ref. [187]. 124

4.5 The vertex positions along the Z-axis, the direction of the beam, for NC-selected events in the FD. The data and MC simulation have good agreement over the length of the detector. This distribution includes all MINOS neutrino data and the first two years of MINOS+ data. 124

4.6 The distribution of the ND data (black points), MC simulation (red), and poorly reconstructed background (hatched) as a function of the maximum number of consecutive planes in the event. The cleaning cut in this variable is set to reject events with less than 3 consecutive planes. 126

4.7 The distribution of the ND data (black points), MC simulation (red), and poorly reconstructed background (hatched) as a function of the slice pulse-height fraction of each event. The cleaning cut in this variable is set to reject all events with less than 0.5 of the slice pulse-height fraction. 127

4.8 The distribution of the FD (upper) and ND (lower) data (black points), MC simulation (red), and CC background (hatched) as a function of the total event length. In order to remove CC backgrounds, all events with length greater than 47 total planes are rejected. 129

4.9 The distribution of the FD (upper) and ND (lower) data (black points), MC simulation (red), and CC background (hatched) as a function track extension of the longest reconstructed track in the event. In order to remove CC backgrounds, all events with a reconstructed track extending greater than 6 planes beyond the reconstructed shower are rejected. 130

4.10 The locations of the CC-selected event vertices (black circles) in the XY-plane of the ND. The large number of events overlap significantly, which prevents resolution of the individual vertex locations. The black region therefore represents the cross sectional face of the fiducial volume. Figure reproduced from Ref. [187]. 133

4.11 The locations of the CC-selected event vertices (black circles) in the XY-plane of the FD. The events roughly indicate the cross sectional area of the fiducial volume. Figure reproduced from Ref. [187]. 134

4.12 Distributions in data (black points), tuned MC simulation (red), and estimated total background (blue) at the ND for the four variable inputs used by the kNN roID selector. Estimated systematic uncertainties on the roID input variable are indicated by the shaded regions. Figures reproduced from Ref. [209]. . . 137

4.13 The distribution at the ND of true MC simulated CC events and NC events as a function of the roID (left) and the comparison of the total MC sample to the ND data (right). The ratio of the ND data to MC indicates reasonable agreement above the cutoff for NC separation, which is set at roID > 0.3 in this selector. The comparison of signal CC to background NC demonstrates the suitability of setting the cut at the stated value. Figure reproduced from Ref. [187] 138

4.14 The ND distributions of the MINOS data (black points) and MC simulation (red line) for the three additional variables used by the jmID selector. The estimated systematic uncertainties of the distributions are given by the shaded bands and the estimated total background is indicated by the blue distribution. The figure is reproduced from Ref. [175]. 141

4.15 A plot of the distribution of MINOS data events as a function of the jmID CC/NC separaton variable. The total MC prediction (red) is plotted in comparison to the data (black points) and the estimated total background (blue). The optimized cut value for background elimination in this variable is set at jmID < 0.5. The figure is reproduced from Ref. [175]. 142

4.16 Efficiency (blue) and purity (red) of the NC selected sample as a function of the reconstructed energy. The ND distributions are plotted with solid lines, while the FD distributions are given by the dashed lines. 146

4.17 Efficiency (blue) and purity (red) of the CC selected sample as a function of the reconstructed energy. The ND distributions are plotted with solid lines, while the FD distributions are given by the dashed lines. 146

5.1 Fractional systematic uncertainties due to mismodeling of detector acceptance as a function of reconstructed energy for CC-selected events (left) and NC-selected events(right). The acceptance systematics quantify the estimated uncertainty due to geometric effects in the ND caused by a shorter baseline and smaller detector volume. The total acceptance uncertainty given by the black line is the sum in quadrature of the underlying components. 155

5.2 Total fractional uncertainty, covariance matrix, and correlation matrix for all acceptance systematic uncertainties in the CC sample. Top: Total of summed CC acceptance systematic uncertainties before and after decorrelation. Bottom: Summed CC acceptance covariance matrix (left) and associated correlation matrix (right). 156

5.3 Total fractional uncertainty, covariance matrix, and correlation matrix for all acceptance systematic uncertainties in the NC sample. Top: Total of summed NC acceptance systematic uncertainties before and after decorrelation. Bottom: Summed NC acceptance covariance matrix (left) and associated correlation matrix (right). 157

5.4 Fractional systematic uncertainties due to mismodeling of background events as a function of reconstructed energy for CC-selected events (top) and NC-selected events (bottom) at the FD (left) and ND (right). The background systematics quantify the estimated uncertainty due to the spectral distortions caused by variations in the proportion of selected background events. The total background uncertainty refers to NC events selected in the CC sample or conversely CC events selected in the NC sample. 160

5.5 Total fractional uncertainty, covariance matrix, and correlation matrix for NC background systematic uncertainty in the CC sample. Top: NC background systematic uncertainty before and after decorrelation. Bottom: NC background covariance matrix (left) and associated correlation matrix (right). 161

5.6 Total fractional uncertainty, covariance matrix, and correlation matrix for CC background systematic uncertainty in the NC sample. Top: CC background systematic uncertainty before and after decorrelation. Bottom: CC background covariance matrix (left) and associated correlation matrix (right). 162

5.7 Fractional systematic uncertainties due to mismodeling of energy reconstruction and calibration as a function of reconstructed energy for CC-selected events (top) and NC-selected events (bottom) at the FD (left) and ND (right). The energy scale systematics quantify the estimated uncertainty arising from errors and mismodeling in determing the energy deposited by both muon tracks and hadronic showers in the detectors. The total energy scale uncertainty given by the black line is the sum in quadrature of the underlying components. 165

5.8 Total fractional uncertainty, covariance matrix, and correlation matrix for energy scale systematic uncertainties in the CC sample. Top: Total of summed CC energy scale systematic uncertainties before and after decorrelation. Bottom: Summed CC energy scale covariance matrix (left) and associated correlation matrix (right). 166

5.9 Total fractional uncertainty, covariance matrix, and correlation matrix for energy scale systematic uncertainties in the NC sample. Top: Total of summed NC energy scale systematic uncertainty before and after decorrelation. Bottom: Summed NC energy scale covariance matrix (left) and associated correlation matrix (right). 167

5.10 Comparison of the ratios of pions and kaons in data and FLUKA MC simulation in bins of transverse and longitudinal momentum. The right column shows the π^+/K^+ ratio, which provides justification for the use of identical weights as a function of kinematic parameters. The figure is reproduced from Ref. [219]. 169

5.11 The spectrum of reconstructed ν_μ CC events decomposed by parent hadron. Pion parents are the dominant parent hadron from 0-25 GeV above which kaon parents dominate. 170

5.12 Plots showing the population of the $p_T - p_Z$ phase space by the predominantly K^+ hadron parents for the range of neutrino energies from 35-40 GeV (upper group of four) and the predominantly π^+ hadron parents for the range of neutrino energies 0-20 GeV (lower group of four). Note that phase spaces are shared only marginally, necessitating the use of an empirical parameterization [220] in order to span the disjoint samples. . 171

5.13 Left: Plot showing the results of MC tuning through the beam fit procedure to the predicted reconstructed energy spectra for PPFX MC simulated pions with horn focusing on (left), PPFX MC simulated pions with horn focusing off (center), and MINOS+ data collected with horn focusing off (right). The PPFX pion flux prediction is fit for reconstructed energies ranging from 0-20 GeV while the MINOS+ data in the range of 40-60 GeV in reconstructed energy is used to constrain the normalization of the fit. The parameters extracted from this beam fit reparameterize the flux predicted by PPFX and are used to correct the flux prediction used in the MINOS and MINOS+ sterile neutrino search. 173

5.14 Fractional systematic uncertainties due to mismodeling of hadron production as a function of reconstructed energy for CC-selected events (top) and NC-selected events (bottom) at the FD (left) and ND (right). Hadron production uncertainties result from generating 100 alternate fluxes reweighted using the PPFX procedure with input parameters randomly varied within their uncertainty. To visualize the uncertainties, the resulting covariance matrix is decomposed into principal components representing the most important correlated sources of variation, the first five of which are plotted as fractional uncertainty bands. . 175

5.15 Total fractional uncertainty, covariance matrix, and correlation matrix for hadron production systematic uncertainties in the CC sample. Top: Total of summed CC hadron production systematic uncertainties before and after decorrelation. Bottom: Summed CC hadron production covariance matrix (left) and associated correlation matrix (right). 176

5.16 Total fractional uncertainty, covariance matrix, and correlation matrix for hadron production systematic uncertainties in the NC sample. Top: Total of summed NC hadron production systematic uncertainty before and after decorrelation. Bottom: Summed NC hadron production covariance matrix (left) and associated correlation matrix (right). 177

5.17 Fractional systematic uncertainties due to mismodeling of the magnetic field of the horns as a function of reconstructed energy for CC-selected events (top) and NC-selected events (bottom) at the FD (left) and ND (right). The sources of systematic uncertainty directly related to the magnetic horns include the position of the horns, the skin depth of the current flowing through the horns, and the magnitude of the current delivered during each beam spill. The total uncertainty given by the black line is the sum in quadrature of the underlying components. 181

5.18 Fractional systematic uncertainties due to mismodeling of the beam optics apart from the magnetic horns as a function of reconstructed energy for CC-selected events (top) and NC-selected events (bottom) at the FD (left) and ND (right). The beam optics uncertainties not directly related to the magnetic field in the horns are due to the beam position and width, the position of the target, and the material error in the beamline. The total uncertainty given by the black line is the sum in quadrature of the underlying components. 182

5.19 Total fractional uncertainty, covariance matrix, and correlation matrix for beam optics systematic uncertainties in the CC sample. Top: Total of summed CC beam optics systematic uncertainties before and after decorrelation. Bottom: Summed CC beam optics covariance matrix (left) and associated correlation matrix (right). 183

5.20 Total fractional uncertainty, covariance matrix, and correlation matrix for beam optics systematic uncertainties in the NC sample. Top: Total of summed NC beam optics systematic uncertainty before and after decorrelation. Bottom: Summed NC beam optics covariance matrix (left) and associated correlation matrix (right). 184

5.21 Fractional systematic uncertainties due to mismodeling of the cross sections as a function of reconstructed energy for CC-selected events (top) and NC-selected events (bottom) at the FD (left) and ND (right). Systematic uncertainties resulting from scaling M_A^{QE}, M_A^{RES}, and KNO scaling parameters can result in shape distortions in the energy spectra. The overall cross section systematic uncertainties are approximately normalization shifts (i.e. uniform with respect to reconstructed energy). The overall CC cross section systematic shift is constrained by experiments analyzing high energy neutinos such as CCFR. The overall NC cross section systematic shift is determined by comparing the rates of events with and without tracks at NOMAD and MINOS. The total uncertainty given by the black line is the sum in quadrature of the underlying components. 187

5.22 Total fractional uncertainty, covariance matrix, and correlation matrix for cross section systematic uncertainties in the CC sample. Top: Total of summed CC cross section systematic uncertainties before and after decorrelation. Bottom: Summed CC cross section covariance matrix (left) and associated correlation matrix (right). 188

5.23 Total fractional uncertainty, covariance matrix, and correlation matrix for cross section systematic uncertainties in the NC sample. Top: Total of summed NC cross section systematic uncertainty before and after decorrelation. Bottom: Summed NC cross section covariance matrix (left) and associated correlation matrix (right). 189

5.24 Total fractional uncertainty, covariance matrix, and correlation matrix for normalization systematic uncertainties in the CC sample. Top: Total of summed CC normalization systematic uncertainties before and after decorrelation. Bottom: Summed CC normalization covariance matrix (left) and associated correlation matrix (right). 191

5.25 Total fractional uncertainty, covariance matrix, and correlation matrix for normalization systematic uncertainties in the NC sample. Top: Total of summed NC normalization systematic uncertainty before and after decorrelation. Bottom: Summed NC normalization covariance matrix (left) and associated correlation matrix (right). 192

5.26 Fractional systematic uncertainties due to mismodeling of the neutral current cleaning cuts as a function of reconstructed energy for CC-selected events (top) and NC-selected events (bottom) at the FD (left) and ND (right). The systematic uncertainties are estimated for the cleaning cuts applied in the procedure for NC selection to remove poorly reconstructed events in the ND and detector noise and cosmic ray muons in the FD. The total uncertainty given by the black line is the sum in quadrature of the underlying components. 195

5.27 Total fractional uncertainty, covariance matrix, and correlation matrix for NC cleaning systematic uncertainties. Top: Total of summed NC cleaning systematic uncertainty before and after decorrelation. Bottom: Summed NC cleaning covariance matrix (left) and associated correlation matrix (right). 196

5.28 Total fractional uncertainty, covariance matrix, and correlation matrix for combination of all sources of systematic uncertainty studied for the CC sample. Top: Combined systmatic uncertainty relative error band before and after decorrelation. Bottom: The combined CC systematic uncertainty covariance matrix used in the steril neutrino search (left) and associated correlation matrix (right). 198

5.29 Total fractional uncertainty, covariance matrix, and correlation matrix for combination of all sources of systematic uncertainty studied for the NC sample. Top: Combined systmatic uncertainty relative error band before and after decorrelation. Bottom: The combined NC systematic uncertainty covariance matrix used in the steril neutrino search (left) and associated correlation matrix (right). 199

6.1 Plotted are oscillation probabilities as a function of L/E showing the effect of neutrino oscillations in the case of a standard three-flavor oscillations paradigm. The probabilities shown indicate muon neutrino survival (blue), electron neutrino appearance (violet), tau neutrino appearance (green), and the sum total of these probabilities (red) given by the expression $1 - P(\nu_\mu \to \nu_s)$ since no sterile neutrinos exist in the case of three-flavor oscillations. A single oscillation maximum is observed in the MINOS/MINOS+ FD (right shaded region) with no oscillations observed in the ND (left shaded region). In the standard oscillations picture, no sterile neutrino appearance probability is present. 203

6.2 Plotted are oscillation probabilities as a function of L/E showing the effect of the mass-squared splitting Δm^2_{32} for ν_μ-CC disappearance (top) and NC disappearance (bottom). The Δm^2_{32} parameter governs the position of the standard atmospheric neutrino oscillation maximum observed in the FD for muon neutrino disappearance and introduces a similarly located deficit associated with sterile neutrino appearance. The black line gives the probabilities associated with the global best-fit parameters in Figure 1.6. For the color lines, parameters not explicitly stated are fixed to the values shown in Table 6.1. 205

6.3 Plotted are oscillation probabilities as a function of L/E showing the effect of the atmospheric mixing angle θ_{23} for ν_μ-CC disappearance (top) and NC disappearance (bottom). The atmospheric mixing angle determines the magnitude of the deficit observed in both muon neutrino and NC disappearance channels. The black line gives the probabilities associated with the global best-fit parameters in Figure 1.6. For the color lines, parameters not explicitly stated are fixed to the values shown in Table 6.1. 206

6.4 Plotted are oscillation probabilities as a function of L/E showing the effect of the mass squared splitting Δm^2_{41} (top row) and the ratios of the probabilities with respect to the three-flavor global fit (bottom row) for ν_μ-CC disappearance (left column) and NC disappearance (right column). MINOS and MINOS+ are primarilty sensitive to Δm^2_{41} and θ_{24} in a search for sterile neutrino-mediated oscillations. The black line gives the probabilities associated with the global best fit parameters in Figure 1.6. For the color lines, parameters not explicitly stated are fixed to the values shown in Table 6.1. 210

6.5 Plotted are oscillation probabilities as a function of L/E showing the effect of the mixing angle θ_{24} (top row) and the ratios of the probabilities with respect to the three-flavor global fit (bottom row) for ν_μ-CC disappearance (left column) and NC disappearance (right column). The θ_{24} parameter is the second of the principle dimensions, along with Δm^2_{41} of the parameter space accessible to this analysis. The black line gives the probabilities associated with the global best fit parameters in Figure 1.6. For the color lines, parameters not explicitly stated are fixed to the values shown in Table 6.1. 213

6.6 Plotted are oscillation probabilities as a function of L/E showing the effect of the mixing angle θ_{34} (top row) and the ratios of the probabilities with respect to the three-flavor global fit (bottom row) for ν_μ-CC disappearance (left column) and NC disappearance (right column). The θ_{34} mixing angle is a free parameter in the fit described in this analysis. The black line gives the probabilities associated with the global best fit parameters in Figure 1.6. For the color lines, parameters not explicitly stated are fixed to the values shown in Table 6.1. 215

6.7 The beam matrix used in the extrapolation of the FD reconstructed energy spectrum for the standard oscillations analysis (left) together with the simulated ND and FD reconstructed energy spectra (right). The transformation of the hatched regions between the FD and ND spectra demonstrates the effect of applying the beam matrix. Figures are reproduced from Reference [92]. 217

6.8 The Far-over-Near ratios for MINOS data (black points) plotted with the three-flavor simulation (red line) for the parameters listed on the plot with the uncorrelated systematic uncertainty given by the red shaded band. Events selected by the CC selector are shown in the upper plot while events selected by the NC selector are shown in the lower plot. The data and three-flavor prediction shown in this plot are reproduced from the similar figure in Reference [155]. 219

6.9 MC simulation of predicted reconstructed energy spectra and Far-over-Near ratio for three-flavor oscillations and (3+1)-flavor oscillations at a test point in parameter space where $\theta_{24} = 0.2$ and $\Delta m^2_{41} = 80.0\, eV^2$. The FD (upper left) and ND (upper center) simulated reconstructed energy spectra are plotted. Using these plots as input, the ratios of the (3+1)-flavor prediction with respect to the standard three flavor prediction are plotted for the FD (lower left) and ND (lower center) as well as the simulated Far-over-Near ratio for 3- and (3+1)-flavor oscillations (upper right). Using the Far-over-Near ratio results, the double Far-over-Near ratios of the simulated spectra with respect to three-flavor oscillations are plotted (lower right). . . 221

6.10 Plotted are the number of ν_μ produced from the decay of π^+ (black) or K^+ (red) and the number of $\bar{\nu_\mu}$ produced from the decay of π^- (blue) or K^- (green) as a function of the distance traveled by the neutrino prior to detection in the ND. The baseline information of the simulated neutrinos is preserved by the generation of L/E versus reconstructed energy matrices which are used to generate oscillated predictions for ND and FD reconstructed energy. 228

6.11 The combined total of systematic and statistical fractional uncertainty for the ν_μ-CC sample is plotted as a function of the reconstructed energy for at the FD (upper left) and ND (upper right). The fractional uncertainty bands are computed from the square roots of the diagonal elements of the summed statistical and systematic matrices. The red band corresponds to the diagonal of the covariance matrix before the decorrelation procedure (lower left), and the blue line corresponds to the diagonal after the decorrelation procedure (lower right) 230

6.12 The combined total of systematic and statistical fractional uncertainty for the NC sample is plotted as a function of the reconstructed energy for at the FD (upper left) and ND (upper right). The fractional uncertainty bands are computed from the square roots of the diagonal elements of the summed statistical and systematic matrices. The red band corresponds to the diagonal of the covariance matrix before the decorrelation procedure (lower left), and the blue line corresponds to the diagonal after the decorrelation procedure (lower right) 233

6.13 Comparison of the Asimov sensitivities computed using the simultaneous Two-Detector fit method for MINOS and MINOS+ simulation (black) with the Far-over-Near ratio method for the MINOS only analysis (green) and the combined MINOS and MINOS+ analysis (orange). The two-detector method has significantly higher sensitivity for all Δm^2_{41} with the greatest improvement at large mass-splitting. 235

6.14 The 90% C.L. Asimov sensitivities computed in the simultaneous Two-Detector fit framework for the isolated ν_μ-CC sample (blue), the isolated NC sample (red), and the joint ν_μ-CC and NC fit (black). The ν_μ-CC sample provides the dominant sensitivity for all regions of the parameter space. The NC sample provides additional sensitivity at very high mass-splitting and in the region surrounding the atmospheric oscillations degeneracy discussed in Chapter 7. 236

6.15 Asimov sensitivities for the simultaneous Two-Detector fit method compared with the independent fits to the ND and FD. The detector contributions are plotted for fits to the isolated ν_μ-CC sample (bottom left), the isolated NC sample (bottom right), and the joint ν_μ-CC and NC fit (top). 238

6.16 The χ^2 function for three flavor fake data scaled by a normalization factor. This implies that the effective normalization systematic is $\sim$3%. 239

6.17 Comparison of the simultaneous Two-Detector Asimov sensitivity (red) to the contributions from the spectral shape variations (green) and the normalization systematic uncertainty (blue) as extracted in post-fit analysis. The normalization component dominates the sensitivity for $\Delta m^2_{41} > 100$ eV^2 while shape information dominates the sensitivity for the remainder of the parameter space. 241

6.18 Ratios of pseudodata samples with symmetrically varied systematics parameters to the Asimov spectrum (right) and the resulting Asimov and fluctuated sensitivities in the sterile parameter space (left). The symmetry observed in the comparison of fluctuated and Asimov spectra is not translated to a symmetric response in the sensitivities. 243

6.19 Demonstration of the effects on the Asimov sensitivity for normalization-only variations to the spectrum. The simulated data samples with normalization shifts 244

6.20 A simulated ν_μ-CC data study of the differences between the Asimov senstivity and median sensitvity of an ensemble of pseudoexperiments for the standard covariance matrix (top row), the covariance matrix with correlations removed (center row), and statistical uncertainty only (bottom row). The left column is generated using the full simulated ND CC sample, while the right column is produced with a scaled down ND CC sample in order to increase the significance of statistical uncertainties. . 246

7.1 The FD CC-selected (left) and ND CC-selected (right) reconstructed energy data sample (black points) compared to the simulated prediction for standard three-flavor oscillations (red) displayed with the uncorrelated systematic uncertainty (red shading). The background events are also plotted in stacked histograms, with the NC events representing the dominant background component. 249

7.2 The FD NC-selected (left) and ND NC-selected (right) reconstructed energy data sample (black points) compared to the simulated prediction for standard three-flavor oscillations (red) displayed with the uncorrelated systematic uncertainty (red shading). The background events are also plotted in stacked histograms, with the ν_μ-CC events representing the dominant background component. The variations in the relative composition of the background events is due to the effects of three-flavor oscillations. 249

7.3 The double ratio of the Far-over-Near ratio in data (black) to the Far-over-Near ratio for the standard three-flavor prediction (dashed red) for the CC-selected sample (left) and the NC-selected sample (right). Relative statistical uncertainties are represented by the black error bars, while the relative decorrelated systematic uncertainties are shown by the red shaded bands. The χ^2 per degree of freedom and p-values are computed using the standard Pearson's χ^2 test [241] and are insufficient to reject the null three-flavor oscillations hypothesis at a reasonable level of confidence. 250

7.4 The χ^2 surfaces in the $(\sin^2(\theta_{24}), \Delta m^2_{41})$ parameter space resulting from the simultaneous Two-Detector fit to data (upper) and to the Asimov spectrum (lower). The contour at the nominal $\Delta\chi^2_{2,0.9} = 4.61$ value for the 90% C.L. is drawn (red) without correction by the FC method. 253

7.5 Contours of constant $\Delta\chi^2$ resulting from the (3+1)-flavor model Two-Detector Fit to MINOS and MINOS+ data are plotted in the parameter space $(\sin^2(\theta_{24}), \Delta m^2_{41})$. The plotted contours are the raw output of the fit framework and have not been corrected by the FC method. 254

7.6 The FD CC-selected (left column) and the ND CC-selected (right column) reconstructed energy data sample (black points) compared to the standard three-flavor oscillations prediction (red) and the best-fit 3+1-flavor predictions (blue). The upper plots show the raw spectra and uncorrelated systematic uncertainties while the lower plots show the spectra and residual uncertainties after the application of the decorrelation procedure to both the three-flavor predictions and the (3+1)-flavor best-fit predictions. 256

7.7 The FD NC-selected (left column) and the ND NC-selected (right column) reconstructed energy data sample (black points) compared to the standard three-flavor oscillations predictions (red) and the best-fit 3+1-flavor predictions (blue). The upper plots show the raw spectra and uncorrelated systematic uncertainties while the lower plots show the spectra and residual uncertainties after the application of the decorrelation procedure to both the three-flavor predictions and the (3+1)-flavor best-fit predictions. 258

7.8 Oscillation probability curves plotted for sets of (3+1)-flavor parameters which result in approximately degenerate solutions to the standard three-flavor oscillations case. The analysis presented here does not strongly distinguish between these approximate degeneracies. 259

7.9 The χ^2 surfaces in the $(\sin^2(\theta_{24}), \Delta m^2_{41})$ parameter space for the CC (left) and NC (right) component samples resulting from the simultaneous Two-Detector fit to data (upper) and to the Asimov spectrum (lower). The contours at the nominal $\Delta\chi^2_{2,0.9} = 4.61$ value for the 90% C.L. are drawn (red) with respect to the best-fit point for the joint fit and without correction by the FC method. The minimum χ^2 point in each component plot is indicated by the green point. 265

7.10 The upper limit contour at 90% C.L. in the parameter space $(\sin^2(\theta_{24}), \Delta m^2_{41})$ resulting from the (3+1)-flavor model Two-Detector Fit to the combined ν_μ-CC and NC samples (black) in comparison to the limits computed from the CC (blue) and NC (red) component surfaces in the joint fit. All contours are constructed by considering the $\Delta\chi^2$ with respect to the joint best-fit point. The plotted contours are the raw output of the fit framework and have not been corrected by the FC method. 267

7.11 Comparison of the simultaneous Two-Detector data fit upper limit at 90% C.L. (red) to the contributions from the spectral shape variations (green) and the normalization systematic uncertainty (blue) as extracted in post-fit analysis. The shape component is the dominant contribution to the total limit for very nearly the entire range of mass-splittings with the normalization constraint providing additional exclusion for $\Delta m^2_{41} > 10$ eV^2. The contours plotted in this figure follow the structure established in Fig. 6.17. 270

7.12 Example simulated spectra for the Asimov experiment (black) and statistically and systematically fluctuated pseudodata used for statistical analysis of the Two-Detector fit. Fluctuated pseudodata are used in the FC correction method (see Figs. 7.13 and 7.14), in the generation of the fluctuated sensitivity band (see Fig. 7.16), and in the CL_s method (see Figs. 7.17 and 7.18). 275

7.13 The $\Delta\chi^2$ distribution at a sample point in the $(\sin^2(\theta_{24}), \Delta m^2_{41})$ parameter space used for the determination of the FC correction. Using the standard 90% C.L. critical value $\Delta\chi^2 = 4.61$ results in the exclusion of this point by 29% of pseudoexperiments. The ensemble of pseudoexperiments indicate that for a true confidence level of 90%, a $\Delta\chi^2_{\acute{c}ritical} = 6.72$ must be observed in order to ensure the proper frequentist coverage. . . . 276

7.14 The FC correction surface as computed for the Two-Detector fit. Corrected $\Delta\chi^2$ critical values are indicated by the shaded scale. The raw data exclusion contour at 90% C.L. (orange) is compared with the exclusion contour at 90% C.L. after the application of the FC correction (red). 277

7.15 Comparison of the simultaneous Two-Detector data fit upper limit at 90% C.L. with previous results from IceCube [156], Super-K [247], CDHS [248], CCFR [230], and SciBooNE/MiniBooNE [131] constraining this parameter space. The Gariazzo et al. region is the result of a fit using a (3+1)-flavor model to global neutrino oscillation data [142]. 280

7.16 Plotted are the MINOS and MINOS+ data upper limit (black) and median fluctuated sensitivity (blue dashed) at 90% C.L. in the $(\sin^2(\theta_{24}), \Delta m^2_{41})$ parameter space resulting from the simultaneous Two-Detector fit after the FC correction. The bands surrounding the median sensitivity indicate the regions containing 68% (green) and 90% (yellow) of the 90% C.L. sensitivity contours resulting from statistically and systematically varied pseudoexperiments. 281

7.17 Comparison of the upper limits derived from the data fit using the FC method and the CL_s method. The limits are mutually consistent within the variations caused by statistical fluctuations in the samples of pseudoexperiments produced in both methods. 283

7.18 The joint exclusion contour at 90% CL_s for the MINOS/MINOS+ and Daya Bay/Bugey-3 combination in the parameter space $(\sin^2 2\theta_{\mu e}, \Delta m^2_{41})$. Previous exclusion results from the MINOS and Daya Bay/Bugey-3 combination [249], KARMEN2 [148], and NOMAD [149] are plotted in addition to allowed regions from short-basline ν_e ($\bar{\nu}_e$) appearance experiments LSND [120] and MiniBooNE [250] for comparison. 286

7.19 Projection of the (3+1)-flavor model 90% C.L. exclusion contour into the space of oscillation probabilities. Upper row: The probability curves associated with the best-fit (3+1)-flavor model parameters at points forming the exclusion contour are plotted for ν_μ-CC disappearance (left) and NC disappearance (right). Lower row: Taking the minimum probability as the conservative (largest) estimate of the oscillation magnitude at each value of L/E in the upper plots results in the excluded regions (dark shading) in probability space. For comparison, the MINOS and MINOS+ data ratio to the null-oscillations hypothesis (black points), estimated residual uncertainty bands (light shading bands), and (3+1)-flavor model best-fit probability curves are plotted for comparison to the excluded region. . 290

8.1 The expected senstivity of the Fermilab SBN program in a three-detector analysis with the listed POT accumulations in Ref. [157] used for scaling the data sample. The LSND, MiniBooNE and global fit allowed regions, and several exclusion limits corresponding to those shown in Fig. 7.18 are also plotted for comparison. 293

8.2 The simulated senstivity of DUNE for 3.5 years each of running in neutrino and antineutrino mode assuming a 40-kt fiducial mass far detector in an 80-GeV, 1.07 MW beam. The LSND, MiniBooNE and global fit allowed regions, and several exclusion limits corresponding to those shown in Fig. 7.18 are also plotted for comparison. Figure taken from Reference [251]. 294

List of Tables

2.1 Summary of data runs collected by the MINOS and MINOS+ experiments. MINOS data is dominated by the low energy (LE) beam configuration with a brief pseudo-high energy (pHE) during the first running period. MINOS+ data was collected exclusively usng the medium energy (ME) beam configuration. MINOS collected data in both ν_μ and $\bar{\nu}_\mu$ mode running, while MINOS+ collected only ν_μ mode data. Data in this table was compiled from Refs. [172] and [173]. 67

4.1 Integrated efficiencies and purities for the CC and NC selectors in the ND and FD. 148

5.1 Sources of systematic uncertainty affecting the normalization of the reconstructed energy spectra and the estimated relative size of each effect. Normalization systematic uncertainties listed here were calculated in [232]. 190

6.1 The nominal (3+1)-flavor oscillation parameters used for the generation of sample probability curves in Figs. 6.2, 6.3, 6.4, 6.5, and 6.6, except when differing values are explicitly stated. 204

6.2 The parameters for the (3+1)-flavor oscillation model analyzed in the simultaneous two-detector fit listed with fit status, either free or fixed, along with the constraints used in the fit. 225

7.1 Critical values defining the tail probability (Confidence Level) of the χ^2_k distribution where k is the number of degrees of freedom. 255

7.2 Best-fit parameter values in the (3+1)-flavor model from the simultaneous Two-Detector fit to the combined MINOS and MINOS+ ν_μ-CC and NC disappearance samples. The preferred parameter values for the CC and NC component contributions to the joint fit are shown for comparison. 257

7.3 The cumulative reduction of the experimental sensitivity as determined from the median of fluctuated pseudoexperiments to the oscillations parameter $\sin^2\theta_{24}$ due to the effects of systematic uncertainties for selected values of Δm^2_{41}. The sources of systematic uncertainty given in this table are described in detail in Chapter 5. 263

7.4 The contributions to the χ^2 test statistic at the (3+1)-flavor best fit to MINOS and MINOS+ ν_μ-CC and NC data. The best-fit χ^2 to the three-flavor hypothesis and the $\Delta\chi^2$ differentiating (3+1)- and three-flavor hypotheses are also given. 266

Chapter 1

Neutrino Physics

In this chapter, we introduce the physics of neutrinos both from a historical perspective and in discussion of the modern theoretical understanding. We first give a chronological overview of the discovery of the leptonic sector including the three flavors of active neutrinos. This is followed by a detailed discussion of the discovery and formalism of the phenomenon of neutrino oscillations. We then discuss results which are anomalous when viewed in the context of the assumed three-flavor oscillations paradigm. The chapter concludes with a discussion of the motivation and formalism describing sterile neutrinos, which will be the target of the search described in this thesis.

1.1 Origins

James Chadwick, while a student of Hans Geiger in 1914 at the *Physikalisch-Technische Reichsanstalt*, used his supervisor's new namesake counting device and a magnetic spectrometer to precisely measure the energy spectrum of β-radiation [1]. The β-particle had already been determined by Henri Becquerel in 1900 to be identical to the electron observed by J.J. Thomson in cathode rays [2], and it was assumed that β-decay consisted of the emission of an elec-

tron from the atomic nucleus in a two-body process [3]. It is in this context that the observations of the energy spectra of β-decay by Chadwick were unexpected; instead of the discrete energies anticipated for the supposed two-body decay process a continuous energy spectrum was observed. After many years of further experimentation [4][5][6], the continuous velocity distribution of the β-particles was finally accepted as a reproducible effect in 1927. The apparent violation of the law of conservation of energy in β-decays very nearly led to the abandonment of this general principle in favor of a mere statistically realized conservation of energy, as was advocated by Niels Bohr [7].

In 1930, Wolfgang Pauli proposed a novel, as-yet-undetected particle in what he called a "desperate remedy" to save the strict conservation of energy, momentum, and angular momentum in β-decays [7]. Pauli called the undetected particle the "neutron" (this was prior to the discovery of the baryon we now know as the neutron by Chadwick in 1932 [8]). Enrico Fermi later introduced the name "neutrino" to distinguish it from Chadwick's neutron at the Paris Conference of July 1932, and again at the Seventh Solvay Conference in October 1933. Incidentally, the name is in fact due to Edoardo Amaldi by way of a conversation with Fermi at the Institute of Physics in *Via Panisperna* in Rome where he used the Italian diminutive *-ino* to denote this new "small neutral thing" [9]. Fermi unified several postulated particles and related models in his theory of β-decay in 1934 [10][11] in which he proposed the interaction

$$n^0 \rightarrow p^+ + e^- + \nu \tag{1.1}$$

where n^0 is Chadwick's neutron, e^- is the ejected β-particle, and the neutrino,

ν, carries away missing energy and spin permitting preservation of the conservation laws. Fermi's theory was met with skepticism and a general lack of interest by contemporaries to such an extent that it was rejected by the journal *Nature* requiring instead publication in *Zeitschrift für Physik* [9].

1.1.1 Neutrino Discovery

Experimental verification of what is now known to be the antineutrino was finally achieved through the Cowan-Reines experiments [12][13][14], the definitive results of which were collected at the Savannah River nuclear power plant and published in 1956 [15]. The experiment specifically searched for the process of inverse beta decay due to nuclear reactor antineutrinos. The detector used by Cowan and Reines consisted of a water target, cadmium chloride neutron absorber, and adjacent liquid scintillator tanks equipped with photomultiplier tubes. The inverse beta decay process, which was studied by Bethe and Peierls as early as 1934 [16], can be written

$$\bar{\nu}_e \ + \ p^+ \ \rightarrow n^0 \ + \ e^+, \tag{1.2}$$

where the absorption by a proton of an electron antineutrino produces a positron that rapidly annihilates with an electron to produce two gamma rays (photons), and a neutron. The neutron was then absorbed by cadmium, a highly effective neutron absorber, in the process

$$n^0 \ + \ {}^{108}\mathrm{Cd} \ \rightarrow \ {}^{109m}\mathrm{Cd} \ \rightarrow \ {}^{109}\mathrm{Cd} \ + \ \gamma \tag{1.3}$$

producing an additional photon, which was expected to follow the two initial photons after an elapsed time $\sim 5\ \mu$s. The detection in the liquid scintillator detectors of a pair of photons from positron-electron annihilation and the subsequent cadminum neutron absorption photon following with the expected time delay proved to be a distinctive signature that antineutrinos were being produced in the nuclear reactor as was predicted. As a result of the successful discovery of the antineutrino, Reines was awarded the 1995 Nobel Prize in Physics (Cowan had died in 1974).

1.1.2 Neutrino Flavors

In 1936, Anderson and Neddermeyer observed evidence for a new particle using a cloud chamber experiment to analyze the constituents of cosmic rays [17]. The new particle, which would later be called the muon, was found to have similar ionization characteristics to fast electrons, indicating an identical charge, but markedly different track curvature in the presence of a magnetic field, indicating a heavier mass than a free electron [18]. Several decades later in 1960, Bruno Pontecorvo would hypothesize the existence of a new neutrino state [19], the muon neutrino ν_μ, which results from the decay of pions to muons and is distinct from the electron neutrino ν_e associated with β-decay.

Motivated by the work of Pontecorvo, an experimental group of Lederman, Schwartz, and Steinberger used the Alternating Gradient Synchrotron (AGS) at Brookhaven National Laboratory (BNL) in order to search for the new muon neutrino [20]. The neutrinos analyzed in this experiment were pro-

duced in a beam of unfocused, decaying pions resulting from the bombardment of a beryllium target using a 15 GeV proton beam. The beam was terminated by a 13.5 m thick iron shield wall at a baseline of 21 m, which allowed neutrinos in the beam to pass through to the detector to the exclusion of other beam particles. The neutrino detector used in the experiment was a 10 ton aluminum spark chamber, which permitted the differentiation between electron and muon tracks. A total of 34 single-track muon events were observed with 5 of these events being attributed to cosmic ray background. However, instead of the 29 electron shower events that would have been predicted by a $\nu_\mu = \nu_e$ model, only six electron events were observed. This result demonstrated that the neutrinos have at least two generations corresponding to known lepton flavors. The Nobel Prize was awarded for the discovery of the muon neutrino and the pioneering work on the neutrino beam method in 1988.

The existence of a third, heavier lepton flavor was explored theoretically in 1971 [21]. The observation of the third lepton was first made indirectly by a joint SLAC-LBL research group under the leadership of Martin Perl using the Stanford Positron Electron Asymmetric Rings (SPEAR) and the SLAC-LBL magnetic detector [22]. Though this early work only reported on events of the type

$$e^+ + e^- \rightarrow e^\pm + \mu^\mp + \text{missing energy} \tag{1.4}$$

subsequent measurements [23] verified that the interaction that had been observed was in fact given by

$$e^+ + e^- \rightarrow \tau^+ + \tau^- \rightarrow e^\pm + \mu^\mp + 4\nu \tag{1.5}$$

where the new heavy lepton was given the name tau (τ) [24] as derived from the Greek $\tau\rho\iota\tau o\nu$ ("triton", meaning third, it having been the third discovered lepton). Perl would be awarded the Nobel Prize for this discovery in 1995. The scientific community having grown accustomed to the correspondence of lepton and neutrino flavors, a third ν_τ neutrino flavor was naturally anticipated. In 2000, the DONUT experiment at Fermilab reported on the first direct observation of interactions involving the tau neutrino [25]. The neutrino beam used in this experiment was generated from 800 GeV protons accelerated in the Tevatron rings, incident on a one-meter long tungsten beam dump. DONUT pioneered the use of emulsion targets in order to search for characteristic "kinks" in the tracks produced by the rapid decay ($\sim$ 2 mm path length) of τ produced at neutrino interaction vertices. A total of four ν_τ interactions were observed with an expected background of 0.34 events in the initial run, while the final report from DONUT contained nine ν_τ candidate interactions with an estimated background of $\sim$ 1.5 events [26].

Thus, the neutrino has been observed participating in weak interactions in three active lepton flavors, namely the electron, muon, and tau, corresponding nicely with the three known generations in the quark sector. The evidence for the three weak flavor eigenstates of neutrinos, and only those three, had been mounting over time, even prior to the direct observation of ν_τ by DONUT. From astrophysical observations, both the measurement of the electron antineutrino flux from supernova SN1987A [27] and the measurement of the relative abundance of Helium-4 in the universe [28] yield results consis-

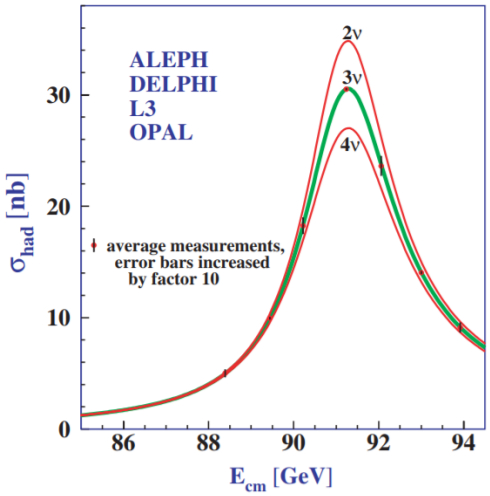

Figure 1.1: The cross section for hadron production in the approximate energy range of the Z^0 boson resonance as measured by the LEP Electroweak Working Group. The curves are plotted for hypotheses of two (red), three (green), and four (red) light, active neutrino flavors. The best agreement is found for a model with three neutrinos. Figure reproduced from Ref. [29].

tent with three weak eigenstates of neutrinos with limits of $N_\nu = 2.5^{+4.1}_{-0.8}$ or $N_\nu < 8$ at 95% C.L. and $N_\nu = 2.3 \pm 0.8$ or $N_\nu < 3.6$ at 95% C.L., respectively. A rather stronger limit was established via indirect and direct measurement of the invisible Z^0 linewidth, which is directly attributable to decay to light, active neutrinos. The global average reported by the Particle Data Group (PDG), which is dominated by ALEPH, DELPHI, L3, and OPAL using the Large Electron-Positron Collider (LEP) at CERN [29], is 2.984 ± 0.008 and 2.92 ± 0.05 for indirect and direct measurement, respectively [30]. The results of the LEP Electroweak Working Group showing the constraint on the number of neutrino species is shown in Figure 1.1.

1.1.3 Neutrino Properties

In the Standard Model (SM), the neutrino is a weakly-interacting, massless fermion. The issue of the mass of the neutrinos will be discussed later in the context of oscillation phenomena. As with all fermions, the neutrino carries half-integer spin. The neutrino carries no electric charge nor color charge, and therefore participates in interactions only via the exchange of $W^{\pm}$ or Z^0 bosons within the SM, and with the graviton in Beyond the Standard Model (BSM) theories. The helicity of a particle is determined by computing the inner product of the particle spin, $\boldsymbol{\sigma}$, with its momentum, $\boldsymbol{p}$. By convention, a right-handed particle is defined by positive helicity ($\boldsymbol{\sigma} \cdot \boldsymbol{p} > 0$) and a left-handed particle is defined by negative helicity ($\boldsymbol{\sigma} \cdot \boldsymbol{p} < 0$). Prior to 1956, it was widely assumed [31] that parity is an intrinsic symmetry of nature, which is to say that interactions involving right-handed particles are equally probable as interactions involving left-handed particles.

In a paradigm altering experiment [32], Chien-Shiung Wu and collaborators demonstrated that parity symmetry is violated in the weak interaction. The experiment considered the process

$$^{60}_{27}\mathrm{Co} \rightarrow {}^{60}_{28}\mathrm{Ni} + e^- + \bar{\nu}_e + 2\gamma \tag{1.6}$$

wherein the decaying Cobalt-60 atoms were cooled to extremely low temperature ($\sim$ 0.003 K) and then uniformly polarized using an external magnetic coil. Conservation of the parity symmetry in this experiment would suggest isotropic distributions of the directions of the γ and e^- produced, however

an approximate bias of 60% was observed in the directional preference of the emitted photons and electrons. The observation of parity violation led to a reformulation of Fermi's theory to a $\boldsymbol{V-A}$ Lagrangian [33][34] for the weak interactions such that only left-handed particles and right-handed antiparticles interact weakly. This has the natural corollary that only left-handed neutrinos and right-handed antineutrinos ought to be observed.

The helicity of the neutrino was first measured directly in 1957 by Goldhabler, Grozdins, and Sunyar at BNL [35]. The experiment studied the K-electron capture of ^{152}Eu in the process

$$^{152}\mathrm{Eu} + e^- \rightarrow {}^{152}\mathrm{Sm}^* + \nu_e \rightarrow {}^{152}\mathrm{Sm} + \gamma + \nu_e \tag{1.7}$$

In this interaction, the nucleus of the ^{152}Eu is spin 0 with odd parity $(0-)$ while the K-electron has spin $\frac{1}{2}$, giving a total spin of $\frac{1}{2}$. The emission of the γ rays is isotropic in the center of mass reference frame, but due to the recoil of the excited $^{152}\mathrm{Sm}^*$ from the ν_e emission, resonant scattering can be observed in γ rays emitted in the direction opposite the neutrino. Since the conservation of angular momentum requires that the final state must have total spin $\frac{1}{2}$, the circularly-polarized, resonant photons must have identical helicity to the neutrino. The observation of the polarization of the resonant γ rays was found to be consistent with 100% negative helicity (left-handedness) for the neutrinos.

1.2 Neutrino Oscillations

As mentioned in the discussion of neutrino properties in Section 1.1.3, the SM assumes that the neutrinos are massless, which would imply stationary neutrino flavor states. However, a series of experimental results, which will now be discussed, raised significant questions challenging the assumption of massless neutrinos.

1.2.1 Solar Neutrino Problem

The first hints of disagreement with the massless SM neutrino expectations arose beginning in 1968 with measurements by Ray Davis at the Homestake Experiment [36], which was designed to analyze the solar electron neutrino flux. Davis collaborated with theorist John Bahcall who was responsible for the computation of the expected neutrino flux due to the known solar nuclear processes. The experiment, the first to perform a radiochemical solar neutrino measurement, was located approximately 1500 meters below the ground in the Homestake Gold Mine. It consisted of a 390 m^3 tank filled with perchloroethylene (C_2Cl_4), selected as a chlorine source, in order to search for the electron neutrino capture process

$$\nu_e + {}^{37}\mathrm{Cl} \rightarrow {}^{37}\mathrm{Ar} + e^- \tag{1.8}$$

which has a threshold energy of 814 keV and is therefore sensitive to neutrinos produced predominantly from the ^{8}B decay [37]. Due to the extremely low probability of this interaction, a long exposure time was required to observe

signifcant results. The argon formed in the interaction was collected by bubbling helium through the tank, and the collected sample was placed in a small gas counter in order to detect the radioactive decay of the unstable argon species. The observed quantity of the unstable argon isotope was found to be consistent with an upper bound of 3×10^{-36} s^{-1} per atom of ^{37}Cl on the rate of neutrino interactions. Calculations by Bahcall et al. predicted a neutrino interaction rate of approximately 7.5×10^{-36} s^{-1} per atom of ^{37}Cl using a set of five variations on solar nuclear fusion models, demonstrating a clear deficit in the experimentally observed rate.

After Davis and Bahcall uncovered this solar neutrino deficit, which would come to be known as the "solar neutrino problem" [37], a series of further experiments attempted to confirm the result. The Kamioka Neutrino Detection Experiment (Kamiokande), consisting of a water Čerenkov detector instrumented with photomultiplier tubes (PMTs), measured the flux of neutrinos from the identical ^{8}B decay via the detection of

$$\nu_e + e^- \rightarrow \nu_e + e^- \tag{1.9}$$

wherein an electron neutrino scatters off an electron. Čerenkov light is produced when a particle travels at superluminal speeds in a given medium, resulting in a conical arrangement of emitted light wavefronts equivalent to the mechanism of a sonic boom in sound waves. In 1986, Kamiokande-II published an observation of the solar neutrino flux indicating a neutrino event rate of 0.46 ± 0.13(stat.)± 0.08(syst.) of the expected value from the Standard Solar Model (SSM) [38]. An updated Kamiokande-II result [39] was

published in 1991 with an observation of the neutrino event rate of $0.46 \pm 0.05(\text{stat.}) \pm 0.06(\text{syst.})$ of the SSM or $0.70 \pm 0.08(\text{stat.}) \pm 0.09(\text{syst.})$ for an alternative model of solar fusion [40]. Further data collected during the Kamiokande-III run period resulted in verification of the previous observations with a net deficit in the neutrino event rate ranging from 49% to 64% [41] In the early 1990s, the Soviet-American Gallium Experiment (SAGE) [42] and the Gallium Experiment (GALLEX) [43] both measured the solar neutrino flux arising from the $p-p$ chain through electron capture by Gallium in the process

$$\nu_e + {}^{71}\text{Ga} \rightarrow e^- + {}^{71}\text{Ge} \tag{1.10}$$

which has a lower threshold energy than the previously discussed experiments at 233 keV. The expected rate for this interaction as predicted by the SSM is 132^{+20}_{-17} SNU (3σ) [44], where SNU is the standardized solar neutrino unit defined by one neutrino capture per second per 10^{36} atoms of the target element. The overall observed event rate for electron neutrino capture by Gallium was $65.4^{+3.1}_{-3.0}(\text{stat.})^{+2.6}_{-2.8}(\text{syst.})$ SNU for the SAGE experiment [45], $77.5 \pm 6.2(\text{stat.})^{+4.3}_{-4.7}(\text{syst.})$ SNU for the GALLEX experiment [46], and $62.9^{+5.5}_{-5.3}(\text{stat.}) \pm 2.5(\text{syst.})$ SNU for the GNO experiment [47], which when combined results in a measurement of 66.1 ± 3.1 SNU [45]. These results represent an apparent depletion of approximately one-half of the expected solar neutrino flux.

The intial attempts to reconcile the apparent deficit in the solar electron neutrino flux involved revisions to modeling of solar fusion processes, partic-

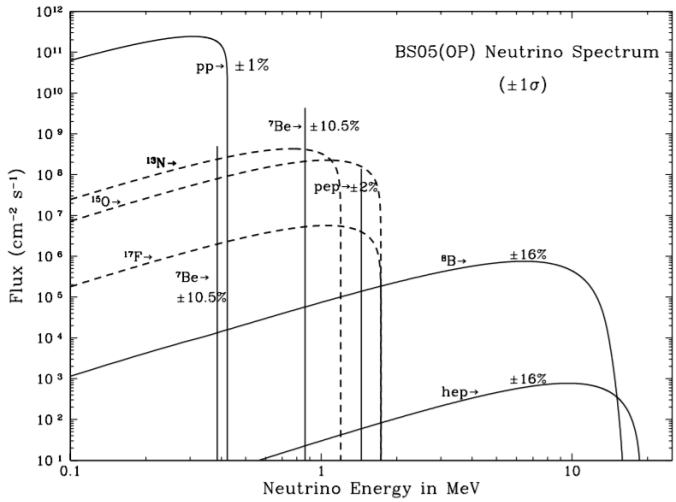

Figure 1.2: Plotted are the predicted solar neutrino energy spectra as computed from the Standard Solar Model. Figure reproduced from Ref. [48]

ularly in variation of the expectatiions from the ^{8}B chain [37]. The predicted spectra of solar neutrinos from various decay chains is shown in Fig. 1.2. The neutrinos from ^{8}B are produced in the decay

$$^8\mathrm{B} \rightarrow {}^8\mathrm{Be}^* + e^+ + \nu_e \tag{1.11}$$

and represent a very small fraction of the total solar neutrino flux at approximately 0.008%, while the uncertainties associated with this chain are very large on the order of ±20% [49]. The difficulty in predicting the ^{8}B neutrino flux comes from the requirement for precision measurement of nuclear cross sections and the effects of the Coulomb barrier at low energies, which is experimentally difficult [50]. This confluence of circumstances led to initial skepticism of the Davis Experiment result [51]. However, the neutrinos resulting from the $p-p$ chain form the dominant component of the solar neutrino flux ($\sim$ 91% [49])

and were known to have much smaller uncertainties on the order of $\sim 3\%$ [52]. The $p-p$ chain neutrinos were being analyzed by the lower energy threshold Gallium neutrino experiments with similar results observed as in the case of the ^{8}B neutrinos. Further, developments in techniques for analyzing helioseismology resulted in validation of temperature and pressure assumptions made in the SSM [53], which began to shift the direction of study to the possibility that the neutrinos were transmuting between the known flavor states as they propagated from the sun.

1.2.2 Atmospheric Neutrino Problem

During the same period in which the study of solar neutrinos was beginning to grow in general interest, other theorists and experimentalists began studying neutrinos produced in the Earth's atmosphere. This area of analysis began as a search for the decay of protons, which required a detailed understanding of neutrino backgrounds [54]. When no proton decay was observed, the experimental focus turned toward atmospheric neutrinos [55]. The bombardment of the upper atmosphere by primary cosmic rays produces hadronic showers of mostly pions, which were known to then readily decay to muons and muon neutrinos. Muons subsequently decay to electrons, which produces both a muon neutrino and an electron antineutrino. This process can be described by

$$\begin{aligned} \pi^- &\rightarrow \mu^- + \bar{\nu}_\mu \\ \mu^- &\rightarrow \nu_\mu + \bar{\nu}_e + e^- \end{aligned} \tag{1.12}$$

as well as the charge conjugate process. Therefore, an experimental measure of the ratio, R, of flux of muon neutrinos and antineutrinos to the flux of electron neutrinos and antineutrinos would be expected to yield

$$R = \frac{\phi(\nu_\mu + \bar{\nu_\mu})}{\phi(\nu_e + \bar{\nu_e})} \approx 2 \tag{1.13}$$

within statistical and systematic fluctuations. Modeling of the hadronic showering in the atmosphere agrees with this basic prediction within an uncertainty of a few percent for neutrino energies on the order of 1 GeV [56], though for significantly higher energies corrections must be made to account for muons traversing the atmosphere without decay and the contributions of the production of kaons instead of pions.

The first experiment to measure the flavor content of the atmospheric neutrinos was Kamiokande, which was first discussed in Section 1.2.1 in the context of solar neutrinos. In 1988, Kamiokande-II reported the observation of 105 electron-like events and 85 muon-like events as compared to the expectation from MC simulation of 106.2 electron events and 144 muon events [57]. Kamiokande was able to distinguish muon and electron neutrino events by analysis of the diffusivity of the Čerenkov rings giving a probability of misidentification on the order of $\sim 2\%$. The data demonstrate agreement with the expected number of events for electron neutrinos while the muon neutrino data represents a deficit of $59 \pm 7\%$ with respect to the MC expectation. The observation of fewer muon neutrino events than electron neutrino events shows clear tension with the expectation for $R \approx 2$.

The Irvine-Michigan-Brookhaven (IMB) detector [58], located in the Fairport salt mine and near to Lake Erie, was another example of a water Čerenkov detector similar in design to Kamiokande. IMB was ideally suited to examine the flavor content of atmospheric neutrinos in order to verify the observations made in Kamiokande-II. In results published in 1992 [59], which included a total of 7.7 kton yr expsoure, IMB reported the observation of 36 ± 2(stat.) ± 2(syst.)% nonshowering events as compared to the expectation from simulation of 51 ± 1(stat.) ± 5(syst.)% nonshowering events. The result reported by IMB represented another example of evidence showing the depletion of muon neutrino events in the flux from atmospheric sources. A summary of the atmospheric neutrino results from both Kamiokande and IMB is shown in Fig. **??**.

A further measurement of the atmospheric neutrino flavor content was made by the Soudan-2 experiment with results published in 1997 [60]. The Soudan-2 experiment was a time projection, tracking calorimeter consisting of approximately 4.3 tons of corrugated steel arranged in a hexagonal structrue and instrumented with plastic drift tubes. The Soudan-2 detector was situated 710 meters beneath the ground in the Soudan Underground Mine State Park. The differing design of the Soudan-2 detector presented an ideal test case to understand whether the apparent muon neutrino deficit from atmospheric sources was due to some mismodeling of systematic effects in the water Čerenkov detectors. The observation by Soudan-2 was quantified in the

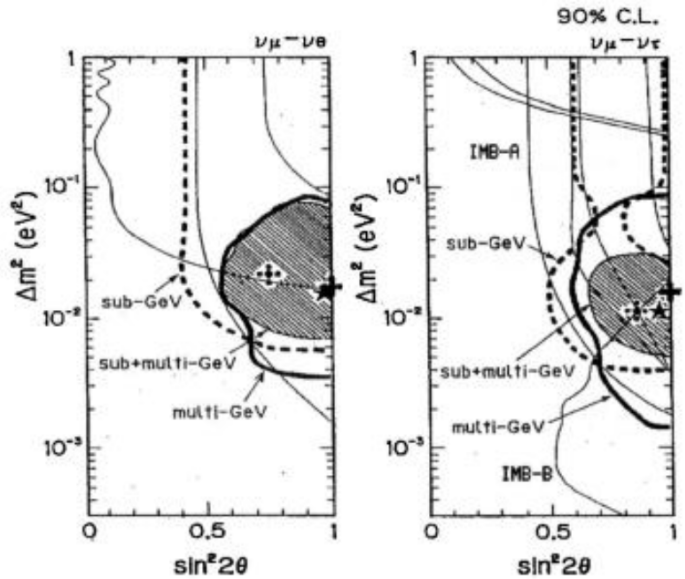

Figure 1.3: Plotted are the allowed regions for atmospheric neutrino mixing parameters in a two-flavor oscillations framework using data from Kamiokande-II [57] and IMB [59]. Figure reproduced from Ref. [61]

form of a double ratio

$$\mathscr{R} = \frac{R_{data}}{R_{MC}} \tag{1.14}$$

where $\mathscr{R}$ is the experimental double ratio and R is the ratio of fluxes given in Equation 1.13. Soudan-2 measured a value of $\mathscr{R} = 0.72 \pm 0.19^{+0.05}_{-0.07}$, which represents a 1.5σ variation from the expected value of 1.0 and provided additional evidence from a unique experimental technique for the depletion of atmospheric muon neutrinos. The collection of these experimental results and the consistent measurement of an atmospheric muon neutrino deficit would come to be known as the "atmospheric neutrino problem".

1.2.3 Neutrino Oscillation Formalism

The accumulation of experimental evidence suggesting neutrino disappearance from both solar and atmospheric sources called for theoretical explanation. One possible solution to the problem came in the form of massive (here implying only non-zero mass) neutrinos, as it would then be possible for the neutrinos to undergo neutral particle oscillation phenomena in a similar manner to the known particle-antiparticle oscillations observed in the quark sector [62]. This type of oscillation phenomena arises due to the existence of distinct eigenstate bases describing the neutrino: the flavor basis in which the neutrinos are created and detected and the mass eigenbasis in which the neutrinos propagate.

The general formalism of neutrino oscillations is based upon a transformation defined by a unitary matrix, U, between the mass eigenstates $|\nu_i\rangle$ and flavor eigenstates $|\nu_\alpha\rangle$, and written

$$|\nu_i\rangle = \sum_\alpha U_{i\alpha} |\nu_\alpha\rangle \tag{1.15}$$

$$|\nu_\alpha\rangle = \sum_i U^*_{\alpha i} |\nu_i\rangle \tag{1.16}$$

where i gives the number of the mass eigenstate and α gives the flavor eigenstate. The matrix U represents a complex rotation where the unitarity condition is given by $U^\dagger U = 1$. The following derivation of the expression for the probability of neutrino flavor transition follows closely with that given in Reference [63]. We can generalize the unitary transformation between flavor

and mass eigenstates to a wave packet construction which takes the form

$$|\nu_\alpha(\boldsymbol{x},t)\rangle = \sum_i U^*_{\alpha i}\Psi_i(\boldsymbol{x},t)\,|\nu_i\rangle\,. \tag{1.17}$$

The wave function Ψ_i^S of a neutrino produced at a source S with mass m_i propagating in a vacuum is given by

$$\Psi_i^S(\boldsymbol{x},t) = \int \frac{d^3p}{(2\pi)^{3/2}}\; f_i^S(\boldsymbol{p}-\boldsymbol{p}_i)\; e^{i\boldsymbol{p}\boldsymbol{x}-iE_i(p)t} \tag{1.18}$$

where $f_i^S(\boldsymbol{p}-\boldsymbol{p}_i)$ is the generalized momentum distribution function for the neutrino produced at the source around the mean momentum $\boldsymbol{p}_i$. The energy of the neutrino is given by $E_i(p) = \sqrt{p^2+m_i^2}$. By expanding the energy about the mean momentum of the distribution function

$$E_i(p) = E_i(p_i) + \frac{\partial E_i(p)}{\partial p^j}\Big|_{\boldsymbol{p}_i}(p-p_i)^j + \frac{1}{2}\frac{\partial^2 E_i(p)}{\partial p^j \partial p^k}\Big|_{\boldsymbol{p}_i}(p-p_i)^j(p-p_i)^k + \ldots \tag{1.19}$$

and retaining the first two leading terms, the wave function becomes

$$\Psi_i^S(\boldsymbol{x},t) \simeq e^{i\boldsymbol{p}\boldsymbol{x}-iE_i(p)t}\; g_i^S(\boldsymbol{x}-\boldsymbol{v}_{gi}t) \tag{1.20}$$

where the shape of the wave function is determined by

$$g_i^S(\boldsymbol{x}-\boldsymbol{v}_{gi}t) = \int \frac{d^3p}{(2\pi)^{3/2}}\; f_i^S(\boldsymbol{p})\; e^{i\boldsymbol{p}(\boldsymbol{x}-\boldsymbol{v}_{gi}t)} \tag{1.21}$$

and the group velocity of the wave packet is

$$\boldsymbol{v}_{gi} = \frac{\partial E_i}{\partial \boldsymbol{p}}\Big|_{\boldsymbol{p}_i} = \frac{\boldsymbol{p}}{E_i}\Big|_{\boldsymbol{p}_i} \tag{1.22}$$

We can follow a similar procedure to write the wave packet expression for the neutrino state detected at a displacement $\boldsymbol{L}$, which is given by

$$|\nu_\beta(\boldsymbol{x}-\boldsymbol{L})\rangle = \sum_i U^*_{\beta i}\Psi_i^D(\boldsymbol{x}-\boldsymbol{L})\,|\nu_i\rangle \tag{1.23}$$

where the wave function Ψ_i^D takes the form

$$\Psi_i^D(\boldsymbol{x}-\boldsymbol{L}) = \int \frac{d^3p}{(2\pi)^{3/2}}\ f_i^D(\boldsymbol{p}-\boldsymbol{p}_i')\ e^{i\boldsymbol{p}(\boldsymbol{x}-\boldsymbol{L})}. \tag{1.24}$$

Shifting the variable of integration to $\boldsymbol{p}_i'$ the wave function may be rewritten

$$\Psi_i^D(\boldsymbol{x}-\boldsymbol{L}) = e^{i\boldsymbol{p}_i'(\boldsymbol{x}-\boldsymbol{L})}\ g_i^D(\boldsymbol{x}-\boldsymbol{L}) \tag{1.25}$$

where the shape factor is given by

$$g_i^D(\boldsymbol{x}-\boldsymbol{L}) = \int \frac{d^3p}{(2\pi)^{3/2}}\ f_i^D(\boldsymbol{p})\ e^{i\boldsymbol{p}(\boldsymbol{x}-\boldsymbol{L})}. \tag{1.26}$$

The amplitude for transition from a created neutrino flavor α to detected flavor β ($\nu_\alpha \to \nu_\beta$) is given by

$$\begin{aligned}\mathscr{A}_{\alpha\beta}(\boldsymbol{L},t) &= \int d^3x\ \langle \nu_\beta(\boldsymbol{x}-\boldsymbol{L})|\nu_\alpha(\boldsymbol{x},t)\rangle \\ &= \sum_i U_{\alpha i}^* U_{\beta i} \int d^3x\ \Psi_i^{D*}(\boldsymbol{x}-\boldsymbol{L})\ \Psi_i(\boldsymbol{x},t).\end{aligned} \tag{1.27}$$

Substituting the wave function expressions into this amplitude gives

$$\mathscr{A}_{\alpha\beta}(\boldsymbol{L},t) = \sum_i U_{\alpha i}^* U_{\beta i}\ G_i(\boldsymbol{L}-\boldsymbol{v}_{gi}t)\ e^{-iE_i(p_i)t+i\boldsymbol{p}_i\boldsymbol{L}} \tag{1.28}$$

where the effective shape factor has the form

$$G_i(\boldsymbol{L}-\boldsymbol{v}_{gi}t) = \int d^3x\ g_i^S(\boldsymbol{x}-\boldsymbol{v}_{gi}t)\ g_i^{D*}(\boldsymbol{x}-\boldsymbol{L})\ e^{i(\boldsymbol{p}_i-\boldsymbol{p}_i')(\boldsymbol{x}-\boldsymbol{L})}. \tag{1.29}$$

The probability for this amplitude is computed in the usual manner

$$P(\nu_\alpha \to \nu_\beta; \boldsymbol{L}, t) = P_{\alpha\beta}(L) = \int_\infty^\infty dt\ |\mathscr{A}_{\alpha\beta}(L,t)|^2 = \sum_{i,k} U_{\alpha i}^* U_{\beta i} U_{\alpha k} U_{\beta k}^* I_{ik}(L), \tag{1.30}$$

where the factor

$$I_{ik}(L) = \int_{-\infty}^{\infty} dt\ G_i(L - v_{gi}t)\ G_k^*(L - v_{gk}t)\ e^{-i\Delta\phi_{ik}(L,t)} \tag{1.31}$$

and the normalizaiton condition

$$\int_{-\infty}^{\infty} dt |G_i(\boldsymbol{L} - \boldsymbol{v}_{gi}t)|^2 = 1 \tag{1.32}$$

must be imposed in order to satisfy unitarity. The phase factor is given by

$$\Delta\phi_{ik} = (E_i - E_k)t - (p_i - p_k)L = \Delta E_{ik}t - \Delta p_{ik}L. \tag{1.33}$$

In the scenario where neutrinos are relativistic, which is to say that $\Delta p \ll p$, then Δp can be expanded in terms of the mass and energy differences

$$\Delta p = \frac{\partial p}{\partial E}\Delta E + \frac{\partial p}{\partial m^2}\Delta m^2 = \frac{1}{v_g}\Delta E - \frac{1}{2p}\Delta m^2 \tag{1.34}$$

where the momentum and group velocity are given by the averages

$$p \equiv \frac{p_i + p_k}{2} \qquad\qquad v_g \equiv \frac{v_{gi} + v_{gk}}{2}. \tag{1.35}$$

Substituting into the phase factor in Eq. 1.33 gives

$$\Delta\phi = \frac{\delta m^2}{2p}L - \frac{1}{v_g}(L - v_g t)\Delta E. \tag{1.36}$$

In a similar way, we can also expand the ΔE in terms of the mass and momentum differences which gives

$$\Delta E = \frac{\partial E}{\partial p}\Delta p + \frac{\partial E}{\partial m^2}\Delta m^2 = v_g\Delta p + \frac{1}{2E}\Delta m^2 \tag{1.37}$$

where the energy is given by

$$E \equiv \frac{E_i + E_k}{2} \tag{1.38}$$

and the group velocity is the same as in the momentum expansion case. Substituting into the phase factor in Eq. 1.33 gives

$$\Delta\phi = \frac{\delta m^2}{2E} t - (L - v_g t)\Delta p. \tag{1.39}$$

In both cases, the phase difference has the general form

$$\Delta\phi = \Delta\phi_{st} + \Delta\phi_{coh}. \tag{1.40}$$

The first term in this expression, $\Delta\phi_{st}$, gives the standard neutrino oscillation phase, which corresponds to the phase acquired by point-like neutrinos with the assumption that the neutrino mass eigenstates have either the same momentum or the same energy during propagation. The second term in this expression, $\Delta\phi_{coh}$, represents the phase acquired by the decoherence effects of finite-sized wave packets propagating at differing group velocities with respect to one another, which allow for the phase acquired to vary along the wave packet. These coherence effects can be neglected if the following interaction coherence condition [63]

$$\frac{|\Delta E_{ik}|\sigma_x}{v_g} \ll 1 \tag{1.41}$$

where σ_x is the length of the wave packet, is satisfied. This coherence condition arises from considering the form of ϕ_{coh} in Eq. 1.36 and the observaton that the shape factors involved in the integral $I_{ik}(L)$ must suppress the neutrino wave

function for $|L - v_g t| > \sigma_x$, which are points that are a greater displacement from the center of the wave packet than the size. Substituting the total phase factor $\Delta\phi$ as expanded in Eq. 1.36 into the effective shape factor expression in Eq. 1.31 yields

$$I_{ik}(L) = e^{-i\frac{\Delta m_{ik}^2}{2p}L} \int_{-\infty}^{\infty} dt\ G_i(L - v_{gi}t)\ G^*(L - v_{gk}t)\ e^{i\frac{1}{v_g}\Delta E_{ik}(L - v_g t)} \tag{1.42}$$

If we now assume that decoherence effects can be neglected, which is to say that the group velocities and shape factors are equivalent ($v_{gi} = v_{gk} = v_g$ and $G_k = G_i$), the remaining integration is the Fourier transform of the shape factor given by

$$\frac{1}{v_g} \int_{-\infty}^{\infty} dx'\ |G_i(x')|^2\ e^{i\frac{1}{v_g}\Delta E_{ik}x'} \tag{1.43}$$

which effectively measures decoherence effects. If the interaction coherence condition given in Eq. 1.41 is satisfied, then the Fourier transform satisfies the unitarity condition and is equal to 1. The standard neutrino oscillation probability equation can then be written from substituting this result into Eq. 1.30 in order to arrive at

$$P(\nu_\alpha \to \nu_\beta; \boldsymbol{L}, t) = P_{\alpha\beta}(L) = \sum_{i,k} U_{\alpha i}^* U_{\beta i} U_{\alpha k} U_{\beta k}^*\ e^{-i\frac{\Delta m_{ik}^2}{2p}L} \tag{1.44}$$

Using again the assumption of relativistic neutrinos, which in this instance implies $m_i \ll E_i$, we can also write the probability of the transition as

$$P_{\alpha\beta}(L) = \sum_{i,k} U_{\alpha i}^* U_{\beta i} U_{\alpha k} U_{\beta k}^*\ e^{-i\frac{\Delta m_{ik}^2}{2E}L} \tag{1.45}$$

It is noteworthy that the same result could be arrived at using the expression for the ϕ_{st} from the energy expansion of the phase difference in Eq. 1.39 and

using the convention of natural units such that $t \simeq L$. We can rewrite this general probability equation in the form

$$P_{\alpha\beta}(L) \;=\; \sum_{i,k} U^*_{\alpha i} U_{\beta i} U_{\alpha k} U^*_{\beta k} \;\left(e^{-i\frac{\Delta m^2_{ik}}{2E}L} \;-\; 1\right) + \sum_{i,k} U^*_{\alpha i} U_{\beta i} U_{\alpha k} U^*_{\beta k} \quad (1.46)$$

The first term of the equation vanishes for $i = k$ since this implies no mass difference, and it is also equivalent to the complex conjugate under an exchange of the indices since $\Delta m^2_{ik} = -\Delta m^2_{ki}$. Thus, the first set of summations can be substituted with

$$P_{\alpha\beta}(L) = 2\sum_{i>k}\sum_{k} \mathrm{Re}\left[U^*_{\alpha i} U_{\beta i} U_{\alpha k} U^*_{\beta k} \;\left(e^{-i\frac{\Delta m^2_{ik}}{2E}L} - 1\right)\right] + \sum_{i,k} U^*_{\alpha i} U_{\beta i} U_{\alpha k} U^*_{\beta k}. \quad (1.47)$$

Since the matrix U satisfies $U^\dagger U = 1$ and $U^\dagger = (U^*)^T$, the second term simplifies via

$$\sum_i U_{\beta i} U^\dagger_{i\alpha} \sum_k U_{\alpha k} U^\dagger_{k\beta} = \delta_{\alpha\beta} \quad (1.48)$$

where $\delta_{\alpha\beta}$ is the Kronecker delta. The form of the probability equation can then be written

$$P_{\alpha\beta}(L) = \delta_{\alpha\beta} + 2\sum_{i>k}\sum_{k} \mathrm{Re}\left[U^*_{\alpha i} U_{\beta i} U_{\alpha k} U^*_{\beta k} \;\left(e^{-i\frac{\Delta m^2_{ik}}{2E}L} - 1\right)\right] \quad (1.49)$$

In order to further simplify the complex phase expression, we employ the trigonometric identity

$$1 - \cos\left(\frac{\Delta m^2_{ik}}{2E}L\right) = 2\sin^2\left(\frac{\Delta m^2_{ik}}{4E}L\right) \quad (1.50)$$

in conjunction with Euler's identity

$$e^{-i\frac{\Delta m^2_{ik}}{2E}L} = \cos\left(\frac{\Delta m^2_{ik}}{2E}L\right) - i\sin\left(\frac{\Delta m^2_{ik}}{2E}L\right) \quad (1.51)$$

to arrive at the probability equation

$$P_{\alpha\beta}(L) = \delta_{\alpha\beta} + 2\sum_{i>k}\sum_{k} \mathrm{Im}\left[U^*_{\alpha i}U_{\beta i}U_{\alpha k}U^*_{\beta k}\ \sin\left(\frac{\Delta m^2_{ik}}{2E}L\right)\right]$$
$$- 4\sum_{i>k}\sum_{k} \mathrm{Re}\left[U^*_{\alpha i}U_{\beta i}U_{\alpha k}U^*_{\beta k}\ \sin^2\left(\frac{\Delta m^2_{ik}}{2E}L\right)\right] \quad (1.52)$$

which is the standard form for the probability of oscillations from flavor α to flavor β for neutrinos in a vacuum. An example of the functional form of two-flavor oscillations is shown in Fig. 1.4 for near-maximal mixing. The modifications to this oscillation probability that arise due to the presence of matter are known as the Mikheyev-Smirnov-Wolfenstein (MSW) effect [64][65] or simply as matter effects. The MSW effect is particularly large in regions of high electron density as this leads to alteration of the mass eigenstates due to charged-current coherent forward scattering in the electron neutrinos. Experimentally, matter effects are most important when searching for electron neutrino appearance and disappearance in solar neutrinos or neutrinos traversing a very long baseline through the Earth [66]. The matter effects have been demonstrated to have a minimal effect for the analysis presented here [67], thus the assumption of vacuum oscillations is employed.

1.2.4 Observation of Oscillations

A proposal was made in 1985 by Herbert Chen [68] to solve the solar neutrino problem through the simultaneous detection of charged-current (CC) and neutral-current (NC) solar neutrino events through the use of a heavy-water (D_2O) Čerenkov detector. This proposal would eventually be

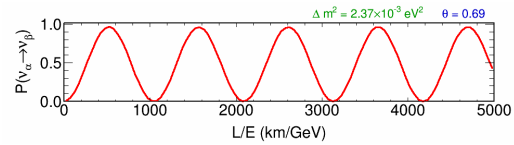

Figure 1.4: Plotted is the transition probability for $\nu_\alpha \to \nu_\beta$ oscillations using a two-flavor oscillations framework with mass-splitting $\Delta m^2 = 2.37 \times 10^{-3}$ eV^2 and mixing angle $\theta = 0.69$ as a function of L/E. The proximity of the mixing angle to $\pi/4$ results in near-maximal mixing, which is demonstrated by the large oscillations in the transition probability.

realized in the Sudbury Neutrino Observatory (SNO) [69] which is located in the Creighton Mine in Sudbury, Ontario, Canada at a depth of 2100 m underground. The SNO detector consisted of 1 kton of highly purified D_2O contained in an acrylic sphere of diameter 12 m and instrumented by 9456 20-cm PMTs supported by a 17.8 m diameter cylindrical stainles steel structure. SNO detected neutrinos from the aforementioned ^{8}B chain (see Section 1.2.1 by simultaneously searching for the processes:

$$\begin{aligned} \nu_e + d &\to p + p + e^- \quad \text{(CC)} \\ \nu_x + d &\to p + n + \nu_x \quad \text{(NC)} \\ \nu_x + e^- &\to \nu_x + e^- \quad \text{(ES)}. \end{aligned} \tag{1.53}$$

where the CC interaction is sensitive to the flux of electron neutrino (ν_e) events alone while the NC interaction provides a measurement of the total neutrino flux independent of flavor, such that $x = e, \mu, \tau$ in ν_x. The final process is the case of elastic scattering (ES), which can involve all neutrino flavors similarly to the NC interactions, though there is a rate suppression for muon and tau neutrinos as compared to electron neutrinos. CC events are detected by the Čerenkov ring created by the outgoing electron. NC events

are observed through a time-delayed process on the order of 10 ms in which the free neutron produced in the interaction is captured by a nucleus resulting in gamma rays which Compton scatter off electrons that are detected.

Initial results from the ES channel in the SNO experiment resulted in a measurement of the total solar neutrino flux consistent with the SSM [70], which is consistent with the apparent depletion of electron neutrinos in the solar neutrino flux from a process unrelated to mismodeling of solar fusion processes. In order to improve the sensitivity to NC events in Phase II and III of the experiment, 2×10^3 kg of NaCl were added to the D_2O in order to increase the capture efficiency of free neutrons by exploiting the high cross section for neutron capture of ^{35}Cl [71]. An additional array of proportional counters called the Neutral Current Detction (NCD) array [72] was added in Phase III to further improve the detection of NC events.

The final verification of oscillations in the solar neutrinos required the comparison of observed and expected fluxes of ν_e and combined ($\nu_e + \nu_\mu + \nu_\tau$. If the disappearance of electron neutrinos is due to oscillations, the rate of observed ν_e should decrease while the combined rate of all flavors remains constant. The results of the solar neutrino flux measurement by SNO are shown in Fig. 1.5. SNO measured the following ^{8}B neutrino fluxes:

$$\begin{aligned} \phi_{CC} &= 1.68^{+0.06}_{-0.06}(\text{stat.})^{+0.08}_{-0.09}(\text{syst.}) \\ \phi_{NC} &= 4.94^{+0.21}_{-0.21}(\text{stat.})^{+0.38}_{-0.34}(\text{syst.}) \\ \phi_{ES} &= 2.35^{+0.22}_{-0.22}(\text{stat.})^{+0.15}_{-0.15}(\text{syst.}) \end{aligned} \tag{1.54}$$

all in units of 10^6 cm^{-2}s^{-1}. The measured NC flux was found to be consistent with the predictions of the SSM [53]. In contrast , the ratio of CC to NC fluxes was observed at $0.340 \pm 0.023(\text{stat.})^{+0.029}_{-0.031}(\text{syst.})$ in comparison to the expectation of unity for the case of invariant neutrino flavor. The SNO experiment thus provided definitive evidence for neutrino oscillations, simultaneously solving the solar neutrino problem and indicating non-zero mass in the neutrino sector.

Super-Kamiokande (Super-K) is a successor experiment to Kamiokande (see Section 1.2.2) and was designed to address both the solar and atmospheric neutrino problems [74]. The Super-K detector is similar conceptually to Kamiokande in that it is a water Čerenkov detector instrumented with PMTs, however it is more than an order of magnitude larger in volume. The detector is located at a depth of 1000 m underground and consists of a cylindrical tank with diameter 39.3 m and height 41.4 m containing 50 kton of ultrapure water. The inner detector region has a diameter of 33.8 m and a height of 36.2 m and is instrumented with 11,146 50 cm diameter PMTs, while the remaining volume forms the outer detector region instrumented by 1,885 20 cm diameter PMTs. As in other water Čerenkov experiments, muon-like and electron-like events are distinguishable by analysis of the opening angle of the Čerenkov rings, effectively a measurement of $\beta = v/c$, for low momentum particles and the amount of diffuse secondary scattering accompanying the ring of Čerenkov light [75]. Electron-like events producing more diffuse rings due to electromagnetic showering.

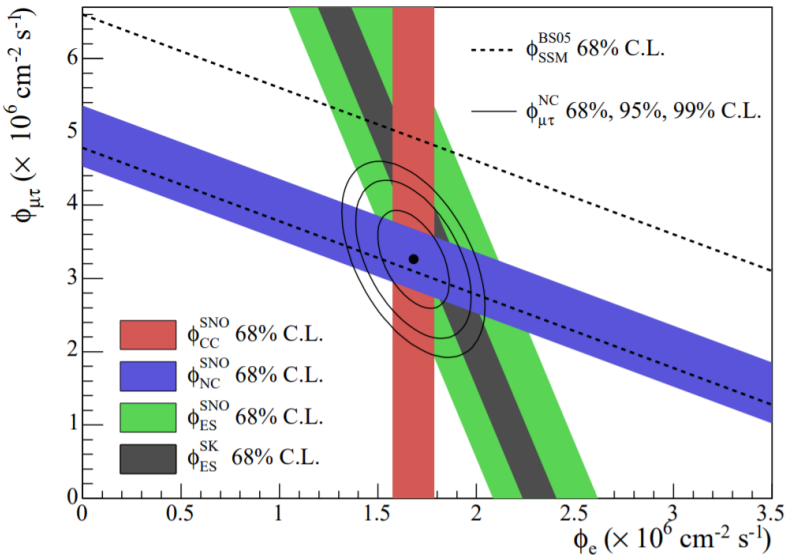

Figure 1.5: The $(\nu_\mu + \nu_\tau)$ solar neutrino flux versus the ν_e solar neutrino flux from ^8B neutrinos as measured by the SNO and Super-K experiments. The blue, red and green bands give the allowed solar neutrino flux as measured by SNO in the independent CC, NC and ES channels, respectively. The black band is the allowed ES channel flux measurement from Super-K [73]. The dashed lines define the allowed region of the total solar neutrino flux in the relevant energy range as predicted by the SSM [53]. The non-zero, favored region for the $(\nu_\mu + \nu_\tau$ component of the NC events is indicated by the solid elipses and gives strong evidence for neutrino oscillations. Figure reproduced from Ref. [71].

The first significant result annonunced by Super-K in 1998 was a confirmation of the atmospheric neutrino problem, observing a reduction in the expected ratio of ν_μ/ν_e by a factor of 0.61 ± 0.03(stat.)± 0.05(syst.) [74]. In addition to an overall reduction in the expected number of ν_μ, the number of muon-type neutrino events and electron-type neutrino events was observed by Super-K to be anisotropic [76][77]. The prediction for invariant neutrino flavor would be for isotropic neutrino flux given that neutrinos rarely interact with the matter in the Earth and were expected to be generated uniformly in the atmosphere. The anisotropic neutrino results found at Super-K agreed well with the expected rates for neutrinos created in the atmosphere above the detector, but showed large deficits in neutrinos moving upward in the detector (those traversing the Earth after having been created in the atmosphere on the opposite side of the detector) [78]. In 2004, Super-K published a measurement of the L/E dependence of the observed neutrino flux and found clear evidence of oscillatory behavior [79]. The observed L/E distribution was found to be consistent with a mass-squared difference $1.9 \times 10^{-3} < \Delta m^2 < 3.0 \times 10^{-3}$ eV^2 with a mixing angle $\sin^2 2\theta > 0.90$ at a 90% confidence level (CL). The Super-K results firmly established the phenomena of neutrino oscillations and solved the atmospheric neutrino problem.

The SNO and Super-K experiments ushered in a new age in neutrino oscillations physics, moving from speculation of neutrino flavor-changing behavior to a definitive observation of oscillations. These experiments showed not only that oscillations do occur but that two different oscillation frequen-

cies are needed in order to describe the observed phenomena in the solar [80] and atmospheric [79] regimes, implying the existence of three differing mass eigenstates. The Nobel Prize was awarded in 2015 to Takaaki Kajita and Arthur McDonald as representitives of Super-K and SNO, respectively, with the citation reading "for the discovery of neutrino oscillations, which shows that neutrinos have mass" [81].

1.2.5 Three-Flavor Formalism

The formalism for three-flavor oscillations is readily computed from the general vacuum oscillations probability given in Eq. 1.52. In this case, the mixing matrix U becomes a 3×3 unitary matrix with four free parameters and is generally known as the Pontecorvo-Maki-Nakagawa-Sakata (PMNS) matrix. The rotation between flavor and mass eigenstates takes the form

$$\begin{pmatrix} \nu_e \\ \nu_\mu \\ \nu_\tau \end{pmatrix} = U^*_{PMNS} \begin{pmatrix} \nu_1 \\ \nu_2 \\ \nu_3 \end{pmatrix} . \tag{1.55}$$

The standard parameterization of the PMNS matrix is in terms of three mixing angles (θ_{12}, θ_{13}, and θ_{23}) and a single CP violating phase (δ), written

$$\begin{aligned} U_{PMNS} &= \begin{pmatrix} U_{e1} & U_{e2} & U_{e3} \\ U_{\mu 1} & U_{\mu 2} & U_{\mu 3} \\ U_{\tau 1} & U_{\tau 2} & U_{\tau 3} \end{pmatrix} \\ &= \begin{pmatrix} 1 & 0 & 0 \\ 0 & c_{23} & s_{23} \\ 0 & -s_{23} & c_{23} \end{pmatrix} \begin{pmatrix} c_{13} & 0 & s_{13}e^{-i\delta} \\ 0 & 1 & 0 \\ -s_{13}e^{i\delta} & 0 & c_{13} \end{pmatrix} \begin{pmatrix} c_{12} & s_{12} & 0 \\ -s_{12} & c_{12} & 0 \\ 0 & 0 & 1 \end{pmatrix} \\ &= \begin{pmatrix} c_{12}c_{13} & s_{12}c_{13} & s_{13}e^{-i\delta} \\ -s_{12}c_{23} - c_{12}s_{23}s_{13}e^{i\delta} & c_{12}c_{23} - s_{12}s_{23}s_{13}e^{i\delta} & s_{23}c_{13} \\ s_{12}s_{23} - c_{12}c_{23}s_{13}e^{i\delta} & -c_{12}s_{23} - s_{12}c_{23}s_{13}e^{i\delta} & c_{23}c_{13} \end{pmatrix} \end{aligned} \tag{1.56}$$

where $s_{ij} = \sin\theta_{ij}$ and $c_{ij} = \cos\theta_{ij}$. The first rotation matrix, which is parameterized by the mixing angle θ_{23}, provides the dominant contribution to the atmospheric neutrino oscillations and generally controls the mixing of ν_μ and ν_τ flavor eigenstates. The third rotation matrix, parameterized by θ_{12}, controls the oscillations of solar neutrinos, and due to the previously mentioned MSW effect, the approximate survival probability for electron neutrinos propagating through the matter of the sun and arriving at terrestrial detectors is given by $P_{ee} \approx \sin^2(\theta_{12})$. The second rotation matrix is parameterized both by the mixing angle θ_{13}, which governs the mixing of predominantly ν_e with the flavor composition of the third mass eigenstate, and δ_{CP}, which determines the strength of CP violation in the lepton sector.

As a demonstration of the computation of experimentally relevant probabilites from the general expression, consider the following probability for muon neutrino survival ($\nu_\mu \to \nu_\mu$) as given by Eq. 1.52

$$\begin{aligned} P_{\mu\mu} = P(\nu_\mu \to \nu_\mu) &= 1 - 4\sum_{i>k} \mathrm{Re}\left[U^*_{\mu i} U_{\mu i} U_{\mu k} U^*_{\mu k}\right] \sin^2\left(\Delta_{ik}/2\right) \\ &\quad + 2\sum_{i>k} \mathrm{Im}\left[U^*_{\mu i} U_{\mu i} U_{\mu k} U^*_{\mu k}\right] \sin\Delta_{ik} \\ &= 1 - 4\left|U_{\mu 3}\right|^2 \left(\left|U_{\mu 2}\right|^2 + \left|U_{\mu 1}\right|^2\right) \sin^2\left(\Delta_{32}/2\right), \end{aligned} \tag{1.57}$$

where we have used the convention

$$\Delta_{ik} \equiv \frac{\Delta m^2_{ik}}{2E} L \tag{1.58}$$

for brevity. We now take an atmospheric or long-baseline approximation in which we neglect the oscillation effects at the solar frequency. This approxi-

mation implies degeneracy between mass eigenstates ν_1 and ν_2, which results in $\sin^2(\Delta_{21}/2) \sim 0$ and $\Delta_{31} \approx \Delta_{32}$. The matrix element contributions are thus given by

$$\begin{aligned}
|U_{\mu 1}|^2 &= \cos^2(\theta_{23})\sin^2(\theta_{12}) \\
&\quad + \cos^2(\theta_{12})\sin^2(\theta_{13})\sin^2(\theta_{23}) \\
&\quad + \frac{1}{2}\cos(\delta_{CP})\sin(2\theta_{12})\sin(\theta_{13})\sin(2\theta_{23}), \\
|U_{\mu 2}|^2 &= \cos^2(\theta_{12})\cos^2(\theta_{23}) \\
&\quad + \sin^2(\theta_{12})\sin^2(\theta_{13})\sin^2(\theta_{23}) \\
&\quad - \frac{1}{2}\cos(\delta_{CP})\sin(2\theta_{12})\sin(\theta_{13})\sin(2\theta_{23}), \\
|U_{\mu 3}|^2 &= \cos^2(\theta_{13})\sin^2(\theta_{23}).
\end{aligned} \tag{1.59}$$

In this case, it is possible to write the transition probability using an effective expression

$$P(\nu_\mu \to \nu_\mu) \approx 1 - A\sin^2(\Delta_{32}/2) \tag{1.60}$$

where $A \approx \sin^2(2\theta_{23})\cos^4(\theta_{13}) + \sin^2(2\theta_{13})\sin^2(\theta_{23})$. Thus, for a long-baseline experiment searching for muon neutrino disapperance, the leading parameters are the mass-splitting Δm^2_{32} and the θ_{23} mixing angle.

1.2.6 Era of Precision

Neutrino oscillations having been definitively observed, experimental focus shifted to the precision measurement of the parameters governing oscillations. The first of these precision experiments was the Kamioka Liquid scintillator Anti-Neutrino Detector (KamLAND) [82], which was designed to

measure electron antineutrino survival ($\bar{\nu}_e \to \bar{\nu}_e$) through the process of inverse beta decay, given by

$$\bar{\nu}_e + p \to e^+ + n \tag{1.61}$$

using a collection of nuclear reactors as the $\bar{\nu}_e$ source with sampling by a detector at a large distance ($L \sim 180$ km). In results published in 2004, KamLAND observed 258 candidate $\bar{\nu}_e$ events in comparison to 365.2 events expected for no oscillations. The disappearance of $\bar{\nu}_e$ corresponded to a mass-squared difference of $\Delta m^2 = 7.9^{+0.6}_{-0.5} \times 10^{-5}$ eV^2 with a mixing angle given by $\tan^2\theta = 0.40^{+0.10}_{-0.07}$ [83]. This observation is consistent with oscillations observed in the solar neutrinos [80]. With increased data collection and in combination with solar neutrino data, KamLAND later improved the measurement to $\Delta m^2_{21} = 7.59^{+0.21}_{-0.21} \times 10^{-5}$ eV^2 and $\tan^2\theta_{12} = 0.47^{+0.06}_{-0.05}$ [84].

Pioneering the concept of a long-baseline neutrino experiment, KEK to Kamioka (K2K) measured the survival of muon neutrinos ($\nu_\mu \to \nu_\mu$) produced by the 12 GeV proton synchotron at KEK and detected at a 1-kiloton water Čerenkov near detector and at the Super-K detector with baselines of 300 m and 250 km, respectively [85]. The data collected by K2K were consistent with the atmospheric oscillation and measured a best fit mass-splitting at $\Delta m^2 = 2.8 \times 10^{-3}$ eV^2 [86].

The successor experiment, Tokai to Kamioka (T2K) [87], uses a neutrino beam produced using 30 GeV protons from the Japan Proton Accelerator Research Complex (J-PARC) Main Ring impinging a graphite target to search for electron (anti)neutrino appearance from a muon (anti)neutrino

beam ($\overset{(-)}{\nu}_\mu \to \overset{(-)}{\nu}_e$) [88] as well as muon (anti)neutrino survival ($\overset{(-)}{\nu}_\mu \to \overset{(-)}{\nu}_\mu$) [89]. The axis of the J-PARC neutrino beam is oriented 2.5° away from the Super-K far detector over a 295 km baseline providing a narrow range of energies with less systematic uncertainty. T2K employs both on-axis and off-axis near detectors located at a baseline of 280 meters from the target. These detectors monitor beam intensity and profile characteristics as well as provide predictive measurements for observations at Super-K [90]. In the most recent analysis of all neutrino and antineutrino samples, T2K reports central values of oscillation parameters for normal (inverted) ordering of $\Delta m^2_{32} = 2.54 \pm 0.08$ $(2.51 \pm 0.08) \times 10^{-3}$ eV^2 and $\sin^2\theta_{23} = 0.55^{+0.05}_{-0.09}$ $(0.55^{+0.05}_{-0.08})$ with a 90% CL allowed region for δ_{CP} of $[-2.95, -0.44]$ ($[-1.47, -1.27]$)[91].

At this point it is important to note for chronological purposes that the Main Inector Neutrino Oscillation Search (MINOS) and MINOS+ experiments, which will be dicussed in great detail for the remainder of this thesis, have played a critical role since 2006 in the precision measurement of Δm^2_{32} and $\sin^2\theta_{23}$ [92][93]. A successor to MINOS and companion experiment to MINOS+, the NUMI Off-Axis ν_e Appearance (NOνA) experiment [94] searches for $\overset{(-)}{\nu}_\mu \to \overset{(-)}{\nu}_e$ and $\overset{(-)}{\nu}_\mu \to \overset{(-)}{\nu}_\mu$ oscillations using a long-baseline concept oriented 14.6 mrad off-axis configuration with respect to the Neutrinos at the Main Injector (NuMI) beam, similar to the arrangement of T2K. The most recent report from NOνA uses both $\nu_\mu \to \nu_e$ and $\nu_\mu \to \nu_\mu$ data to determine one standard deviation confidence intervals on oscillation parameters in the normal ordering of $\Delta m^2_{32} \in [2.37, 2.52] \times 10^{-3}$ eV^2, $\sin^2\theta_{23} \in [0.43, 0.51] \cup [0.52, 0.60]$,

and $\delta_{CP} \in [0, 0.12\pi] \cup [0.91\pi, 2\pi]$ [95].

The Oscillation Project with Emulsion-tRacking Apparatus (OPERA) located at Laboratori Nazionali del Gran Sasso (LNGS) was uniquely designed for the direct observation of tau neutrino appereance in a muon beam ($\nu_\mu \to \nu_\tau$) [96]. While not an example of precision measurement of oscillation parameters, a precise detector design is required to detect this elusive process. The OPERA detector consisted of 150,000 stacked nuclear emulsion bricks [97] and a magnetic spectrometer for momentum and charge identification of outgoing particles [98]. The CERN Neutrinos to Gran Sasso (CNGS) neutrino beam analyzed by OPERA originated from the bombardment of a carbon target by protons accelerated in the Super Proton Synchrotron (SPS) at CERN and was sampled at a baseline of 730 km [99]. In the full period of data collection between 2008 and 2012, OPERA observed a total of 10 ν_τ candidate events which represents a significance of 6.1σ and permitted the measurement of $\Delta m^2_{23} = 2.7^{+0.7}_{-0.6}$ eV^2 under the assumption that $\sin^2 2\theta_{23} = 1$ [100].

At the close of 2011, the only mixing angle left without a precise measurement was θ_{13}. In 2003, the Chooz experiment published results on the search for $\bar{\nu}_e \to \bar{\nu}_x$ oscillations in the neutrinos produced at the nuclear power station of the same name [101]. Chooz observed no significant evidence for these oscillations and placed an upper bound of $\sin^2_{13} \leq 0.16$. This result, in conjunction with the measured values for the atmospheric and solar mixing, led to a great deal of speculation about the possibility of tribimaximal mixing in the PMNS matrix [102] [103] [104].

In early 2012, three separate yet similar experiments, Daya Bay [105], the Reactor Experiment for Neutrino Oscillation (RENO) [106], and Double Chooz [107], realeased results indicating the observation of $\bar{\nu}_e$ disappearance in the flux from nuclear reactor produced neutrinos. Each of these experiments employed similar layered detector designs with an outer veto region, a mineral oil buffer layer, and inner detector regions containing liquid scintillator with Gadolinium-doping used in the innermost volume. Double Chooz [108] is a successor experiment to Chooz and observes antineutrinos produced at the nuclear power station of that name in northern France initially with a single far detector at a baseline of 1050 m and presently with the addition of a near detector at a baseline of 415 m. Daya Bay [109] observes antineutrinos produced from the nuclear complex of the same name in southeastern China using a total of six identical antineutrino detectors (ADs) with two near ADs positioned at a baseline of 470 m, one near AD at a baseline of 576 m, and three far ADs at a baseline of 1648 m. RENO [110] observes antineutrinos produced at the Hanbit (previously Yonggwang) Nuclear Power Plant in South Korea with a near detector situated at a baseline of 294 m and an identical far detector at a baseline of 1383 m. In the most recent available results from each of the experiments, the measurement of $\sin^2 2\theta_{13}$ is most constrained by Daya Bay with a value given by $\sin^2 2\theta_{13} = 0.0841 \pm 0.0027(\text{stat.}) \pm 0.0019(\text{syst.})$ [111] in comparison to the values measured by RENO at $\sin^2 2\theta_{13} = 0.0896 \pm 0.0048(\text{stat.}) \pm 0.0048(\text{syst.})$ [112] and by Double Chooz at $\sin^2 2\theta_{13} = 0.088 \pm 0.033(\text{stat+syst.})$ [113]. In addition to the most constraining measurement on

NuFIT 3.2 (2018)

	Normal Ordering (best fit)		Inverted Ordering ($\Delta\chi^2 = 4.14$)		Any Ordering
	bfp $\pm 1\sigma$	3σ range	bfp $\pm 1\sigma$	3σ range	3σ range
$\sin^2\theta_{12}$	$0.307^{+0.013}_{-0.012}$	$0.272 \to 0.346$	$0.307^{+0.013}_{-0.012}$	$0.272 \to 0.346$	$0.272 \to 0.346$
$\theta_{12}/^\circ$	$33.62^{+0.78}_{-0.76}$	$31.42 \to 36.05$	$33.62^{+0.78}_{-0.76}$	$31.43 \to 36.06$	$31.42 \to 36.05$
$\sin^2\theta_{23}$	$0.538^{+0.033}_{-0.069}$	$0.418 \to 0.613$	$0.554^{+0.023}_{-0.033}$	$0.435 \to 0.616$	$0.418 \to 0.613$
$\theta_{23}/^\circ$	$47.2^{+1.9}_{-3.9}$	$40.3 \to 51.5$	$48.1^{+1.4}_{-1.9}$	$41.3 \to 51.7$	$40.3 \to 51.5$
$\sin^2\theta_{13}$	$0.02206^{+0.00075}_{-0.00075}$	$0.01981 \to 0.02436$	$0.02227^{+0.00074}_{-0.00074}$	$0.02006 \to 0.02452$	$0.01981 \to 0.02436$
$\theta_{13}/^\circ$	$8.54^{+0.15}_{-0.15}$	$8.09 \to 8.98$	$8.58^{+0.14}_{-0.14}$	$8.14 \to 9.01$	$8.09 \to 8.98$
$\delta_{\rm CP}/^\circ$	234^{+43}_{-31}	$144 \to 374$	278^{+26}_{-29}	$192 \to 354$	$144 \to 374$
$\frac{\Delta m^2_{21}}{10^{-5}\ \mathrm{eV}^2}$	$7.40^{+0.21}_{-0.20}$	$6.80 \to 8.02$	$7.40^{+0.21}_{-0.20}$	$6.80 \to 8.02$	$6.80 \to 8.02$
$\frac{\Delta m^2_{3\ell}}{10^{-3}\ \mathrm{eV}^2}$	$+2.494^{+0.033}_{-0.031}$	$+2.399 \to +2.593$	$-2.465^{+0.032}_{-0.031}$	$-2.562 \to -2.369$	$\begin{bmatrix} +2.399 \to +2.593 \\ -2.536 \to -2.395 \end{bmatrix}$

Figure 1.6: The best-fit oscillation parameters in a three-flavor model to global neutrino oscillations data available as of November 2017. The first column gives the best-fit parameters for the normal mass ordering while the second column gives the best fit parameters for inverted mass ordering, which is disfavored at $\sim 2\sigma(\Delta\chi^2 = 4.14)$. The third column shows the result when minimizing with respect to the mass ordering. Table reproduced from Ref. [114].

θ_{13}, Daya Bay measures the atmospheric mass-splitting to high precision with reported values $\Delta m^2_{32} = (2.45 \pm 0.06\ (\text{stat.}) \pm 0.06\ (\text{syst.})) \times 10^{-3}\ \text{eV}^2$ in the case of normal ordering and $\Delta m^2_{32} = (-2.56 \pm 0.06\ (\text{stat.}) \pm 0.06\ (\text{syst.})) \times 10^{-3}\ \text{eV}^2$ in the case of inverted mass ordering [111].

A collection of global fit efforts have been undertaken in order to combine the plethora of experimental results discussed in this section into a unified result summarizing the collective knowledge of neutrino oscillation parameters [115] [116] [117] [118] [119]. A summary of the status of the neutrino oscillations parameters as computed by NuFit [116] [114] is shown in Fig. 1.6. The remaining ambiguities in the three-flavor oscillation parameters are:

- Mass ordering: Since neutrino oscillations experiments are most sensitive only to the differences in the squared mass of the mass eigenstates, the absolute ordering of these states is undetermined. The two possibilities for mass ordering are the normal ordering ($\nu_1 < \nu_2 < \nu_3$; $\Delta m^2_{32} > 0$) and the inverted ordering ($\nu_3 < \nu_1 < \nu_2$; $\Delta m^2_{32} < 0$). The data available as of November 2017 show an emerging preference for the normal mass ordering at a significance of $\sim 2\sigma$.

- θ_{23} octant: The leading term for the disappearance of muon neutrinos is given by $\sin^2(\theta_{23})$, which is not sensitive to whether θ_{23} is greater than or less than $\pi/4$. Conducting precision studies of oscillation probabilities sensitive to sub-leading asymmetric contributions of θ_{23} are necessary to break this degeneracy. Current global data tend to prefer an upper octant ($\theta_{23} > \pi/4$) solution, however lower octant and maximal mixing solutions are not disfavored significantly.

- CP violation: The δ_{CP} parameter determines the strength of CP violation in the neutrino sector and it has not yet been precisely measured. The current best fit to global data shows a preference for significant CP violation but persitent large uncertainties have prevented a definitive measurement.

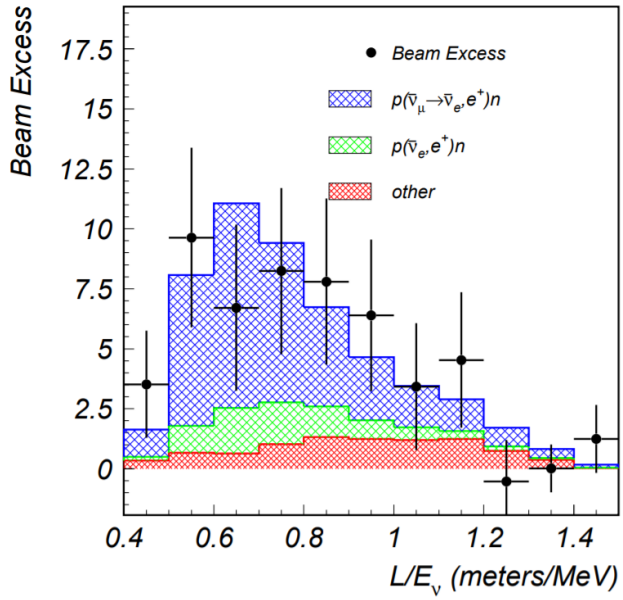

Figure 1.7: The total excess of $\nu_\mu \to \nu_e$ appearance events observed by LSND as a function of L/E. The data are shown by the black points, and the best fit is shown for background sources given by the red and green histograms and an oscillation signal shown by the blue histogram. The figure is taken from Ref. [120].

1.3 Anomalous Results

Neutrino oscillations amongst the three weak flavor eigenstates having been established by both theory and experiment to high precision, the oscillation results observed by a particular subset of eperiments has proved anomalous. These anomalous results are presented in detail in this section.

1.3.1 LSND

The Liquid Scintillator Neutrino Detector (LSND), consisting of a single cylindrical 167 ton tank containing mineral oil and a small amount of

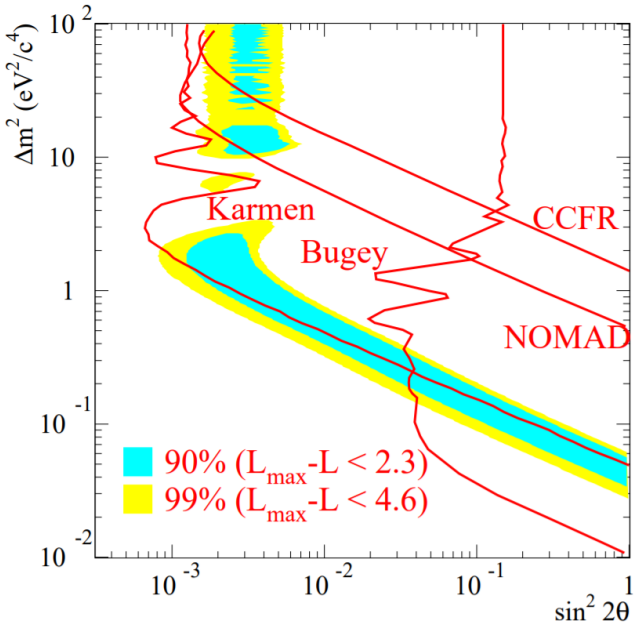

Figure 1.8: The allowed region in a two-flavor oscillations parameter space as derived from the ν_e excess observed by LSND. The yellow and blue shaded regions show the 90% and 99% confidence intervals respectively. Exclusion limits from a selection of experiments obtaining null results are also shown by the red lines for comparison. The figure is taken from Ref. [120].

organic scintillator b-PBD, was designed to observe $\bar{\nu}_\mu \rightarrow \bar{\nu}_e$ and $\nu_\mu \rightarrow \nu_e$ oscillations [121]. The neutrino beam sampled by LSND was produced by the Los Alamos Meson Physics Facility (LAMPF) via 800 MeV protons bombarding a beam stop with a baseline to the detector of approximately 30 m. The primary source of neutrinos arises through the decay-at-rest (DAR) of pions and muons within the 30 cm water beam stop in the processes

$$\pi^+ \rightarrow \mu^+ + \nu_\mu \mu^+ \rightarrow e^+ + \nu_e + \bar{\nu}_\mu \ . \tag{1.62}$$

The observation of $\bar{\nu}_\mu \rightarrow \bar{\nu}_e$ is dependent upon the suppression of the charge conjugate interaction, which would produce contaminating $\bar{\nu}_e$ not due to oscillations, due to an order of magnitude less π^- production as compared to π^+ in the beam stop, high probability for π^- absorption prior to decay, and high probability of μ^- capture prior to decay [122]. The combination of these factors results in a ratio of 7.8×10^{-4} between beam $\bar{\nu}_e$ from μ^- DAR and $\bar{\nu}_\mu$ from μ^+ DAR. The detection of $\bar{\nu}_e$ in LSND was observed in the interaction

$$\bar{\nu}_e + p \rightarrow e^+ + n \ , \tag{1.63}$$

however LSND had no experimental apparatus for determing the charge of outgoing particles, so the particular detection of $\bar{\nu}_e$ required the observation of a correlated photon produced in the neutron capture process

$$n + p \rightarrow d + \gamma \tag{1.64}$$

where the exiting photon has an energy of 2.2 MeV [123]. LSND further suppressed the ν_e background by requiring an energy threshold $E_e > 36$ MeV in order to eliminate misidentification with uncorrelated photons.

In 1996, LSND first reported a fitted excess of $51.8^{+18.7}_{-16.9} \pm 8.0$ $\bar{\nu}_e$ candidate events with an expected background level of 4.6 ± 0.6 events [121]. In terms of neutrino oscillation parameters, the observed excess requires a mass-splitting $\Delta m^2 \geq 4 \times 10^{-2}$ eV^2 assuming a two-flavor oscillation framework, which is an order of magnitude larger than the previoulsy observed mass-splitting scales and defines the anomalous nature of this result. LSND also searched for $\nu_\mu \to \nu_e$ oscillations in a study published in 1998, and observed an excess of 40 ν_e candidate events in comparison to an expected background of 21.9 ± 2.1 events due to ν_e beam contamination, which was found to be compatible in terms of oscillation parameters with the observation in antineutrinos [124]. The final published result from LSND [120], which is shown in Figs. 1.7 and 1.8, claimed a total observed excess of $87.9 \pm 22.4 \pm 6.0$ $\bar{\nu}_e$ event candidates in the energy range of 20 to 60 MeV with a stated significance of 3.8σ and corresponding to an oscillation probability of $(0.264 \pm 0.067 \pm 0.045)\%$ with a Δm^2 between 0.2 and 10 eV^2.

1.3.2 MiniBooNE

Motivated by the anomalous $\bar{\nu}_e$ excess observed by LSND, the MiniBooNE (Mini Booster Neutrino Experiment) was designed to confirm the observation of LSND and to precisely measure the oscillation parameters governing the $\nu_\mu \to \nu_e$ transition [126]. The MiniBooNE detector is a spherical tank with diameter 12.2 m containing 800 t of mineral oil (CH_2) with an optical barrier dividing the inner detector region from an outer veto region. The in-

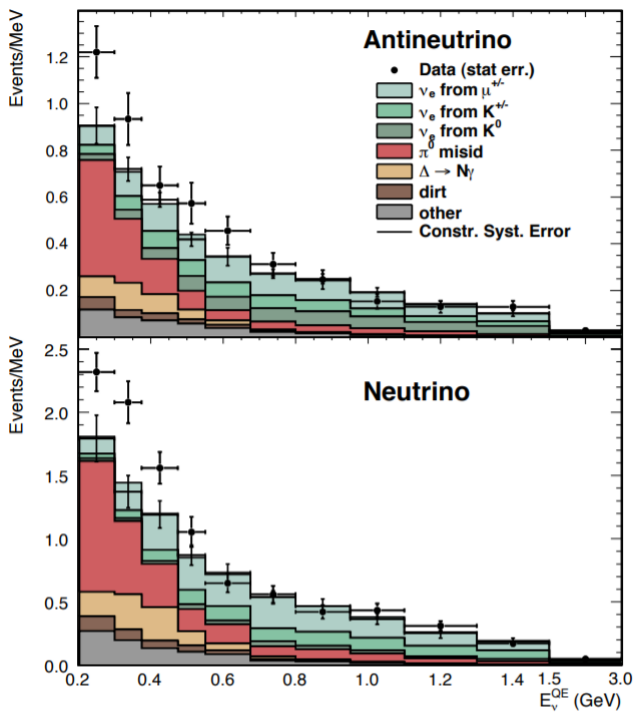

Figure 1.9: The total excess of $\nu_\mu(\bar{\nu}_\mu) \rightarrow \nu_e(\bar{\nu}_e)$ appearance events observed by MiniBooNE as a function of visible energy. The data are shown by the black points, which are observed above the level of estimated backgrounds (shaded histograms) in the low energy region. The figure is taken from Ref. [125].

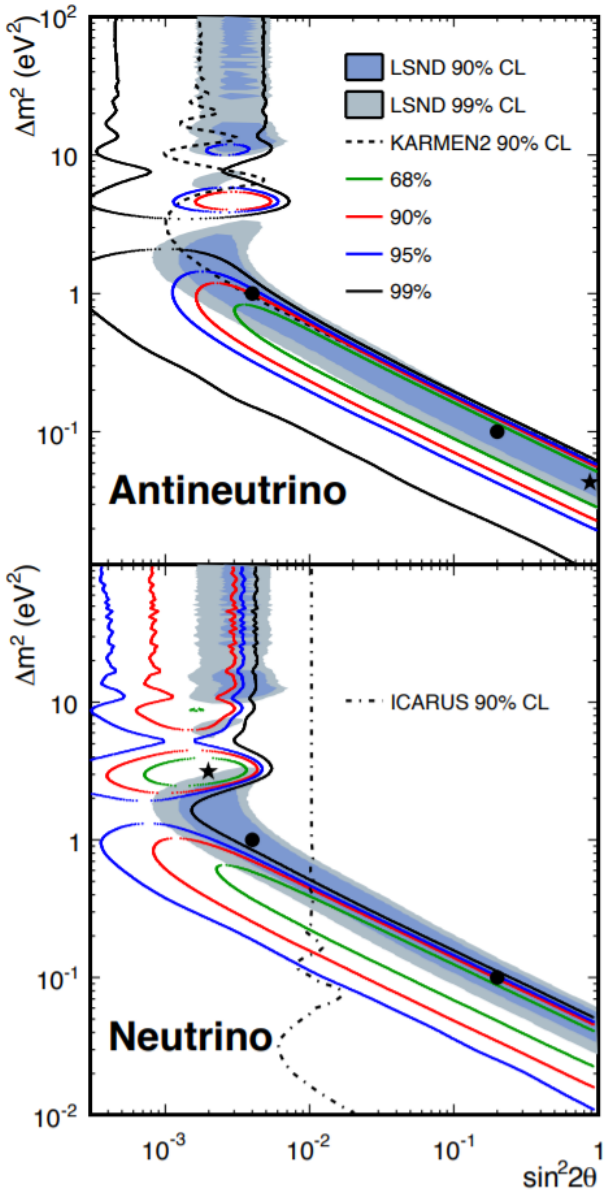

Figure 1.10: The allowed region in a two-flavor oscillations parameter space as derived from the $\nu_e(\bar{\nu}_e$ excess observed by MiniBooNE. The colored lines show the MiniBooNE results at the listed confidence levels. The identical LSND allowed regions as shown in Fig. 1.8 are plotted as the shaded regions. Exclusion limits from the null results observed by KARMEN2 and ICARUS are also plotted for comparison. The figure is taken from Ref. [125].

ner detector has a radius of 5.75 m and is instrumented by 1280 PMTs, which provide 10% photocathode coverage. The veto region is instrumented with 240 additional PMTs and detects background particles entering from outside the detector. MiniBooNE samples the Fermilab Booster neutrino beam, which is produced by 8 GeV protons impinging on a beryllium target of length 71 cm and diameter 1 cm, at a baseline of 541 m with the center of the detector displaced from the beam center by a distance of 1.9 m. MiniBooNE detects particles by capture of both Čerenkov light and isotropic scintillation light in order to classify each event candidate as a μ, e, or π^0 candidate [127], with the oscillations signal extracted from the electron candidate events.

In the earliest search for $\nu_\mu \to \nu_e$ oscillations produced by MiniBooNE, no significant excess compatible with the LSND observation was found [127]. An analysis with increased data collection published in the following year reported an excess of $128.8 \pm 20.4 \pm 38.3$ electron candidate events in the energy range from 200 to 475 MeV, though no further excess was observed in the energy range from 475 to 1250 MeV [128]. The results of the MiniBooNE observed excess are shown in Figs. 1.9 and 1.10. In 2009, MiniBooNE reported no observation of muon neutrino ($\nu_\mu \to \nu_\mu$) or antineutrino disappearance for mass-splitting scales in the range $\Delta m^2 \in [0.1, 10]$ eV^2 [129], which would be later confirmed in a dual baseline search using the SciBar detector (referred to as SciBooNE) [130] to exclude muon (anti)neutrino disappearance first for $0.5\,\text{eV}^2 < \Delta m^2 < 40\,\text{eV}^2$ [131] and later for $0.1\,\text{eV}^2 < \Delta m^2 < 100\,\text{eV}^2$ [132]. In the release of analysis results from this year, MiniBooNE has reported a total

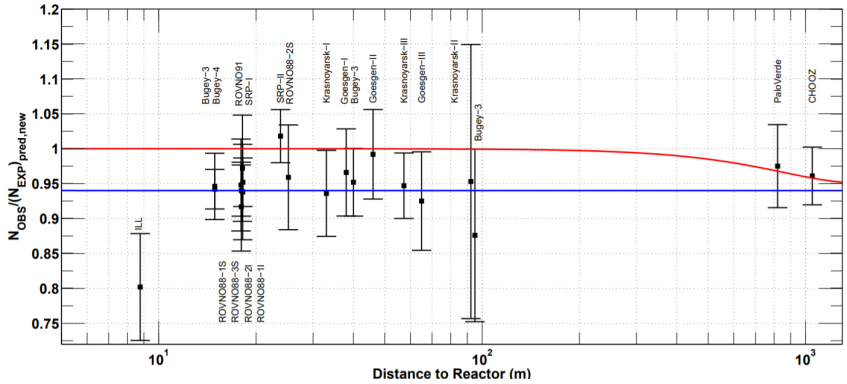

Figure 1.11: A plot illustrating the reactor electron antineutrino anomaly. Under the assumption of standard three flavor oscillations, the data points shown in the plot measured at a menagerie of nuclear reactor neutrino experiments should agree with the red line. However, solutions such as the blue line, which is not a fit but is for illustration purposes, could describe the data given the overall average rate deficit observed with respect to the standard three-flavor prediction. The figure is taken from Ref. [134].

observed excess from the combined ν_e and $\bar{\nu}_e$ channels of 460.5 ± 95.8 events, corresponding to a reported significance of 4.8σ. Further, the MiniBooNE result is fit in combination with the final LSND data in order to derive a combined significance of 6.1σ with oscillation parameters measured at $\Delta m^2 = 0.041$ eV^2 and $\sin^2 2\theta = 0.958$ under the assumption of two-flavor oscillations [133].

1.3.3 Reactor Antineutrino Anomaly

The interpretation of observed neutrino event rates from nuclear reactor neutrino sources is highly dependent on the modeling of the expected neutrino flux arising from the decays of nuclear isotopes ^{235}U, ^{238}U, ^{239}Pu, and

^{241}Pu, and the change in relative composition of these isotopes during the nuclear fuel aging process [134]. Recent detailed recalculations [135] [136] of the expected neutrino flux for reactor neutrino experiments results in a prediction of increased neutrino flux of approximately 3.5% [137]. With the previous flux predictions, the global average for the ratio of observed to expected event rates for reactor experiments with baselines < 100 m was 0.976 ± 0.024, however, the new flux prediction shifts this observed to expected ratio to 0.943 ± 0.023 implying a deficit of $> 2\sigma$ significance in $\bar{\nu}_e$ flux from reactor experiments, as is illustrated in Fig. 1.11. This effect has been called the "reactor antineutrino anomaly" [134]. This heretofore unnoticed $\bar{\nu}_e$ disappearance observed in various short-baseline reactor experiments can be interpreted in the context of oscillations with parameters $|\Delta m^2_{new}| > 1.5$ eV^2 and $\sin^2(2\theta_{new}) = 0.14 \pm 0.08$ at a 95% CL.

1.3.4 Gallium Anomaly

A further anomaly has been observed in the solar neutrino experiments GALLEX and SAGE, the experimental details of which were discussed in Section 1.2.1. The initial observation of a deficit of solar neutrinos motivated further study in the calibration of detector response in both of these experiments. The detector calibration was performed by exposing the detectors to a monoenergetic ν_e flux from source material containing either ^{51}Cr or ^{37}Ar [138]. As in the detection of solar neutrinos, the GALLEX and SAGE detectors measure the electron neutrino capture by Gallium nuclei shown in Eq. 1.10

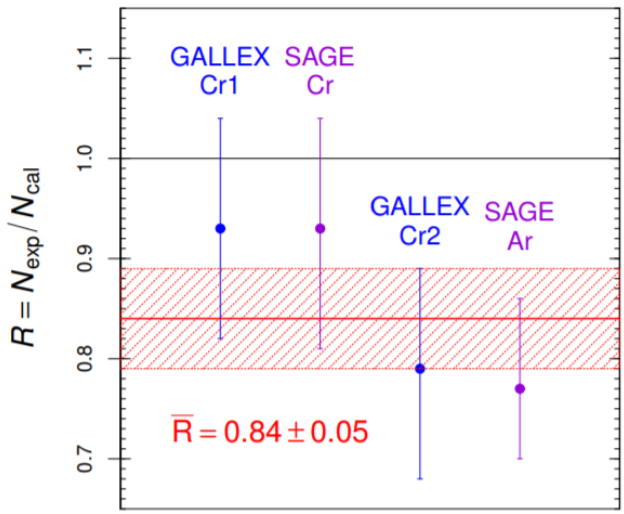

Figure 1.12: Plot summarizing the Gallium anomaly. The ratios of expected to calculated electron neutrino events are shown for the GALLEX [139] [140] and SAGE [141] along with the combined average from all of the plotted measurements (red-hatched band). Figure reproduced from Ref. [142].

by extraction of the resulting Germanium and detection via Geiger counter.

The first source experiment conducted by SAGE [141] used a 19.13 PBq source of ^{51}Cr with an expected neutrino emission energy of 747 keV. The ratio of the observed to theoretical cross section was found to be $0.95 \pm 0.12(\text{expt.})^{+0.035}_{0.027}(\text{theor.})$ using calculations by Bahcall. The second source experiment at SAGE [143] used a source of ^{37}Ar with intial strength 15.13 ± 0.07 PBq and an expected neutrino emission energy of 811 keV. The ratio of observed to theoretical cross section for this source was found to be $0.791^{+0.084}_{-0.078}$.

GALLEX performed two source experiments [139] [140], both using a ^{51}Cr with initial strength approximately 60 PBq. GALLEX compared the strength of each source of the ^{51}Cr samples as derived from the measurement

of the neutrino flux with the independently measured source strengths. The ratios of observed to expected neutrino flux upon initial measurement was found to be $1.01^{+0.12}_{-0.11}$ for the first source [139] and $0.84^{+0.12}_{-0.11}$ for the second source with a combined ratio of 0.93 ± 0.08 [140]. A later reanalysis of the reults [144], which more accurately accounts for detector efficiencies, reduced the observed ratios to $0.953^{+0.11}_{-0.11}$ for the first source, $0.812^{+0.10}_{-0.11}$ for the second source, and 0.882 ± 0.078 for the combination of both source experiments.

Combining the source experiment results observed in SAGE and GALLEX results in an average observed ratio, $\bar{R}$, of observed to expected neutrino fluxes of $\bar{R} = 0.84 \pm 0.05$, which represents a deficit from unity with significance of 2.9σ and is shown graphically in Fig. 1.12 [142]. This effect is called the gallium anomaly [138]. Given that the average traveling distances of detected neutrinos from the radioactive sources can be computed at 1.9 m for GALLEX and 0.6 m for SAGE, the observed ν_e deficit can be interpreted in the context of neutrino oscillations with parameters $\sin^2 2\theta > 0.07$ and $\Delta m^2 > 0.35$ eV^2 assuming two-flavor oscillations.

1.3.5 Null Results

Following the observation of excess ν_e and $\bar{\nu}_e$ appearance by LSND, the Karlsruhe Rutherford Medium Energy Neutrino (KARMEN) experiment [145], the Neutrino Oscillation Magnetic Detector (NOMAD) experiment [146], the previously discussed OPERA experiment (see Section 1.2.6), and the Bugey nuclear reactor experiment [147], in addition to the aforementioned Mini-

BooNE attempted to verify the LSND observation and to determine the underlying oscillation parameters. In each of these experiments, with the exception of LSND and MiniBooNE, null results [148] [149] [150] [151] were found which disfavor neutrino oscillations at a new mass-splitting scale.

More recently, the reactor antineutrino anomaly has found a possible explantion outside of anomalous oscillations interpretation. In 2017, the Daya Bay experiment (see Section 1.2.6) published a measurement of the changes in the flux rate of the reactor neutrinos as a function of the relative fraction of the fissile isotopes ^{235}U and ^{239}Pu [152]. This measurement finds that the oscillations explanation for the anomalous reactor deficit is inconsistent with the observation of linear dependence between the flux and isotope fractions at a 2.6σ significance. Instead Daya Bay found a significant discrepancy between the observation and prediction from the Huber-Mueller model for the flux resulting from the decay of the ^{235}U isotope, which is determined to be a potential cause of the reactor antineutrino anomaly.

Another unique source of evidence comes from analysis fo the power spectrum of the cosmic microwave background (CMB). The Planck satellite [153] has measured the variations in the CMB to high precision, and a fit to the power spectrum of these variations constrains the number of effective relativistic species N_{eff}, a measurement of the number of neutrino flavors, and the sum of the masses of the neutrinos $\sum m_\nu$. Mapping the constraints provided by the CMB measurements to the parameter space of neutrino oscillations results in a highly constrained null result [154], which is shown in Fig. 1.13.

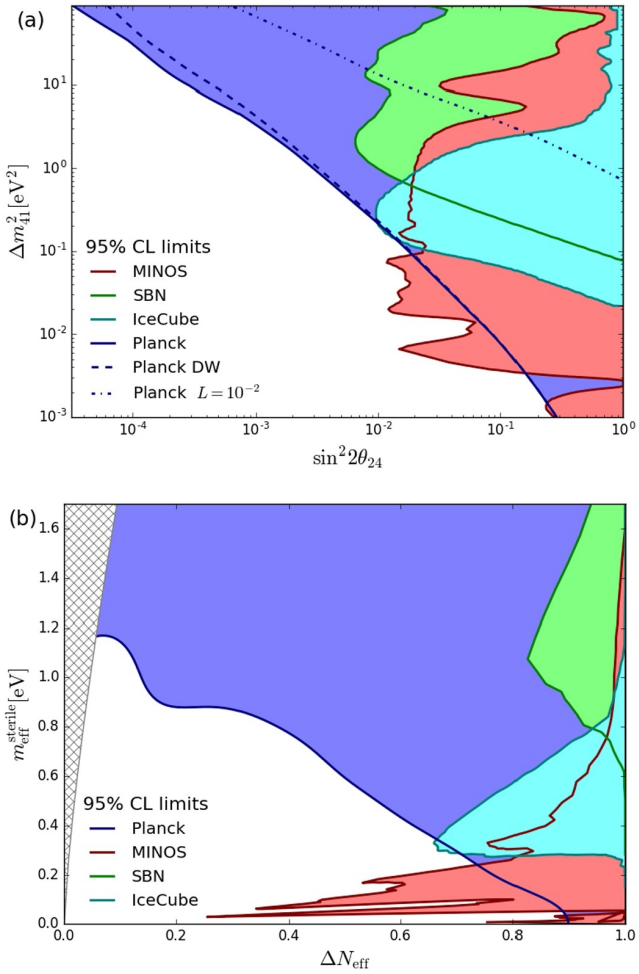

Figure 1.13: (a) Excluded regions (shaded) at a 95% CL of the neutrino oscillations parameter space (Δm^2_{41}, $\sin^2 2\theta_{24}$) for a fourth mass eigenstate corresponding to the existence of a sterile neutrino. The limits shown are from MINOS [155], IceCube [156], the forecast of the Fermilab Short-Baseline Nuetrino (SBN) program [157], and three scenarios from the Planck experiment detailed in [154]. (b) The excluded regions from the top panel mapped into the parameter space ($m^{sterile}_{eff}$,ΔN_{eff}) which are those relevant to neutrino oscillations in the fit to the power spectrum of the CMB. Differences between the Planck scenarios are negligible in the CMB parameter space. Figure reproduced from Ref. [154].

The continuous tension between the anomalous and null results, including those discussed in this section and others [156] [158] [159] serves as motivation for the search for anomalous neutrino oscillations detailed in this thesis.

1.4 Sterile Neutrinos

As was discussed in Section 1.2.6, experimental evidence has consistently agreed with the existence of three light neutrino flavors with numerical correspondence between the mass and weak eigenstates. Thus, if additional neutrino flavors were to exist, such as to allow for a fourth mass eigenstate to be accommodated, these must in fact be "sterile" with respect to the weak interaction.

1.4.1 Properties

Sterile neutrinos are described by a right-handed singlet representation with respect to the weak and strong interactions with zero weak hypercharge and isospin [160]. Such a theory represents an extension to the SM, which contains only left-handed neutrinos and right-handed antineutrinos in doublets with associated leptons [30], though as it has been noted, any theory describing massive neutrinos is in fact BSM. In addition to sterility with respect to the weak interaction, the sterile neutrinos would also not participate in the strong interaction, as with other leptons since they have no color charge, nor in the electromagnetic interactions given that they have electric charge of zero.

The only interactions in which the sterile neutrinos would participate are gravitation and the Higgs field [161]. The Yukawa interactions with the SM leptons and the Higgs field would allow for mixing of the sterile neutrinos with the weakly interacting neutrino flavors allowing for indirect observation of sterile neutrinos via oscillation measurements [162]. While the three weak-flavored neutrinos are restricted in number, the number of right-handed singlet sterile neutrinos is not restricted given that they represent a BSM extension. Given that much remains unknown with respect to sterile neutrinos, and given that the existence of sterile neutrinos could provide explanations for Majorana or Dirac masses of the neutrinos, the evolution of supernovae, and represent candidates for either warm or cold dark matter, sterile neutrino searches have garnered increased interest in neutrino detection experiments.

1.4.2 Oscillations in a 3+1 Flavor Model

The simplest model allowing for the addition of sterile neutrinos to the three known flavors is the so-called 3+1 model, wherein a fourth flavor state ν_s is added, corresponding to a fourth mass eigenstate ν_4 allowing for the construction of a 4×4 unitary mixing matrix similar to those presented previously. The mixing matrix has the structure

$$U = \begin{pmatrix} U_{e1} & U_{e2} & U_{e3} & U_{e4} \\ U_{\mu 1} & U_{\mu 2} & U_{\mu 3} & U_{\mu 4} \\ U_{\tau 1} & U_{\tau 2} & U_{\tau 3} & U_{\tau 4} \\ U_{s1} & U_{s2} & U_{s3} & U_{s4} \end{pmatrix} \tag{1.65}$$

The additional mass eigenstate gives rise to a new mass-splitting, Δm^2_{41}, as well as three new mixing angles (θ_{14},θ_{24},θ_{34}) and two new CP violating phases (δ_{14},δ_{24}). Carrying out calculations in the same manner as those detailed for three-flavor oscillations, the probability for muon neutrino survival in the 3+1 model may be written

$$\begin{aligned} P(\nu_\mu \to \nu_\mu) &= \delta_{\mu\mu} - 4\sum_{i>k} \mathrm{Re}[U^*_{\mu i}U_{\mu i}U_{\mu k}U^*_{\mu k}]\sin^2\Delta_{ik} \\ &\quad + 2\sum_{i>k} \mathrm{Im}[U^*_{\mu i}U_{\mu i}U_{\mu k}U^*_{\mu k}]\sin\ 2\Delta_{ik} \\ &= \delta_{\mu\mu} - 4\sum_{i>k} \mathrm{Re}[|U_{\mu j}|^2|U_{\mu j}|^2]\sin^2\Delta_{ik} \\ &\quad + 2\sum_{i>k} \mathrm{Im}[|U_{\mu j}|^2|U_{\mu j}|^2]\sin\ 2\Delta_{ik}. \end{aligned} \tag{1.66}$$

By definition the Kronecker delta reduces to $\delta_{\mu\mu} = 1$ and the second sum is zero since the squared modulus of complex numbers does not retain an imaginary component. Expanding the first sum yields

$$\begin{aligned} P(\nu_\mu \to \nu_\mu) = 1 - 4\Big(&|U_{\mu 1}|^2|U_{\mu 2}|^2\sin^2\Delta_{21} + |U_{\mu 1}|^2|U_{\mu 3}|^2\sin^2\Delta_{31} \\ &+|U_{\mu 1}|^2|U_{\mu 4}|^2\sin^2\Delta_{41} + |U_{\mu 2}|^2|U_{\mu 3}|^2\sin^2\Delta_{32} \\ &+|U_{\mu 2}|^2|U_{\mu 4}|^2\sin^2\Delta_{42} + |U_{\mu 3}|^2|U_{\mu 4}|^2\sin^2\Delta_{43}\Big). \end{aligned} \tag{1.67}$$

As in the three-flavor oscillations computation, we use the atmospheric approximation such that $\Delta_{41} \simeq \Delta_{42}$ and $\Delta_{32} \simeq \Delta_{31}$. Collecting terms and employing the unitarity relation $\sum_k |U_{\mu k}|^2 = 1$ gives

$$\begin{aligned} P(\nu_\mu \to \nu_\mu) \approx 1 &- 4(1 - |U_{\mu 3}|^2 - |U_{\mu 4}|^2)|U_{\mu 3}|^2\sin^2\Delta_{31} \\ &- 4(1 - |U_{\mu 3}|^2 - |U_{\mu 4}|^2)|U_{\mu 4}|^2\sin^2\Delta_{41} \\ &- 4|U_{\mu 3}|^2|U_{\mu 4}|^2\sin^2\Delta_{43}. \end{aligned} \tag{1.68}$$

In the ordinary parameterization, the relevant terms needed for the matrix elements in Eq. 1.68 are

$$\begin{aligned}
|U_{\mu 3}|^2 = \; & s_{13}^2 s_{14}^2 s_{24}^2 \; + \; c_{13}^2 s_{23}^2 c_{24}^2 \\
& - \frac{1}{2} s_{23} s_{14} \sin(2\theta_{13}) \sin(2\theta_{24}) \cos(\delta_{CP} - \delta_{14} + \delta_{24}), \\
|U_{\mu 4}|^2 = \; & c_{14}^2 s_{24}^2.
\end{aligned} \tag{1.69}$$

Further, assuming that $\Delta_{32} \approx \Delta_{31}$ and $\Delta_{43} \approx \Delta_{41}$, and taking $\theta_{13}, \theta_{14} \ll 1$, the form of the survival probability may be condensed and simplified to the form

$$P(\nu_\mu \to \nu_\mu) \approx 1 - \sin^2(2\theta_{23}) \cos^4(\theta_{24}) \sin^2 \Delta_{32} - \sin^2(2\theta_{24}) \sin^2 \Delta_{41}. \tag{1.70}$$

Similarly, the oscillation probability for the transition from a muon neutrino to a sterile neutrino is given by

$$\begin{aligned}
P(\nu_\mu \to \nu_s) \approx \delta_{\mu s} & - 4 \sum_{i>k} \mathrm{Re}[U_{\mu i}^* U_{si} U_{\mu k} U_{sk}^*] \sin^2 \Delta_{ik} \\
& + 2 \sum_{i>k} \mathrm{Im}[U_{\mu i}^* U_{si} U_{\mu k} U_{sk}^*] \sin \; 2\Delta_{ik} \\
\approx & - 4 \sum_{i>k} \mathrm{Re}[U_{\mu i}^* U_{si} U_{\mu k} U_{sk}^*] \sin^2 \Delta_{ik} \\
& + 2 \sum_{i>k} \mathrm{Im}[U_{\mu i}^* U_{si} U_{\mu k} U_{sk}^*] \sin \; 2\Delta_{ik}.
\end{aligned} \tag{1.71}$$

Considering the first summation:

$$-4 \sum_{i>k} \mathrm{Re}[U_{\mu i}^* U_{si} U_{\mu k} U_{sk}^*] \sin^2 \Delta_{ik} \tag{1.72}$$

we expand the indices to obtain

$$\begin{aligned}
-4 \Big(& \mathrm{Re}[U_{\mu 2}^* U_{s2} U_{\mu 1} U_{s1}^*] \sin^2 \Delta_{21} + \mathrm{Re}[U_{\mu 3}^* U_{s3} U_{\mu 1} U_{s1}^*] \sin^2 \Delta_{31} \\
& + \mathrm{Re}[U_{\mu 4}^* U_{s4} U_{\mu 1} U_{s1}^*] \sin^2 \Delta_{41} + \mathrm{Re}[U_{\mu 3}^* U_{s3} U_{\mu 2} U_{s2}^*] \sin^2 \Delta_{32} \\
& + \mathrm{Re}[U_{\mu 4}^* U_{s4} U_{\mu 2} U_{s2}^*] \sin^2 \Delta_{42} + \mathrm{Re}[U_{\mu 4}^* U_{s4} U_{\mu 3} U_{s3}^*] \sin^2 \Delta_{43} \Big)
\end{aligned} \tag{1.73}$$

Using the previously discussed atmospheric approximation we can write

$$\begin{aligned}-4\Big(&\operatorname{Re}[U^*_{\mu 3}U_{s3}U_{\mu 1}U^*_{s1}+U^*_{\mu 3}U_{s3}U_{\mu 2}U^*_{s2}]\sin^2\Delta_{31}\\&+\operatorname{Re}[U^*_{\mu 4}U_{s4}U_{\mu 1}U^*_{s1}+U^*_{\mu 4}U_{s4}U_{\mu 2}U^*_{s2}]\sin^2\Delta_{41}\\&+\operatorname{Re}[U^*_{\mu 4}U_{s4}U_{\mu 3}U^*_{s3}]\sin^2\Delta_{43}\Big),\end{aligned} \tag{1.74}$$

and using the unitarity relation $\sum_k U_{\mu k}U^*_{sk}=0$, the expression is simplified to

$$\begin{aligned}4\Big(&\operatorname{Re}[U^*_{\mu 3}U_{s3}\ (U_{\mu 3}U^*_{s3}+U_{\mu 4}U^*_{s4})]\sin^2\Delta_{31}\\&+\operatorname{Re}[U^*_{\mu 4}U_{s4}\ (U_{\mu 3}U^*_{s3}+U_{\mu 4}U^*_{s4})]\sin^2\Delta_{41}\\&-\operatorname{Re}[U^*_{\mu 4}U_{s4}U_{\mu 3}U^*_{s3}]\sin^2\Delta_{43}\Big).\end{aligned} \tag{1.75}$$

In order to permit collecting of terms, we must note that

$$\operatorname{Re}[U_{\mu 4}U^*_{s4}U^*_{\mu 3}U_{s3}]=\operatorname{Re}[U^*_{\mu 4}U_{s4}U_{\mu 3}U^*_{s3}] \tag{1.76}$$

such that the sum in Eq. 1.75 is approximated by

$$\begin{aligned}\approx\ &4|U_{s3}|^2|U_{\mu 3}|^2\ \sin^2\Delta_{31}+4|U_{s4}|^2|U_{\mu 4}|^2\ \sin^2\Delta_{41}\\&+4\operatorname{Re}[U^*_{\mu 4}U_{s4}U_{\mu 3}U^*_{s3}]\ (\sin^2\Delta_{31}+\sin^2\Delta_{41}-\sin^2\Delta_{43})\end{aligned} \tag{1.77}$$

Returing to the second sum in Eq. 1.71, a similar procedure as is used for the first sum may be employed. In order to simplify and collect terms we must use $\operatorname{Im}[U_{\alpha k}U^*_{\alpha k}]=0$ and the opposite condition to Eq. 1.76 given by

$$\operatorname{Im}[U_{\mu 4}U^*_{s4}U^*_{\mu 3}U_{s3}]=-\operatorname{Im}[U^*_{\mu 4}U_{s4}U_{\mu 3}U^*_{s3}] \tag{1.78}$$

so that the second sum in Eq. 1.71 is approximated as

$$\approx 2\operatorname{Im}[U^*_{\mu 4}U_{s4}U_{\mu 3}U^*_{s3}]\ (\sin\ 2\Delta_{31}-\sin\ 2\Delta_{41}+\sin\ 2\Delta_{43}). \tag{1.79}$$

We can therefore write the simplified form of transition probability from muon neutrino to sterile neutrino given in Eq. 1.71 under the atmospheric approximation as

$$\begin{aligned} P(\nu_\mu \to \nu_s) \approx\ & 4|U_{s3}|^2|U_{\mu 3}|^2\ \sin^2\Delta_{31} + 4|U_{s4}|^2|U_{\mu 4}|^2\ \sin^2\Delta_{41} \\ & + 4\,\mathrm{Re}[U^*_{\mu 4}U_{s4}U_{\mu 3}U^*_{s3}]\ (\sin^2\Delta_{31} + \sin^2\Delta_{41} - \sin^2\Delta_{43}) \\ & + 2\,\mathrm{Im}[U^*_{\mu 4}U_{s4}U_{\mu 3}U^*_{s3}]\ (\sin\ 2\Delta_{31} - \sin\ 2\Delta_{41} + \sin\ 2\Delta_{43}) \end{aligned} \tag{1.80}$$

In terms of the mixing angles and CP violating phases, the relevant combinations of matrix elements for this oscillation probability are given by

$$\begin{aligned} \mathrm{Im}[U^*_{\mu 4}U_{s4}U_{\mu 3}U^*_{s3}] &= -\frac{1}{4}c^2_{13}c^2_{24}s_{24}\sin(2\theta_{23})\sin(2\theta_{34})\sin(\delta_{24}), \\ \mathrm{Re}[U^*_{\mu 4}U_{s4}U_{\mu 3}U^*_{s3}] &= -c^2_{13}c^2_{24}c_{34}s_{23}s_{24}[c_{34}s_{23}s_{24} + c_{23}s_{34}\cos(\delta_{24})], \\ |U_{s4}|^2 &= c^2_{14}c^2_{24}c^2_{34}, \\ |U_{s3}|^2 &= c^2_{23}s^2_{34}c^2_{13} + c^2_{34}s^2_{23}s^2_{24}c^2_{13} \\ &\quad + \frac{1}{2}s_{24}c^2_{13}\sin(2\theta_{23})\sin(2\theta_{34})\sin(\delta_{24}). \end{aligned} \tag{1.81}$$

Inspection of the probability expressions for both muon neutrino survival and sterile neutrino appearance under the atmospheric approximation demonstrate that these oscillation types have greatest sensitivity to the parameters θ_{23}, θ_{24}, θ_{34}, Δm^2_{32}, and Δm^2_{41}.

Chapter 2

MINOS and MINOS+ Experiments

In this chapter, we present a brief overview of the MINOS and MINOS+ experiments including the long-baseline concept and the production of the NuMI neutrino beam, which the detectors sample. The MINOS and MINOS+ detectors are discussed in detail including the design, instrumentation, electronics, and differences between the detectors. The conclusion of the chapter gives an explanation of interactions observed in the detectors and the event topologies that are produced.

2.1 MINOS and MINOS+

MINOS (Main Injector Neutrino Oscillation Search) [163] is a long-baseline neutrino oscillation experiment. The long-baseline accelerator neutrino concept [164] involves the sampling of a neutrino beam at two points along the beam separated by a long distance. In the case of MINOS, the beam sampled is the NuMI (Neutrinos at the Main Injector) beam [165], predominantly made up of muon neutrinos or antineutrinos, and the two detectors are the Near Detector (ND) and Far Detector (FD), positioned 1.04 km and 735 km downstream of the beam target, respectively. An illustration of the layout

of the MINOS experiment is shown in Fig. 2.1. The downstream positions of the ND and FD were selected in order to maximize the sensitivity in MINOS to the disappearance of muon neutrinos as mediated by the atmospheric mass-splitting scale (i.e. maximizing $\sin^2(\Delta m^2_{atm} L/4E_\nu)$). In this scenario, the ND measures the content of the neutrino beam before oscillations occur, and the FD measures the first neutrino oscillations maximum. The MINOS ND is located at Fermilab in Chicago, IL, and the MINOS FD was located in the Soudan Underground Laboratory in Minnesota.

2.1.1 MINOS

MINOS collected data during the period of March 2005 to April 2012 with various periods of beam optimization for either muon neutrinos or muon antineutrinos. The amount of data collected is quantified by the number of protons delivered to the target by the NuMI beam (protons-on-target, POT), and the per-week and cumulative POT exposure collected by MINOS is shown by the green and orange histograms plotted in Fig. 2.2. The MINOS era running was divided into ten run periods a summary of which may be found in Table 2.1. The largest sample accumulated by MINOS was in the muon neutrino mode with an energy spectrum peaking at approximately 3 GeV, which results in an L/E parameter of 500 km/GeV in the FD. In addition to the beam samples collected by MINOS, an additional atmospheric neutrino sample was collected with a total exposure of 37.88 kt-yr using the FD at a depth of 705 m below ground level (2070 mwe) [168].

Figure 2.1: A map indicating the locations of the MINOS and MINOS+ ND and FD. The ND is located at Fermilab at a baseline of 1.04 km from the target while the FD is located in the Soudan Underground Laboratory at a baseline of 735 km. Figure is reproduced from Ref. [166].

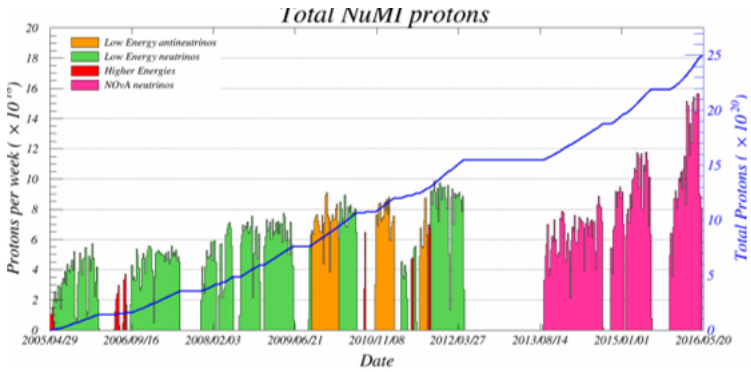

Figure 2.2: The cumulative and per-week POT data exposure for the full period of MINOS and MINOS+ running. MINOS and MINOS+ collected beam data from approximately 25×10^{20} POT over a total of 13 years of running. Figure is taken from Ref. [167].

The MINOS Collaboration has produced several important physics results in areas including standard three-flavor oscillations, non-standard interactions (NSI) of neutrinos, atmospheric and cosmic neutrino measurements, and sterile neutrino searches. The MINOS experimental measurement of the atmospheric oscillation parameter Δm^2_{32} was world-leading from the time of publication [92] until 2016, when MINOS+ completed data taking, and remains one of the most competitive measurements in that parameter amongst global experiments.

A recent MINOS and MINOS+ combined three-flavor analysis uses an exposure of 10.71×10^{20} protons-on-target (POT) with the beam in ν_μ running mode, 3.36×10^{20} POT with the beam in $\bar{\nu}_\mu$-enhanced running mode, and 48.70 kton-years of atmospheric neutrino data [169]. Charged-current (CC) events of both muon neutrinos and electron neutrinos are used in the analysis with

neutral-current (NC) events removed as background contamination. The total number of observed CC events in the FD for ν_μ ($\bar{\nu}_\mu$) is 2579 (312) fiducial events in comparison to the 3201 (363) which would be expected for no oscillations. The reconstructed energy spectra for the various event channels is displayed in Fig. 2.3.

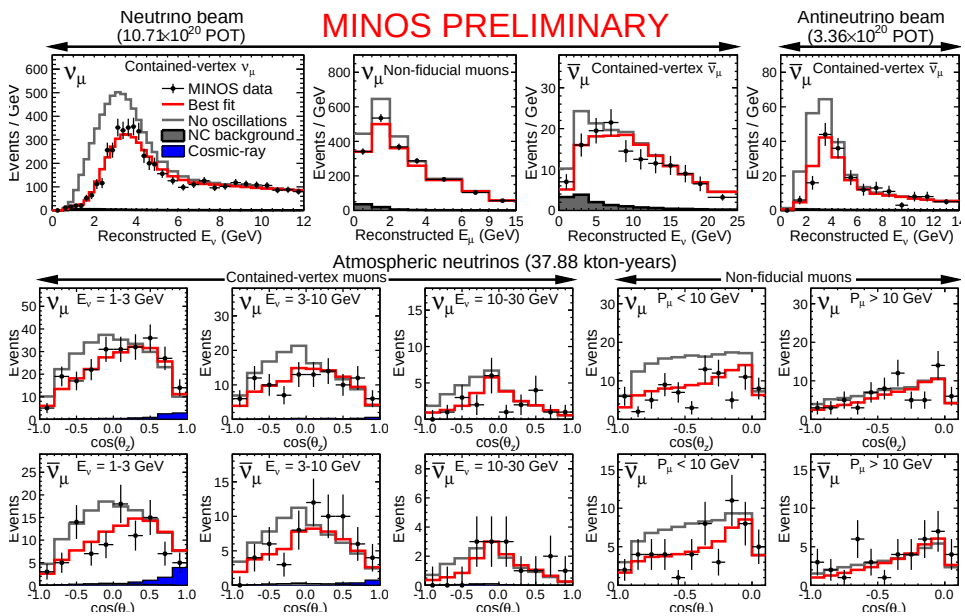

Figure 2.3: The selection of spectra plots show the samples used in the standard three-flavor MINOS and MINOS+ analysis. The top four spectra show the MINOS beam data. The lower plots show the atmospheric neutrino data obtained by both MINOS and MINOS+. The atmospheric data is plotted as a function of zenith angle and are differentiated by contained-vertex muons, non-fiducial muons, and reconstructed energy of the neutrinos. Observed data are shown as points and are compared to the unoscillated (grey) and best fit oscillated spectra(red), while cosmic ray and NC background are shown in solid grey and blue, respectively. Figure reproduced from Ref. [169].

In the three-flavor analysis, the FD sprectra are fitted to predicted FD spectra as extrapolated from the measurements of the beam content at the

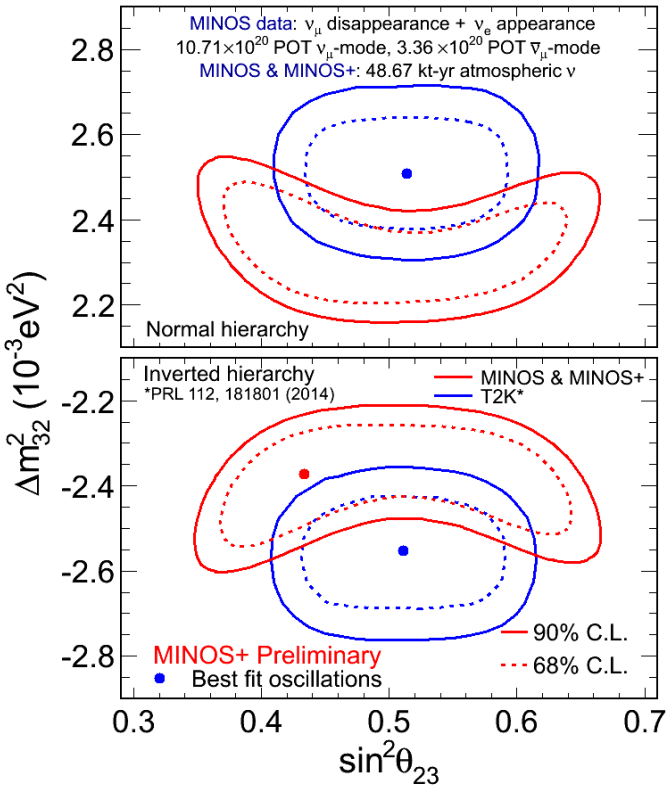

Figure 2.4: Plot showing the results of the combined three flavor analysis in terms of contours in (Δm^2_{32}, $sin^2\theta_{23}$), with the T2K results for comparison. Figure reproduced from Ref. [169].

ND using probabilities calculated from the PMNS matrix parameterization. The fitter is subjected to the external constraint of $sin^2\theta_{13} = 0.0242 \pm 0.0025$ as determined by weighted averaging of Daya Bay [105], RENO [106], and Double Chooz [107] reactor experimental results. The analysis is sensitive to θ_{13}, the octant of θ_{23}, the ordering of neutrino masses (the mass hierarchy), and the value of δ_{CP} (the CP-violating phase in neutrino oscillations). The best combined fit values obtained by the analysis, including a highly competitive measurement of Δm^2_{32}, are $|\Delta m^2_{32}| = 2.34^{+0.09}_{-0.09} \times 10^{-3}$ eV^2 and $\sin^2\theta_{23} = 0.43^{+0.16}_{-0.04}$ for the normal mass hierarchy and $|\Delta m^2_{32}| = 2.37^{+0.11}_{-0.07} \times 10^{-3}$ eV^2 and $\sin^2\theta_{23} = 0.43^{+0.19}_{-0.05}$ for the inverted mass hierarchy [169]. The contours showing the 68% and 90% C.L. ranges for each of the paramters are shown in Fig. 2.4 with the results published by the T2K Collaboration for comparison. As can be observed in these contours, the best-fit point favors marginally the inverted hierarchy and the lower octant of θ_{23} with non-maximal mixing.

2.1.2 MINOS+

MINOS+ [170] is the extension to the MINOS experiment using the identical detectors and sampling the NuMI beam in the medium-energy configuration. The NuMI beam medium-energy configuration was designed for use by NOvA, a latest generation long-baseline neutrino experiment, in order to measure electron neutrino appearance. The MINOS+ energy spectrum peaks at approximately 7 GeV, whereas the NOvA energy spectrum has a peak at approximately 2 GeV due to the 14.6 milliradian off-axis orientation

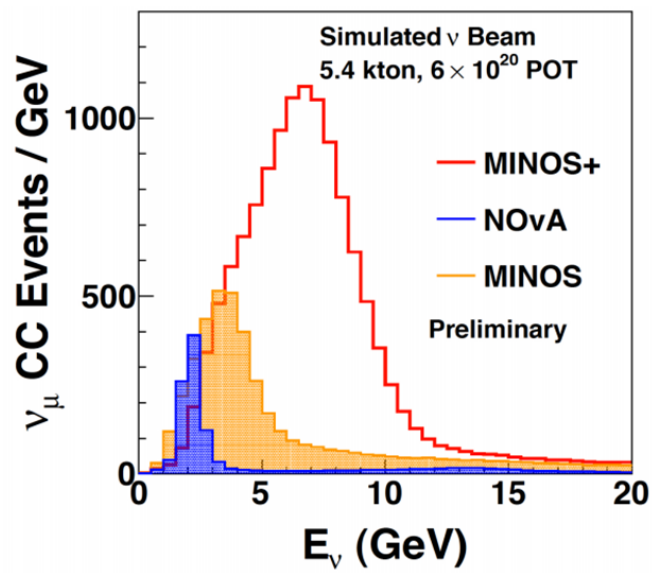

Figure 2.5: Plotted is the NuMI neutrino beam simulated reconstructed energy spectrum for the MINOS+ medium-energy configuration as the red line, the NOνA spectrum (using the same energy as the MINOS+ spectrum but at a 14 mrad offset from the beam axis, along which MINOS+ is located) as the blue shaded histogram, and the MINOS low-energy beam configuration as the shaded golden histogram. Figure reproduced from Ref. [171].

of the detectors. The simulated energy spectra for the beam configurations in MINOS, MINOS+, and NOvA is shown in Fig. 2.5.

MINOS+ collected data during the period of September 2013 to June 2016 with the beam optimized for muon neutrino production. The total POT exposure during MINOS+ running is shown by the pink histogram plotted in Fig. 2.2, with the run periods summarized in Table 2.1. The higher energy of the MINOS+ era data allows for further refinement of the measurement of atmospheric oscillation parameters in addition to providing a probe for models beyond standard neutrino oscillations. The neutrino oscillation behaviors be-

Experiment	Run	Configuration	Mode	Data POT($\times 10^{18}$)
MINOS	1	LE	ν_μ	126.93
	1	pHE	ν_μ	15.31
	2	LE	ν_μ	194.27
	3	LE	ν_μ	388.71
	4	LE	ν_μ	8.84
	4	LE	$\bar{\nu}_\mu$	170.85
	5	LE	ν_μ	45.89
	6	LE	ν_μ	61.62
	7	LE	$\bar{\nu}_\mu$	124.08
	8	LE	ν_μ	12.58
	9	LE	$\bar{\nu}_\mu$	40.80
	10	LE	ν_μ	238.31
MINOS+	11	ME	ν_μ	298.52
	12	ME	ν_μ	281.72
	13	ME	ν_μ	389.12

Table 2.1: Summary of data runs collected by the MINOS and MINOS+ experiments. MINOS data is dominated by the low energy (LE) beam configuration with a brief pseudo-high energy (pHE) during the first running period. MINOS+ data was collected exclusively usng the medium energy (ME) beam configuration. MINOS collected data in both ν_μ and $\bar{\nu}_\mu$ mode running, while MINOS+ collected only ν_μ mode data. Data in this table was compiled from Refs. [172] and [173].

yond the standard three flavor paradigm include sterile neutrinos, large extra dimensions (LED), and non-standard neutrino interactions (NSI) [170].

2.1.3 NuMI Beam

The Neutrinos from the Main Injector (NuMI) neutrino beam provides the source of accelerator neutrinos analyzed by the MINOS and MINOS+ experiments. The beam is generated by accelerating protons to 120 GeV

in the Fermilab Main Injector ring which subsequently bombard a graphite hadron production target. The intensity of the bombarding protons averaged approximately 350 kW during the MINOS era running, and the MINOS+ era running permitted further beam design improvements and upgrades such that a maximum intensity of 560 kW was achieved. The particles showering from the target, predominantly pions and kaons, are then focused by a pair of parabolic electromagnetic horns, illustrated in Fig. 2.7 and following the design first proposed by Simon van der Meer [174]. The focusing horns can be tuned in both the direction and magnitude of current and position with respect to the target in order to determine the dominant charge of focused particles and the shape of the resulting energy spectra. The reversibility of the horn current is the critical element allowing the NuMI beam to run in either neutrino or antineutrino rich modes, which was exploited during MINOS era running, as either pi+ and K+ or pi- and K- may be selectively focused. The higher energy peak energy in MINOS+ is the result of repositioning the second focusing horn a further 13 m down the beamline and moving the graphite target 95 cm up the beamline. Particles focused by the horns then pass through a 675 m decay pipe, which was evacuated in early MINOS running and subsequently filled with helium as a safety precaution against catastrophic implosion. At the end of the decay pipe, the non-neutrino particle beam is terminated by a series of stopping features and monitoring stations including 220 m of rock for muon absorption. An artistic representation of the structure of the NuMI beam facility is shown in Fig. 2.6.

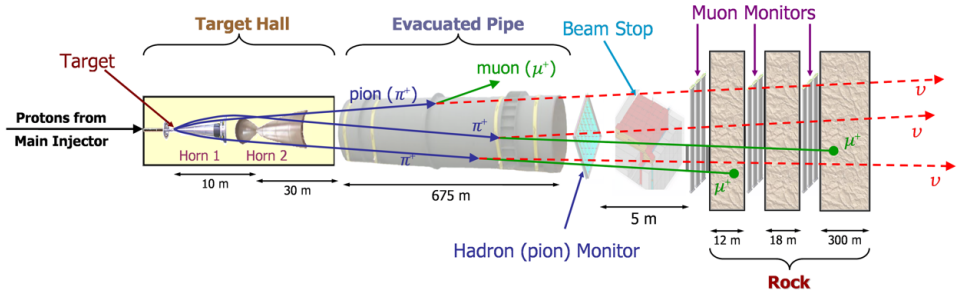

Figure 2.6: Shown is a schematic drawing of the components of NuMI Beam. The beam is initiated at the left with Main Injector protons bombarding the target. Then moving rightward through the diagram, showering hadrons are focused in the electromagnetic horns and allowed to decay in the decay pipe or pass throug the hadron monitor into the absorber. Muons produced from hadronic decays pass on to muon monitors and terminate in the rock, while the neutrinos from these decays proceed on to the MINOS/MINOS+ detectors. This drawing was reproduced from Ref. [165].

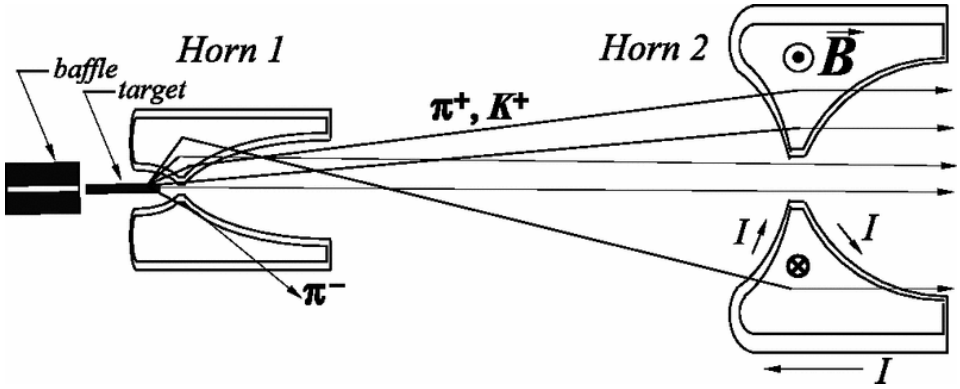

Figure 2.7: Diagram illustrating the focusing properties of the NuMI horns. In the horn current orientation shown positively charged hadron parents are focused while negatively charged parents are defocused. The relative position of the target with respect to the first horn generally controls the position of the energy peak. The horns are separated by a distance of 10 m and the vertical scale in the diagram is four times as large as the horizontal scale. Figure reproduced from [93].

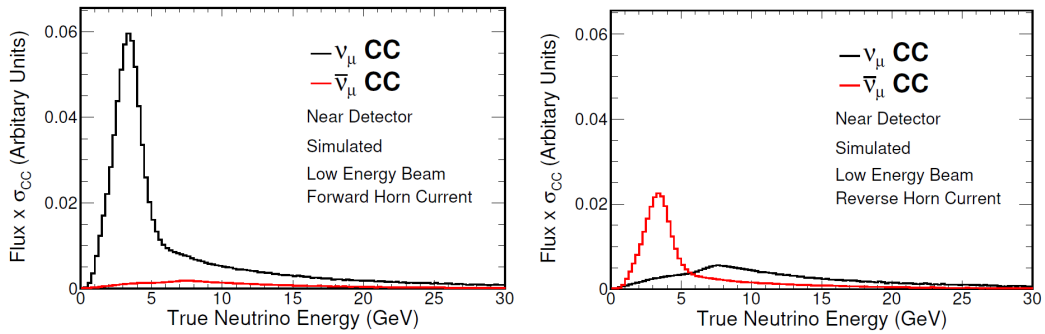

Figure 2.8: The predicted neutrino (black) and antineutrino (red) flux at the MINOS ND for configuration of the NuMI beam in neutrino optimized (left) and antineutrino optimized mode (right). The figure is reproduced from Ref. [175].

Neutrinos are produced in the beam through three primary decay channels for pions, kaons, and muons:

$$\pi^{\pm} \rightarrow \mu^{\pm} + \nu_{\mu}/\bar{\nu}_{\mu}, \tag{2.1}$$

$$K^{\pm} \rightarrow \mu^{\pm} + \nu_{\mu}/\bar{\nu}_{\mu}, \tag{2.2}$$

$$K^{\pm} \rightarrow \pi^{0} + e^{\pm} + \nu_{e}/\bar{\nu}_{e}, \tag{2.3}$$

$$\mu^{\pm} \rightarrow e^{\pm} + \bar{\nu}_{\mu}/\nu_{\mu} + \nu_{e}/\bar{\nu}_{e}. \tag{2.4}$$

The resulting beam is made up of predominantly muon neutrinos or antineutrinos depending upon the direction of the horn current, which is demonstrated in Fig. 2.8. The composition of the combined MINOS and MINOS+ ν_{μ}-mode beams is shown in Fig. 2.9.

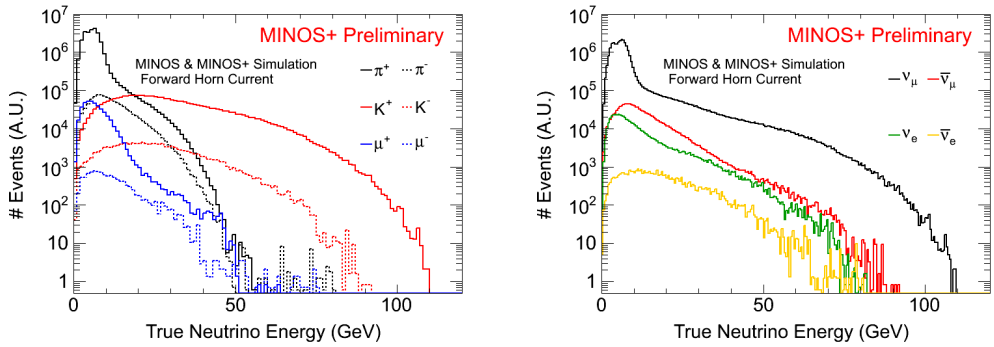

Figure 2.9: The decomposition of the combined MINOS and MINOS+ ν_μ-mode neutrino beams by hadron parent (left) and beam neutrino flavor (right) as a function of the true neutrino energy. In this configuration, the beam is dominated by π^+ and K^+ parents for low- and high-energy neutrinos, respectively.

2.1.4 NuMI Target Design

The NuMI target consists of a series of graphite fins with dimensions 20 mm by 15 mm by 6.4 mm. During normal beam running the target has 47 fins, while an additional 48th fin is added during beam scans in order to aid in beam alignment. In the target module the fins are spaced by 0.3 mm which means that the entire target had a length of approximately 954 mm, which corresponds to about 1.9 hadronic interaction lengths. The graphite fins are contained within an aluminum casing and cooled by a water jacket as can be seen in the drawing of the technical design of the target module shown in Fig. 2.10. Due to the rapid heating, cooling, and intensive radiation, the target is known to degrade over time. The ablation of the target material reduces the flux of primary hadronic showers, which in turn reduces the expected neutrino flux at the detectors. In order to mitigate the target degradation effects, a

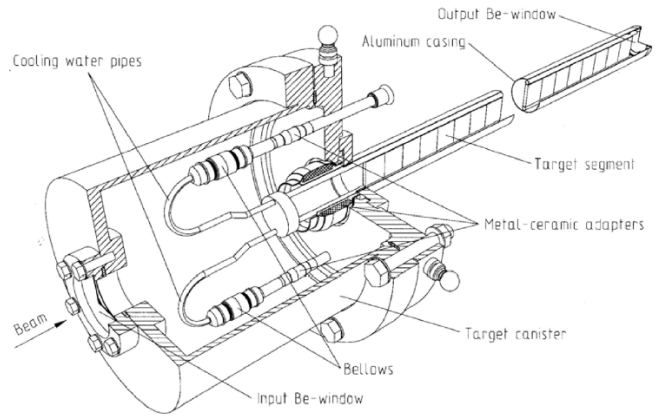

Figure 2.10: A schematic of the design of the NuMI graphite fin target and the canister house the target assembly. Figure is reproduced from Ref. [176].

total of seven target modules were used during data taking in the MINOS-era. Near the conclusion of the MINOS+-era beam running, a video target autopsy was conducted, which demonstrated significant delamination and cracking in the target fins.

2.2 The MINOS/MINOS+ Detectors

The MINOS ND and FD are two functionally identical magnetized steel-scintillator tracking sampling calorimeters. The near identical nature of the two detectors permits the cancellation or mitigation of many sources of systematic uncertainties, such as neutrino cross-sections, relative normalization, beam flux uncertainties, etc., which will be discussed in detail in Chapter 5. The detectors consist of steel planes with thickness 2.54 cm oriented transversely to the beamline and instrumented on the downstream face

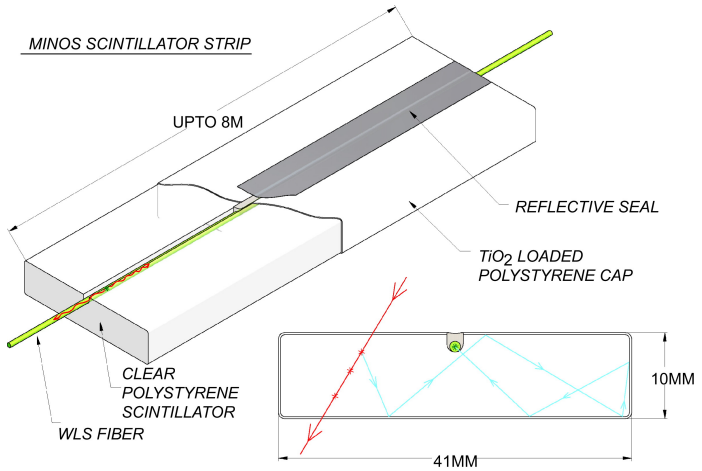

Figure 2.11: Diagram of the scintillator strip assembly used to intstrument the MINOS and MINOS+ detector planes. Scintillaton light from ionizing particles is internally relfected in the strip until it is collected by the WLS fiber. Reemission occurs isotropically so that only those photons emitted in the direction of the fiber are transmitted to the PMT assembly at the strip end. The diagram is taken from Ref. [177].

with polystyrene scintillator strips. The steel planes serve as a neutrino interaction target and the average density of the steel used in the planes was $7.85 \pm 0.03\text{g/cm}^3$ [177], which serves to increase the likelihood of interaction. The separation between each of the steel planes was 5.95 cm. The detectors are both magnetized using an electromagnetic coil passing through the planes in the direction of the beamline. The resulting magnetic field allows the determination of the charge of particles produced in the detectors, and thus the isolation of neutrino and antineutrino samples.

2.2.1 Scintillator Strips

The scintillator strips instrumenting the steel planes are made from polystyrene doped with fluors PPO (1% w/w) and POPOP (0.030% w/w) and extruded with cross-sectional dimensions of 1.0 cm x 4.1 cm. A diagram of the scintillator strip design is shown in Fig. 2.11. The strips were coated with a uniform layer of TiO2 (10% w/w) containg polystyrene in order to increase internal reflectivity and improve the light yield [177] Light produced in the scintillator strips is collected by a wavelength-shifting (WLS) fiber with a diameter 1.20 +0.02/-0.01 mm, which is embedded in a groove in the center of the wide profile of the scintillator strips and fixed in place by a reflective seal. The WLS fiber is double-clad polystyrene containing 175 ppm Y11 (K27) fluorescent emitter which absorbs light at approximately 430 nm and fluoresces at a wavelength of about 470 nm, which prevents re-absorption of scintillation photons and promotes higher quantum efficiency in the light collection. Scintillator modules are formed by joining 14, 20, or 28 scintillator strips together at the narrow face and covering with thin aluminum sheets to prevent light loss. The number of scintillator modules which form the scintillator planes is dependent on the location in each of the detectors as will be detailed in the subsequent sections. Photons collected in the WLS fibers from a scintillator strip module are transported via optical connector and clear polystyrene fibers to a photomultiplier tube (PMT) assembly.

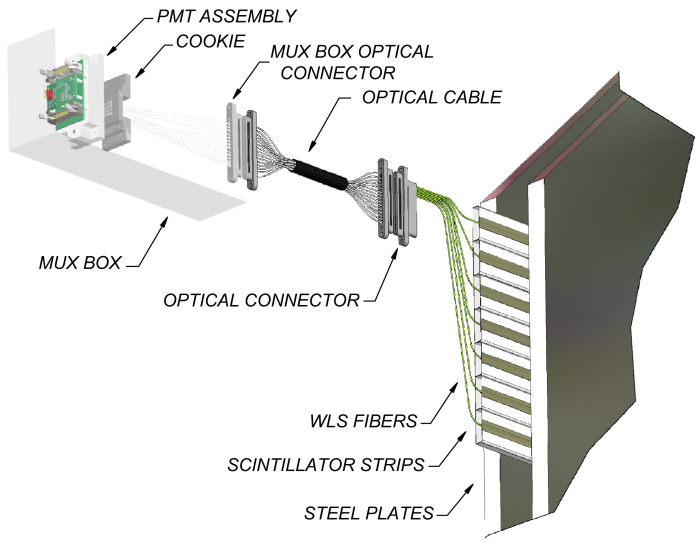

Figure 2.12: Diagram of the readout assembly for the scintillator strips. The scintillation light colleced and transmitted by the WLS fiber is guided through a clear optical fiber to a single PMT pixel. The diagram is taken from Ref. [177].

2.2.2 Instrumentation

The photodetectors used in both detectors are produced by Hamamatsu with the ND using a 64-anode (M64) PMT and the far detector using a 16-anode (M16) PMT. The PMTs are shielded with steel enclosures from electronic noise and the detector magnetic field. In the ND the M64 PMTs are individually shielded, while in the FD three M16 PMTs are contained within a multiplex (MUX) box. A diagram showing the interface between the scintillator modules and PMT assembly is shown in Fig. 2.12. The ND used a total of 194 PMTs with an average gain over all pixels of 8.0×10^5. In the FD, a total of 1452 PMTs were required in order to read out signals at each end of the scintillator strips, which corresponds to 484 MUX boxes. The gains in the

FD were adjusted such that the highest gain for any pixel in each M16 was 1×10^6. The voltage required to achieve the gains in both the ND and FD was approximately 800 V.

The front-end electronics designs required very different performance characteristics at the ND and FD due to highly disparate event rates at the two locations. The FD had a cosmic muon event rate of approximately 0.5 Hz, which is orders of magnitude less than the electronic noise rate of approximately $\sim$ 10 kHZ per plane side. Additionally, the FD expected to see only on the order of a few events per day from beam neutrinos. This is contrasted to the ND where the expected event rate is 1 MHz since as many as 10 neutrino interactions may occur per 8-10 microsecond beam spill, which occur every 2.2, 1.69, or 1.33 seconds depending upon the beam era. Thus, the ND readout was specifically designed to operate at a constant 53.103 MHz in order to avoid any downtime during beam spills, whereas the FD was safely operated by commercial digitizers serving multiple channels at a rate of 5 MHz. A more thorough description of the ND and FD electronics may be found in Refs. [178] and [179], respectively.

2.2.3 Far Detector

The MINOS FD had a total mass of 5,400 metric tons and was constructed at a depth of 705 m underground, corresponding to a 2070 mwe overburden. The FD had an approximately octagonal cross-section transverse to the beamline with height and width of 8 m, and the FD is 486 planes in length.

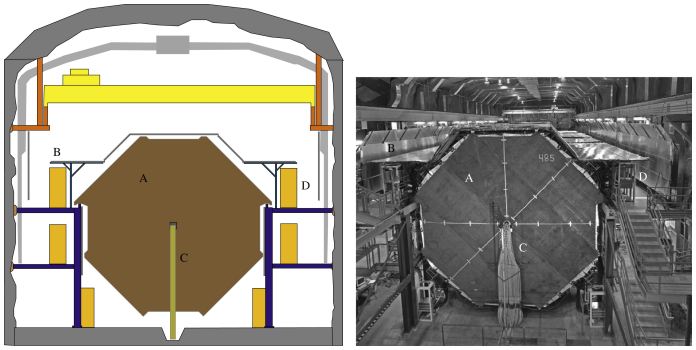

Figure 2.13: A schematic diagram (left) and photograph (right) of the end view of the second of two FD supermodules viewed toward the target. The labeled components in the diagram are: (A) the final FD steel plane, (B) the cosmic ray veto shield, (C) the exit point of the magnetic coil from the supermodule, and (D) one of the electronics racks situated along the sides of the detector. Other elements of the diagram are non-detector machinery or fixed structures within the FD cavern. Figure reproduced from Ref. [177].

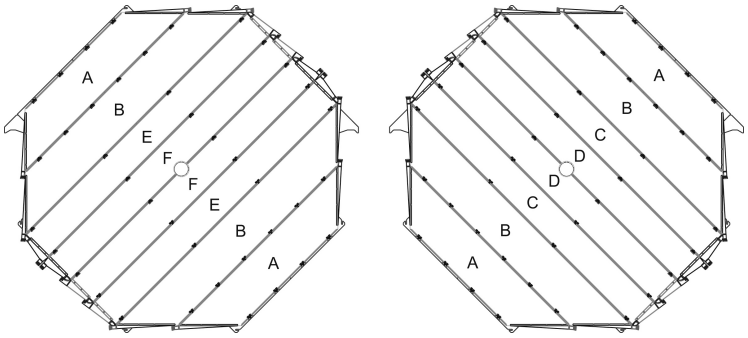

Figure 2.14: Diagram showing the orientation of the U and V orientation of scintillator strips for the FD planes. The planes alternate between U and V views in order to provide stereo readout of the position of detector hits. Figure reproduced from Ref. [177].

The much larger size of the FD is necessary in order to achieve a significant event rate given the loss in intensity due to the long baseline. A diagram of the profile of the FD and the hall in which it was contained is shown in Fig. 2.13. The full FD is formed from two supermodules that are separated by a gap of 1.15 m. The upstream supermodule is formed by 249 planes and is 14.78 m in length while the downstream supermodule is formed by 237 planes and is 14.10 m in length. Each of the supermodules has an independent magnetic coil running through the center of the planes resulting in an average FD magnetic field of 1.42 T. In the FD, all planes are fully instrumented with the exception of the first plane in each of the supermodules. In order to provide stereo readout of track hits, alternating scintillator planes are oriented with the long axis of the modules +45 degrees, the V-planes, or -45 degrees, the U-planes, from the vertical such that these planes are perpendicular to each other. Six types of scintillator strip modules were produced for the FD with widths of 20 or 28 strips, which permits instrumentation of the 99% steel face without any module crossing the vertex of the octagon. The FD is covered along the top and sides of the detector by a cosmic ray veto shield that is assembled from the same type of scintillator modules used in the detector planes. The veto shield allows the differentiation between beam neutrino events and cosmic ray tracks entering the detector.

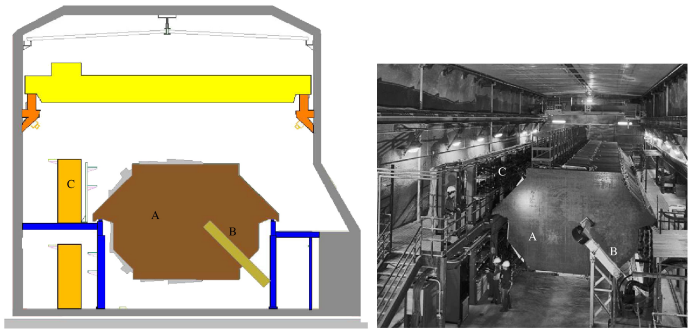

Figure 2.15: A schematic diagram (left) and photograph (right) of the end view of the ND viewed in the direction of the NuMI beam. The labeled components in the diagram are: (A) the first ND steel plane, (B) the exit of the magnetic coil from the front face of the ND, (C) one of the electronics racks situated along the sides of the detector. The position of the (A) label also indicates the center of the beam spot on the ND. Figure reproduced from Ref. [177].

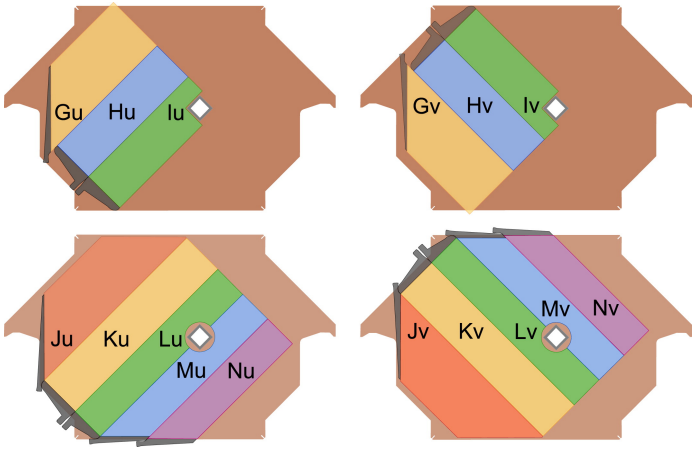

Figure 2.16: A schematic of the four configurations of plane instrumentation used in the ND. The configurations are the partial U-view (upper left), the partial V-view (upper right), the full U-view (lower left), and the full V-view (lower right). The U and V view planes are alternated in the detector in order to give a stereo readout of particle track position in the detector. The partially instrumentation on the upper plane diagrams is situated to the left of the magnetic coil in order to cover the beam spot location. Diagrams are reproduced from Ref. [177].

2.2.4 Near Detector

The MINOS ND has a total mass of 980 metric tons and was constructed at a depth of approximately 100 m below ground level, which gives a 225 mwe overburden. The cross-section of the ND, with respect to the beamline, is approximately 4.8 m by 3.8 m, and the ND is 282 planes in length. A diagram of the ND and the underground hall in which it is contained is shown in Fig. 2.15. The magnetic coil in the ND extends for the full detector length and is located 1.48 m from the center of the beamline in order to reduce the number of tracks passing through the coil-hole region. The ND magnetic field intensity was determined to average 1.28 T. The ND is divided into two regions, the calorimeter and the spectrometer. The calorimeter is formed by the 120 upstream planes of the ND, which are fully instrumented at every fifth plane and partially instrumented for the remaining planes, and contains the target fiducial volume. As in the far detector, a stereo view of the tracks in the detector is achieved by alternating U and V planes which have a +/- 45 degree rotation with respect to the vertical. The two possible plane orientations in combination with either full or partial instrumentation results in four distinctive scintillator plane configurations shown in Fig. 2.16: full U-view (FU), full V-view (FV), partial U-view (PU), and partial V-view (PV). The spectrometer is the remaining downstream planes 121 through 282, which are fully instrumented at only every fifth plane with remaining planes not instrumented. The function of the spectrometer is tracking muons from neutrino interactions with sufficiently high energy to create long tracks.

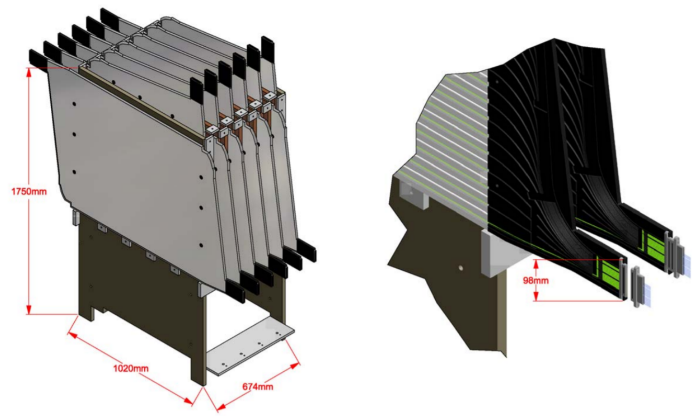

Figure 2.17: A schematic model of a single subsection of the MINOS CalDet, consisting of 12 planes with alternating vertical and horizontal scintillator strip orientation. The diagram shows the readout modules on both sides of each plane, which were used to simultaneously readout signals using both FD and ND electronics. Figure reproduced from Ref. [180].

2.2.5 Calibration Detector

The MINOS Calibration Detector (CalDet) was a specially designed small-scale detector analogue to the MINOS ND and FD, which was exposed to the PS T7 test beam at CERN. The primary design purpose of this detector was to better understand the topology and energy deposition of expected particles in the MINOS detectors and investigate the differing electronic readout systems in the FD and ND. The CalDet had 60 unmagnetized 1 m by 1 m square steel planes with thickness of 2.50 cm as compared to the 2.54 cm thickness used in the FD and ND as shown in Fig. 2.17. The scintillator planes in the CalDet were formed from 24 scintillator strips of similar construction to that described previously and were each 100 cm in length. The scintillator planes alternate between orientations that are rotated 90 degrees with respect

to one another in order to achieve three-dimensional tracking as in the ND and FD. The CalDet was simultaneously instrumented with the ND and FD electronics, in order to allow for calibration of these two differing systems to high precision given the same light exposure. CalDet facilitated the development of a calibration method (described in Chapter 3), which achieved a hit-by-hit response in agreement between the ND and FD electronic readout systems to within approximately 2.5% over a significant range of energies.

2.2.6 Light Injection System

The MINOS ND and FD had a light injection (LI) system designed to periodically expose the detector photoreceptors to a known light source in order to map the linearity of instrumentation and to monitor stability of the PMTs and the light collection system. Ultra-violet (UV) light pulses were generated by LEDs contained in pulser boxes in order to illuminate the WLS fibers at the ends of the scintillation modules. The flash from the LEDs simulates a signal generated by the scintillation light in the strips and can be simultaneously read out by a Positive Intrinsic Negative (PIN) photodiode for comparison. The intensity of the light pulses are tuned such that a given PMT pixel should receive approximately 50 photoelectrons per pulse, though due to variance in the fibers and PMTs this can vary by as much as a factor of two.

2.2.7 Electronics Trigger

Readout of the PMTs and storage of data is initiated by a triggering mechanism, which is prompted by one of two different sources: (1) beam spills delivered by NuMI or (2) cosmic muons entering the detector.

The NuMI beam delivers protons to the target in quantized units called spills, which are made up of batches of protons. The structure of the spill and the number of protons it contains are features of the particular mechanism by which the protons are injected in, accelerated, and extracted from the Main Injector, though a typical spill could contain on the order of 4×10^{13} protons. The NuMI spills are delivered at intervals of approximately 2.2 s for the MINOS era, 1.69 s for the early MINOS+ era, and 1.33 s for the remainder of MINOS+, and can last for as long as 10 microseconds. For each beam spill, a beam trigger signal is sent to both the FD and ND causing a readout of the PMT data and digitization of signals for a window of 100 microseconds. At the FD, there is significantly more interference in proper triggering at a frequency of approximately 5 kHz due to dark noise in the PMTs and spontaneous photon emission occurring in the WLS fibers. In order to avoid these false signals, an additional trigger level is applied in the FD electronics, which requires that 2 out of each group of 36 PMTs be activated by a signal within a period of 400 ns in order for the data to be readout and digitized.

The second source of triggering occurs outside of the beam spill windows and is initiated by cosmic muons interacting with the detector. The cosmic muon trigger is an offline trigger based on a threshold for energy deposits in the

detector or interactions being recorded in a group of planes isolated spatially in the detector. If either of these criteria are met, the interaction is presumed to be a cosmic muon event and the detector is readout in the region of the triggering interaction.

2.3 Detecting Neutrino Interactions

2.3.1 Interaction Types and Cross sections

Neutrinos interact via the weak interaction, either through charged-currents (CC) mediated by the $W^{\pm}$ bosons or through neutral-currents mediated by the Z^0 boson, and via gravitation, though this type of interaction is irrelevant to the present analysis. Another manner of division for neutrino interactions naturally arises from considering the kinematics and cross section associated with the energy of the scattering neutrino. In this analysis, neutrinos with energies ranging from 0.25 to 40 GeV will be considered, which corresponds to three types of scattering processes. Figure 2.18 shows the relative contributions from each of these scattering processes to the overall observed neutrino cross section.

For neutrino (antineutrino) energies greater than $\sim$5 (7) GeV, the dominant interaction type is deep inelastic scattering (DIS). In a DIS interaction, the neutrino has sufficient energy to penetrate the inner structure of the target and scatters with individual partons (quarks or gluons) in one of the nucleons by the exchange of a virtual W or Z boson. Computation of the cross section with the partons requires a treatment accounting for the structure functions

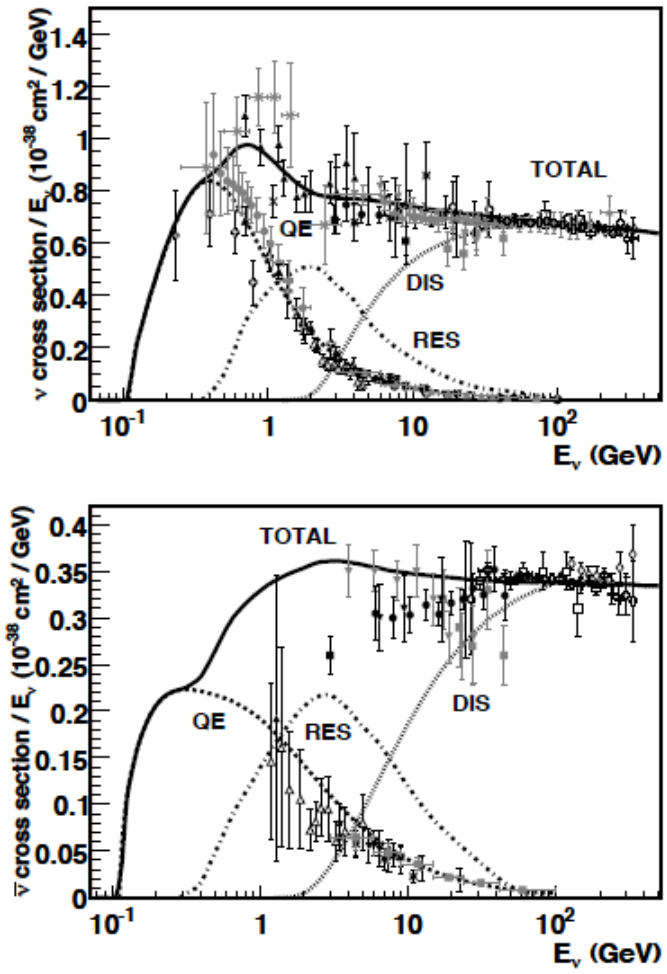

Figure 2.18: The per nucleon total CC cross section for neutrinos (upper) and antineutrinos (lower) divided by and plotted as a function of the neutrino energy. The contributions from quasi-elastic (QE), resonant (RES), and deep inelastic scattering (DIS) interactions to each total cross sections are shown by various broken line styles. A selection of experimental scattering data is also plotted in order to compare with the theoretical calculations. Figure reproduced from Ref. [181].

of the nucleons as described in Ref. [182]. The resulting state is a composite of a lepton and hadronic particles.

At low energies, generally less than 1 GeV, neutrino interactions are generally dominated by quasi-elastic (QE) scattering. In a QE interaction, the neutrino scatters off a nucleon as a single particle instead of interacting with partons. QE scattering is confined to the CC interactions and has the form:

$$\begin{aligned} \nu_\mu + n &\rightarrow \mu^- + p \\ \overline{\nu}_\mu + p &\rightarrow \mu^+ + n \end{aligned} \tag{2.5}$$

The QE events in MINOS generally result in only an outgoing leptonic track and do not contain significant hadronic activity.

In the intermediate energies between QE scattering events and DIS events, various modes of resonant production become relevant. Resonant production results from sufficient energy being delivered to the target nucleon to produce an excited baryon resonance in addition to the outgoing lepton. Most frequently, the excited baryon decays to the ground state via the production of a pion, which is called resonant single pion production:

$$\begin{aligned} \nu_\mu + N &\rightarrow \mu^- + N^* \\ N^* &\rightarrow \pi + N' \end{aligned} \tag{2.6}$$

The resulting pion can either produce a track in addition to a leptonic track or it can cause further hadronic showering beyond the baryonic system.

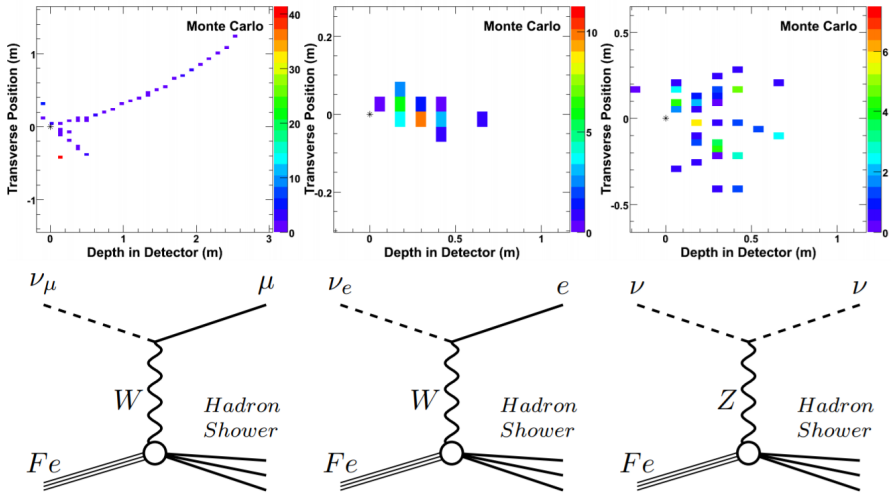

Figure 2.19: Simulated MC event topologies in the MINOS detectors for ν_μ-CC (left), ν_e-CC (center), and NC (right) interactions. Feynman diagrams describing the reactions are shown below the event displays. Figure reproduced from Ref. [183].

2.3.2 Event Topologies

The MINOS detectors observe three general event topologies of interest to the muon neutrino disappearance search, which are illustrated in Fig. 2.19. The events used for the atmospheric oscillations disappearance search, and the main sample used in the analysis described in this thesis are ν_μ CC events:

$$\nu_\mu + N \rightarrow \mu^- + X \tag{2.7}$$

The ν_μ CC events are characterized by the significant outgoing muon track. The steel planes of the detector are designed to contain muons by forcing the deposit of a large amount of energy. Additionally, the magnetic field in the planes causes bending in the muon tracks in a charge dependent manner such that the neutrino can be identified as ν or $\bar{\nu}$. Numu CC events can also have

showering hadronic activity near the interaction vertex depending upon the elasticity of the scattering process.

The second topology used in this analysis arises from NC events:

$$\nu + N \rightarrow \nu + X \tag{2.8}$$

NC events are agnostic to the flavor of the interacting neutrino as no lepton is produced for identification. NC events are characterized by the presence of a diffuse hadronic shower at the interaction vertex with no significant outgoing tracks produced.

The third topology observed is due to electron neutrino CC interactions:

$$\nu_e + N \rightarrow e^- + X \tag{2.9}$$

The outgoing electron produced in a ν_e CC event produces an electromagnetic shower, which is more compact than the hadronic showers observed in other events, and displays a typical electromagnetic shower energy profile. In MINOS, the ν_e CC topology is difficult to identify due to energy being deposited very quickly in relatively few planes of the high density detector material, which is $\sim 1.5X_0$ per plane for electrons. Thus, significant confusion can arise between the ν_e CC and NC events and the similar showering activity.

Chapter 3

Calibration and Reconstruction

In this chapter, the full method of calibration for both MINOS detectors is presented. A discussion of the detector and data simulation packages used along with the choice of flux model is discussed. The chapter concludes with the method of event reconstruction used for both data and simulations in the analysis.

3.1 Calibration

The MINOS and MINOS+ calibration procedure is designed to measure the amplitude of the electronic output, or pulse height response, in the ND and FD so that data in each detector can be compared to simulation and so that the detectors can be directly compared to each other. The MINOS detectors measure the output of scintillation light produced by particles traversing the detector planes in order to determine the energy deposited in the detector and therefore estimate the energy of the interacting neutrinos. Given that the concept of a neutrino oscillations analysis is to search for modulations in the neutrino energy spectra in either the ND, FD, or both, it is particularly important to accurately and precisely measure the calorimetric energy in order

to measure oscillation parameters. The MINOS calibration procedure, which is represented by the schematic in Fig. 3.1, converts raw detector pulse height $Q_{raw}(s, x, t, d)$, where s is the scintillator strip, x is the position along the strip, t is the time, and d is the detector containing the strip, into a corrected signal $Q_{corr}(s, x, t, d)$ through a series of multiplicative calibration constants:

$$Q_{corr} = D(t, d) \times L(s, d, Q_{raw}) \times C(s, t, d) \times A(s, x, d) \times M(d) \times Q_{raw} \quad (3.1)$$

These correction constants are the drift and gains correction $D(t, d)$ described in Section 3.1.1, the linearity correction $L(s, d, Q_{raw})$ described in Section 3.1.2, the strip-to-strip correction $C(s, t, d)$ described in Section 3.1.3, the attenuation correction $A(s, x, d)$ described in Section 3.1.4, and the absolute energy scale factor $M(d)$ described in Section 3.1.6.

3.1.1 Drift and Gains Calibration

The general purpose of the gains and drift calibration, which is summarized in Fig. 3.2, is to correct variation in the detector response as a function of time. The dominant cause of drift in the detector response is due to temperature fluctuations that occur in the detector halls. The ambient temperature and environment of the caverns containing the detectors is largely stabilized by a climate control system, but seasonal variations and detector aging still cause an approximate 4% loss in detector signal response per year [177].

The primary method of correction for the gains response is the LI system discussed in Chapter 2. The LI system pulses each FD scintillator strip

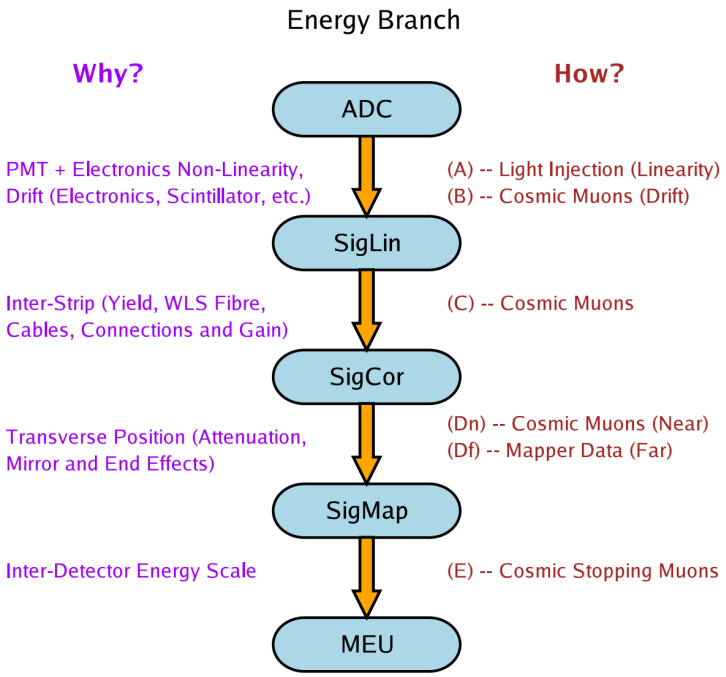

Figure 3.1: Schematic of the calibration chain used in MINOS and MINOS+ to convert electronic signals into units of enegy. Diagram reproduced from Ref. [184].

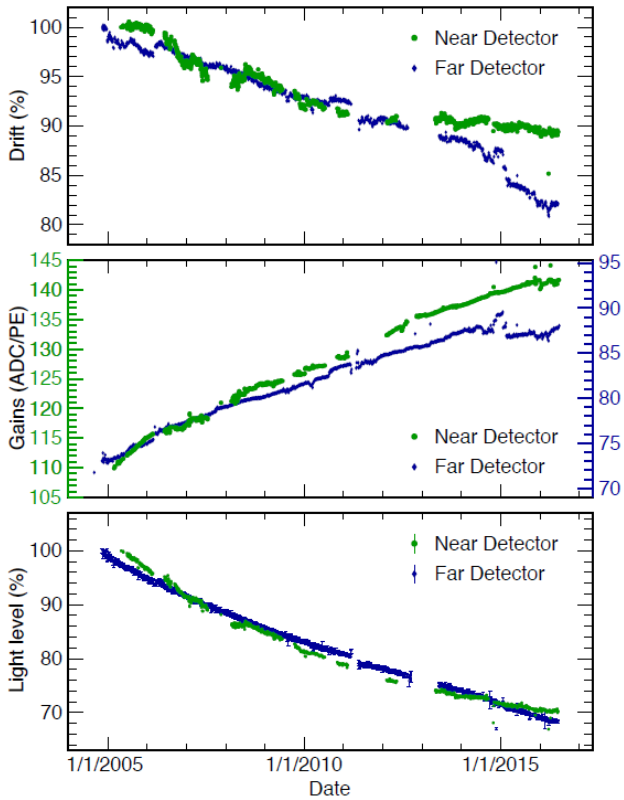

Figure 3.2: Time dependent variation in the ND (green) and FD (blue) response used in the drift and gains calibration. The drift (top) shows the daily changes in detector response normalized to the first day of data. The PMT gains (middle) show the changes in number of ADC per photoelectron averaged over three day intervals. The relative light level (bottom) is the ratio of the drift to gains. The figure is reproduced form Ref. [185].

approximately 300 times per hour and the rate is even larger in ND at approximately 1000 times per hour. The data from these pulses are collated at regular intervals and the average response per photoelectron is computed using photon statistics. The comparison of the rms widths of the measured pulses to the mean provides a correction on the number of Analog-to-Digital Converter (ADC) counts measured per photoelectron, which is used to calibrate both Monte Carlo (MC) simulation and data reconstruction.

The smaller overall drift of the response in fibers and electronics across the detector due to longer term aging and temperature effects must be handled outside of the LI system since the PIN diode and PMT systems readout using the same electronics. Instead of the LI system, the median response of the detector planes to cosmic muons is used for drift calibration. The cosmic ray muon spectra in the two detectors vary greatly due to differing detector mass, overburden, etc. with the average energy and rate being 200 GeV at 0.5 Hz for the FD and 55 GeV at 10 Hz for the ND. For each of these through-going cosmic ray muons, the total pulse height per plane is measured. The amount of energy deposited by cosmic ray muons is different in each detector, however the average amount of energy deposited should be a constant over time. Therefore, one can compute the ratio of the response at an initial time t_0 with the response at some later time t to give the drift correction:

$$D(t, d) = \frac{\text{Median response at time } t_0}{\text{Median response at time } t} \tag{3.2}$$

Thus, the drift correction is only a relative measurement of the response of

one detector over time and gives no absolute energy information. In MINOS and MINOS+ the drift correction constants were computed daily.

3.1.2 Linearity Calibration

The linearity calibration is designed to account for large energy deposits in the MINOS detectors that can potentially overwhelm the PMTs and causes them to behave non-linearly. Non-linear behavior in PMTs on the order of 5-10% occurs when the light level exceeds 100 photoelectrons. The LI system discussed in the previous section delivers light pulses of various intensities to the PMTs in order to quantify the response. The LEDs are tuned so that full range of interest for the PMT response is covered in the average scintillator strip. The PIN diodes in the LI system determine a linear scale for the true light level being delivered by the LED flashes. The two pin diodes are tuned to have differing gains such that one has a high gain and the other a low gain. In this configuration, the high gain diode provides better measurements under low light levels, while the low gain diode better measures high light levels. The PIN diode response was determined to be linear to within 1% for intensities producing 5-100 PMT photoelectrons. The light pulses determine a functional form for PMT behavior in the PIN diode linear region such that non-linear behavior can be extrapolated for all intensities and a pulse height dependent linearity correction factor $L(s, d, Q_{raw})$ can be found for each scintillator strip.

The method of electronics non-linearity calibration takes different forms in the two detectors. The ND electronics system, particularly the PIN-pre-

amplifier and QIE components, which are used to read out the response from the PIN diodes during the linearity calibration are known to be linear within less than 1% variation [186]. The ND utilizes special current injection runs in order to calibrate the linearity of response in the QIE electronics system online, that is during experimental running. This type of online calibration for linearity is not possible in the FD as the VA electronics, which read out the PIN diodes at the FD must be calibrated offline.

The FD offline calibration for electronic readout linearity is facilitated by a special charge-injection (CI) system incorporated into the front-end electronics. The CI system exposes the FD channels to known quantities of charge of increasing intensity in order to determine the variations from linear behavior. This CI system is only used to calibrate the linearity of the electronics directly reading out the PIN diode systems. For the VA electronics, which read out the response from the PMTs, the combined non-linear response of both the PMT and electronics readout is treated jointly such that one correction as determined by the LI system can be used to compensate for both effects.

3.1.3 Strip-to-Strip Calibration

It has been demonstrated that the light response from the scintillator strips in both detectors can vary by as much as 30%. In order to ensure a consistent response from each of the strips across each detector, cosmic muons are again employed as a standard for energy deposition. The strip-to-strip correction factor is computed by taking the ratio of the mean response of the

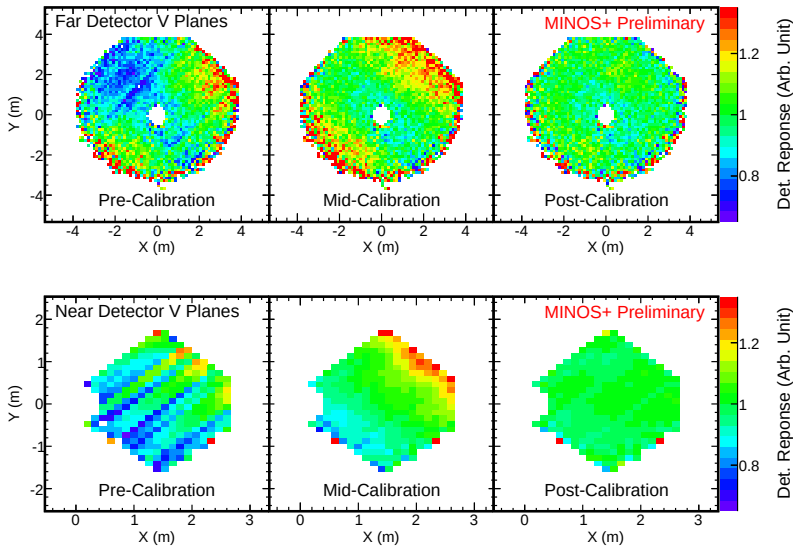

Figure 3.3: Plots showing the response of the ND (lower) and FD (upper) at different stages of the calibration procedure. Left: The raw ADC distribution. Center: Detector response after the linearity, drift, and strip-to-strip calibrations have been implemented. Right: The final post-calibration detector response after correcting fiber attenuation. Plots are shown for the V planes and similar effects are observed in the U planes. Figure taken from Ref. [187]

full detector to the mean response of each strip end:

$$C(s,t,d) = \frac{\text{Mean detector response}(t,d)}{\text{Mean strip end response}(s,t,d)} \tag{3.3}$$

The source of the variability between the response from individual strip ends can include the light yield from the scintillator, efficiency of light collection in the WLS fibers, and the quantum efficiency and gain in individual PMTs. These various sources of miscalibration are all corrected with the single strip-to-strip correction factor. The cosmic ray muon tracks used for the strip-to-strip calibration are corrected using the linearity calibration discussed previously along with attenuation and path-length corrections in order to remove any effects due to position or angle of the track hits. The result of these corrections is the computation of the strip response to a cosmic muon interacting at the center of the strip and normal to the plane of the detector. One difficulty in this method is the potential for a track interacting very near the edge of the scintillation strip, which in turn produces a very low light level on the order of 2-10 photoelectrons. The scenario of tracks passing very near the edges of the strips is dealt with by assuming a Poisson process of energy deposition and photoelectron emission and iteratively modifying the calibration constants in order to account for the probability of a zero contribution from each subsequent muon. The iterative technique for strip-to-strip calibration is successful in reducing the statistical variation in mean response of the strip ends to $\sim 2.1\%$ in the ND and $\sim 4.8\%$ in the FD. The results of the calibration chain up to the point of the strip-to-strip calibration is shown in the center plot of Fig. 3.3.

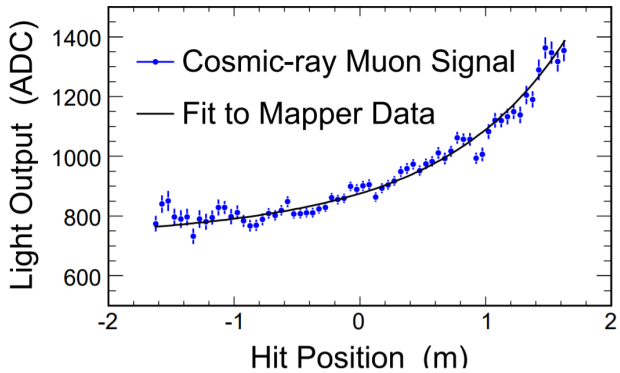

Figure 3.4: The light output observed from cosmic ray muon data (blue points) compared with the module mapper fit result (black line) for a sample ND detector strip. Figure reproduced from Ref. [177].

3.1.4 Attenuation Calibration

During the construction of the scintillator strips, prior to the construction of the detectors, a module mapping procedure was used in order to provide quality control as well as an attenuation calibration tool for the WLS fibers. The module-mapping procedure involved the sequential exposure of the entire surface of the scintillator modules to a well-known 5 mCi Cesium-137 source, which produced gamma rays that illuminated a 4×4 cm^2 area of the scintillator module. The PMT signal output of the strip modules was integrated for 10 ms out of every 40 ms and measurements of the activity were made for exposures at every 8 cm along the length of the strips. The result of the measurements is a detailed map of the response of the scintillation strips to ionizing radiation. This map of data is fit to a double exponential function

$$A(x) = A_1 e^{-\frac{x}{L_1}} + A_2 e^{-\frac{x}{L_2}} \tag{3.4}$$

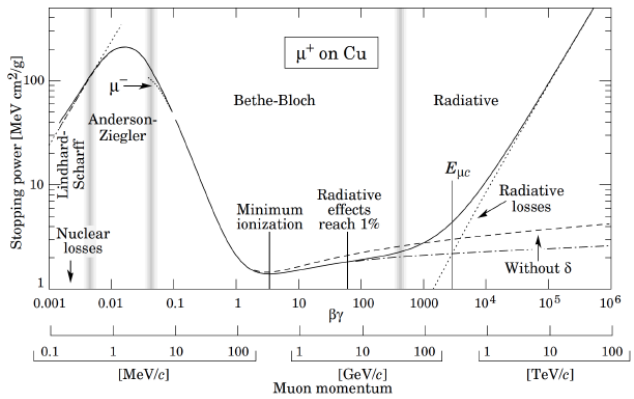

Figure 3.5: The stopping power of copper on muons as computed by the Bethe-Bloch equation as a funtion of the muon momemtum. The relevant region in MINOS and MINOS+ is near the point of minimum ionization. Figure taken from Ref. [30].

where x is the position from the readout end of the strip, L_1 and L_2 are the attenuation lengths and A1 and A2 are normalization constants. The fitted functional form is then used to derive the attenuation correction. The attenuation correction was then checked using a sample of through-going cosmic ray muons. The position of the muon transit along the scintillation strip was measured by the orthogonal plane view and a similar map of the scintillation module response as a function of position was created. The cosmic ray muon fit agreed with the module mapper data to about 4% as can be seen in Fig. 3.4. In the final calibration procedure, the module map data is used for attenuation calibration in the FD due to the finer granularity whereas the cosmic muon data is used in the ND for performing the attenuation fit.

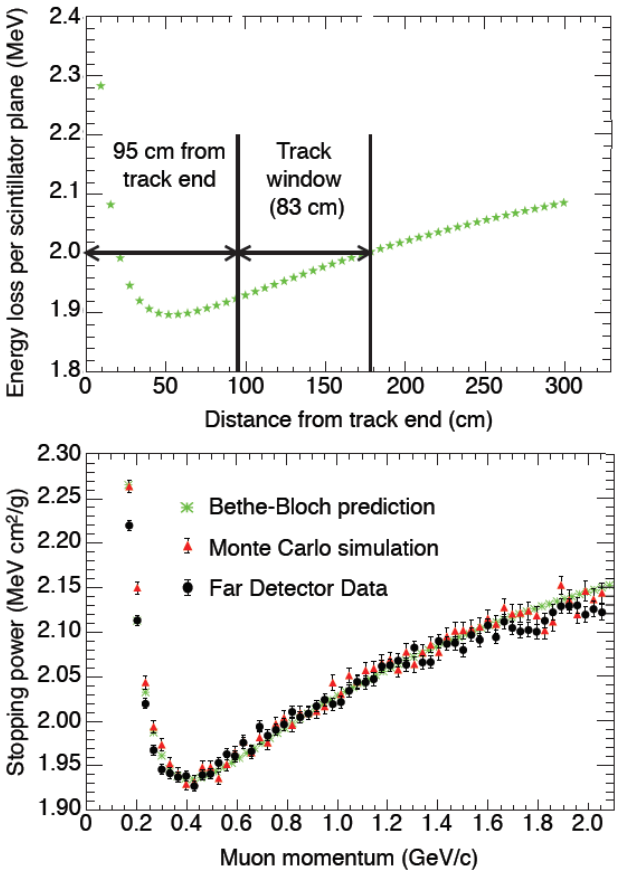

Figure 3.6: Plot of the energy loss per scintillator plane along muon tracks (upper) and the mean energy loss as a function of distance for stopping muons in the FD as a function of momentum (lower). The track window used for the inter-detector calibration is shown in the upper plot, while the lower plot shows the strong agreement between the analytical Bethe-Bloch prediciton, MC simulation, and the observed FD data. Figure reproduced from Ref. [185].

3.1.5 Inter-detector Calibration

Before a final conversion to absolute energy deposition can be made, an inter-detector calibration must be applied in order to arrive at a standardized Muon Energy Unit (MEU). The inter-detector calibration uses muons to as a normalization of the response of the scintillator modules in both detectors due to the relevant abundance of muons and the ability to determine the momentum of the muons without reliance on calorimetry. The MINOS detectors can measure muon momentum either by range in the detector, which applies to contained muons only, or by the measurement of the curvature of the muon track in the magnetic field. For the purpose of the inter-detector calibration, it is necessary to determine the total energy deposited in the detector so contained cosmic muons are used. It would be convenient if the average response of all muons in the detectors could be utilized in order to make a statement on the relative calibration between the detectors. However, as was discussed in Section 3.1.1, the spectrum of cosmic muons in each detector varies widely, and this makes a measurement of the average response of all muons a poor calibration choice. The energy loss of the contained muons in the MINOS detectors can by determined by the Bethe-Bloch equation, which gives the rate of energy loss of a muon as it traverses a medium. The stopping power, which is given by the Bethe-Bloch formula, is shown for muons interacting with copper in Fig. 3.5. Given the range of energies of muons observed in both the MINOS ND and FD are in the range from 1-200 GeV, these muons fall in the range of minimally ionizing particles (MIPs). The Bethe-Bloch formula yields

approximately constant values in this region of energies, implying that the energy deposition by cosmic muons is very nearly constant on a plane-by-plane basis.

The method used for the inter-detector calibration is known as a track-window technique and is directly related to the relative flatness of the energy loss for muons of a given range of momenta. The range of For a typical muon momentum of 1.5 GeV/c, the loss in energy as a function of interaction length, dE/dx, varies rapidly on the order of $\sim 100\%$ increase near the end of the path through the detector due to a significant increase in ionization, as is plotted in Fig. 3.6. This same muon has a variability in dE/dx of only $\sim 8\%$ during the period that the momentum reduces from 1.1 GeV to 0.5 GeV. Thus, the track window technique only measures the detector response of the muons during this window of momenta where the energy deposition is approximately constant. Taking advantage of this nature of the muon ionization, the 2% error on the final position of muon stopping in the detector is translated to an uncertainty in the MEU of 0.2%. The calibration of the MEU ensures that a particle traversing a plane in either the MINOS ND or FD generates a response which agrees between the two detectors within the established errors of the calibration procedure. A caveat applies to this standard calibration in the case of the first 190 planes of the FD, which are in fact approximately 1% thicker than the remaining FD steel planes. Due to this additional steel thickness, an additional correction must be applied to only these planes in order to arrive at the standardized MEU.

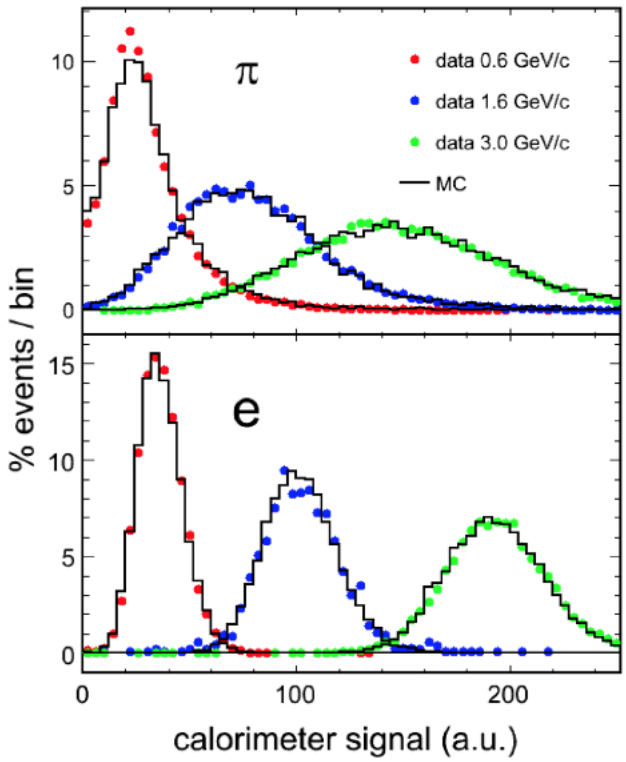

Figure 3.7: Plotted are the calorimetric energy response data for pions (upper) and electrons (lower) with momenta 0.6 GeV/c (red), 1.6 GeV/C (blue), and 3.0 GeV/c (green), compared with MC simulation (black). Figure reproduced from Ref. [177].

3.1.6 Absolute Energy Scale Calibration

The calibration procedure which arrives at a standard MEU as described in the previous sections is still only a relative statement of the energy deposited in the detectors. In order to determine the absolute energy deposit in the detector that corresponds to the MEU, it is necessary to expose the detectors to hadrons and leptons with known momenta. The mapping of relative energy units to absolute energy was accomplished using the CalDet [180],

which is described in Chapter 2. The CalDet was exposed to a source of protons, pions, electrons and muons with a range of momenta from 0.2-10 GeV/c using various test beams at CERN. The test beam data in the CalDet was taken from a momentum of 200 MeV/c to 3.6 GeV/c in 200 MeV/c increments and then from 4 GeV/c to 10 GeV/c in 1 GeV/c increments. Particles in the test beam were identified by time-of-flight or threshold Čerenkov detectors, with pion and muon separation achieved by event topology. For each of the data points, a comparison was made between the collected data and MC simulations, which can be seen in Fig. 3.7. The results of the CalDet data allow for the establishment of an absolute energy scale for the detector response and further demonstrates that the energy resolution can be parameterized by $56\%/\sqrt{E} \oplus 2\%$ for hadronic showers and $21.4\%/\sqrt{E} \oplus 4\%/E$ for electromagnetic showers, where E is the particle energy in GeV [188][189]. The final results in terms of the detector response after the completion of the calibration chain is shown in Fig. 3.3.

3.2 Simulation

In order to study the behavior of neutrinos in MINOS and MINOS+, it is necessary to carefully and completely simulate the entirety of the experiment in order to establish the expected behavior based upon theoretical modeling and to search for deviations from the expectation. The MC simulation for the MINOS and MINOS+ experiments occurs in two main stages: (1) simulation of the NuMI neutrino beam and (2) simulation of the MINOS detectors. These

two phases of simulation are discussed in detail below.

3.2.1 NuMI Beam Simulation

The simulation of the NuMI beam is performed by the `FLUGG` MC software package, which is a hybridization of a `FLUKA` simulation of the hadronic interactions that occur in the target and a `GEANT4` geometrical model of the focusing and beamline apparatus. The simulation begins with 120 GeV protons impinging on the graphite target and tracks the production of any secondary mesons. The interaction of the mesons with the focusing horn is then simulated in order to properly capture the kinematics of particles entering the decay pipe. The simulated beam of secondary mesons is then allowed to either decay or strike the beam absorbers at the termination of the decay pipe. If a simulated meson decays and produces a neutrino, the properties of the flavor, energy, and momentum of the neutrino are recorded in addition to the identity and properties of the parent meson. Given the spectrum of possible momenta for the parent mesons and the isotropic decay of neutrinos in the rest frame of the decaying meson, it is possible for a neutrino produced in the beam to travel in a direction that ensures no interaction with the detectors can take place. In order to increase computational efficiency, all neutrinos from the beam simulation are propagated to the known locations of the ND and FD, though a system of weights is applied in order to account for the solid angle swept out by the detectors in relation to the production point of the neutrino in order to arrive at the proper expectation for the neutrino flux at each detector.

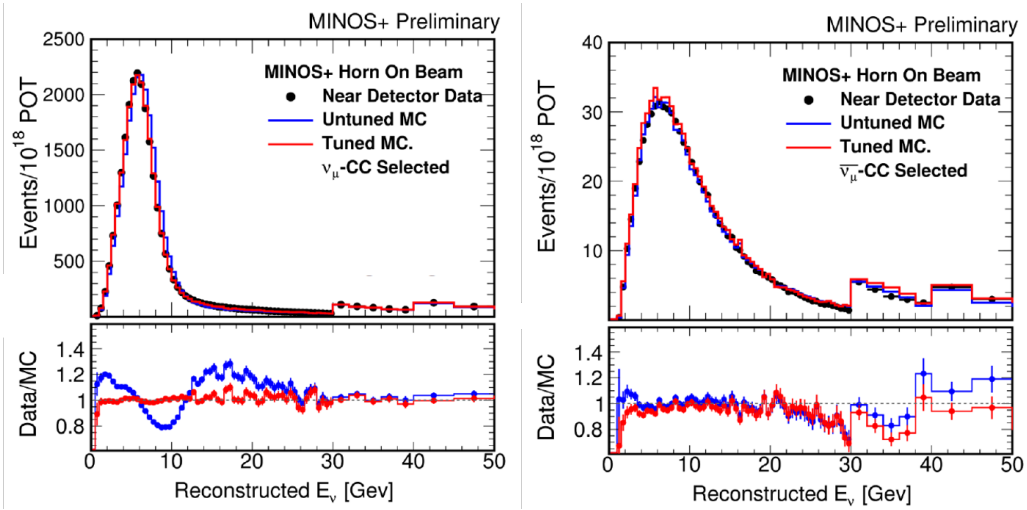

Figure 3.8: The ND reconstructed energy spectrum for focused neutrinos (left) and defocused antineutrinos (right). The spectra are plotted prior to the SKZP beam fit (blue) and after the beam fit (red). Figure taken from Ref. [167].

3.2.2 Selecting Flux Model

The flux model predicted by MC simulation using the `FLUGG` framework discussed in the previous section has significant disagreements with observed data. In standard oscillations analyses, the ND can be used to correct the flux prediction since no neutrino oscillations driven at the atmospheric mixing scale are expected to occur before traversing the ND. The method employed to correct known flux model deficiencies is a reweighting of the predictions for neutrino flux based upon the parent meson and the kinematic properties at the time of decay. The resulting set of weights, called SKZP weights, are discussed in detail in Reference [190], and result in a significant improvement in agreement between observed data and MC simulation, as can be seen in Fig. 3.8. The strongest improvement in agreement realized by the SKZP weights

is between 20-40% for neutrinos with energies greater than 7 GeV.

In the analysis presented here, the use of the SKZP weights is precluded given that it is possible for neutrino oscillations to occur either in the midst of the ND or earlier along the beamline. Thus, an alternative method of improving the flux prediction is required. Recently, the MINERvA experiment made an *in situ* measurement in conjunction with both thin and thick target modeling in order to improve the prediction of the expected neutrino flux from the NuMI beam. The MINERvA detector sits in the NuMI beam line, upstream of the MINOS ND, and is thus ideally suited for measuring the expected neutrino flux at the MINOS detectors. As a part of the MINERvA flux measurement program, a new software package called `PPFX`(Package to Predict the Flux) [191] was designed in order to provide an experiment-independent platform for the computation of expected neutrino flux at the various experiments sampling the NuMI beam. The analysis presented here uses a modification of the standard MINOS flux prediction from `FLUGG`, where the expected flux at the MINOS detectors is predicted using the `PPFX` framework and the ratio of the two flux models are used as a set of weights as a function of true energy in order to transform the flux model. This strategy is chosen in order to promote computational efficiency and to avoid a complete reproduction of the MC simulations using the updated flux prediction. The uncertainties associated with the `PPFX` flux prediction are derived from a multi-universes method, which is discussed in greater detail in Chapter 5.

3.2.3 MINOS Detector Simulation

Neutrinos generated in the beam simulation are selected using pseudo random number sampling and are then propagated through geometric models of the detectors and the detector halls in order to model any possible interactions. Simulation of the interactions of neutrinos in the MINOS Detectors is facilitated by the `NEUGEN` software package [192], which has the ability to simulate elastic, quasi-elastic, and inelastic neutrino interactions over an energy range from $\sim$ 100 MeV to $\sim$ 100 GeV. The `NEUGEN` package uses the `MODBYRS-4` model for calculating neutrino cross sections. Quasi-elastic interaction cross sections are calculated using the Llewellyn-Smith model [193]. Resonant neutrino interactions are modeled according to the Rein Sehgal framework [194] [195], which involves a summation over possible resonances assuming each corresponds to a Breit-Wigner distribution. The remaining deep-inelastic scattering interactions are simulated using the modified Bodek-Yang model [196]. The hadronic production in the detectors is modeled by a hybridization of `PYTHIA/JETSET` [197] for large invariant mass hadrons with a continuous transition to the KNO phenomenological model [198] for lower invariant mass hadrons. This combination is known as the AGKY model [199]. If a neutrino interaction is sufficiently energetic, it is possible that hadrons produced in the collision may be liberated from the struck nucleus, which is modeled using the `INTRANUKE` software package [200].

Subsequent to the simulation of the neutrino interaction, any of the particles produced from the various platforms are then propagated through the

geometric model of the detector where the interaction has taken place, which is simulated by `GMINOS` framework [201]. The simulated detector geometry crucially accounts for the effects of the magnetic field in the steel planes on charged particles using `GEANT4` and interactions between the particles and the elements of the detector, which usually results in the deposit of energy, is modeled using the `GCALOR` software package [202]. The `GMINOS` software framework accounts for the energy deposited in each strip of the detector by each of the simulated particles. A threshold energy of 10 keV is used for determining the end of particle propagation in the detectors and the remaining energy is assumed to be deposited at the subsequent track hit.

Using the simulated energy deposit information, a separate software package called `PhotonTransport` [203] is used to determine the resulting production of photons in the scintillator and to simulate the WLS fibers conveying these photons to the PMTs. The `PhotonTransport` simulation includes systematic fluctuations designed to account for known features of the detector components such as electronic noise, non-linearity, and triggering. A random number generator using Poisson statistics is used to convert the collected photons into a count of photoelectrons for readout by the electronics. The concluding step of detector simulation involves the conversion of perfect simulated data to a raw data sample, which can be passed directly into the MINOS reconstruction package in the same manner as collected real-world data. This process is handled by the DetSim software package [203] and requires the introduction of effects in the data that are removed or mitigated by detector

calibration. In order to produce uncalibrated data, the inverse of the standard calibration constants from a randomly selected timestamp are applied to the simulated data sample, and the data is marked with this timestamp such that the process can be reversed at the time of reconstruction.

3.3 Event Reconstruction

The goal of the reconstruction software in MINOS and MINOS+ is to identify the relevant topology of energy deposition associated with the event types that are known to occur in the detectors and were initially discussed in Section 2.3. The reconstruction software uses the energy deposition information after passing through the calibration procedure in addition to timing information in order to establish hadronic showers, electromagnetic showers, and track-like structures and associate these topologies into aggregated events that can be further analyzed offline.

3.3.1 Digitization and Slicing

The initial step in the reconstruction procedure is the identification of the exact timing of individual deposits of energy occurring in the detector. Charged particles passing through the scintillation strips produce photons which are collected as described in Section **??**, and the pulse height associated with the produced electronic signal stored in the form of digits, which are associated both to a particular timestamp as well as the possible scintillator strips from which they may have originated. At this step it is not possible to

determine the precise scintillator that produced the signal due to multiplexing of strips in the PMT readout. The digits are then further grouped by timestamp in order to reassemble the strip into which energy was deposited. The high occupancy of the ND, approximately 20 to 40 neutrino interactions per beam spill, requires that the strips be further associated to one another by nearby timestamp and physical location in the detector in order to construct units called slices. Ideally, the separation into slices ensures that only energy deposits associated with a single event are contained within a single slice. The slicing step is not required in the FD as the occupancy is low enough that multiple events occurring in the beam spill time interval is improbable. Thus, the entirety of the FD for the entire spill duration is treated as a slice. The slices resulting from this initial phase of reconstruction are then passed to further methods for shower and track reconstruction.

3.3.2 Track Reconstruction

The track reconstruction software begins by searching for strips within the slice that contain track-like segments. Here a track-like segment means hits recorded on strips that are on neighboring planes and are sufficiently close to a line passing through the hits. Any track-like segments found in this stage of reconstruction are combined into a seed track, which is passed to a Kalman filter for further reconstruction. The Kalman filter, otherwise known as linear quadratic estimation, is an algorithm which attempts to improve the initial seed track by estimation of the underlying track parameters using joint

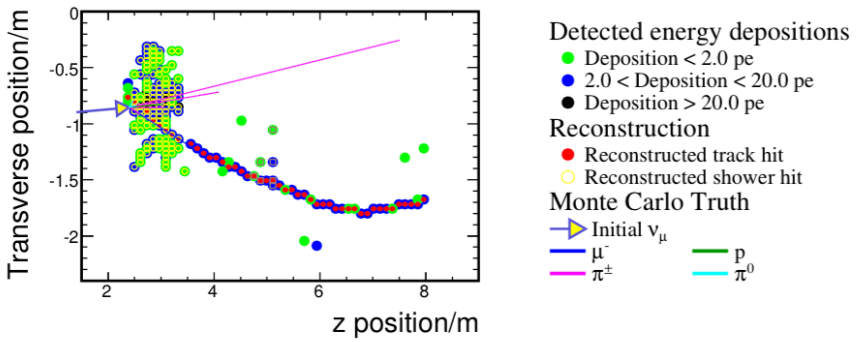

Figure 3.9: A simulated reconstructed event display for a ν_μ-CC event in the MINOS FD. The red points indicate hits reconstructed as part of a track, which follows closely the MC true μ^- indicated by the blue line. Long muon tracks of this form are an identifying feature of the CC events. Figure reproduced from Ref. [204].

probability distributions. In the specific case of the MINOS and MINOS+ reconstruction, the main goal of Kalman filtering is to estimate the momentum of the particles generating tracks and extrapolate the true path of the track, which may include planes traversed without visible energy being deposited. During the momentum fitting procedure, the Kalman filter makes two passes along the full track and accounts for underlying effects that may cause inaccuracies such as electronics noise, multiple scattering, and erroneous track-like elements in the seed track. The resulting fitted track is assigned estimated measurements for the ratio of charge to momentum, q/p, and the error on this value, which are both crucial in offline analysis for the determination of neutrino or antineutrino events. An example of a reconstructed track is shown in the event displayed in Fig. 3.9. Assuming that the charged particles producing tracks in the detector are muons, the estimation of momentum also gives an

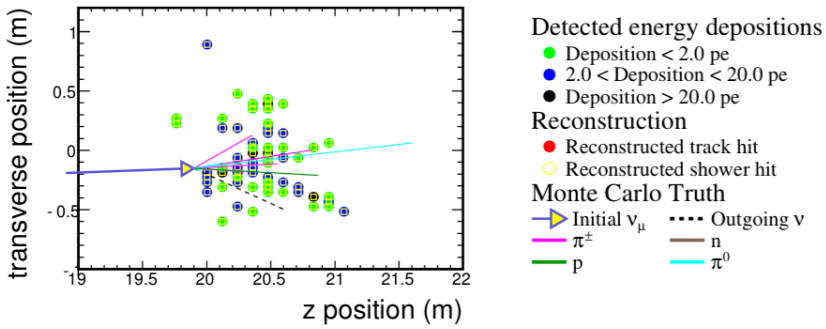

Figure 3.10: A simulated reconstructed event display for an NC event in the MINOS FD. In this event, all of the energy deposits given by the green, blue, and black circles are identified as elements of a shower feature, indicated by the yellow circles. The absence of reconstructed tracks is indicative of an NC event. Figure reproduced from Ref. [204].

estimation of the particle energy based upon the track curvature. The estimation of energy from curvature is less efficacious in general then determining the particle energy from range in the detector, though range estimation is only possible if the track is fully contained. For example, for a muon with energy of 3 GeV the resolution achieved using curvature is 11% while the resolution from range is 4.6% [180].

3.3.3 Shower Reconstruction

All hits not associated with tracks by the Kalman filter are grouped by spatial proximity in the detector into showers. Hits that occur both in the region of a shower and along a fitted track have the energy deposit separated into track and shower contributions by subtraction of the standard amount of

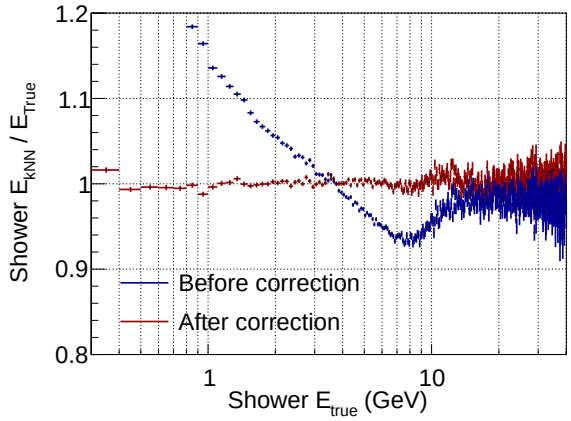

Figure 3.11: The ratio of the kNN shower energy to the simulated true shower energy as a function of true shower energy before and after energy corrections. A 14th order polynomial function is used in three iterations to fit and correct the kNN shower energy to improve agreement with the true shower energy. Figure taken from Ref. [187].

energy deposited by a muon traversing the detector plane steel and scintillator and treating any remaining energy deposit as a component of the shower. An example of a reconstructed hadronic shower is shown in the event displayed in Fig. 3.10. A pulse height threshold requirement of two photoelectrons is applied to shower detector hits in order to reduce contributions from events that are poorly modeled by the MC. A shower energy estimation is made by a kNN algorithm which is discussed in more detail in the next section and is based upon analysis of data collected with the CalDet.

3.3.4 kNN Estimation of Shower Energy

The reconstructed energy of an observed CC event is the sum of the energy contributions from the particle track and the hadronic shower. The

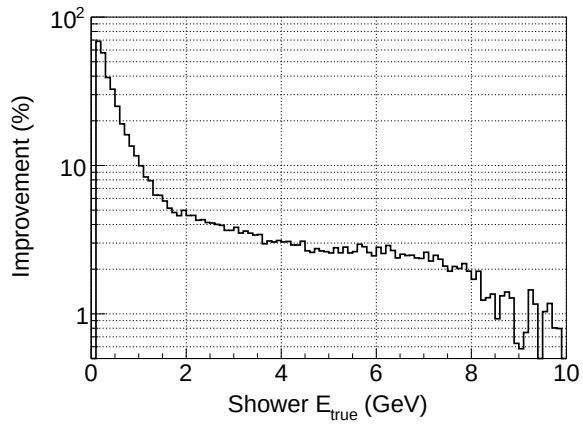

Figure 3.12: The fractional improvement in the energy resolution due to using the kNN shower energy estimation as opposed to the calorimetric shower energy as a function of the true shower energy. Improvement along the y-axis is defined as the fractional reduction of the deviation between the mean kNN shower energy and the true shower energy. Figure reproduced from Ref. [187].

design of the MINOS detectors allows for precise estimation of track energy. Thus, the limiting factor in energy reconstruction is the resolution of hadronic shower energies. One method of shower energy estimation is simply a summation over all the apparent energy deposits in strips associated with the shower, which is known as the calorimetric shower energy. It has been demonstrated in more recent MINOS analyses that an improvement in the shower energy estimation can be achieved by using a k-Nearest-Neighbor (kNN) method which better exploits features of the shower topology.

Generally, a kNN algorithm is designed to search for a collection of number k of the nearest neighbors to a given point in parameter space. In the case of the shower energy estimation, this becomes a search for the k nearest

neighbor events in MC to a data event, such that the shower energy of the data event can be estimated from the average of the known energies of the MC events. In order to determine the nearest neighbors, a metric for distance must be defined, which in the case of MINOS is the Euclidean metric given by:

$$d = \sqrt{\sum_{i=1}^{3} \frac{(y_i - x_i)^2}{\sigma_i^2}} \tag{3.5}$$

where x represents the data event, y represents the MC event, the index i = 1,2,3 defines the shower variables in the parameter space, and $1/\sigma_i^2$ defines the importance weight of each of the shower variables. In the shower energy kNN estimation for MINOS and MINOS+, the 400 and 440 nearest neighbors are used, respectively. The following three shower variables are used to the define the parameter space for the nearest neighbor search:

1. The number of planes in the primary shower
2. The deweighted energy within 1m of the track vertex
3. The calorimetric energy in the first two showers if there is more than one shower

The dramatic improvement in both the ratio of the kNN estimated shower energy to true energy in MC samples and the energy resolution for the kNN method as opposed to ordinary calorimetric shower energy is shown in Figs. 3.11 and 3.12. A more detailed description of the kNN method and results can be found in Reference [205] for MINOS and Reference [187] for MINOS+.

3.3.5 Event Building

The basic components of detector events are the tracks and showers reconstructed in the previous algorithms. After all tracks and showers have been reconstructed, a further algorithm is applied, which groups tracks and showers into events based upon the relevant spatial and timing information. The events are not categorized at the reconstruction stage as either CC or NC, nor are they assigned a neutrino flavor as it is possible for all events to contain a number of tracks and/or showers associated with particles produced in the interaction. The event reconstructing algorithm assigns a primary track and primary shower to each event, which allows for the determination of the vertex of the interaction and for calculation of the length of the event and extension of any tracks from the vertex. In the ND, cuts must be applied at the reconstruction stage in order to prevent erroneous reconstruction of tracks and showers from different events into a single event. This applies to the ND because the large event rate in the ND leads to high occupancy of the electronics and overlapping event features. In the FD, the event rate is sufficiently low that a single event is generally expected to occur for any given spill, and this allows reconstruction to proceed with a much lower chance of failure.

Chapter 4

Event Selection

In this chapter, a detailed explanation of the methods used for event selection in this analysis is discussed. In the standard three-flavor oscillations analysis, MINOS searched for the disappearance of muon neutrinos, which can only be detected via the selection of CC events. For beyond three-flavor oscillations models, such as the 3+1 flavor extension presented here, the NC event sample becomes relevant as a probe for anomalous neutrino disappearance not observed in the three-flavor case. Thus, we select separate samples of CC and NC events for analysis in this study, while endeavoring to remove backgrounds events arising from cosmic muons, electron neutrinos, and antineutrinos of any flavor.

4.1 Common Preselection

The aim of the preselection phase of the event selection procedure is to ensure good data quality and to remove contaminant events unrelated to the beam. A primary set of cuts is applied to all events in both detectors in order to remove events that took place when the detector was not operating correctly, the magnetic field was unstable, or the beam quality was in some

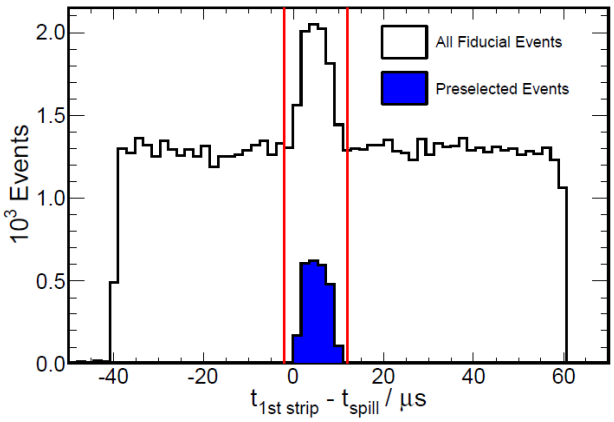

Figure 4.1: Fiducial volume events in the MINOS/MINOS+ FD as a function of the time elapsed between the most recent beam spill and the time of the first event hit. Rejection of cosmic muon contamination is achieved by accepting only those events occuring within the $10\mu s$ window indicated by the red lines. The blue distribution represents those events passing the remainder of the preselection cuts. Figure reproduced from Ref. [175].

manner compromised. Events occurring outside of the triggered beam spill window of 10 microseconds are also discarded along with any events registered during one of the calibration LI runs. A plot of the preselected events is shown in Fig. 4.1. Events may also be rejected during preselection as if the Kalman filter registered failure to properly reconstruct the track by assigning the value on the error of the ratio of muon track momentum to charge to 1×10^{-4} GeV^{-1}. Additionally, any events where the muon track forms an angle with respect to the beam-line axis, θ, such that $\cos(\theta) < 0.6$ are excluded in order to prevent contamination of the beam spills by cosmic muons entering the detector.

The large distance separating the FD from the beam target makes it unfeasible to prevent the LI system from flashing during all beam spills [206].

The beam spills containing LI activity are generally identified by the trigger PMT (tPMT), which is a distinct PMT illuminated directly by the LI system. Due to the direct illumination of the tPMT, the threshold for the trigger can be set at a high level in order to avoid false triggering and corresponding inefficiency that can arise from the deadtime that occurs immediately subsequent to triggering. Using a test MC sample, the tPMT successfully identified all LI contamination except for approximately 1 in 10^4 LI containing beam spills.

The approach used to remove remaining LI contamination in beam spills is a set of criteria known as the LISieve, which may be summarized as follows:

1. High number of hits per plane: The LI system illuminates a large number of strips (either 8 or 10) on a single plane during the LED flash. Due to cross-talk in the PMT electronics, the apparent illumination during an LI run can be the maximum per plane amount allowed by the demultiplexing algorithm, which corresponds to a total of 24 strips or 1 m wide region in the detector. These levels of illumination on a single plane are not observed in neutrino interactions as the energy deposits are spread across multiple planes through the detector. Therefore, a high average number of hits per plane in an event is indicative of an LI activity.

2. High East-West asymmetry of hits: The pulser boxes used to generate the flashes for the LI system are near the edges of the detectors, which means that attenuation in the WLS fibers yields a response approxi-

mately five times greater along the side of the detector originated as opposed to the response detected on the opposite side. Neutrino interactions will originate in the centered fiducial volume of the detector, which implies that the light readout will be more symmetric with respect to the sides of the detector. The asymmetry of the light readout in the detector can be defined according to:

$$A_{WE} = \frac{\sum PH_W - \sum PH_E}{\sum PH_W + \sum PH_E} \tag{4.1}$$

Events exhibiting a high amount of asymmetry in this quantity are considered potentially LI activity contaminants.

3. High single pulser box fraction: Each pulser box illuminates planes in only a given region of the detector. True neutrino interactions deposit energy across many planes in the detector and are generally not confined to a region that corresponds to a single pulser box. Therefore, if an event is observed, which has a high fraction of the total hits occurring only in the region of the detector that receives flashes from a single pulser box then the event may be indicative of LI activity in the run. The threshold used to determine if the activity is sufficiently high to warrant the suspicion of LI activity is a fraction greater than 0.85 of the planes in the region of any single pulser box.

4. Pulser box double ratio: The obverse approach of the previous condition is that an event having a large number of hits in planes within a given pulser box region may or may not have a similarly large number of hits

in other pulser box regions. Neutrino interactions tend to deposit energy across many pulser box regions due to showering activity and potentially long bending tracks. This is the opposite of a contaminant LI event since the majority of hits from an LED flash will only illumine the planes associated with the given pulser box. The double ratio may be computed of the penultimate pulser box fraction to the highest pulser box fraction, which is given as the third criteria above. If the pulser box double ratio is found to be less than 0.05, then this is considered evidence of potentially LI contamination in the event.

Each of the listed criteria above give only a small indication of the possibility of LI contamination and would result in false positive indications if taken in isolation. However, the strength of the LISieve is the use of all of the criteria in conjunction with the requirement that all of the criteria be met for any event to be flagged as LI contamination. The design of this method of LI event removal is uncorrelated to the tPMT cut and can therefore be used in tandem in order to have an overall removal effectiveness leaving only approximately 1 in 10^7 LI contaminated spills.

4.2 NC Selection

4.2.1 NC Fiducial Volume Cuts

A neutrino interaction that deposits energy in the MINOS detectors may originate either within the detector volume or in the rock walls of the cavern containing the detector. If an event vertex occurs in the rock outside

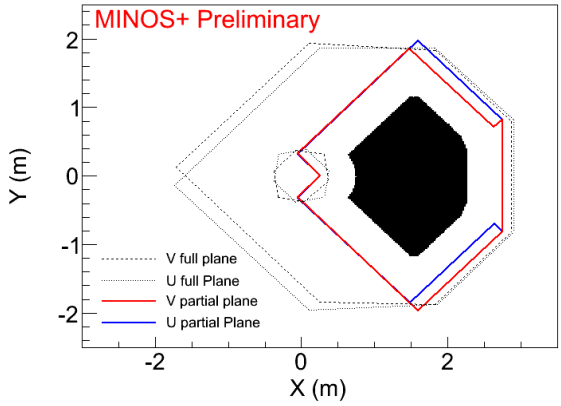

Figure 4.2: The locations of the NC-selected event vertices (black circles) in the XY-plane of the ND. The large number of events overlap significantly, which prevents resolution of the individual vertex locations. The black region therefore represents the cross sectional face of the fiducial volume. Figure reproduced from Ref. [187].

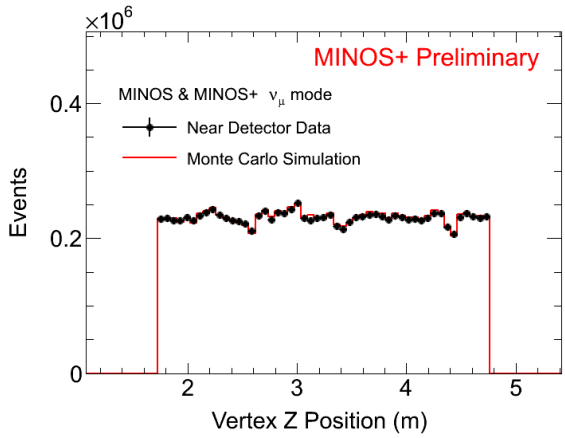

Figure 4.3: The vertex positions along the Z-axis, the direction of the beam, for NC-selected events in the ND. The data and MC simulation have good agreement over the length of the detector. This distribution includes all MINOS neutrino data and the first two years of MINOS+ data.

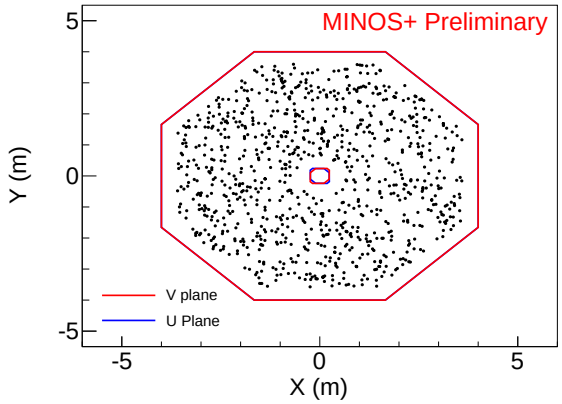

Figure 4.4: The locations of the NC-selected event vertices (black circles) in the XY-plane of the FD. The events roughly indicate the cross sectional area of the fiducial volume. Figure reproduced from Ref. [187].

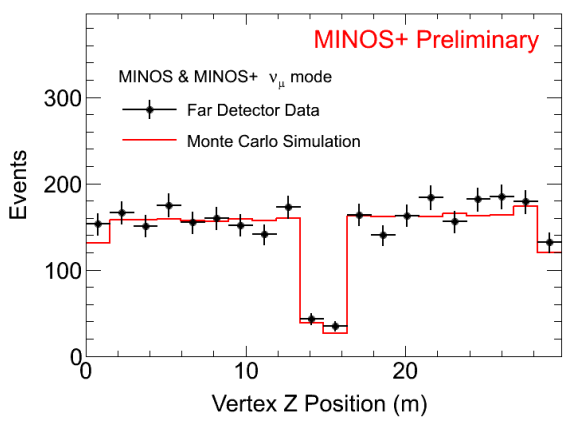

Figure 4.5: The vertex positions along the Z-axis, the direction of the beam, for NC-selected events in the FD. The data and MC simulation have good agreement over the length of the detector. This distribution includes all MINOS neutrino data and the first two years of MINOS+ data.

the detector then it is strictly impossible to reconstruct the full energy of the event even if the detector records some energy deposit. Additionally, some events occurring near the edge of the detector may allow particles to exit the detector carrying away some fraction of the total event energy. In order to ensure the reconstruction of the full visible energy of neutrino interactions, it is necessary to define a volume within the detector in which the majority of events with vertices in said volume are well contained. This defined volume is known as the fiducial volume, and containment in this context refers to the deposit of the full energy of all particles produced in an interaction within the detector volume.

The XY-plane of the NC fiducial volume in the ND is defined as the region of the partially instrumented U and V scintillator planes where 50 cm nearest the edges are excluded. Due to the shape and extent of the partially instrumented planes, this cut excludes the region of the detector containing the magnetic coil hole. The extent of the fiducial volume in the Z-direction (i.e. along the beamline) is defined as 1.7 m $< Z <$ 4.7368 m. The primary vertices of the observed events must lie within this fiducial volume region in order to be considered for further selection. Figure 4.2 shows the vertices for events in the fiducial volume projected into the XY-plane, while Fig. 4.3 gives the Z distribution of the vertices.

The XY-plane of the NC fiducial volume in the FD is defined by the region of the U and V scintillator planes with the 40 cm nearest the external edges and a 60 cm radius centered at the magnetic coil excluded. The resulting

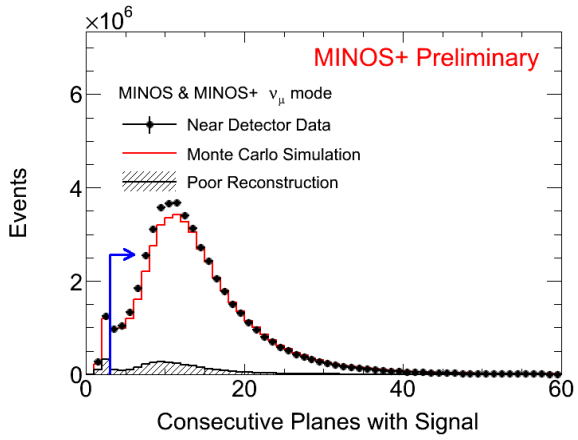

Figure 4.6: The distribution of the ND data (black points), MC simulation (red), and poorly reconstructed background (hatched) as a function of the maximum number of consecutive planes in the event. The cleaning cut in this variable is set to reject events with less than 3 consecutive planes.

cross section of the fiducial volume is an octagon with a circular hole at the center. The longitudinal extent of the fiducial volume is defined by 0.21 m $< Z <$ 13.72 m and 16.12 m $< Z <$ 28.96 m, where Z is the distance along the beamline from the front face of the first plane and the break in the fiducial volume is due to the bi-modular design of the FD. Figure 4.4 shows event with vertices in the fiducial volume projected into the XY-plane, while Fig. 4.5 gives the Z distribution of the vertices.

4.2.2 NC Cleaning Cuts

The relatively abundance of ND events on the order of 10 events per beam spill in combination with the requirement of a confined fiducial volume due to the detector geometry and instrumentation characteristics ensures high

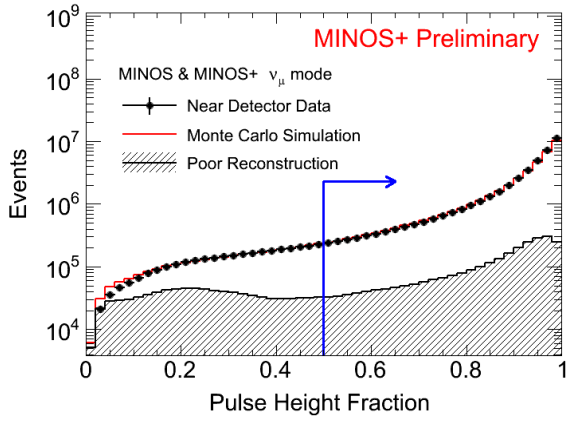

Figure 4.7: The distribution of the ND data (black points), MC simulation (red), and poorly reconstructed background (hatched) as a function of the slice pulse-height fraction of each event. The cleaning cut in this variable is set to reject all events with less than 0.5 of the slice pulse-height fraction.

detector occupancy. While this yields very large samples for analysis, pile-up effects can arise in reconstruction, which has the greatest effect on NC-like candidate events. The most common effect seen due to event pile-up is poorly reconstructed events, which are defined at those events where the ratio of reconstructed energy to the true energy is less than 30%. These poorly reconstructed events usually tend to arise due to errors in slicing where a single event is divided amongst several slices and thus treated as multiple events.

The mitigation of the detrimental effects of poorly reconstructed events in the NC selection is achieved through the application of two ND NC cleaning cuts. The first of the cleaning cuts is based on the fraction of the total event pulse height that is contained in the initial slice. The distribution of the slice

pulse height fractions for well (signal) and poorly (background) reconstructed events in MC compared to the data spectrum is shown in Fig. 4.7. An event is generally assumed to be contained within a slice, which would ideally result in a fraction event pulse height in the slice of 1.0. If the initial slice fails to adequately contain a single event due to the aforementioned pile-up effects and the event becomes smeared over several initial slices, then the fractional pulse height in the initial slice will be reduced. In order to discriminate between well sliced and poorly sliced events, a cut value of greater than 0.5 is required to pass an event through the cleaning process.

The second cleaning cut is based on the straightforward topological feature of the maximum number of consecutive detector planes on which hits from a given event are registered. The distribution of the maximum number of consecutive planes variable for well and poorly reconstructed events in MC compared to the data spectrum is shown in Fig. 4.6. A hand-scan of NC events in the MINOS detectors found that poorly reconstructed events tend to have a low number of total hits, which may be expected given that a small amount of the possible visible energy is reconstructed. Since relatively few hits are seen, the poorly reconstructed events tend to have a low maximum number of consecutive planes with hits recorded. Thus, events are required to have hits on greater than three consecutive planes in order to be passed through the cleaning cuts.

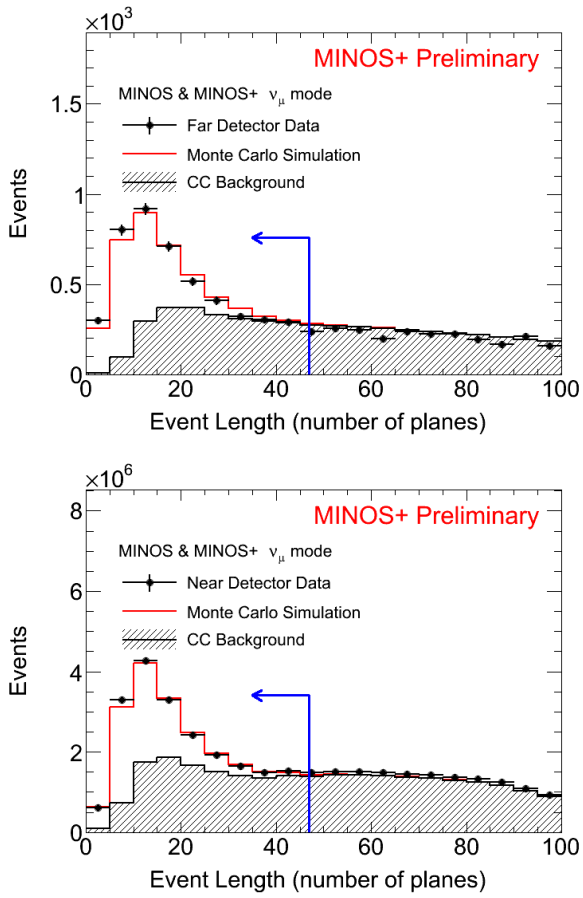

Figure 4.8: The distribution of the FD (upper) and ND (lower) data (black points), MC simulation (red), and CC background (hatched) as a function of the total event length. In order to remove CC backgrounds, all events with length greater than 47 total planes are rejected.

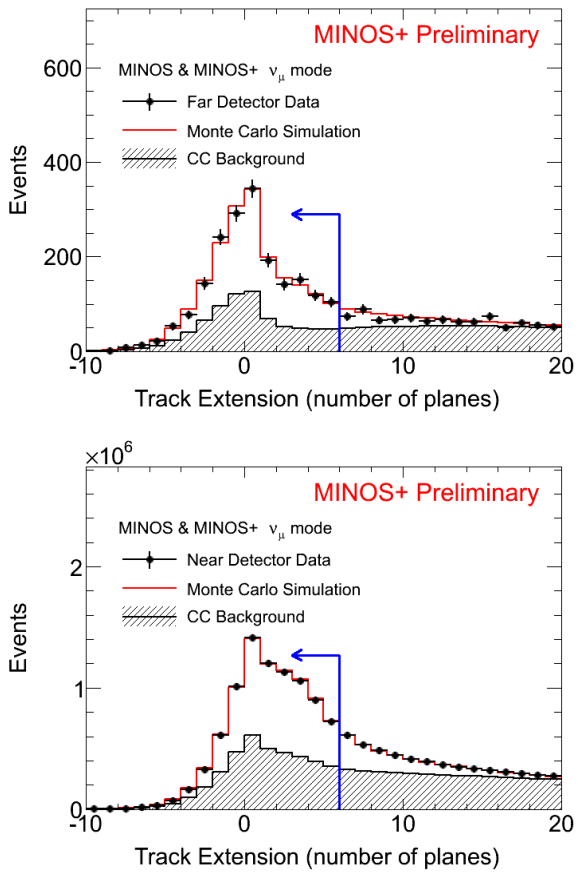

Figure 4.9: The distribution of the FD (upper) and ND (lower) data (black points), MC simulation (red), and CC background (hatched) as a function track extension of the longest reconstructed track in the event. In order to remove CC backgrounds, all events with a reconstructed track extending greater than 6 planes beyond the reconstructed shower are rejected.

4.2.3 NC Selection Cuts

The NC selection in this analysis is a cut-based method used to eliminate events which do not have necessary topological traits that are typical of NC interactions. The NC selection is performed immediately subsequent to the preselection described above and prior to the CC selection. The ND events are also passed through the NC cleaning cuts prior to consideration for selection. Only events which explicitly fail the NC selection are passed to the CC selection algorithm in order to ensure that no events are included in both samples. NC events are defined by the presence of a hadronic shower and the absence of the extended track associated with an outgoing muon as was discussed in Section **??**. The functionally identical design of the ND and FD ensures that the topological structure of the events will be similar in both detectors allowing the use of a uniform set of selection cuts.

The first NC selection variable is based upon the size and extent of NC hadronic showers in comparison to the shower-plus-track topology of the CC events. Hadronic showers tend to deposit energy rapidly, meaning across fewer planes, in comparison with a MIP such as the muons produced in CC events. For this reason, the overall length of an event in the detector, which is defined by the number of planes between the first and last plane of the fully reconstructed interaction, is a discriminator between CC and NC events. Though highly energetic NC events can produce extensive showers that cross a significant number of planes, these are generally still shorter then CC events which can have very long muon tracks. The distribution of the event lengths for

the total MC sample in comparison with data along with the CC background event spectra is shown in Fig. 4.8 for both the ND and FD. Events selected as candidate NC events are those with lengths less than 47 total planes as indicated by the arrows in the figures.

The second and final topological cut used for NC selection is based upon the extension of track-like features beyond the hadronic shower associated with the event vertex. CC events must by definition containing a muon track. It is also possible for tracks to be reconstructed within an NC event due to highly energetic hadrons participating in the showering activity. Hadronic tracks differ from muon tracks in several respects that will be more thoroughly discussed during the CC selection description in the following section. For the purposes of the NC selection, it is only necessary to note that hadrons deposit more energy in each plane than the typical muon, and therefore produce shorter tracks. In addition, these tracks tend to be part of the larger shower structure and not distinct prong-like extensions. Therefore, a variable called track extension may be defined by subtracting the number of planes in the reconstructed shower from the number of planes in the reconstructed track. This number may be positive or negative given that the track may terminate in a shorter or longer distance than the corresponding shower. The distribution of the track extensions for the full MC sample in comparison with data along with the CC background event spectra is shown in Fig. 4.9 for both the ND and FD. Events are selected as NC candidates if the track extension variable is less than 6 planes as indicated by the arrows in the figures.

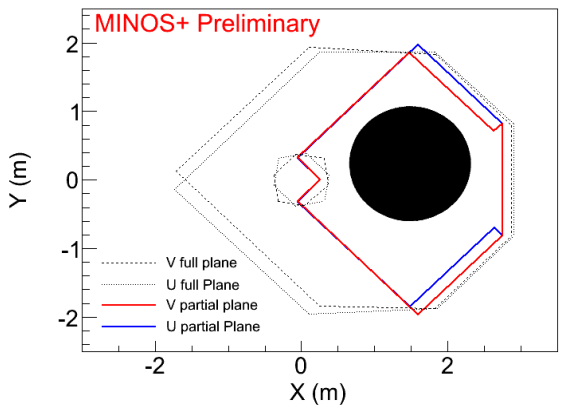

Figure 4.10: The locations of the CC-selected event vertices (black circles) in the XY-plane of the ND. The large number of events overlap significantly, which prevents resolution of the individual vertex locations. The black region therefore represents the cross sectional face of the fiducial volume. Figure reproduced from Ref. [187].

Events passing both of the aforementioned cuts form the NC-selected sample used in this analysis. The quality of the NC selection method is quantified in Section 4.4 in terms of the efficiency and purity of selection.

4.3 CC Selection

4.3.1 CC Fiducial Volume Cuts

The same principles with regards to event containment discussed for NC events apply to the CC event selection as well. In the CC sample, events with vertices in the rock of the cavern walls can produce muons that enter the detector and are referred to as rock muons. These muons are not useful for analysis given that the event vertex is not established, and therefore the

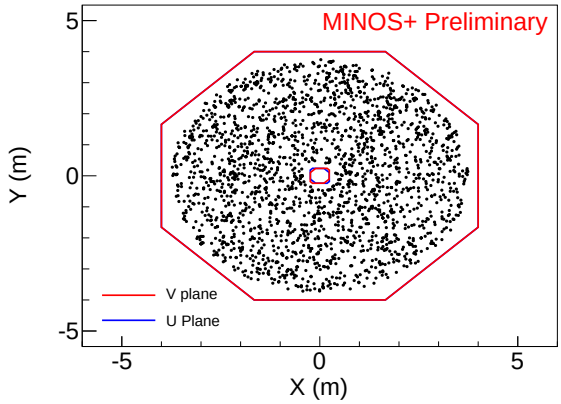

Figure 4.11: The locations of the CC-selected event vertices (black circles) in the XY-plane of the FD. The events roughly indicate the cross sectional area of the fiducial volume. Figure reproduced from Ref. [187].

hadronic energy deposited near the vertex is not reconstructed. The fiducial volume for the CC events attempts to define a region of possible vertex locations such that both the hadronic activity near the interaction vertex and the muon track produced are typically well contained within the detector volume. Due to the different nature of the CC event topologies and parallel analyses within the MINOS experiment, the fiducial volume used for the CC event selection differs in some respects from the NC fiducial volume.

The fiducial volume cuts for CC events in the ND are defined by a cylinder oriented along the beamline, which is not centered in the detector. Defining a coordinate system where the origin lies at the front face of the ND at the center of the magnetic coil hole and the detector planes form the XY-plane, the beam spot is located at (X,Y) = (1.4828 m, 0.2384 m). The fiducial volume is centered around this beam spot, and the XY cross section

is defined as a disk with radius of 0.8 m. The extent of the fiducial volume in the Z-direction (i.e. along the beamline) is defined as 0.81 m $< Z <$ 4.08 m. Events with primary vertices within the defined fiducial volume are passed through for further selection. Figure 4.10 shows the vertices for events in the fiducial volume projected into the XY-plane.

A special fiducial volume cut applied for CC events in the ND is on events with tracks terminating in the vicinity of the magnetic coil hole. These events are not well-modeled by the MC simulation of the ND as the reconstruction of the tracks can often fail when passing through the coil hole region. Therefore, events with a track ending within 0.6 m of the magnetic coil are rejected. While a significant number of events are eliminated by this cut, the high overall event rate in the ND means that the benefits of reduction in systematic uncertainty outweighs any increase in statistical uncertainties.

The fiducial volume for CC in the FD is centered on the magnetic coil and is cylindrical with the exception of the removed coil hole region. The XY plane is defined by the orientation of the detector planes and the cross section of the fiducial volume is a disk with radius from the center of the coil from 0.5 m to 3.74 m. The Z-axis, as in the ND, lies along the beam line with the origin at the front of the FD. The fiducial volume in this direction is then defined by 0.49 m $< Z <$ 14.29 m and again by 16.27 m $< Z <$ 27.08 m, where the discontinuity in the fiducial volume is due to the bi-modular design of the FD. Figure 4.11 shows event with vertices in the fiducial volume projected into the XY-plane.

4.3.2 CC Selection Algorithm

The initial requirement for CC selected events is the presence of at least one reconstructed track emerging from the event. However, it is still possible for an NC event to contain tracks due to highly energetic hadrons ejected from the target nucleus in certain interactions or simply an erroneous reconstruction of a track-like feature that is part of the hadronic shower. Therefore, some NC background events may evade this initial selection criteria. In order both to classify the charge of CC events and to remove the remaining NC backgrounds, a kNN selection algorithm is employed.

The concept of a kNN algorithm was described in Section 3.3.4, and a similar Euclidean metric may be used in the context of event selection to compute distances between events in the parameter space. However, in this instance, the result of the algorithm must be an evaluation of the likelihood that an event is a right-sign (numu) charged current event. The CC/NC separation variable used for the selector is the fraction of simulated signal events contained in the set of nearest neighbors and is written:

$$f_S = \frac{k_S}{k_S + k_B} \tag{4.2}$$

where k_S and k_B are number of signal and background MC events in the group of k nearest neighbors. This likelihood value is in general termed a particle identification (PID). In the MINOS CC selection, two PIDs called roID [207] and jmID [208] were developed. The PID cuts used in this analysis are discussed in more detail in the subsequent sections, and the quality of the

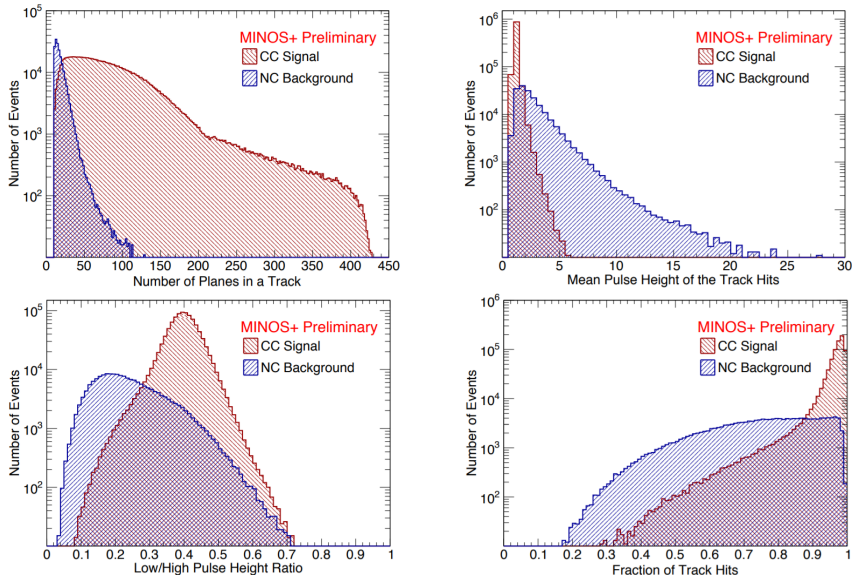

Figure 4.12: Distributions in data (black points), tuned MC simulation (red), and estimated total background (blue) at the ND for the four variable inputs used by the kNN roID selector. Estimated systematic uncertainties on the roID input variable are indicated by the shaded regions. Figures reproduced from Ref. [209].

CC selection method is quantified in Section 4.4.

4.3.3 The roID Selector

The roID variable is calculated by searching for nearest neighbors in the space of four features, which are found to discriminate between muon tracks and tracks due to non-muon contaminants. In order to isolate the features of tracks that are separate from shower features, an adjustable fraction of the planes nearest the vertex of reconstructed tracks are generally removed from consideration in the construction of the PID variables.

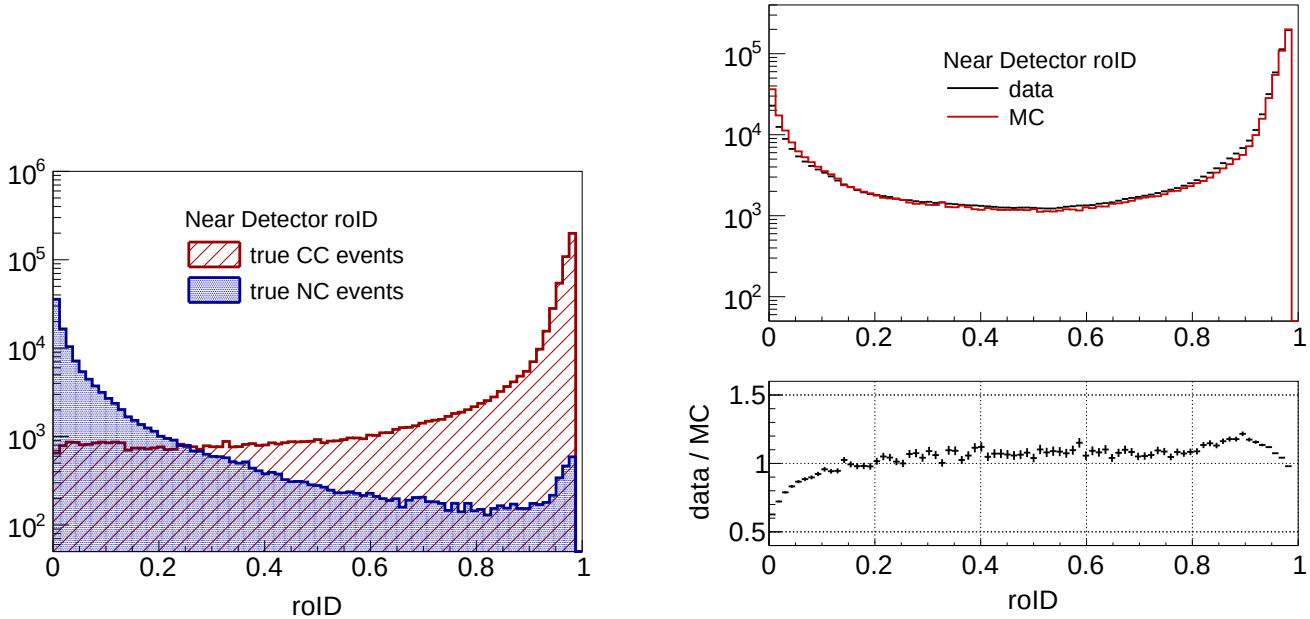

Figure 4.13: The distribution at the ND of true MC simulated CC events and NC events as a function of the roID (left) and the comparison of the total MC sample to the ND data (right). The ratio of the ND data to MC indicates reasonable agreement above the cutoff for NC separation, which is set at roID > 0.3 in this selector. The comparison of signal CC to background NC demonstrates the suitability of setting the cut at the stated value. Figure reproduced from Ref. [187]

The first feature used in the parameter space is the length of the tracks in the detector. This distance is computed by the number of scintillator planes traversed by the reconstructed track. The muons observed in MINOS and MINOS+ are almost exclusively MIPs that can travel a very long distance in the detector, whereas hadronic tracks tend to be much shorter due to more rapid energy deposition. Thus, selecting for long tracks with a large number of scintillator planes hit is a good discriminator of muons. The distribution of track lengths for both signal and background are shown in Fig. 4.12.

The second feature is the average energy loss in scintillator strips, which is given by the mean pulse height of track hits. The mean pulse height for this selection variable is computed by excluding the 30% of hit scintillator planes that are closest to the primary vertex of the neutrino interaction and summing over the remaining track hits. Muons tend to be low energy depositors, and therefore form a narrow peak of pulse height contributions. Hadrons instead have a much broader spectrum of energy deposition resulting in both large and small pulse height fractions. The distributions of mean pulse height due to track hits can be found in Fig. 4.12.

The third feature used in the roID are the fluctuations in deposited energy in the scintillator strips. The variable used in the selection is computed by taking a ratio of the means of low pulse height and high pulse height hits as given in more detail in [207]. The principle being exploited by this variable is that the energy deposits of muons along the track are relatively uniform in each plane, while hadronic tracks can deposit widely different quantities of

energy in subsequent scintillator planes. The signal fluctuation discrimination variable will thus indicate a narrower distribution of interplane energy deposit fluctuations for signal events as opposed to background, a feature which can be seen in the variable plots in Fig. 4.12.

The fourth and final feature is the transverse profile of the track in the scintillator planes. In order to identify this feature, a variable is computed that takes the ratio of the scintillator hits associated with the track to the total of all hits occurring within a selected window of scintillator strips containing the track. This computation is intended to identify the spatial extent across the scintillator strips of energy deposits associated with the particle forming the track. The energy deposition associated with a muon interacting with the scintillator plane is generally confined to a single scintillator strip, again due to the minimum ionizing nature of muons produced in the detectors. Conversely, hadrons tend to produce broad energy depositions across multiple strips when interacting with the scintillator. Thus, the muon signal events can be expected to have a distribution in this ratio variable very near unity, while the background events have a more uniform distribution. The distributions of the transverse track profile variable for both signal and background events can be seen in Fig. 4.12.

Once the parameter space is established using the MC training sample, data events can be evaluated by the kNN algorithm. For the roID selector, the number of nearest neighbors used for computing the CC/NC separation variable discussed above (hereafter referred to as roID) is k = 80 for both the

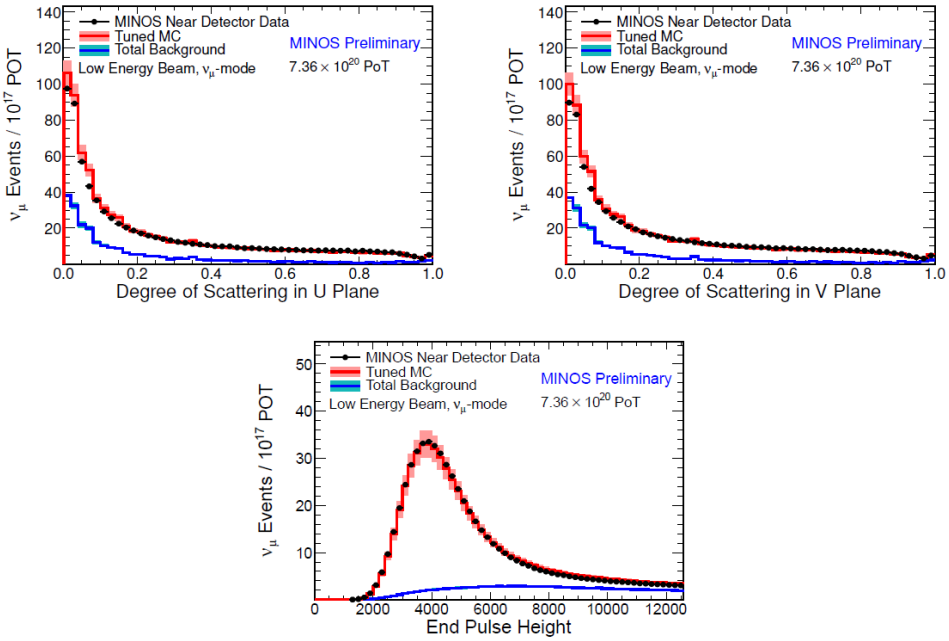

Figure 4.14: The ND distributions of the MINOS data (black points) and MC simulation (red line) for the three additional variables used by the jmID selector. The estimated systematic uncertainties of the distributions are given by the shaded bands and the estimated total background is indicated by the blue distribution. The figure is reproduced from Ref. [175].

MINOS and MINOS+ selections. The distribution of the roID is plotted in Fig. 4.13. In order to determine the value of roID used for CC event selection, separate optimization procedures were undertaken using the measurement of a set of injected standard atmospheric oscillation parameters as a target. The maximum sensitivity to the oscillation parameters were achieved for the MINOS sample defined by roID > 0.25 and the MINOS+ sample defined by roID > 0.3.

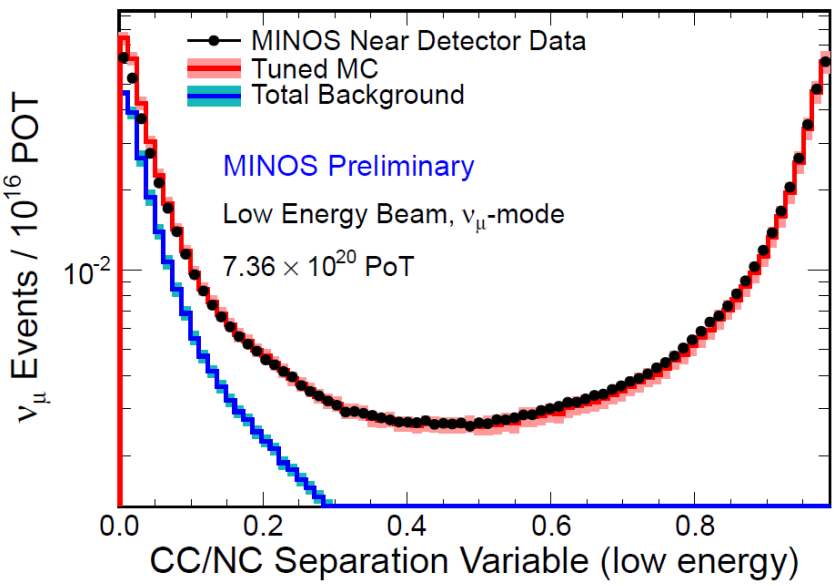

Figure 4.15: A plot of the distribution of MINOS data events as a function of the jmID CC/NC separaton variable. The total MC prediction (red) is plotted in comparison to the data (black points) and the estimated total background (blue). The optimized cut value for background elimination in this variable is set at jmID < 0.5. The figure is reproduced from Ref. [175].

4.3.4 The jmID Selector

Similarly to the roID selector, the jmID uses a four variable parameter space in searching for nearest neighbor events. The aim of the alternative jmID selection algorithm is the inclusion of lower energy CC events. The roID selector has the removal of a selected portion of the track nearest the interaction vertex built into each of the variables. This has the effect of rejecting all events with tracks that are short in comparison to the hadronic shower, which is biased against low energy events. The jmID selector has no explicit removal of any part of the track. In order to separate CC and NC interactions in this class of lower energy events, three of track features used in the roID were replaced with new variables. The variable maintained from the roID is the track length, with the only alteration being that the full length of the track is considered.

The first new feature introduced in the jmID selector is the amount of energy deposited near the end of a reconstructed track. The variable computed to capture this feature is sum of the pulse height of hits at the track end, which is defined as the final five planes in the track. Muons begin to increase the amount of energy deposited per track plane near the end of the track as the momentum drops and transition out of the minimally ionizing region begins. Hadrons can have much larger energy deposits near the end of the track due to nuclear interactions, such as pion exchange. Therefore, muon signal events are expected to generally lower pulse height near the culmination of the track as compared to hadronic background events. The distribution of the track end

pulse height for both signal and background events is shown in Fig. 4.14.

The second and third new features for the jmID are derived from considering the amount of scattering that occurs along the tracks. Muons tend to traverse the detector planes without a significant amount of secondary scattering. Hadronic particles in contrast scatter more widely between planes due to the combined effects of nuclear interactions and Coulomb scattering. Additionally, false tracks may be reconstructed in the hadronic showers associated with NC events, and these false tracks tend to exhibit apparent scattering to a high degree. In order to quantify the amount of scattering along the track a Pearson coefficient is computed using the sum:

$$\rho = \frac{1}{N} \frac{\sum_i^N x_i z_i}{\sigma_x \sigma_z} \tag{4.3}$$

where x_i and z_i identify the x and z position of each of the N number of track hits and σ_x and σ_z are the standard deviation of the distribution of x and z track hits. Using the Pearson coefficient, the scattering variable used in the kNN algorithm is given by

$$P = \frac{0.01}{1.01 - \rho} \tag{4.4}$$

Muon signal tracks can generally be differentiated by smaller values in the scattering variable as compared to similar hadronic track backgrounds. The scattering variable is computed identically but separately for the U and V orientations of the scintillator planes in order to generate the two distinct additional variables in the kNN parameter space. The distributions for both

signal and background in each of the U and V plane views is shown in Fig. 4.14.

The jmID kNN parameter space is established similarly to the roID by a MC training sample and data events are subsequently evaluated. The number of nearest neighbors used for computing the jmID CC/NC separation variable (hereafter referred to as rmID) is k = 80 and was only used a part of the MINOS selection. The jmID is loses effectiveness in selecting low energy events in the MINOS+ era data as there are an insufficient number of low energy CC events observed. The distribution of the jmID is plotted in Fig. 4.15. In order to determine the value of jmID used for CC event selection, an optimization procedure was undertaken considering the changes in likelihood of a given set of given oscillations hypotheses in addition to the changes in a likelihood contour in the oscillations parameter space for differing jmID values. The maximum sensitivity to the oscillation parameters was achieved for a requirement of jmID > 0.5 in logical union with the previously stated roID cut.

4.4 Efficiency and Purity of Selection

The two figures-of-merit (FOMs) used to determine the efficacy of the CC and NC selections are efficiency and purity. The efficiency and purity are evaluated using the selection of MC samples since the truth information is known regardless of the determinations of the selection methods, which is clearly impossible for data. As can be noted in the mathematical expressions

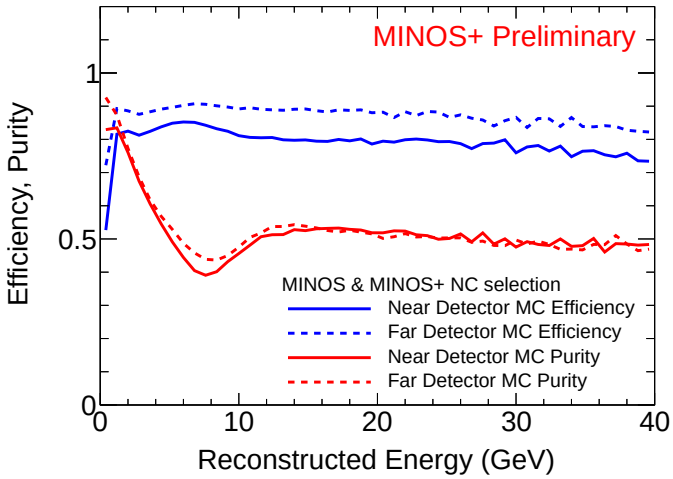

Figure 4.16: Efficiency (blue) and purity (red) of the NC selected sample as a function of the reconstructed energy. The ND distributions are plotted with solid lines, while the FD distributions are given by the dashed lines.

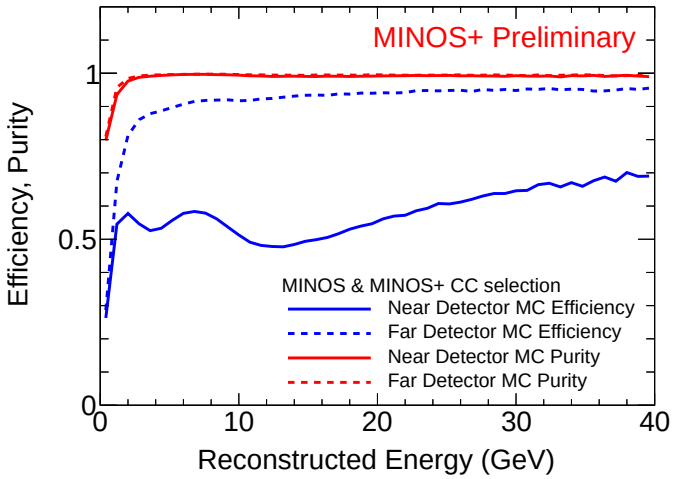

Figure 4.17: Efficiency (blue) and purity (red) of the CC selected sample as a function of the reconstructed energy. The ND distributions are plotted with solid lines, while the FD distributions are given by the dashed lines.

that will follow, the efficiency and purity are measured as fractional ratios and are thus bounded on a scale from zero to unity, with unity being considered favorable.

Efficiency is designed to give a measurement of the proportion of true signal events that pass the selection algorithm. The efficiency of a selection can be defined with the expression:

$$\text{Efficiency} = \frac{\text{Selected Signal Events}}{\text{Total True Signal Events}} \tag{4.5}$$

If the efficiency value is low, then the selection method is rejecting a large fraction of the desired events available for selection. If the quantity of events is very large, then the loss of efficiency may not be given priority if greater purity can be achieved. However, if low event counts are expected as is true for the MINOS FD, then the efficiency of a selection method must be high.

Purity is a measurement of the true signal events that have been selected in proportion to the entire selected sample including backgrounds. Therefore, the purity of the selection can be defined by the expression

$$\text{Purity} = \frac{\text{Selected Signal Events}}{\text{Total Events Selected}}, \tag{4.6}$$

which is the ratio of true positives to the sum of true and false positives. Purity is generally given the highest priority in the choice of a selection method as it can have the most direct impact on measuring and constraining model parameters. If contaminant background events that behave differently from the desired signal are present in a sample, an otherwise observable effect may be completely lost to signal-to-background noise.

Detector	Selector	Efficiency (%)	Purity (%)
ND	CC	54.2	98.8
FD	CC	86.8	99.4
ND	NC	79.7	56.7
FD	NC	87.3	60.1

Table 4.1: Integrated efficiencies and purities for the CC and NC selectors in the ND and FD.

The efficiencies and purities of the MINOS and MINOS+ combined selection methods can be seen plotted in Figs. 4.16 and 4.17 for both the ND and FD as well as the NC and CC selected samples. A summary of the integrated efficiency and purity for all samples can be found in Table 4.1. In general, high efficiency is achieved for all selections, but this FOM is greatest in the FD CC selection, which is reflective of the optimization in the MINOS design for detecting these long baseline muon neutrinos. The ND selection efficiency is reduced significantly for reconstructed neutrino energies greater than 4 GeV due to the application of the coil hole cut, which was first discussed in Section 4.3.1 when defining the CC selection fiducial volume. The motivation of this cut as discussed previously highlights the trade-off decision taken in order to improve energy resolution and related uncertainties at the expense of overall efficiency. The purity of the CC selection is very high, which is again substantially linked to detector design and optimization of performance. The NC selection has regions of less purity due to the presence of irreducible, highly-inelastic CC background events. This is particularly

exacerbated near the focusing peak of the CC events spectrum, as can be identified by the rather sharp reduction in purity at lower energies followed by a flattening of purity spectral features for increasing energies.

Chapter 5

Systematic Uncertainties

The analysis presented here handles the effects of systematic uncertainties through the use of a covariance matrix. In this chapter, we discuss the general methodology employed to compute a relative uncertainty band as a function of reconstructed energy and the subsequent procedure to create a covariance matrix with the appropriate level of correlation between bins of the energy spectrum. An overview of every source of systematic uncertainty is given, while specific attention is dedicated to systematic uncertainties reassessed, recomputed, or improved in the time since the previous MINOS sterile neutrino analysis [155]. Finally, we present the combined systematic uncertainties which are used in the simultaneous two-detector search for sterile neutrinos for both the CC and NC samples.

5.1 Methodology

Each of the sources of systematic uncertainty present in this analysis have been carefully re-evaluated from previous sterile neutrino searches conducted by MINOS, particulary with regard to the magnitudes of correlations betweeen bins of reconstructed energy. All statements in this chapter relating

to the treatment of correlations of systematic uncertainties amongst the reconstructed energy bins are based on the findings in Ref. [210]. The importance of the correlations between systematic uncertainties is expounded at length in Section 6.3.3. The effects of systematic and statistical uncertainties are assessed in the fit by the use of a covariance matrix. The method for generation of the covariance matrix begins with an estimation of the effect on the reconstructed energy spectra of the FD and ND of both a positive and negative one standard deviation ($\pm$ 1σ) shift in each source of systematic uncertainty. The relative uncertainty on the reconstructed energy spectrum is calculated from

$$\frac{S_{shifted}}{S_{nominal}} - 1 \tag{5.1}$$

where $S_{shifted}$ is the systematically shifted FD or ND spectra and $S_{shifted}$ is the corresponding nominal spectra. In order to construct a covariance matrix from the $\pm$ 1σ error bands, a sample of $N = 10000$ random numbers is sampled from a zero-mean unit Normal distribution. If the kth random number falls within the range [-1,1], then the interpolated uncertainty in the ith bin of reconstructed energy ϵ_{ik} is calculated from:

$$\epsilon_{ik} = \frac{1}{2}\delta_k(\delta_k - 1)\sigma_{-,i} + \frac{1}{2}\delta_k(\delta_k + 1)\sigma_{+,i} \tag{5.2}$$

where δ_k is the kth random number and $\sigma_{\pm,i}$ is the $\pm$ 1σ relative systematic shift in the ith bin of reconstructed energy. If the sampled random number δ_k is outside the range [-1,1] then the interpolated uncertainty is given by:

$$\epsilon_{ik} = \delta_k \sigma_{\pm,i} \tag{5.3}$$

where $\sigma_{+,i}$ is used for $\delta_k > 1$ and $\sigma_{-,i}$ is used for $\delta_k < 1$. The elements of the covariance matrix for the given systematic uncertainty are given by:

$$cov_{ij} = \frac{1}{N} \sum_{k=1}^{N} \epsilon_{ik} \times \epsilon_{jk} \tag{5.4}$$

The general structure of the systematics matrices is four quadrants corresponding to the FD covariance matrix, the ND Covariance matrix, and cross-term matrices encoding the covariance between the detectors. The matrix produced from this method encodes the relative systematic uncertainties, which necessitates rescaling the magnitude of the absolute uncertainties to the prediction at each iteration in the fit. The covariance matrix method is described in greater detail in Chapter 6.

5.2 Acceptance

The systematic uncertainty related to the mismodeling of event acceptance and efficiency of reconstruction is unique to the ND and contributes to the overall uncertainty for both CC and NC events. Though the FD and ND are functionally identical, the detectors vary significantly in terms of geometry in a number of characteristics [211]. First, the relatively small size of the ND as compared to the FD results in a higher probability for tracks to be partially contained. Second, the magnetic coil in the ND is offset from the center

of the beam spot as was discussed previously, and this results in significant magnetic field fringe effects near the edges of the fiducial volume. Finally, the spectrometer region of the ND described in Section 2.2.4 has only 1 out of every 5 planes instrumented, resulting in a factor of 4 reduction in sampling with respect to the ND calorimeter region and the FD.

We estimate the systematic uncertainty associated with the acceptance of a particular set of events by varying the fiducial volume selection cuts and comparing the variations in the energy spectra in both MC simulation and the data spectra. The acceptance uncertainty is evaluated differently from the other systematics due to the use of ND data as an estimator for the systematic shifts. In brief, the double ratio defined by

$$\frac{(data/MC)_{shifted}}{(data/MC)_{nominal}} - 1 \tag{5.5}$$

where the nominal data to MC ratio is the ratio with a standard selection cut and the shifted ratio is the ratio using a modified selection cut, is taken to be an estimate of the $+1\sigma$ and -1σ uncertainties for each bin of the predicted energy spectra. The acceptance systematic uncertainty fractional errors are shown in Fig. 5.1, and the corresponding total error and covariance matrices are shown in Fig. 5.2 for the CC sample and Fig. 5.3 for the NC sample. The selection criteria modifications studied for CC events were:

- Selecting events in either the left or right half of the fiducial volume
- Selecting events with tracks entering the coil hole region

- Excluding events with tracks ending in the 10 plane region of transition between calorimeter and spectrometer
- Tightening the fiducial volume radius from 80 cm to 60 cm
- Tightening the fiducial volume length from 4.077 m to 2.5 m
- Excluding events with tracks exiting or ending within 10 planes of the back of the detector
- Excluding events with tracks exiting the sides of the detector

For NC events, only two of the above criteria apply and some adjustment is required given the differing geometry of the fiducial volume. The selection criteria studied for the NC events were:

- Selecting events in either the left or right half of the fiducial volume
- Tightening the fiducial volume length from 4.7368 m to 2.5 m

A detailed explanation of the variations of the fiducial volume cuts for the purposes of this uncertainty estimate is found in Ref. [187]. The geometric effects considered here serve only to probe the level of mismodeling due to geometrical effects and are not a reliable statement with respect to shape variations of the spectrum. For example, given that data events are selected in both the right and left sides of the detectors, it is an impossible scenario that only events from the left or right side of the detector have been accepted

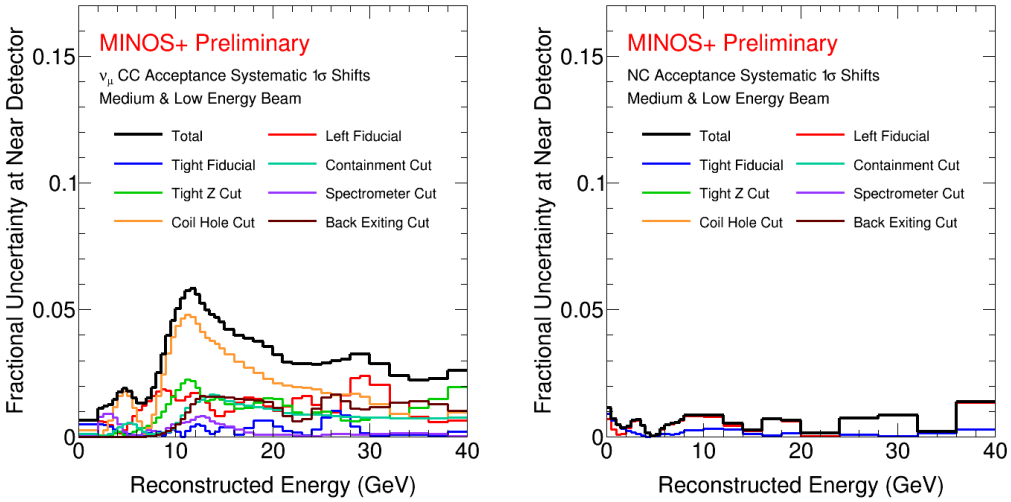

Figure 5.1: Fractional systematic uncertainties due to mismodeling of detector acceptance as a function of reconstructed energy for CC-selected events (left) and NC-selected events(right). The acceptance systematics quantify the estimated uncertainty due to geometric effects in the ND caused by a shorter baseline and smaller detector volume. The total acceptance uncertainty given by the black line is the sum in quadrature of the underlying components.

in this analysis. On the contrary, the uncertainty estimated here is similar to a statistical effect caused by a fluctuated bias to one side of the detector instead of the other. Given that the spectral shape information is not relevant to the analysis, we treat the acceptance systematic uncertainties as uncorrelated between bins of reconstructed energy.

5.3 Backgrounds

The procedure for CC and NC event selection used in this analysis was discussed in Chapter 4, resulting in selection purities of $\sim 99\%$ and $\sim 58\%$

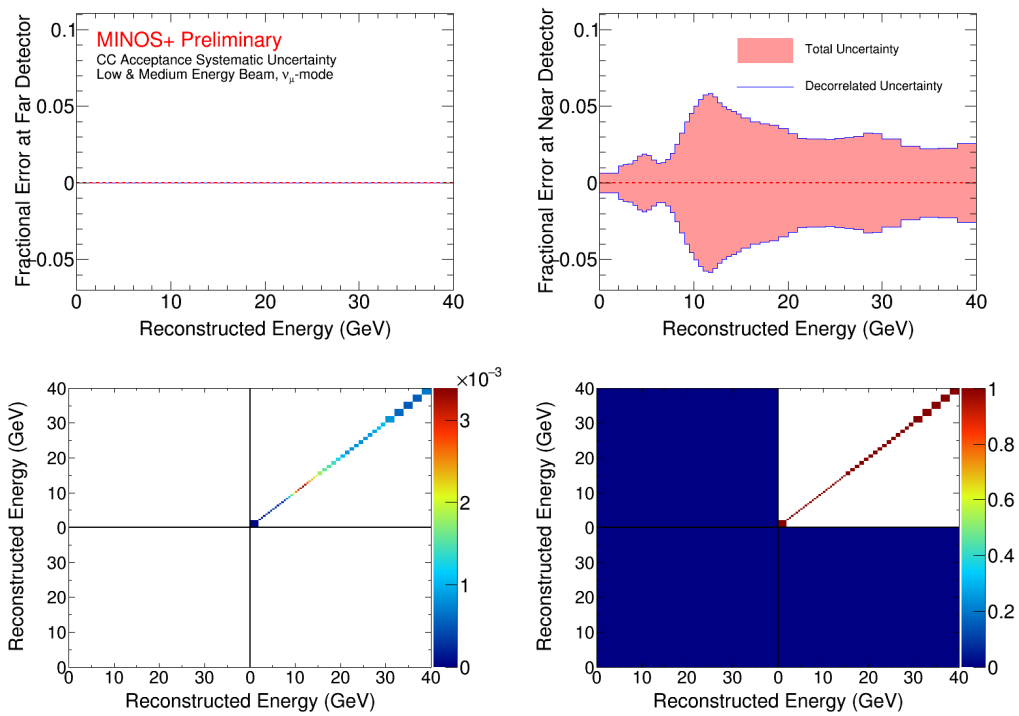

Figure 5.2: Total fractional uncertainty, covariance matrix, and correlation matrix for all acceptance systematic uncertainties in the CC sample. Top: Total of summed CC acceptance systematic uncertainties before and after decorrelation. Bottom: Summed CC acceptance covariance matrix (left) and associated correlation matrix (right).

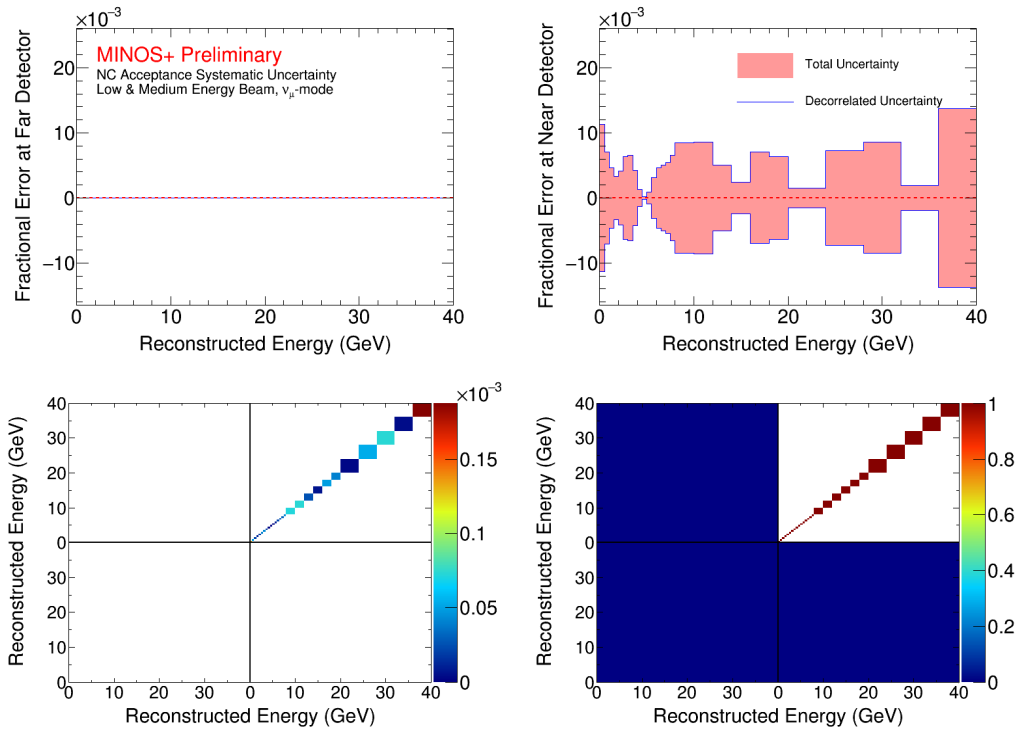

Figure 5.3: Total fractional uncertainty, covariance matrix, and correlation matrix for all acceptance systematic uncertainties in the NC sample. Top: Total of summed NC acceptance systematic uncertainties before and after decorrelation. Bottom: Summed NC acceptance covariance matrix (left) and associated correlation matrix (right).

for the CC and NC selections, respectively. To estimate the systematic uncertainty due to the remaining backgrounds, we generate the reconstructed energy spectra under the assumption of increased or decreased number of background events in order to capture the $\pm$ 1σ error bands. The background systematic uncertainty fractional errors are shown in Fig. 5.4, and the corresponding total error and covariance matrices are shown in Fig. 5.5 for the CC sample and Fig. 5.6 for the NC sample.

For the CC-selected event sample, the effects of the NC backgrounds were quantified by taking the quadrature sum of errors arising from two methods. The first method utilized muon-removed charged-current events (MRCC) as an independent proxy for the hadronic showers and found a discrepancy of 15% between data and MC [212]. The second method involved the independent scaling of the CC and NC components of the ND PID spectra, while taking into account potential ND oscillations, which found that the best agreement between data and MC required a 11% [212] and 24.4% [187] shift for MINOS and MINOS+ respectively. The total + 1σ error band is thus defined as an increase in the NC background events by 20% in the case of the MINOS era data and 30% for the MINOS+ era data.

In the NC-selected event sample, the variation in the CC background was estimated by modeling a series of alternate beam configurations, which captures potential spectral distortions arising from differing CC and NC cross sections. The result is the increase in background events by 15% for both the MINOS and MINOS+ eras in order to define the specra with a + 1σ shift

[213].

The background energy spectrum of either CC or NC events has a well-defined shape. Given that the systematic shifts applied to these backgrounds result in the uniform scaling of the background spectra, the variations in the spectra of each sample carry meaningful shape features that must be treated as fully correlated between reconstructed energy bins.

5.4 Energy Scale

The systematic uncertainties relating to energy scales are designed to capture the uncertainty in the reconstruction and calibration of both hadronic showers and muon tracks. As discussed in Chapter 4, muon tracks are only reconstructed for CC events, which implies that track energy uncertainties are only considered for the CC sample. The track energy can either be computed from the range or curvature of the track and each approach carries a differing degree of systematic uncertainty. The muon track energy is varied $\pm$ 2% if the track energy was computed using the track range, which is estimated by propagating errors from MC simulation of the detector and particle flight to the track energy measurement. If instead the track energy is computed using track curvature a variation of $\pm$ 3% is used [214]. This uncertainty is larger because it includes the same simulation uncertainties as in the case of a range calculation combined with an additional level of uncertainty due to discrepancies found in a study of individual tracks between the range and curvature energy measurements. Both of the systematic uncertainties affect

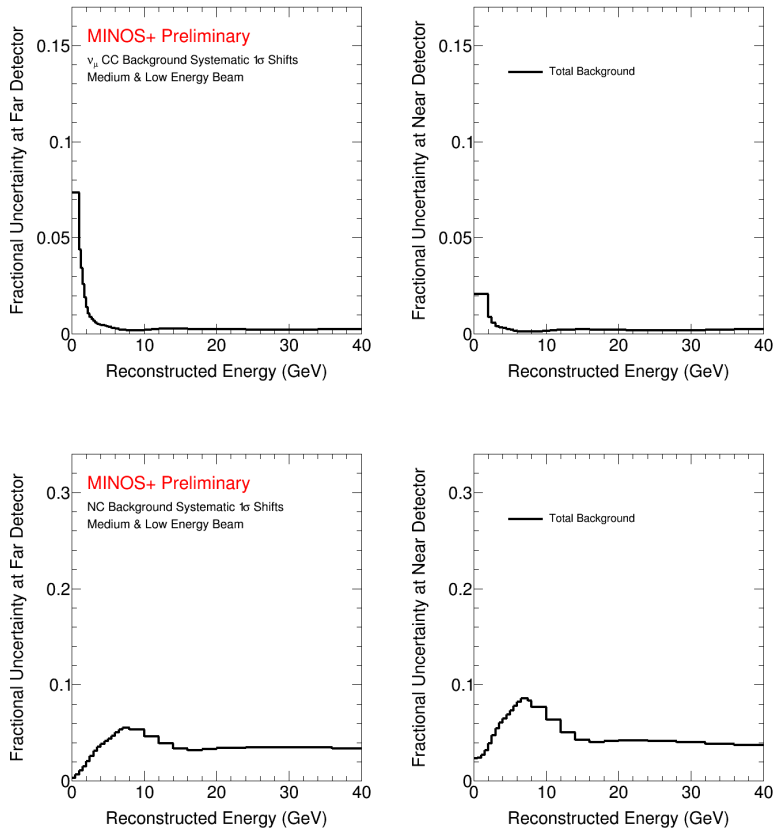

Figure 5.4: Fractional systematic uncertainties due to mismodeling of background events as a function of reconstructed energy for CC-selected events (top) and NC-selected events (bottom) at the FD (left) and ND (right). The background systematics quantify the estimated uncertainty due to the spectral distortions caused by variations in the proportion of selected background events. The total background uncertainty refers to NC events selected in the CC sample or conversely CC events selected in the NC sample.

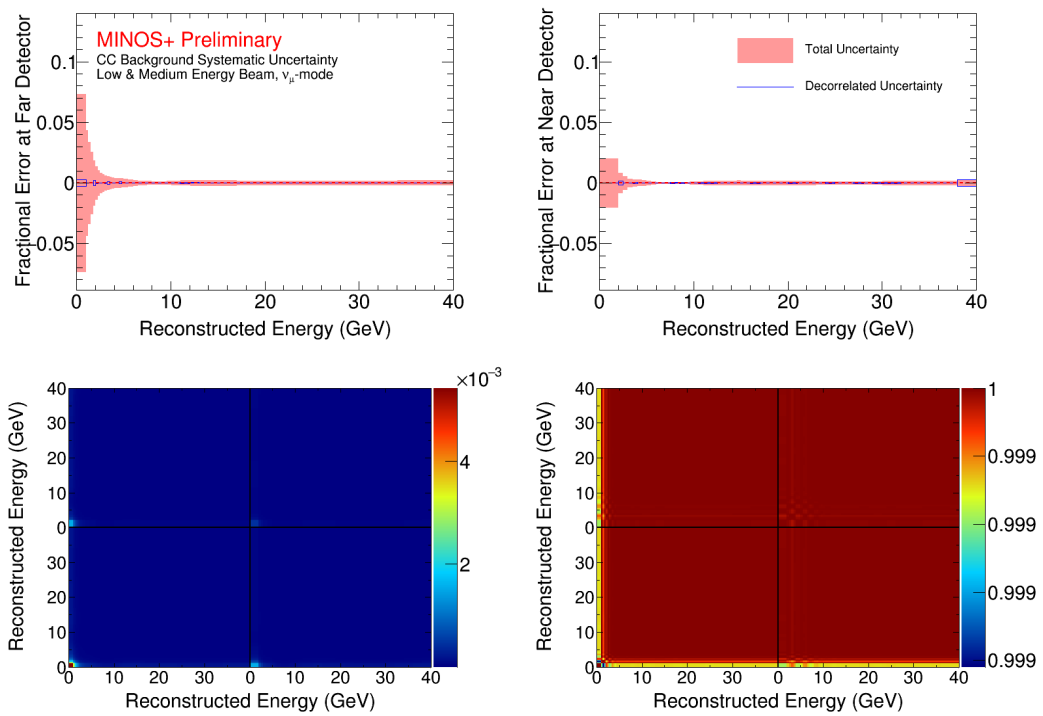

Figure 5.5: Total fractional uncertainty, covariance matrix, and correlation matrix for NC background systematic uncertainty in the CC sample. Top: NC background systematic uncertainty before and after decorrelation. Bottom: NC background covariance matrix (left) and associated correlation matrix (right).

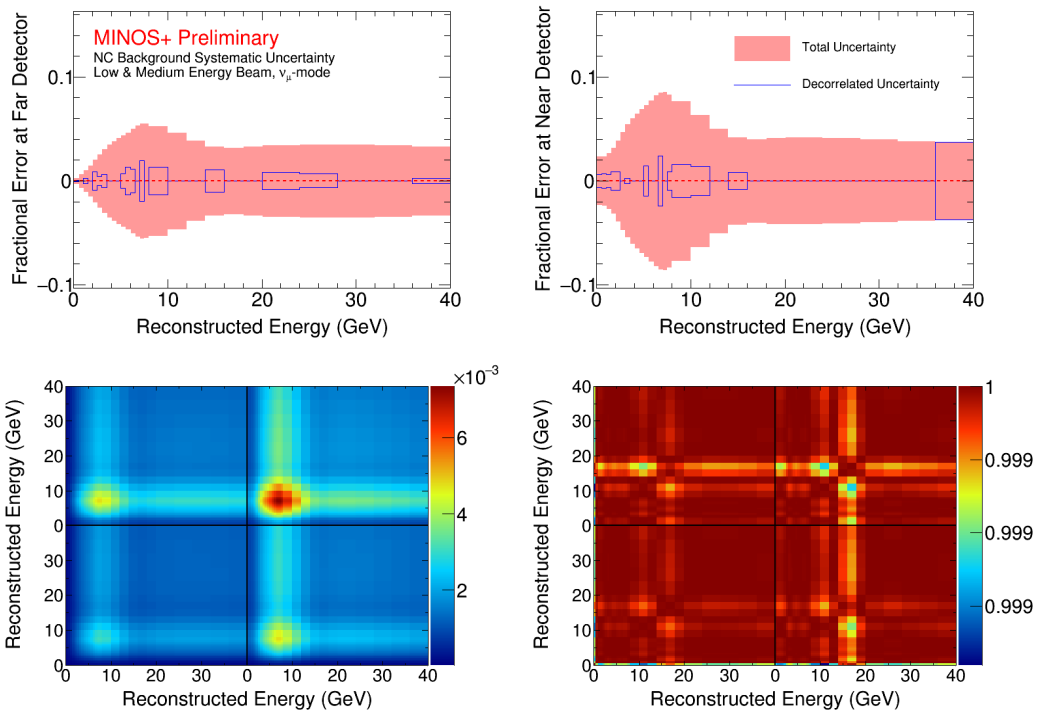

Figure 5.6: Total fractional uncertainty, covariance matrix, and correlation matrix for CC background systematic uncertainty in the NC sample. Top: CC background systematic uncertainty before and after decorrelation. Bottom: CC background covariance matrix (left) and associated correlation matrix (right).

the event distribution as a function of energy and therefore have energy bin-to-bin correlations, which are included in the covariance matrix.

Hadronic showers are present in both CC and NC events, which results in similar calculations to determine the systematic uncertainties. The hadronic shower energy scale uncertainty can be divided into two sources, namely calibration uncertainties and modeling errors. The calibration uncertainties are estimated from the response from pions in the CalDet test beam, which resulted in a shift of $\pm$ 5.7% in the reconstructed hadronic shower energy [215]. An additional relative calibration uncertainty due to differences in the response of the FD and ND is assessed in the calibration procedure described in Chapter 3, and this gives estimated uncertainties of $\pm$ 1.9% and $\pm$ 0.9% for the ND and FD, respectively [184]. Since any function of energy encodes spectral shape information, the calibration systematics are treated as correlated between bins of reconstructed energy.

The remaining energy dependent uncertainty in the hadronic shower reconstruction comes in the form of varied model parameters in the INTRANUKE, which is a computational tool used to simulate the scattering processes undergone by hadrons produced in neutrino interactions as they propagate through the surrounding nuclear material [216]. The shower energy response from the INTRANUKE simulation was determined for the following variations:

- Cross section of pions
- Cross section of nucleons

- Branching ratios for pion producing processes
- Rate of secondary pion production from pions and nucleons
- Cross section for pion absorption
- Cross section for nucleon absorption
- Formation time for liberated hadrons

A descriptive listing of the alterations to the INTRANUKE parameters is given in Ref. [187]. The effects of each of the parameter variations on the shower energy was added in quadrature [217], and the result was approximated using an exponentially decaying function with maximum value of 3.5% for low-energy hadronic showers [218]. This approximated uncertainty band estimates the total variation due to a set of underlying parameters, which lack well-defined correlations. As a result, this systematic uncertainty is treated as uncorrelated amongst reconstructed energy bins. The energy scale systematic uncertainty fractional errors are shown in Fig. 5.7, and the corresponding total error and covariance matrices are shown in Fig. 5.8 for the CC sample and Fig. 5.9 for the NC sample.

5.5 Hadron production

As discussed in Section 6.2, a beam fit mechanism was used in the context of MINOS three-flavor analyses in order to modify the hadronic phase space of the MC prediction in order to improve data/MC agreement in the

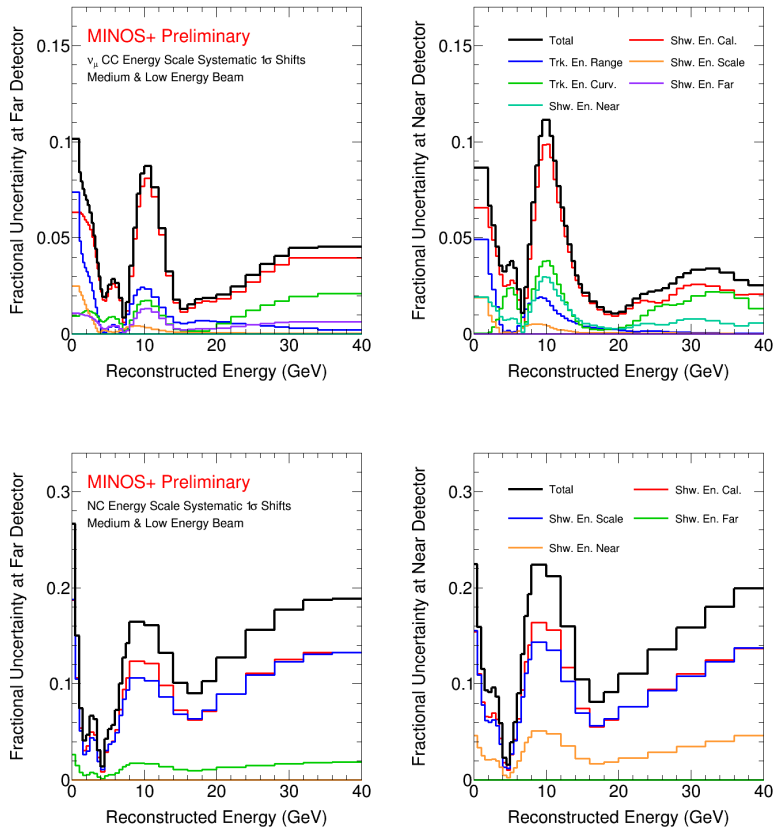

Figure 5.7: Fractional systematic uncertainties due to mismodeling of energy reconstruction and calibration as a function of reconstructed energy for CC-selected events (top) and NC-selected events (bottom) at the FD (left) and ND (right). The energy scale systematics quantify the estimated uncertainty arising from errors and mismodeling in determing the energy deposited by both muon tracks and hadronic showers in the detectors. The total energy scale uncertainty given by the black line is the sum in quadrature of the underlying components.

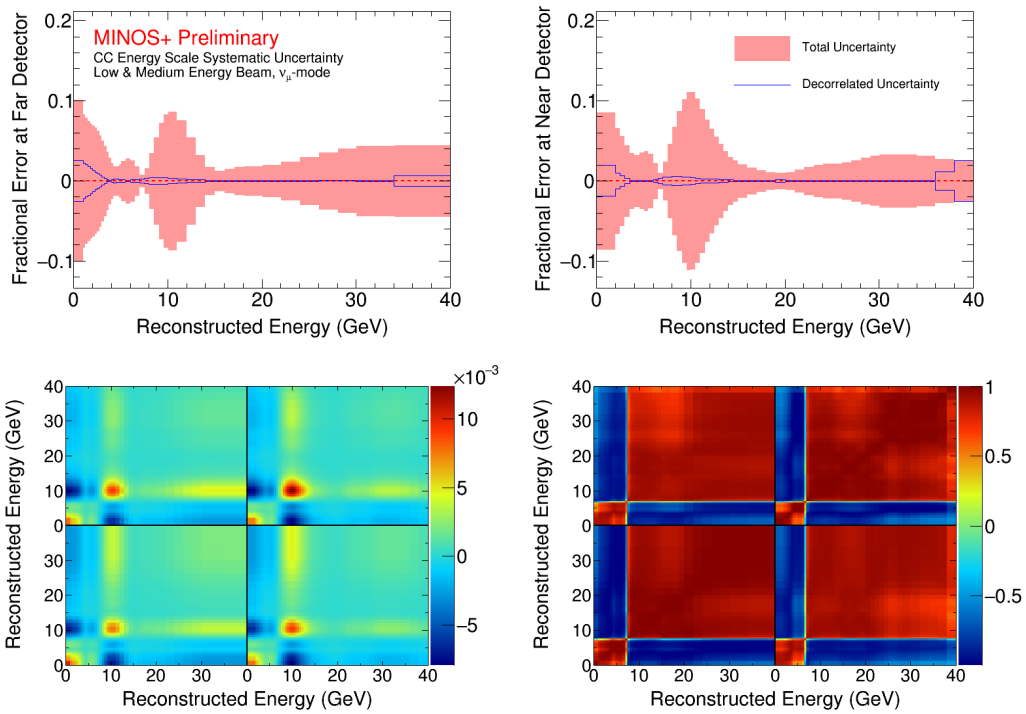

Figure 5.8: Total fractional uncertainty, covariance matrix, and correlation matrix for energy scale systematic uncertainties in the CC sample. Top: Total of summed CC energy scale systematic uncertainties before and after decorrelation. Bottom: Summed CC energy scale covariance matrix (left) and associated correlation matrix (right).

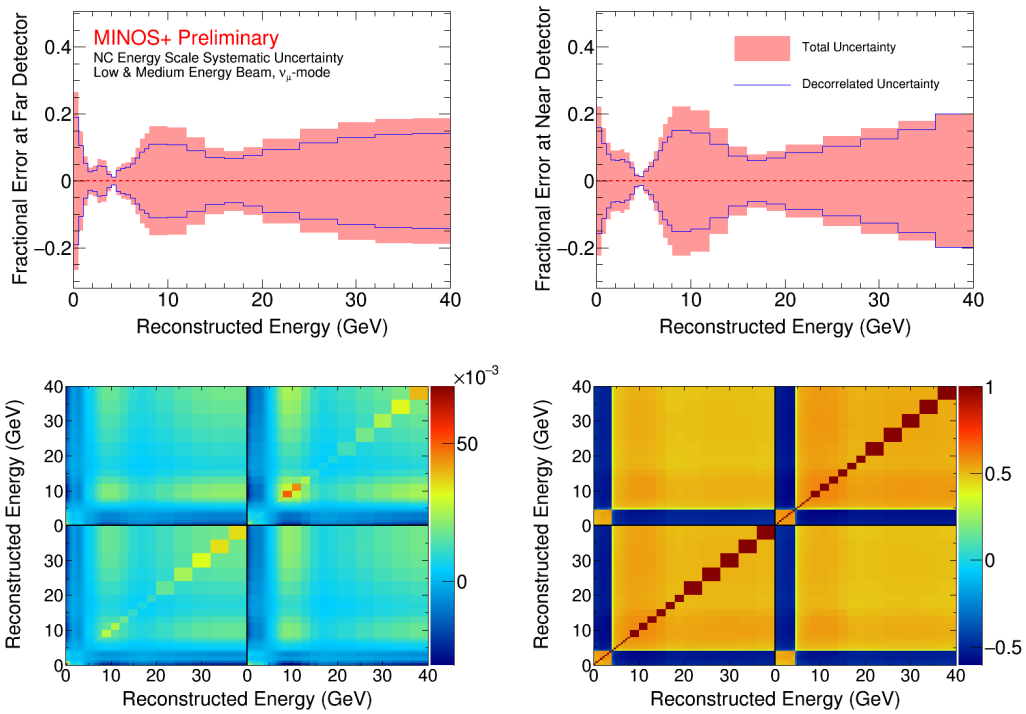

Figure 5.9: Total fractional uncertainty, covariance matrix, and correlation matrix for energy scale systematic uncertainties in the NC sample. Top: Total of summed NC energy scale systematic uncertainty before and after decorrelation. Bottom: Summed NC energy scale covariance matrix (left) and associated correlation matrix (right).

reconstructed energy spectrum. The systematic shifts determined by this beam fit could then be propagated through the simulation of the FD in order to arrive at the most accurate possible prediction. It is clear that the beam fit is contraindicated when disagreement between data and simulation in the ND may be attributable to some oscillation phenomenon, as is the case in a search for sterile neutrinos of unknown mass scale, which is discussed in detail in Chapter 6.

The most recent MINOS simulation of the neutrino flux in the NuMI beamline was discussed in Chapter 3. The phase space of the parent hadrons produced in the target can be described using the kinematic parameters transverse momentum (p_T) and the longitudinal momentum (p_Z). An initial fit using the BMPT parameterization to the raw FLUKA simulation permits the determination of the effective functional form of the flux prediction in the p_Z-p_T phase space, and the beam fit is then carried out through a set of warping parameters which modify the effective BMPT curves as a function of p_Z. The result of this fit mechanism is the modification of the spectrum of neutrino events as a function of reconstructed neutrino energy based upon the underlying kinematic distribution of parent hadrons. It has been shown in previous studies that the ratio of π^+/K^+ hadron production in the p_Z-pT phase space in the FLUKA simulation is well-tuned to data observations [219] as can be observed in Figure 5.10. Using this information, identical weights are used for π^+ and K^+ parent hadrons sharing identical kinematic parameters.

For the present analysis, as was outlined in Chapter 3, the new PPFX

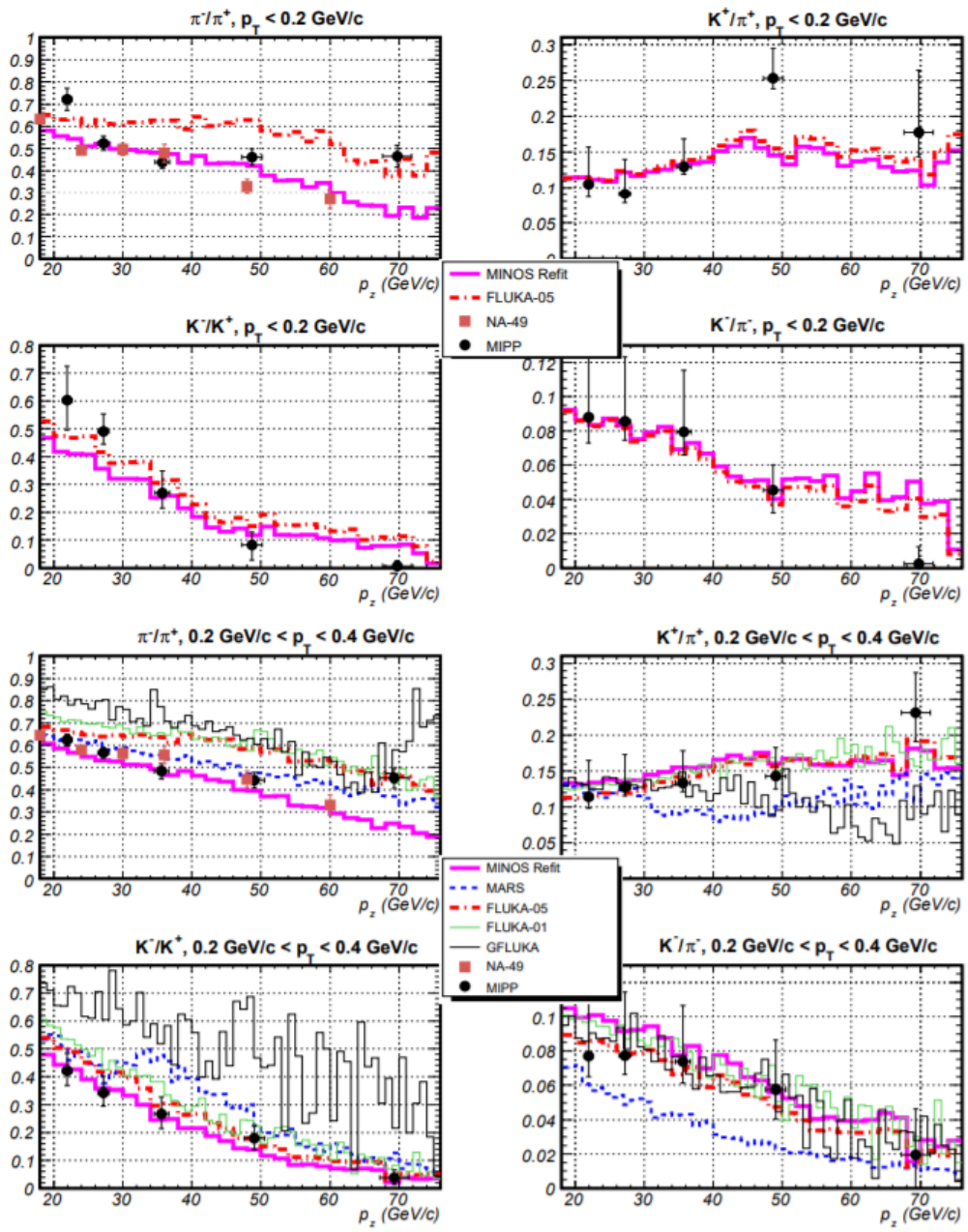

Figure 5.10: Comparison of the ratios of pions and kaons in data and FLUKA MC simulation in bins of transverse and longitudinal momentum. The right column shows the π^+/K^+ ratio, which provides justification for the use of identical weights as a function of kinematic parameters. The figure is reproduced from Ref. [219].

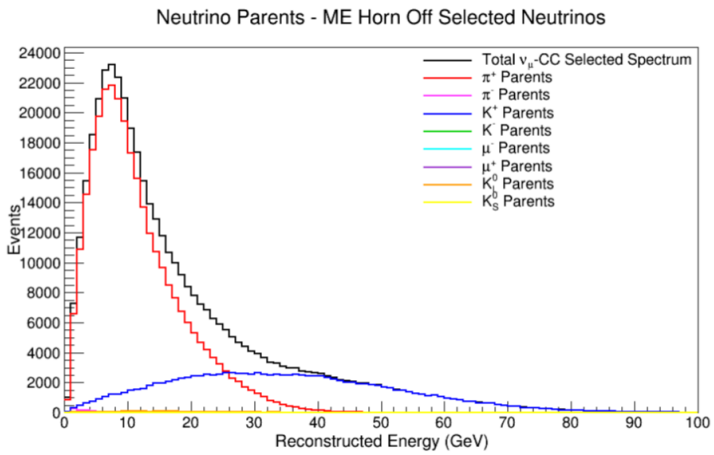

Figure 5.11: The spectrum of reconstructed ν_μ CC events decomposed by parent hadron. Pion parents are the dominant parent hadron from 0-25 GeV above which kaon parents dominate.

simulation of the flux from the NuMI beam was made available by the MINERvA experiment [221] in a form not including the ν_e scattering constraint employed in [222]. The PPFX framework derives an *a priori* flux prediction from hadron production experiments independent of the NuMI beam without the use of any data from MINERvA or MINOS/MINOS+. The new flux prediction was incorporated into the spectra generated for this analysis via the reparameterization of PPFX using a variation on the beam fit mechanism described above. The PPFX mechanism is only validated in the literature [221] [191] for neutrino energies < 20GeV, and the MINOS and MINOS+ spectra are dominated by pion parents below this threshold as is shown in Figure 5.11. Therefore, the beam fit mechanism was applied to the PPFX flux prediction for neutrinos with pion parents in both the horn-on and horn-off beam configurations in order to determine the warping parameters describing the PPFX

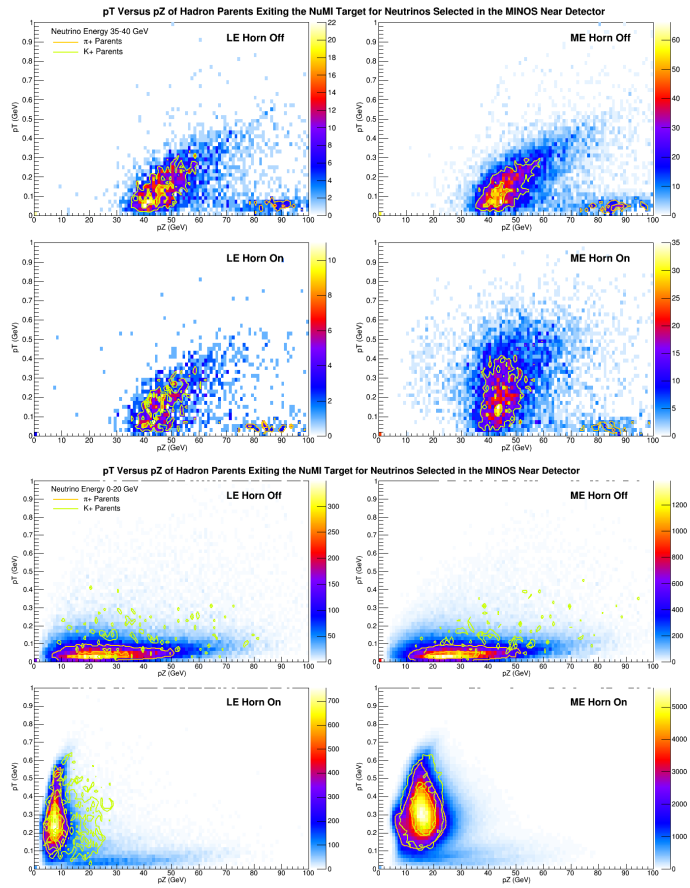

Figure 5.12: Plots showing the population of the $p_T - p_Z$ phase space by the predominantly K^+ hadron parents for the range of neutrino energies from 35-40 GeV (upper group of four) and the predominantly π^+ hadron parents for the range of neutrino energies 0-20 GeV (lower group of four). Note that phase spaces are shared only marginally, necessitating the use of an empirical parameterization [220] in order to span the disjoint samples.

modifications to the raw FLUKA prediction. For reconstructed energies ranging from 20-40 GeV contributions arising from kaon parents become significant, and the phase space populated by pion parents, which is shown in Figure 5.12, is insufficient for the BMPT parameterization to give an accurate description of the required flux modifications. In order to bridge the gap between the pion and kaon dominated regions of phase space, a new empirical parameterization [220] of the p_Z-p_T phase space was developed, which more precisely maps the contributions to the neutrino plux from hadron parents in the FLUKA simulation. This new parameterization and fit method effectively transforms the underlying neutrino flux into the de facto PPFX universes flux simulation for reconstructed energies < 20 GeV while improving data/MC agreement for the energy range 20-40 GeV independently of any neutrino oscillations data. The results of the joint-fit for the MINOS+ era are shown in Figure 5.13 and an identical fit was performed to improve the flux prediction for the MINOS era.

Given that the underlying flux simulation was novel for this analysis, the hadron production systematic uncertainty was recalculated using a method similar to the multi-universe construction employed by MINERvA [191]. In the standard application of PPFX, an ensemble of many fluxes corresponding to various "universes" is produced using a set of correlated input parameters. In order to propagate the uncertainties associated with these parameters to the MINOS and MINOS+ flux prediction, each of the PPFX multi-universes was fit according to the method described above. The ensemble of fit results

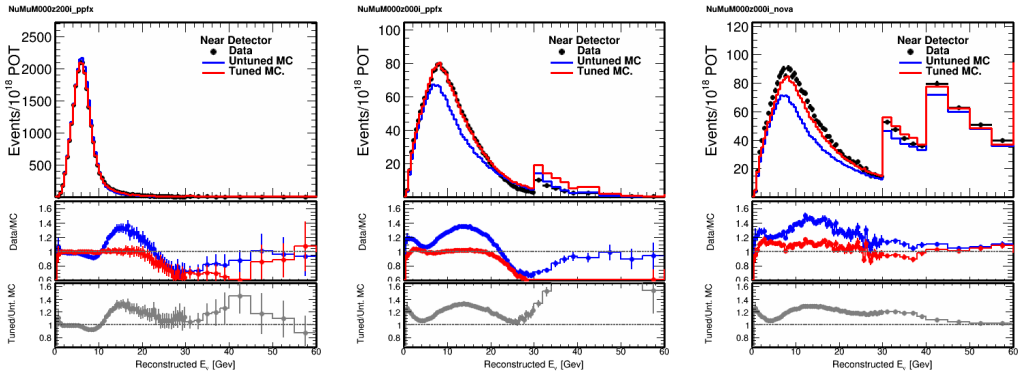

Figure 5.13: Left: Plot showing the results of MC tuning through the beam fit procedure to the predicted reconstructed energy spectra for PPFX MC simulated pions with horn focusing on (left), PPFX MC simulated pions with horn focusing off (center), and MINOS+ data collected with horn focusing off (right). The PPFX pion flux prediction is fit for reconstructed energies ranging from 0-20 GeV while the MINOS+ data in the range of 40-60 GeV in reconstructed energy is used to constrain the normalization of the fit. The parameters extracted from this beam fit reparameterize the flux predicted by PPFX and are used to correct the flux prediction used in the MINOS and MINOS+ sterile neutrino search.

permits the construction of a covariance matrix using the standard formalism

$$V_{ij} = \frac{1}{N}\sum_{\alpha}^{N}(n_{i\alpha} - \bar{n}_i)(n_{j\alpha} - \bar{n}_j) \tag{5.6}$$

where N is the number of universes simulated and i and j are indices of the ith and jth energy bins. The $\bar{n}_i$ and $\bar{n}_j$ are not necessarily equivalent to the central value weight in each bin and are instead the average over the simulated universes, which is computed from

$$\bar{n}_i = \frac{1}{N}\sum_{\alpha}^{N} n_{i\alpha} \tag{5.7}$$

The total hadron production systematic uncertainty band and covariance matrix are shown in Fig. 5.15 for the CC sample and Fig. 5.16 for the NC sample.

Although the full covariance matrix is used in the oscillation fit, to enable the visualization of the spectral information encoded by the hadron production multi-universe method the covariance matrix is decomposed into principal components by Principal Component Analysis [223]. The first five principal components, which represent nearly the total variance of the matrix, are plotted in Figure 5.14.

5.6 Beam optics

The beam optics systematics estimate the uncertainty associated with systematic biases in the focusing apparatus of the NuMI beam. Spectra of relative uncertainties for each of the beam optics categories are found in Figure 5.17 and 5.18. A total of seven sources of uncertainty are known to affect the focusing of the beam [93] [224]:

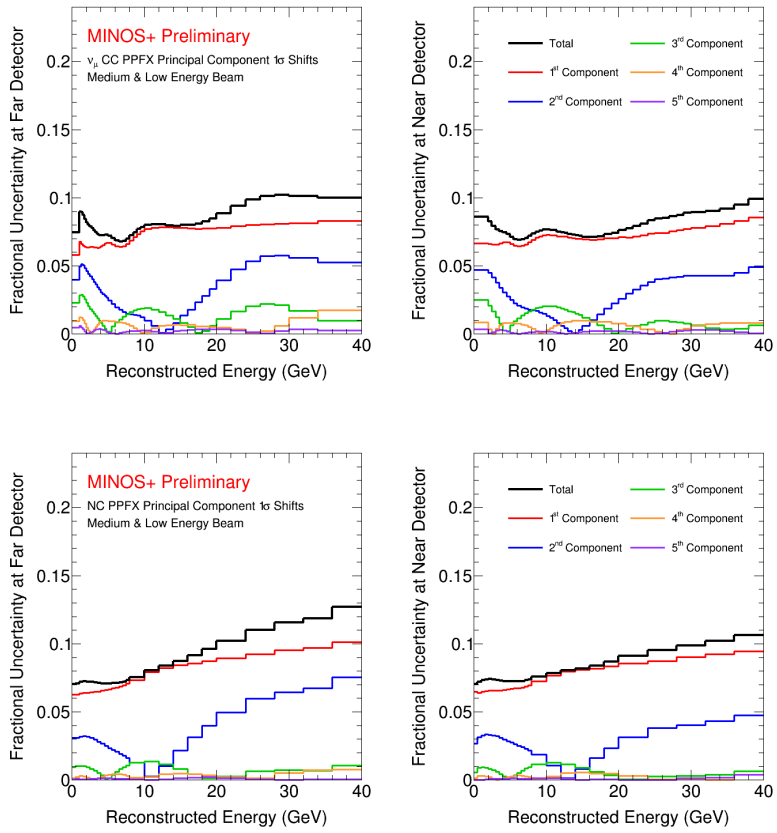

Figure 5.14: Fractional systematic uncertainties due to mismodeling of hadron production as a function of reconstructed energy for CC-selected events (top) and NC-selected events (bottom) at the FD (left) and ND (right). Hadron production uncertainties result from generating 100 alternate fluxes reweighted using the PPFX procedure with input parameters randomly varied within their uncertainty. To visualize the uncertainties, the resulting covariance matrix is decomposed into principal components representing the most important correlated sources of variation, the first five of which are plotted as fractional uncertainty bands.

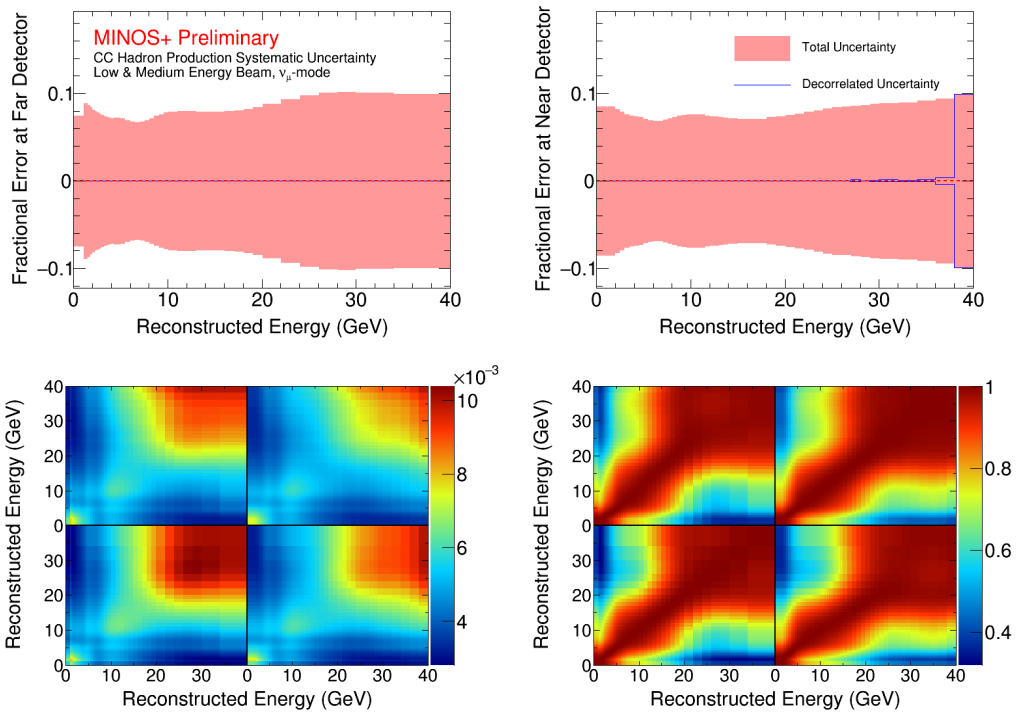

Figure 5.15: Total fractional uncertainty, covariance matrix, and correlation matrix for hadron production systematic uncertainties in the CC sample. Top: Total of summed CC hadron production systematic uncertainties before and after decorrelation. Bottom: Summed CC hadron production covariance matrix (left) and associated correlation matrix (right).

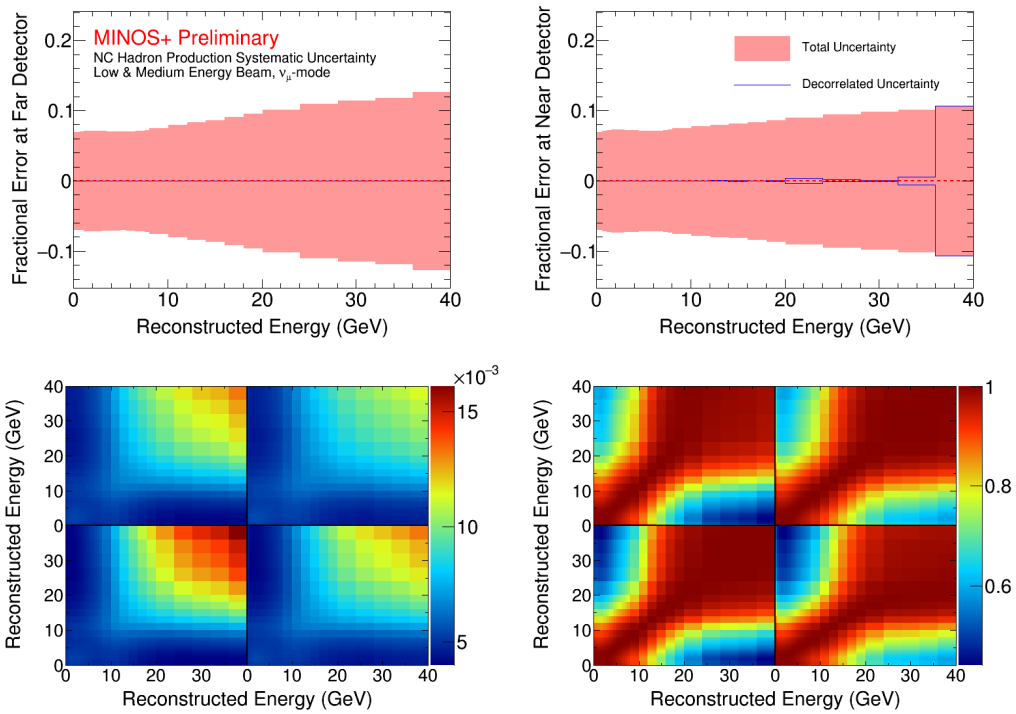

Figure 5.16: Total fractional uncertainty, covariance matrix, and correlation matrix for hadron production systematic uncertainties in the NC sample. Top: Total of summed NC hadron production systematic uncertainty before and after decorrelation. Bottom: Summed NC hadron production covariance matrix (left) and associated correlation matrix (right).

- Horn Current Miscalibration
- Horn Current Skin Depth
- Horn 1 Position Offset
- Target Position
- Material Error
- Beam Spot Position
- Beam Width

Due to thermal variations in the focusing horns during the cycle of beam incidence and the corresponding changes in electrical resistance, it is difficult to precisely determine the instantaneous current delivered to the focusing horns. The magnitude of the horn current has a direct effect on the ultimate position of the peak of the energy spectrum and is critical to the oscillations analyses [93]. Miscalibration of the horn current represents the largest individual contribution to the focusing systematic uncertainty and is computed by assuming a deviation of $\pm$ 4 kA in the delivered horn current, which had nominal values of 185 kA in the MINOS era and 200 kA for the MINOS+ era.

If the focusing horns were ideal conductors, the entirety of the current delivered during a beam spill would pass along the outer surfaces [225]. Since the horns are non-ideal conductors, the skin depth δ to which the current

can penetrate the surface of the horns must be considered. Calculation of this skin depth indicates that it is in excess of the measured thickness of ~ 3 mm for the horn conductor thickness, indicating that a model of uniform current distribution may be assumed. The uncertainty on this model choice is quantified by taking the relative difference between spectra modeled using $\delta = 6$ mm and the nominal infinite skin depth.

The modeling of the position and alignment of both the focusing horns and the production target is an additional important element in determining the position and shape of the predicted energy spectrum. The uncertainties for the horn and target positions were computed for offsets of 0.5 mm and 0.2 cm, respectively [224]. In order to estimate the possible impurities in the material composition of the focusing horns, the beam spectrum is simulated assuming the horns have the atomic number of air. The systematic uncertainty is then estimated by taking the shift $\pm$ 5% of the variation between the aluminum and air horn composition spectral simulations [165].

The final sources of uncertainty affecting the beam optics are related to the position and width of the beam spot on the target and focusing geometry. A variation in either of these parameters can lead to a significant number of protons missing the target. In order to minimize beam loss, only a single profile monitor is maintained in the beamline in order to determine the beam width, which leads to a significant increase in the uncertainty of the ultimate beam spot size. The relative uncertainties for the beam spot are computed for variations of $\pm$ 0.5 mm in the position and $\pm$ 0.2 mm in the width [224].

All beam focusing effects encode relevant spectral shape information which requires preserving the full correlations of all systematics between reconstructed energy bins. The total systematic uncertainty band and covariance matrices for the beam optics systematics are shown in Fig. 5.19 for the CC sample and Fig. 5.20 for the NC sample.

5.7 Cross Sections

Neutrino cross sections in MINOS and MINOS+ are simulated using the NEUGEN [192] event generator, which permits the estimation of cross section uncertainties by altering the NEUGEN parameter inputs. Modifications to the neutrino cross section are dependent on the neutrino energy, and are therefore correlated in bins of reconstructed energy. The axial mass parameter is used to modify both the QE interaction cross section and the resonance cross section. The QE cross section is modified by the axial mass parameter, M_A^{QE}, which was varied by +35%/-15%. The asymmetry of the range of variation is designed to encapsulate both the random phase approximation (RPA) effect [226], which is caused by charge screening within the nucleus, and 2p2h processes wherein neutrinos scatter with correlated nucleon pairs instead of individual nucleons [227]. The resonance cross section is modified by the axial mass parameter M_A^{Res} varied by +25%/-15%. The resonance cross section uncertainty has reduced asymmetry as only the RPA effect applies in this case.

As discussed in Section 2.3, neutrino interactions with energies $\sim$ 2-10 GeV are predominantly resonant or DIS interactions. The transition region in

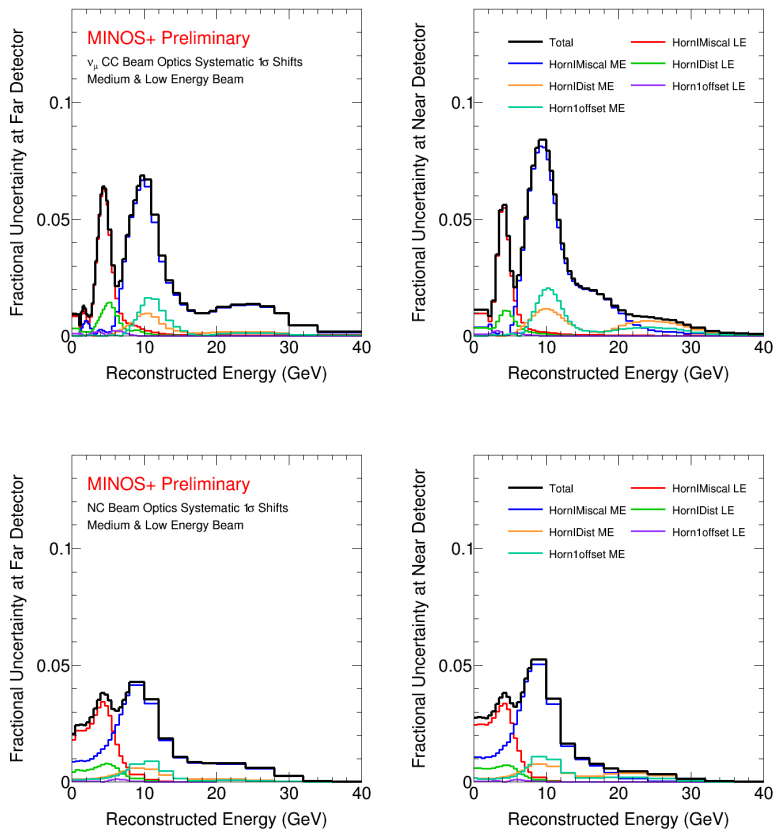

Figure 5.17: Fractional systematic uncertainties due to mismodeling of the magnetic field of the horns as a function of reconstructed energy for CC-selected events (top) and NC-selected events (bottom) at the FD (left) and ND (right). The sources of systematic uncertainty directly related to the magnetic horns include the position of the horns, the skin depth of the current flowing through the horns, and the magnitude of the current delivered during each beam spill. The total uncertainty given by the black line is the sum in quadrature of the underlying components.

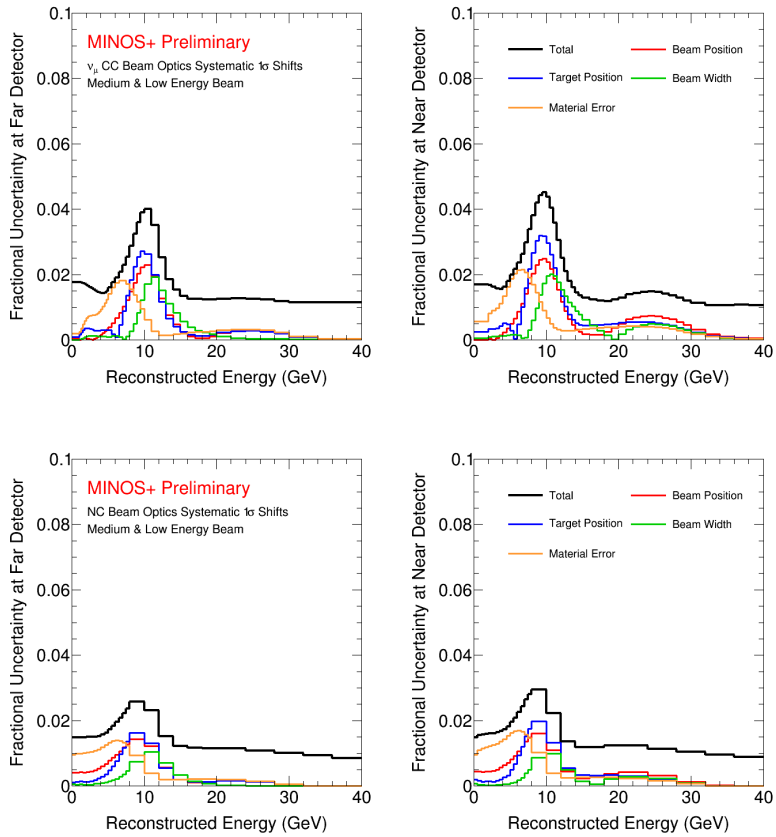

Figure 5.18: Fractional systematic uncertainties due to mismodeling of the beam optics apart from the magnetic horns as a function of reconstructed energy for CC-selected events (top) and NC-selected events (bottom) at the FD (left) and ND (right). The beam optics uncertainties not directly related to the magnetic field in the horns are due to the beam position and width, the position of the target, and the material error in the beamline. The total uncertainty given by the black line is the sum in quadrature of the underlying components.

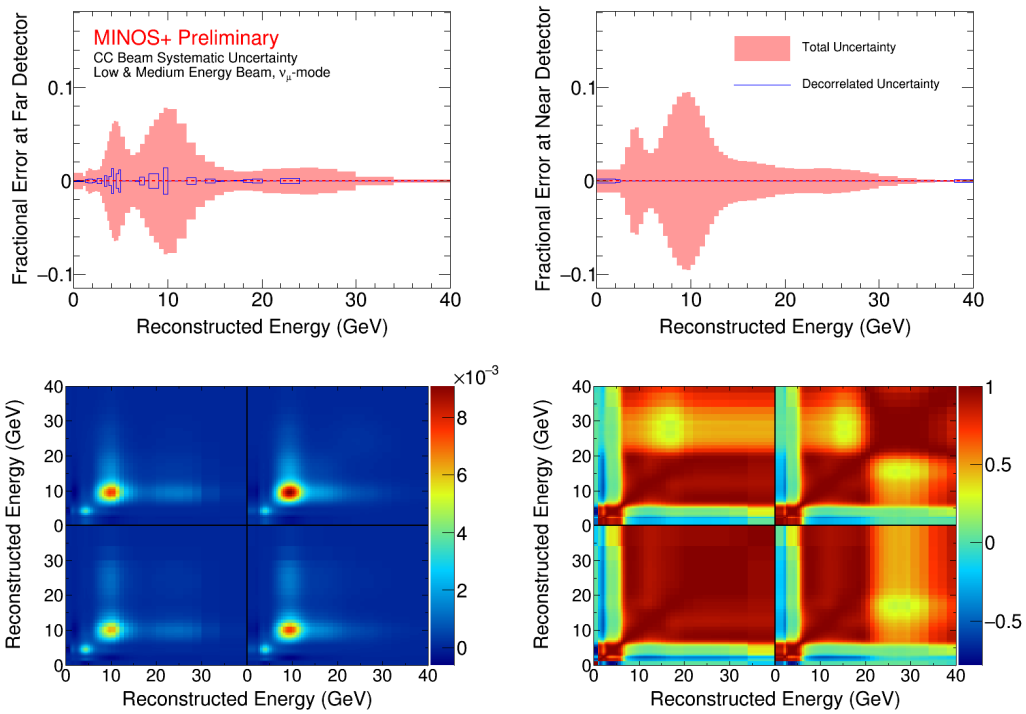

Figure 5.19: Total fractional uncertainty, covariance matrix, and correlation matrix for beam optics systematic uncertainties in the CC sample. Top: Total of summed CC beam optics systematic uncertainties before and after decorrelation. Bottom: Summed CC beam optics covariance matrix (left) and associated correlation matrix (right).

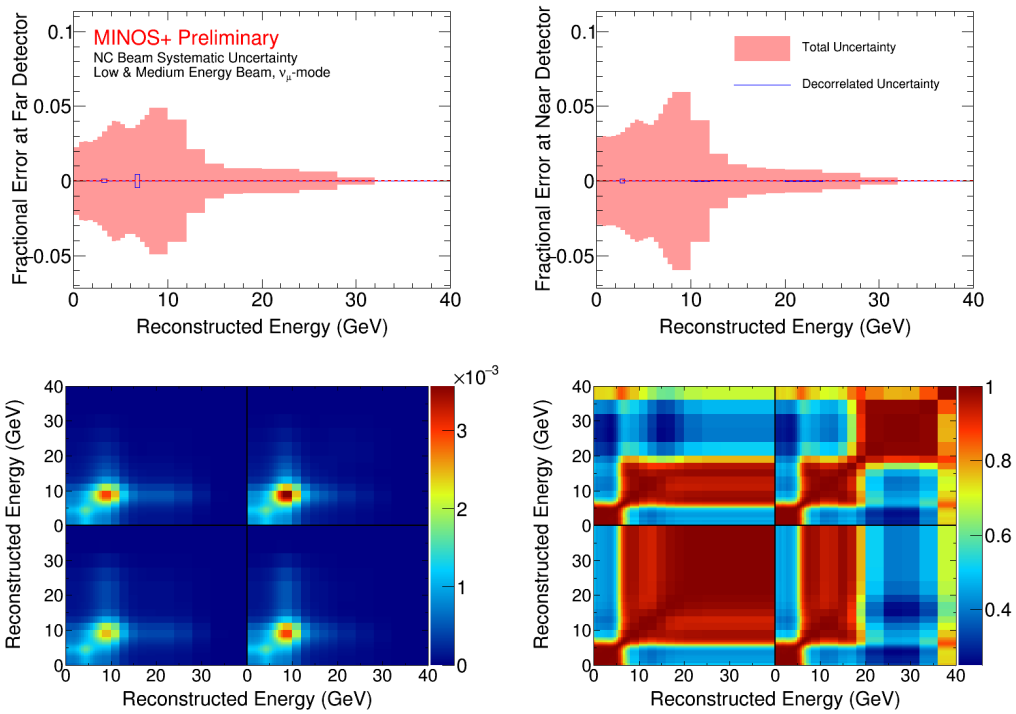

Figure 5.20: Total fractional uncertainty, covariance matrix, and correlation matrix for beam optics systematic uncertainties in the NC sample. Top: Total of summed NC beam optics systematic uncertainty before and after decorrelation. Bottom: Summed NC beam optics covariance matrix (left) and associated correlation matrix (right).

the neutrino energy spectrum between the resonant and DIS modes is modeled by KNO multiplicity parameters, r_{ijk} [198]. The parameter indices describe the characteristics of the interaction such that $i = 1, 2$ indicates the type of interaction (CC = 1, NC = 2), $j = 1, 2, 3, 4$ indicates the particles participating in the interaction ($\nu p = 1$, $\nu n = 2$, $\bar{\nu} p = 3$ $\bar{\nu} n = 4$), and k indicates the multiplicity of the final state. In order to estimate the uncertainties in modeling of hadronization, we shift r_{1j2} by ± 0.1, r_{1j3} by ± 0.2, $r_{1(3,4)2}$ by ± 0.2, and $r_{2,j,(2,3)}$ by ± 0.33 [228]. As may be noted from the indices of the KNO coefficients, the uncertainties for antineutrinos are modeled in the same manner as neutrinos for the purposes of the multiplicity uncertainty. In order to account for uncertainties in the ratio of $\sigma(\nu)/\sigma(\bar{\nu})$ an additional ± 8 % variation is applied to QE and resonance interactions. The high energy region is dominated by DIS interactions where the uncertainty is treated by an overall cross section systematic.

In the CC sample, we set an overall cross section systematic of 3.5%, which serves as a pure normalization systematic. The magnitude of the overall cross section uncertainty can be justified by high energy cross section studies. As an example, the CCFR experiment probed neutrinos and antineutrinos with energies ranging from 30 to 300 GeV, and the results reported in that study constrain the total cross section to $\pm$ 3.0% up to an otherwise linear energy dependence [229]. The baseline used in the CCFR experiment was sufficiently short that spectral shape distortions caused by sterile neutrino mediated oscillations would have been detectable for mass-splitting scales as high as 10^3 eV^2,

and since no evidence for such an oscillation behavior was observed [230], we conclude that the cross section constraint is well-founded. In the case of the NC sample, the overall cross section uncertainty was estimated to be $\pm 5\%$ as determined by the comparison of the ratio of the number of events tracks to the number without tracks in both the NOMAD and MINOS experiments [231]. For antinuetrinos, an additional 4% variation is applied to the overall cross section to cover the aformentioned potential differences between neutrino and antineutrinos cross sections. The component cross section systematic uncertainty bands are shown in Figure 5.21. The total systematic uncertainty band and covariance matrices for the cross section systematics are shown in Fig. 5.22 for the CC sample and Fig. 5.23 for the NC sample.

5.8 Normalization

Normalization systematic uncertainties estimate the degree to which mismodeling or mismeasurement of the intervals of data collection or beam and detector materials alters the observed neutrino event rate. The individual components of normalization uncertainty affecting both CC and NC samples are listed in Table 5.1 and are found in Ref. [232]. The systematic effects due to the properties of the steel and scintillator as well as the error on FD live time are treated as fully correlated between bins of reconstructed energy as the spectrum is changed uniformly over all energies by these effects. The fiducial bias estimates assigned to the ND are computed from calculating the changes to the event rate when comparing subregions of the fiducial volume divided

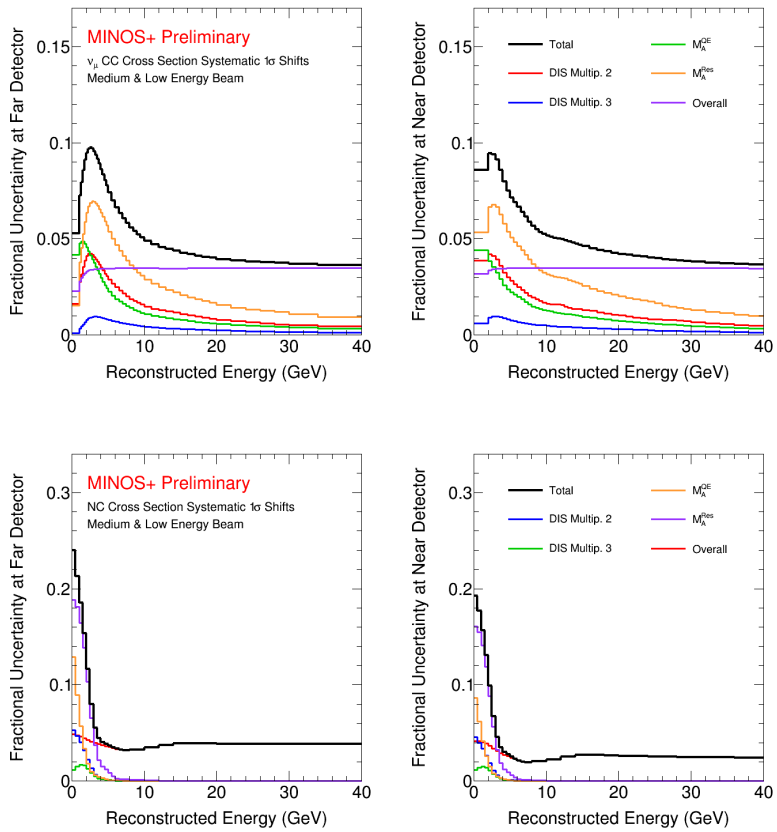

Figure 5.21: Fractional systematic uncertainties due to mismodeling of the cross sections as a function of reconstructed energy for CC-selected events (top) and NC-selected events (bottom) at the FD (left) and ND (right). Systematic uncertainties resulting from scaling M_A^{QE}, M_A^{RES}, and KNO scaling parameters can result in shape distortions in the energy spectra. The overall cross section systematic uncertainties are approximately normalization shifts (i.e. uniform with respect to reconstructed energy). The overall CC cross section systematic shift is constrained by experiments analyzing high energy neutinos such as CCFR. The overall NC cross section systematic shift is determined by comparing the rates of events with and without tracks at NOMAD and MINOS. The total uncertainty given by the black line is the sum in quadrature of the underlying components.

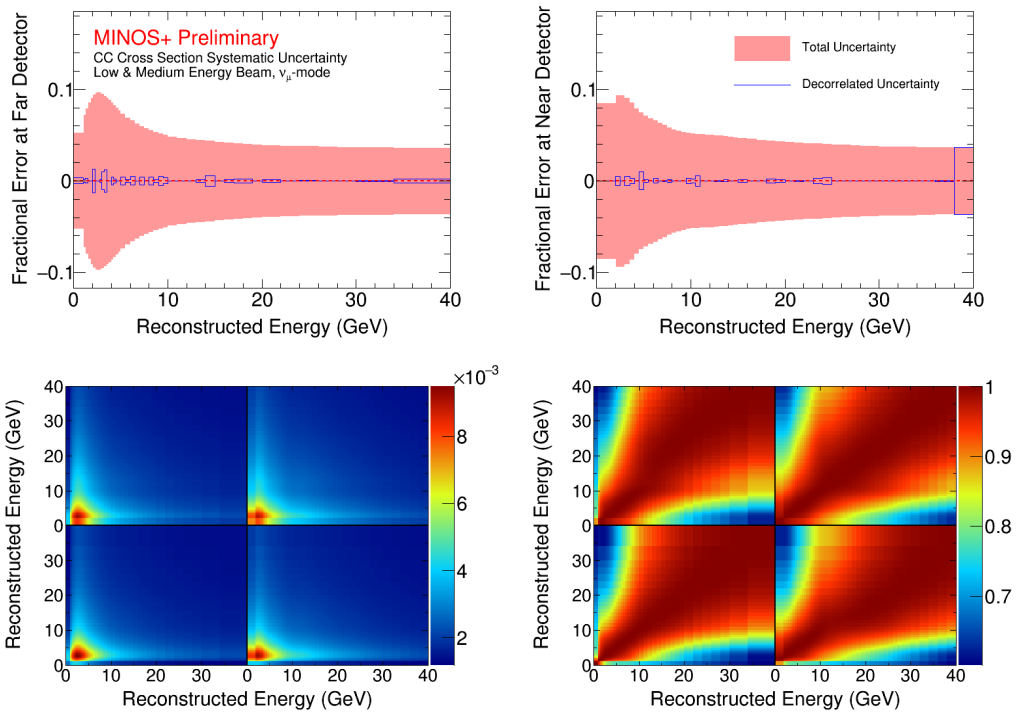

Figure 5.22: Total fractional uncertainty, covariance matrix, and correlation matrix for cross section systematic uncertainties in the CC sample. Top: Total of summed CC cross section systematic uncertainties before and after decorrelation. Bottom: Summed CC cross section covariance matrix (left) and associated correlation matrix (right).

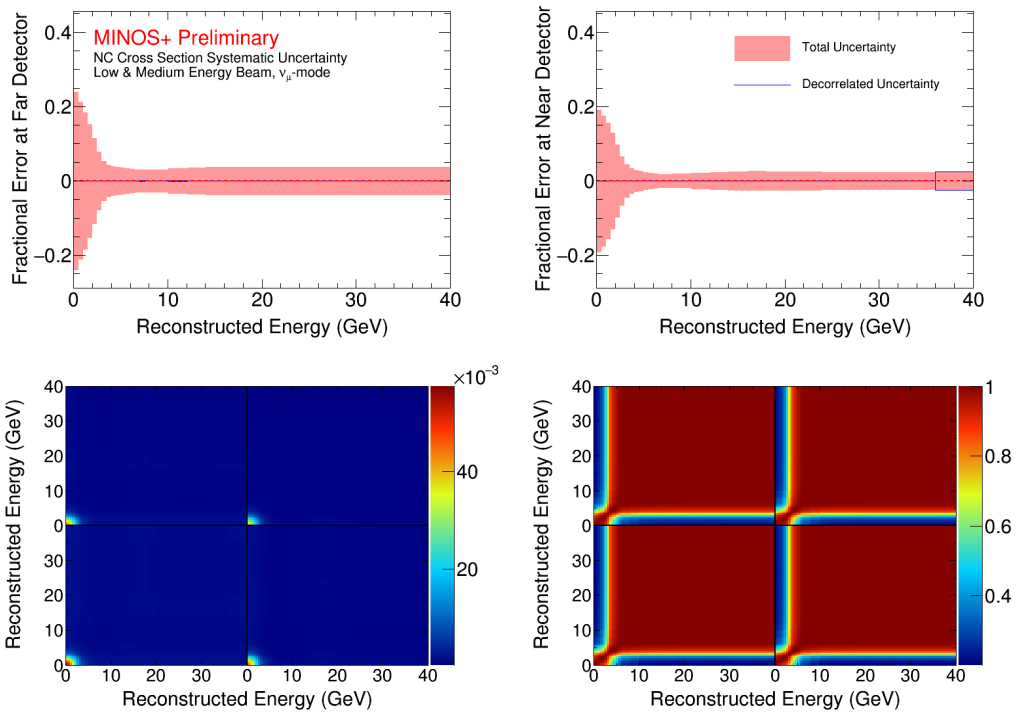

Figure 5.23: Total fractional uncertainty, covariance matrix, and correlation matrix for cross section systematic uncertainties in the NC sample. Top: Total of summed NC cross section systematic uncertainty before and after decorrelation. Bottom: Summed NC cross section covariance matrix (left) and associated correlation matrix (right).

Source	Relative Uncertainty (%)
Steel Thickness	0.2
Scintillator Thickness	0.2
FD Live Time	0.32
ND Fiducial Bias x	0.54
ND Fiducial Bias y	0.14
ND Fiducial Bias z	0.43

Table 5.1: Sources of systematic uncertainty affecting the normalization of the reconstructed energy spectra and the estimated relative size of each effect. Normalization systematic uncertainties listed here were calculated in [232].

along the detector axes, and since this requires integration over all energies, the systematics have no bin-to-bin correlations.

The bias in the event rate due to the particular constraints of the event selection method discussed in Chapter 4 were also considered independently for the CC and NC samples. For the CC sample, a hand-scan of events was performed in order to determine the relative efficiency of event selection or rejection in the ND and FD, yielding an estimation of $\pm 0.7\%$ and $\pm 1.12\%$ relative uncertainty for the ND and FD, respectively [233]. In the case of the NC sample, MRCC events were used to determine the reconstruction efficiencies for hadronic and systematic uncertainties, which were found to be $\pm 2.4\%$ and $\pm 0.4\%$ for the ND and FD, respectively [234]. The selection biases for both CC and NC samples are estimated from the integrated behavior of all neutrino energies and therefore are treated as uncorrelated between reconstructed energy bins. The total systematic uncertainty band and covariance matrices for the normalization systematics are shown in Fig. 5.24 for the CC sample and

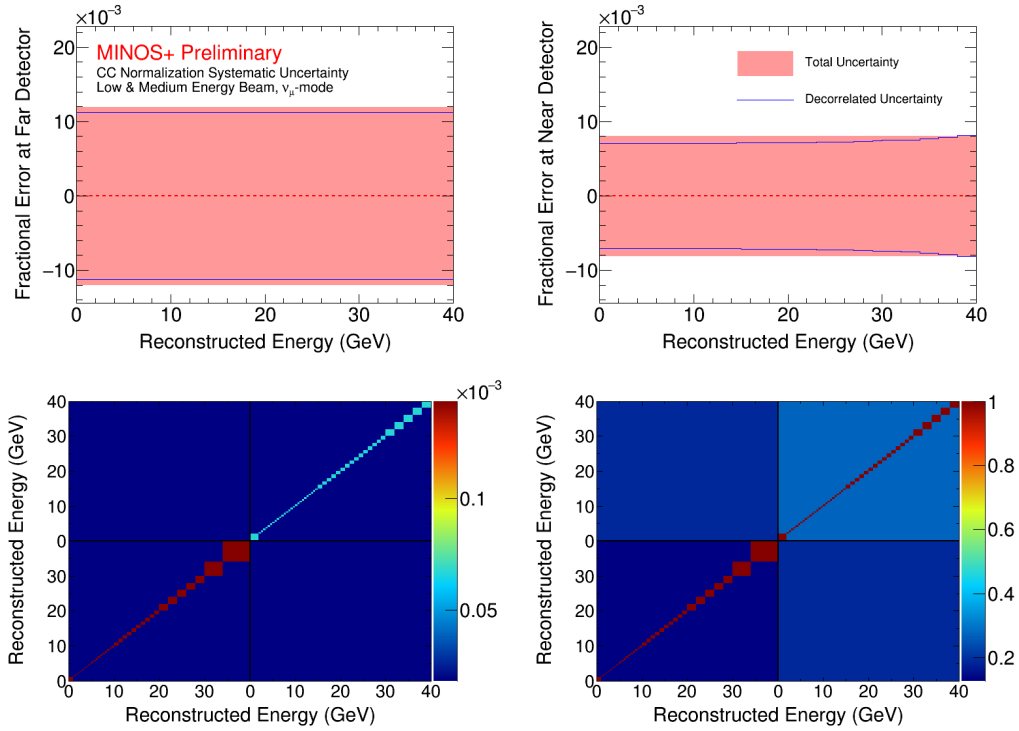

Figure 5.24: Total fractional uncertainty, covariance matrix, and correlation matrix for normalization systematic uncertainties in the CC sample. Top: Total of summed CC normalization systematic uncertainties before and after decorrelation. Bottom: Summed CC normalization covariance matrix (left) and associated correlation matrix (right).

Fig. 5.25 for the NC sample.

5.9 Neutral Current Cleaning

The NC selection procedure outlined in Chapter 4 includes additional cleaning cuts in both the FD and ND which are designed to exclude poorly-reconstructed events [187], which are those events reconstructed with less than

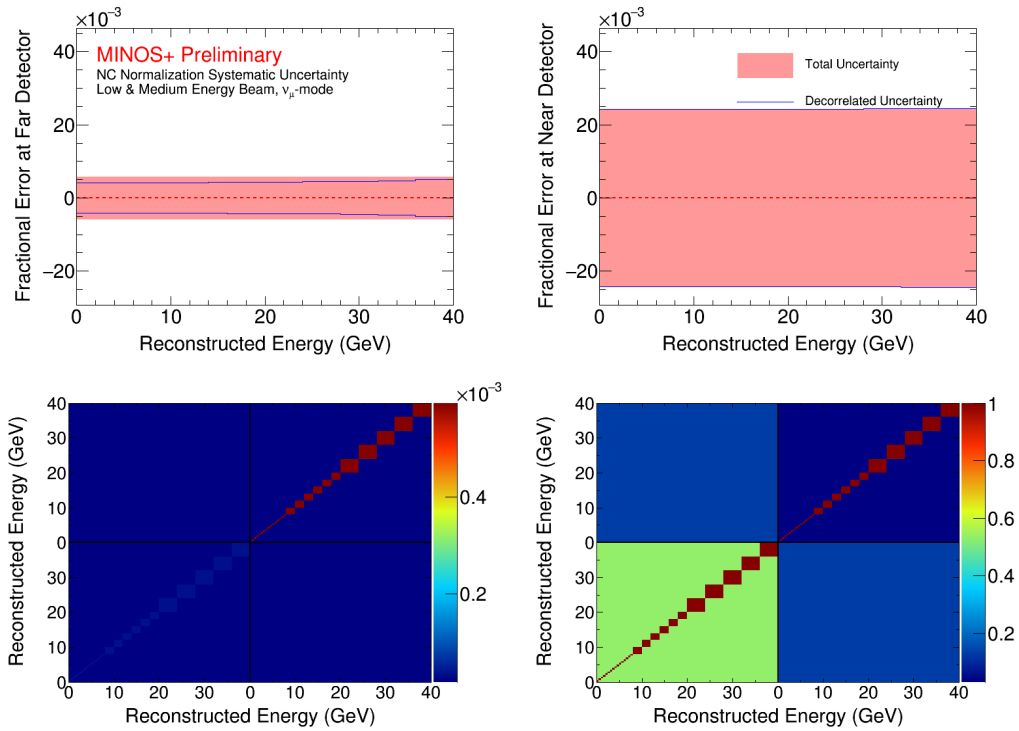

Figure 5.25: Total fractional uncertainty, covariance matrix, and correlation matrix for normalization systematic uncertainties in the NC sample. Top: Total of summed NC normalization systematic uncertainty before and after decorrelation. Bottom: Summed NC normalization covariance matrix (left) and associated correlation matrix (right).

30% of the true visible energy in MC simulation, as well as filter out detector noise at low energies and remove cosmic events [235]. As in the case of the acceptance systematic uncertainties, the introduction of a specific cut on events has the potential to introduce systematic biases in the sample. In contrast to the acceptance systematic, the cut variations used in the cleaning systematic permit the generation of a well-formed, functional energy variation permitting the perservation of bin-to-bin correlations of the uncertainty. The systematic uncertainty bands estimated from variations in the NC cleaning cuts are shown in Figure 5.26.

The FD cleaning cuts are divided into those that are intended to reduce detector noise and those which remove cosmic muon events. As a result, two distinct systematic uncertainties are considered for these sets of cuts. The specific ranges of energy and corresponding systematic shifts are detailed in Ref. [236], which is based on the study conducted in Ref. [235] wherein the position of individual cuts is shifted using an interval determined by the RMS of the underlying MC distribution. In summary, the systematic energy shift associated with FD noise cleaning cut is maximal for $E_{Reco}^{shower} \leq 0.5\ GeV$ with an estimated relative error of $\pm 4.9\%$ and is reduced exponentially to less than $\pm 1\%$ for higher energies. The systematic energy shift for the FD cosmic muon cleaning cut is maximal for $0.5 < E_{Reco}^{shower} \leq 1.0 GeV$ with a value of $\pm 2.7\%$ and similarly is exponentially reduced with increaing energy.

The systematic uncertainty associated with the ND cleaning cuts was specifically evaluated for the context of a sterile neutrino search by the con-

sideration of ND oscillations [187]. The ND cleaning cuts were varied for a series of possible sterile neutrino mixing parameters, and the largest deviations between the shifted cut, oscillated MC prediction and the nominal were used to estimate the systematic uncertainty. The uncertainty measurement was parameterized in function form as:

$$1 + \frac{0.98}{1 + (E/0.54)^2} \tag{5.8}$$

which results in very large systematic shifts at low energies with rapid decay as energy increases. The total systematic uncertainty band and covariance matrices for the NC cleaning systematics are shown in Fig. 5.27.

5.10 Combined Systematic Uncertainties

The systematic uncertainties derived from each of the sources presented in this chapter are combined into a single covariance matrix for each of the CC and NC samples in the two-detector fit. The combined matrix for each sample is constructed by summing over the relevant component covariance matrices, which is equivalent to a summation in quadrature. A simple summation over the individual systematics assumes that each source of uncertainty is independent of and uncorrelated with each of the other sources of uncertainty. This assumption is justifiable as a conservative approach since any correlations between sources of systematic uncertainty would tend to increase the resulting sensitivity to sterile oscillation parameters. The combined covariance matri-

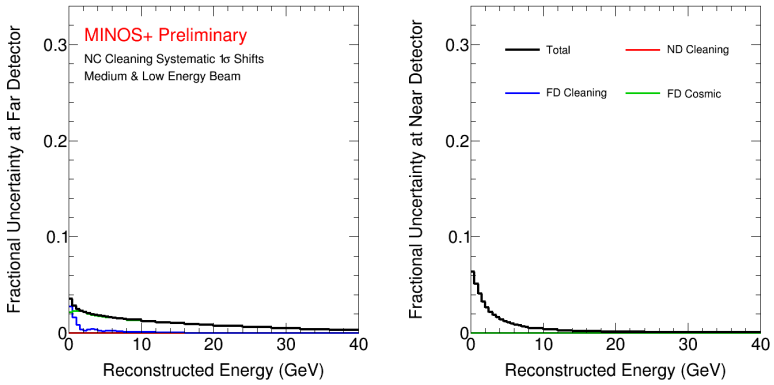

Figure 5.26: Fractional systematic uncertainties due to mismodeling of the neutral current cleaning cuts as a function of reconstructed energy for CC-selected events (top) and NC-selected events (bottom) at the FD (left) and ND (right). The systematic uncertainties are estimated for the cleaning cuts applied in the procedure for NC selection to remove poorly reconstructed events in the ND and detector noise and cosmic ray muons in the FD. The total uncertainty given by the black line is the sum in quadrature of the underlying components.

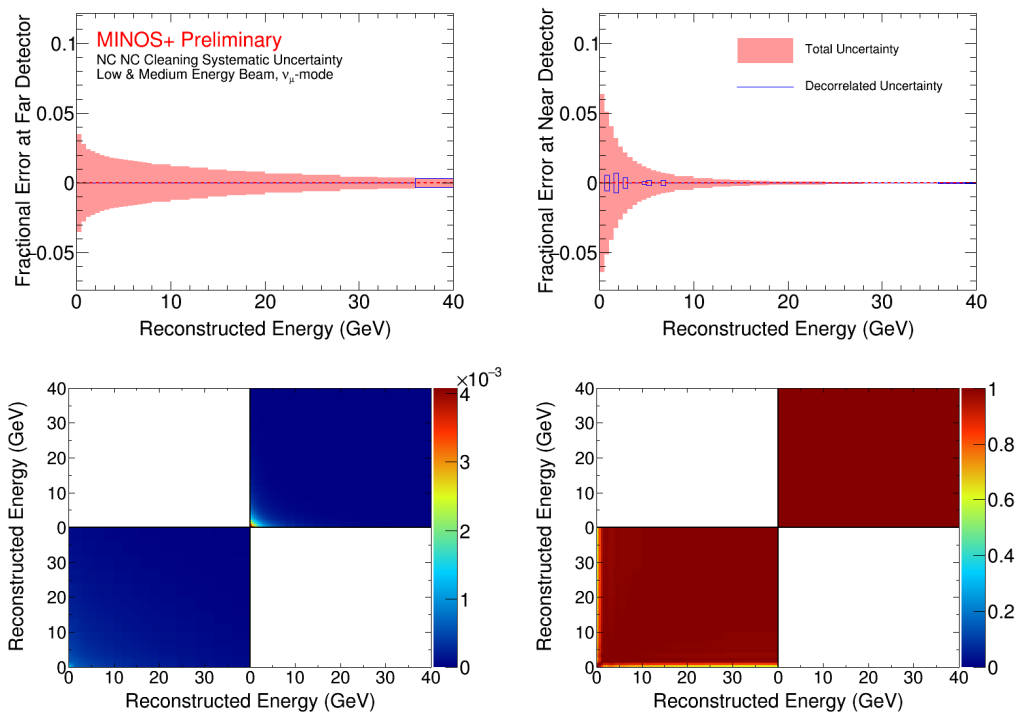

Figure 5.27: Total fractional uncertainty, covariance matrix, and correlation matrix for NC cleaning systematic uncertainties. Top: Total of summed NC cleaning systematic uncertainty before and after decorrelation. Bottom: Summed NC cleaning covariance matrix (left) and associated correlation matrix (right).

ces, which account for all systematic uncertainties considered in this analysis, are presented in Fig. 5.28 for the CC sample and Fig. 5.29 for the NC sample.

An overall error band can be extracted from the combined systematic uncertainty covariance matrix by taking the square root of the diagonal elements. This error band reflects the envelope of uncertainty under the assumption of no correlations between energy bins. In order to produce a more accurate measurement of the true magnitude of uncertainty as a function of the reconstructed energy, the decorrelation procedure described in Chapter 6 is used to quantify the cancellation effects due to bin-to-bin systematic correlations.

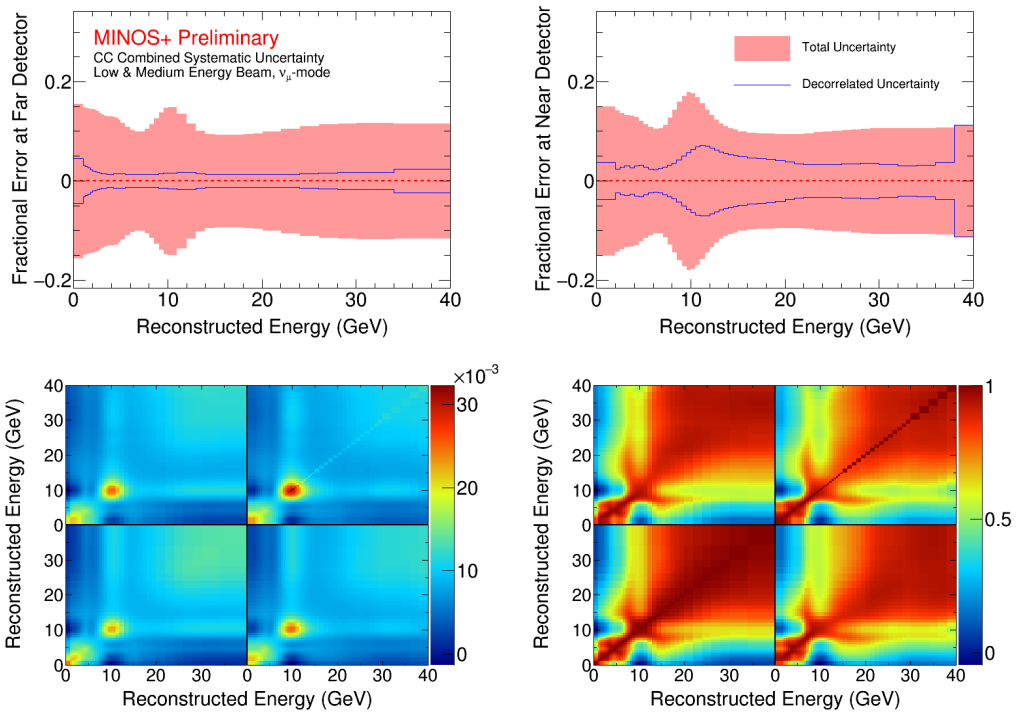

Figure 5.28: Total fractional uncertainty, covariance matrix, and correlation matrix for combination of all sources of systematic uncertainty studied for the CC sample. Top: Combined systmatic uncertainty relative error band before and after decorrelation. Bottom: The combined CC systematic uncertainty covariance matrix used in the steril neutrino search (left) and associated correlation matrix (right).

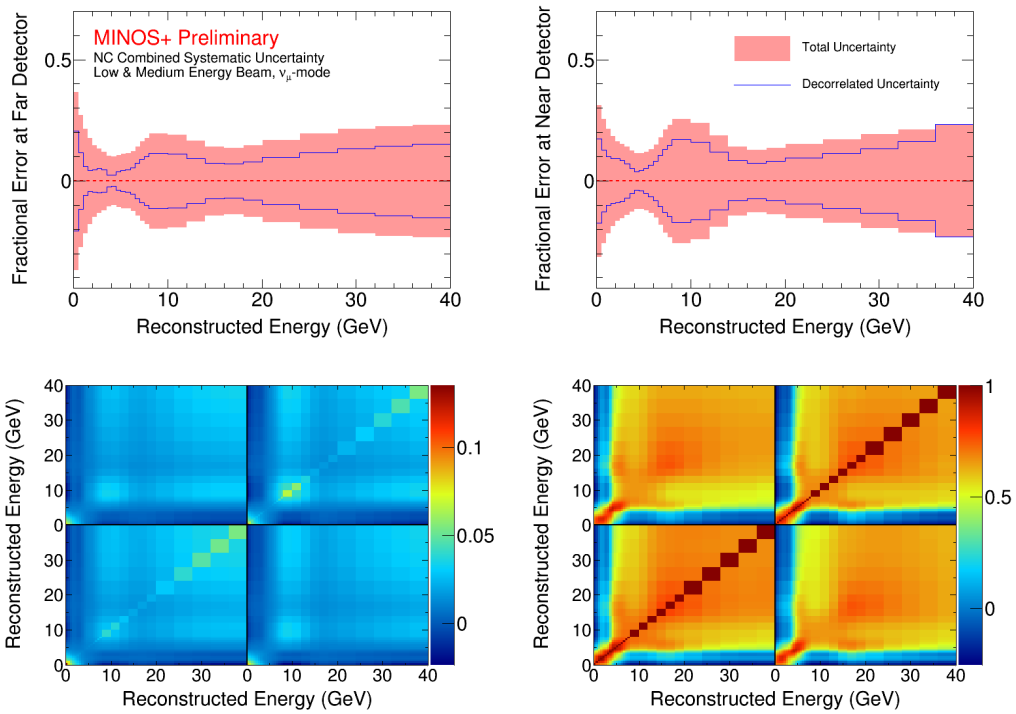

Figure 5.29: Total fractional uncertainty, covariance matrix, and correlation matrix for combination of all sources of systematic uncertainty studied for the NC sample. Top: Combined systmatic uncertainty relative error band before and after decorrelation. Bottom: The combined NC systematic uncertainty covariance matrix used in the steril neutrino search (left) and associated correlation matrix (right).

Chapter 6

Search Methodology

In this chapter, we present the methodology employed to search for sterile neutrino oscillations over a long-baseline in MINOS and MINOS+. We begin with a brief description of the phenomenology of sterile neutrino oscillations relevant for this analysis. Next, we discuss the motivation for using a simultaneous Two-Detector fit in comparison to previous methods. We then describe the strategy and mechanics of the fit with special consideration for the treatement of systematics via covariance matrices. The chapter concludes with a presentation of the Asimov sensitivities computed for this analysis along with a comparison to median fluctuated sensitivities, which leads to a cautionary discussion about the limited usefulness of Asimov experiments in general.

6.1 Phenomenology of Sterile Neutrino Oscillations

The phenomenology of sterile neutrino driven oscillations at long baselines consists of complicated interference phenomena arising from at least two distinct oscillation frequencies and several scale-determining mixing angles. For the purposes of discussion, we will consider approximate forms of the probabilities describing the various oscillations phenomena, though it must be

noted that in the analysis framework discussed here the exact probabilities are calculated using the extended unitary matrix transformation presented in Section 1.4. The approximate form of the probability for the transition $\nu_\mu \to \nu_\mu$, the survival of muon neutrinos, was given in Eq. 1.70 as:

$$P(\nu_\mu \to \nu_\mu) \approx 1 - \sin^2(2\theta_{23})\cos^4(\theta_{24})\sin^2\Delta_{32} - \sin^2(2\theta_{24})\sin^2\Delta_{41}. \tag{1.70 revisited}$$

This probability function and the corresponding parameters are sampled by searching for the apparent disappearance of expected ν_μ-CC with respect to the MC simulation. The probability equation makes manifest the dependence of the ν_μ-CC disappearance behavior on the mass-splitting scale Δm^2_{41}, the mixing angle θ_{24}, and the atmopheric oscillations parameters Δm^2_{32} and θ_{23}. Similarly, the approximate probability for the complementary probability to the transition $\nu_\mu \to \nu_s$ using the atmospheric approximation may be written

$$\begin{aligned} 1 - P(\nu_\mu \to \nu_s) \approx 1 &- \cos^4(\theta_{14})\cos^2(\theta_{34})\sin^2(2\theta_{24})\sin^2\Delta_{41} \\ &- \sin^2(\theta_{34})\sin^2(2\theta_{23})\sin^2\Delta_{31} \\ &+ \frac{1}{2}\sin(\delta_{24})\sin(\theta_{24})\sin(2\theta_{23})\sin\Delta_{31}. \end{aligned} \tag{6.1}$$

This probability corresponds to the survival of all active neutrino flavors, which is visible only by searching for disappearance in the spectrum of NC events since the NC interaction topology is flavor-independent. Any deficit in the NC events would be indicative of transition to the sterile flavor state, since the sterile neutrino does not couple to the Z boson. The probability in Eq. 6.1 introduces dependence upon an additional mixing angle, θ_{34}, beyond the four parameters given by the ν_μ-CC survival probability.

The parameter θ_{14} also appears in Eq. 6.1, but given that it is the argument of a cosine and has been strongly constrained by reactor neutrino experiments [237], we will neglect it in this discussion. This can be interpreted as the exclusion of mixing between ν_e and the additional sterile neutrino state ν_s. Further, the CP violating phases δ_{13}, δ_{14}, and δ_{24} have been shown [175] to contribute negligibly to the observation of anomalous NC disappearance. This is due to subleading effects on the oscillation probabilities in the case of δ_{13} and δ_{14} and due to low NC energy resolution and obscuration of the observable signal by the presence of ν_μ- and ν_e-CC background events in the case of δ_{24}. Thus, each CP violating phase is set to zero for the purposes of this analysis. The following sections outline the effects of each of the five dominant parameters, namely Δm^2_{32}, Δm^2_{41}, θ_{23}, θ_{24}, and θ_{34}, on the phenomenology of oscillations considered by this analysis.

6.1.1 Atmospheric Oscillations Parameters

Atmospheric neutrino oscillation parameters θ_{23} and Δm^2_{32}, which MINOS and MINOS+ were optimized to measure, are relevant in both the case of standard three-flavor neutrino oscillations and in the case of sterile mediated oscillations. In the case of standard oscillations, which is shown in Fig. 6.1, a single oscillation maximum is observed in the FD with the position in the energy spectra, as manifested as a function of L/E, determined by Δm^2_{32} and the magnitude dictated by the value of θ_{23}.

In a model with an additional sterile neutrino, the value of Δm^2_{32} not

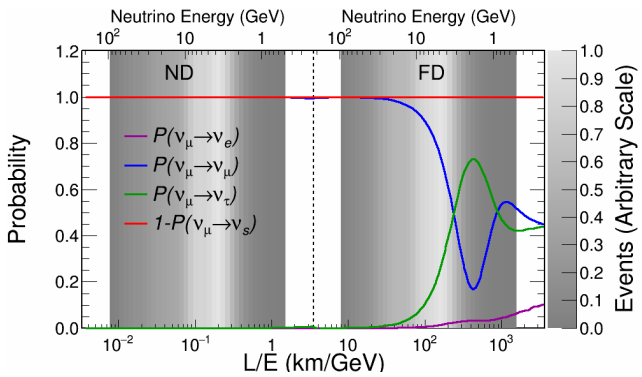

Figure 6.1: Plotted are oscillation probabilities as a function of L/E showing the effect of neutrino oscillations in the case of a standard three-flavor oscillations paradigm. The probabilities shown indicate muon neutrino survival (blue), electron neutrino appearance (violet), tau neutrino appearance (green), and the sum total of these probabilities (red) given by the expression $1 - P(\nu_\mu \to \nu_s)$ since no sterile neutrinos exist in the case of three-flavor oscillations. A single oscillation maximum is observed in the MINOS/MINOS+ FD (right shaded region) with no oscillations observed in the ND (left shaded region). In the standard oscillations picture, no sterile neutrino appearance probability is present.

Parameter	Value
Δm^2_{21}	7.40×10^{-5} eV^2
Δm^2_{32}	2.49×10^{-3} eV^2
Δm^2_{41}	0.5 eV^2
θ_{12}	0.587
θ_{13}	0.149
θ_{23}	0.824
θ_{14}	0
θ_{24}	0.2
θ_{34}	0.4
δ_{13}	0
δ_{14}	0
δ_{24}	0

Table 6.1: The nominal (3+1)-flavor oscillation parameters used for the generation of sample probability curves in Figs. 6.2, 6.3, 6.4, 6.5, and 6.6, except when differing values are explicitly stated.

only determines the position of an oscillation maximum in the muon neutrino disappearance channel but additionally in the NC disappearance channel, as shown in Fig. 6.2. The θ_{23} mixing angle determines the magnitude of the deficits in both channels as shown in Fig. 6.3. Due to the energy resolution effects in the MINOS/MINOS+ detectors, variations in the mass-splitting scale also result in apparent differences in the magnitude of the oscillation deficit, though given the global observations of the atmospheric mass-splitting, this is demonstrated to be a sub-leading effect.

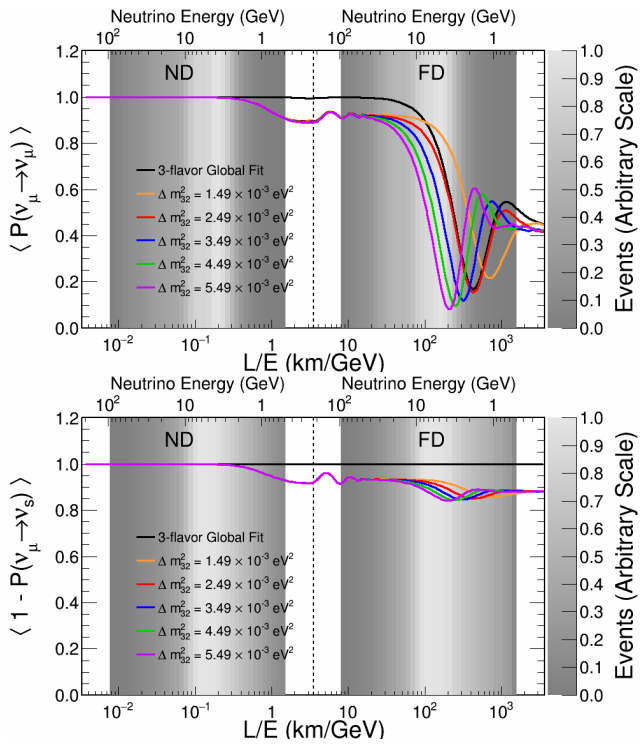

Figure 6.2: Plotted are oscillation probabilities as a function of L/E showing the effect of the mass-squared splitting Δm^2_{32} for ν_μ-CC disappearance (top) and NC disappearance (bottom). The Δm^2_{32} parameter governs the position of the standard atmospheric neutrino oscillation maximum observed in the FD for muon neutrino disappearance and introduces a similarly located deficit associated with sterile neutrino appearance. The black line gives the probabilities associated with the global best-fit parameters in Figure 1.6. For the color lines, parameters not explicitly stated are fixed to the values shown in Table 6.1.

6.1.2 The Sterile Mass-Splitting Δm^2_{41}

The new mass-splitting scale introduced by the addition of a sterile flavor eigenstate, here given by Δm^2_{41}, contributes to a variety of phenomena dependent on the relationship to the atmospheric oscillations mass-splitting.

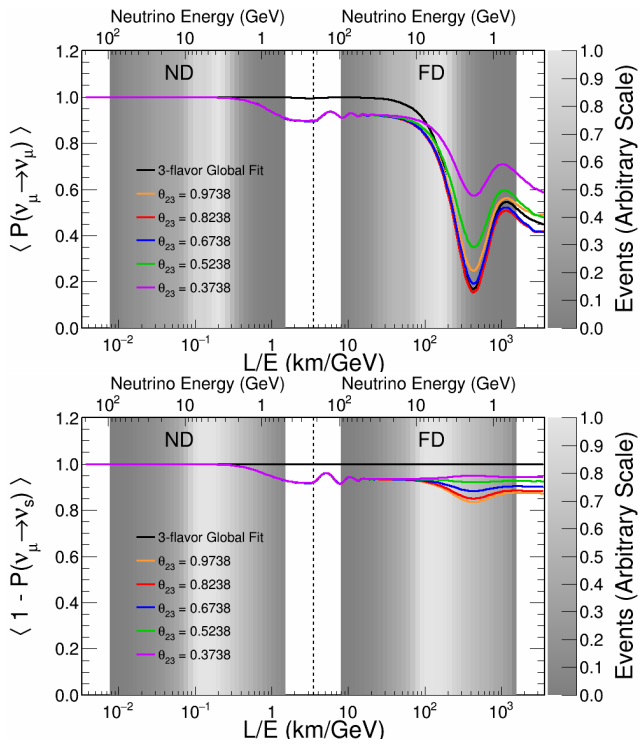

Figure 6.3: Plotted are oscillation probabilities as a function of L/E showing the effect of the atmospheric mixing angle θ_{23} for ν_μ-CC disappearance (top) and NC disappearance (bottom). The atmospheric mixing angle determines the magnitude of the deficit observed in both muon neutrino and NC disappearance channels. The black line gives the probabilities associated with the global best-fit parameters in Figure 1.6. For the color lines, parameters not explicitly stated are fixed to the values shown in Table 6.1.

The effect on the probability for a selection of possible Δm^2_{41} is shown in Figure 6.4. First considering the case of $\Delta m^2_{41} \approx \Delta m^2_{32}$, the oscillation behavior due to the sterile mass-splitting is degenerate with oscillations observed in the atmospheric neutrinos for the ν_μ-CC sample, with both oscillations isolated to the FD region of the L/E domain. In this case, anomalous oscillation phenomena would be still be observed in the NC events with an oscillation

maximum consistent with the atmospheric mass-splitting scale.

For the region of parameter space where 0.01 eV$^2 < \Delta m^2_{41} <$ 0.1 eV^2, modulations are observed in the high energy region of the FD L/E domain in the ν_μ-CC disappearance probability in conjunction with a modification to the atmospheric oscillations maximum that is observed for all larger Δm^2_{41}, which will be discussed in the context of the mixing angle θ_{24}. A similar pattern of modulations is also observed for the NC disappearance probability in addition to the already anomalous atmospheric oscillation maximum.

In the case where 0.1 eV$^2 < \Delta m^2_{41} <$ 1 eV^2, the oscillatons maximum due to sterile neutrino mixing occurs in the L/E domain between the MINOS ND and FD. This results in the indirect observation of the oscillatons in the ν_μ-CC sample through an overall FD normalization deficit and the aforementioned modification to the atmospheric oscillations. The NC sample still provides a method of direct observation of the effects of sterile neutrino mediated oscillations in this region through the anomalous atmospheric mixing.

For $\Delta m^2_{41} >$ 1 eV^2, the oscillation probabilities observed in the ND L/E domain can be further simplifed from those given in Eqs. 1.70 and 6.1 to the short-baseline approximations such that the ν_μ-CC disappearance probability is given by

$$P(\nu_\mu \to \nu_\mu) \approx 1 - \sin^2(2\theta_{24}) \sin^2 \Delta_{41}, \tag{6.2}$$

and the NC disappearance probability becomes

$$1 - P(\nu_\mu \to \nu_s) \approx 1 - \cos^2(\theta_{34}) \sin^2(2\theta_{24}) \sin^2 \Delta_{41}. \tag{6.3}$$

Both of these approximations have the same form as the effective two-flavor oscillations probability given in Eq. 1.60 with the replacement of Δm^2_{32} with Δm^2_{41}. It must be noted that this approximation only applies to the probability form in the ND domain and that the FD behavior remains unchanged from the above descriptions for arbitrarily increasing Δm^2_{41}. This means that the short-baseline approximation is never valid for the two-detector analysis, but would only apply to a ND-only version of the analysis presented here. The oscillations observed in the short-baseline regime for both ν_μ-CC and NC probabilities are marked by the presence of an initial oscillations maximum at a particular neutrino energy with oscillations smeared to some effective normalization deficit for significantly lower energies.

Finally, considering the case of $\Delta m^2_{41} \approx 1000$ eV^2, the approximate ν_μ disappearance probability is given by

$$P(\nu_\mu \to \nu_\mu) \approx 1 - \frac{1}{2}\sin^2(2\theta_{24}), \tag{6.4}$$

and the NC disappearance probability is given by

$$1 - P(\nu_\mu \to \nu_s) \approx 1 - \frac{1}{2}\cos^2(\theta_{34})\sin^2(2\theta_{24}). \tag{6.5}$$

where the oscillations due to Δm^2_{41} are too rapid to be resolved by either detector due to the energy resolution and baseline uncertainties from the length of the decay pipe. This results in a constant normalization deficit with respect to the standard three-flavor oscillations probability for all energies in both detectors, with the exception of the modification to the atmospheric oscillations maximum discussed in the next section.

6.1.3 The Sterile Mixing Angle θ_{24}

The general role of the mixing angle θ_{24} is to govern the magnitude of the neutrino oscillations between the muon and sterile flavor eigenstates. This results in both the disappearance of ν_μ-CC and NC events at differing rates. Inspecting the short-baseline approximaton given in Eq. 6.2, we find that θ_{24} functions in the same effective two-flavor manner for the MINOS ND as θ_{23} functions in the atmospheric approximation for the FD given in Eq. 1.60. A sample of the range of oscillation magnitudes that may be explored by the variation of the θ_{24} parameter is shown in Figure 6.5 for an oscillation maximum occuring at the low energy edge of the ND L/E domain. Since θ_{24} enters the oscillation probabilities as the argument of the function $\sin^2(2\theta_{24})$, the magnitude of the short-baseline oscillations is both maximized by and symmetric with respect to a value of $\theta_{24} = \pi/4$.

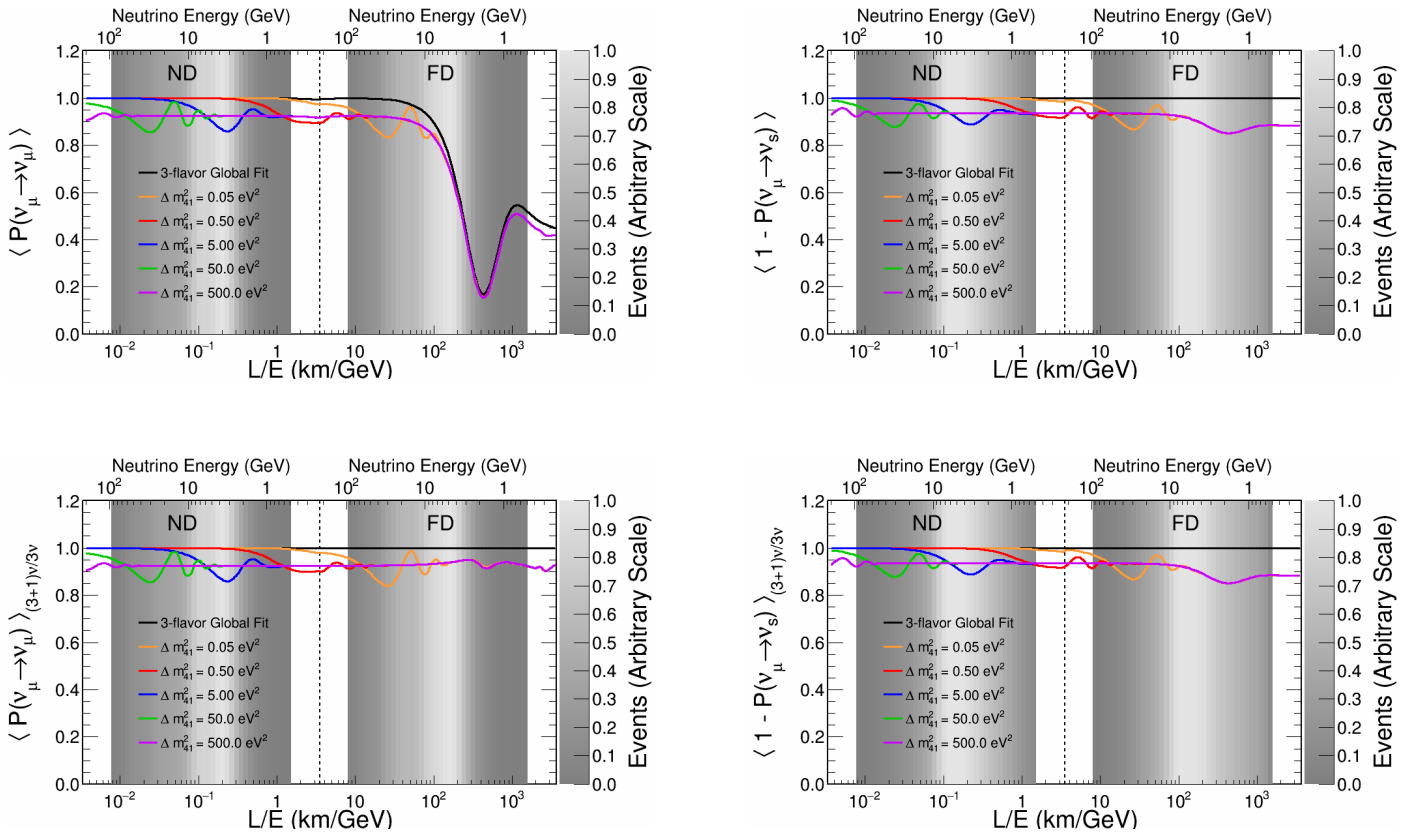

Figure 6.4: Plotted are oscillation probabilities as a function of L/E showing the effect of the mass squared splitting Δm^2_{41} (top row) and the ratios of the probabilities with respect to the three-flavor global fit (bottom row) for ν_μ-CC disappearance (left column) and NC disappearance (right column). MINOS and MINOS+ are primarilty sensitive to Δm^2_{41} and θ_{24} in a search for sterile neutrino-mediated oscillations. The black line gives the probabilities associated with the global best fit parameters in Figure 1.6. For the color lines, parameters not explicitly stated are fixed to the values shown in Table 6.1.

In the previous discussion of Δm^2_{41} we saw that the existence of a sterile neutrino flavor eigenstate results not only in the short-baseline oscillation effects mentioned here, but also in the modification of the atmospheric oscillations. The first term in the atmospheric approximation for ν_μ-CC disappearance given in Eq. 1.70 is driven by the atmospheric mass-splitting Δm^2_{32}. For all Δm^2_{41} values, this term does not change frequency and therefore does not transition to rapid oscillations. Thus, the mixing angle θ_{24} contributes to the determination of the observed oscillations of muon neutrinos at the atmospheric frequency independent of the value of Δm^2_{41}. In order to determine the magnitude of the Δm^2_{41}-independent effect, we define an effective atmospheric mixing angle which accounts for both standard and sterile oscillations given by

$$\sin^2(2\theta^{\text{eff}}_{23}) = \sin^2(2\theta_{23})\cos^4(\theta_{24}). \tag{6.6}$$

The effective mixing angle θ^{eff}_{23} would correspond to the measured value for all atmospheric oscillation experiments to date that use a standard three-flavor framework. A priori, the observation of this effective mixing angle gives no constraint on the possible values of the mixing angles θ_{23} and θ_{24} since various combinations of these inputs can span the possible probability space. It can be noted from this expression that due to the functional form of the $\cos^4\theta_{24}$ factor, a non-zero θ_{24} can only force $\sin^2(2\theta^{\text{eff}}_{23})$ to smaller values than the maximal value of unity. This feature can be seen in the lower left plot of Figure 6.5, which shows the ratio of the (3+1)-flavor oscillation probability to the standard three-flavor probability for increasing θ_{24}. The plot shows that for larger values

of θ_{24} a clear upward protrusion is observed at the atmospheric oscillations frequency, implying reduction in the magnitude of the atmospheric oscillation maximum with respect to three-flavor oscillations. The analysis presented here is sensitive to such a modification to the atmospheric oscillation minimum.

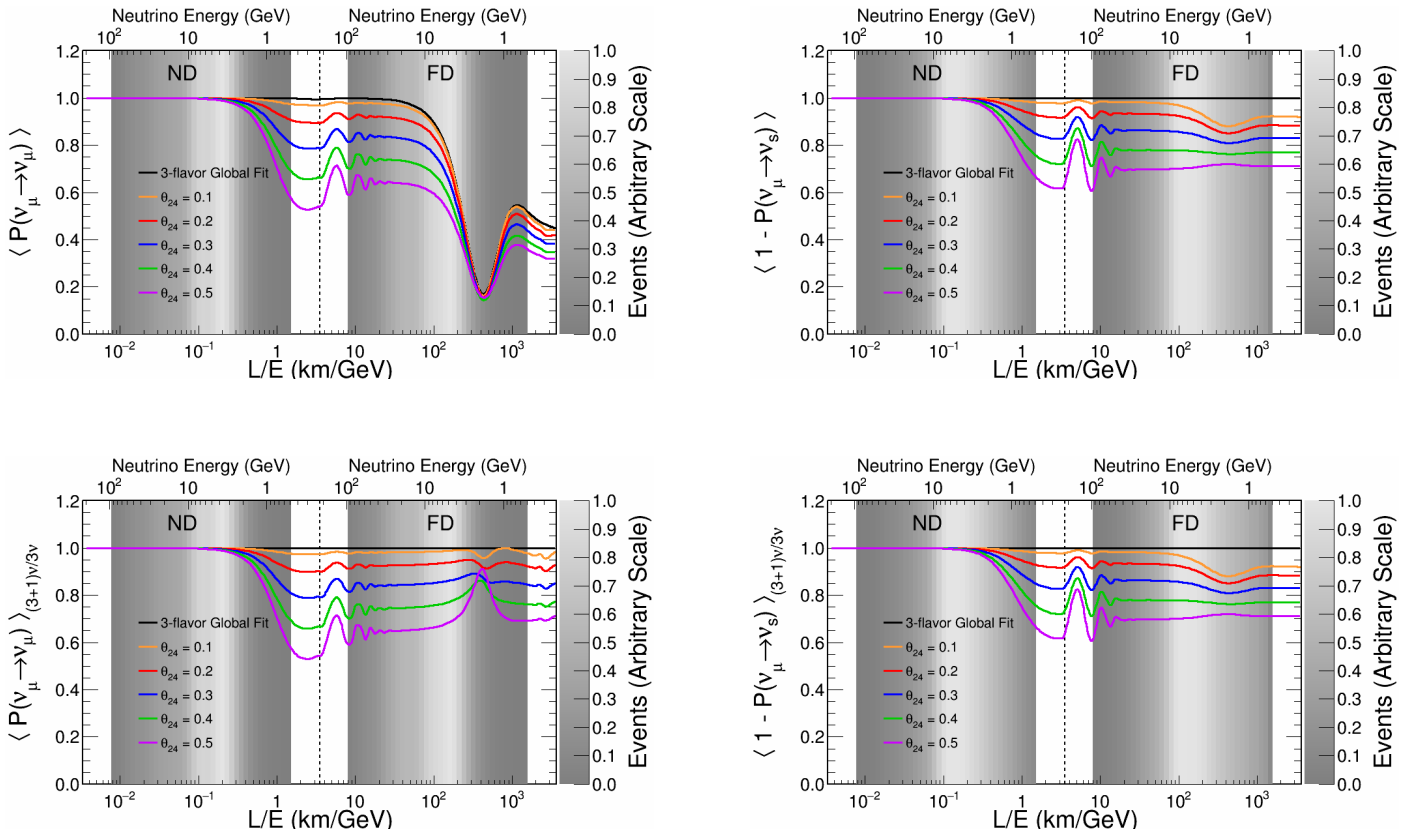

Figure 6.5: Plotted are oscillation probabilities as a function of L/E showing the effect of the mixing angle θ_{24} (top row) and the ratios of the probabilities with respect to the three-flavor global fit (bottom row) for ν_μ-CC disappearance (left column) and NC disappearance (right column). The θ_{24} parameter is the second of the principle dimensions, along with Δm^2_{41} of the parameter space accessible to this analysis. The black line gives the probabilities associated with the global best fit parameters in Figure 1.6. For the color lines, parameters not explicitly stated are fixed to the values shown in Table 6.1.

6.1.4 The Sterile Mixing Angle θ_{34}

The mixing angle θ_{34} is most significant in the observation of NC disappearance as a result of sterile-mediated neutrino oscillations. The effects of varying θ_{34} on both the ν_μ-CC and NC disappearance probabilities are plotted in Figure 6.6 for a large range of θ_{34} values. The magnitude of the atmospheric oscillations maximum in the NC disappearance probability is directly controlled by θ_{34} as function of $\sin^2(\theta_{34})$ in the second term of Eq. 6.1. This functional form implies that maximal NC disappearance at the atmospheric scale occurs for $\theta_{34} = \pi/2$.

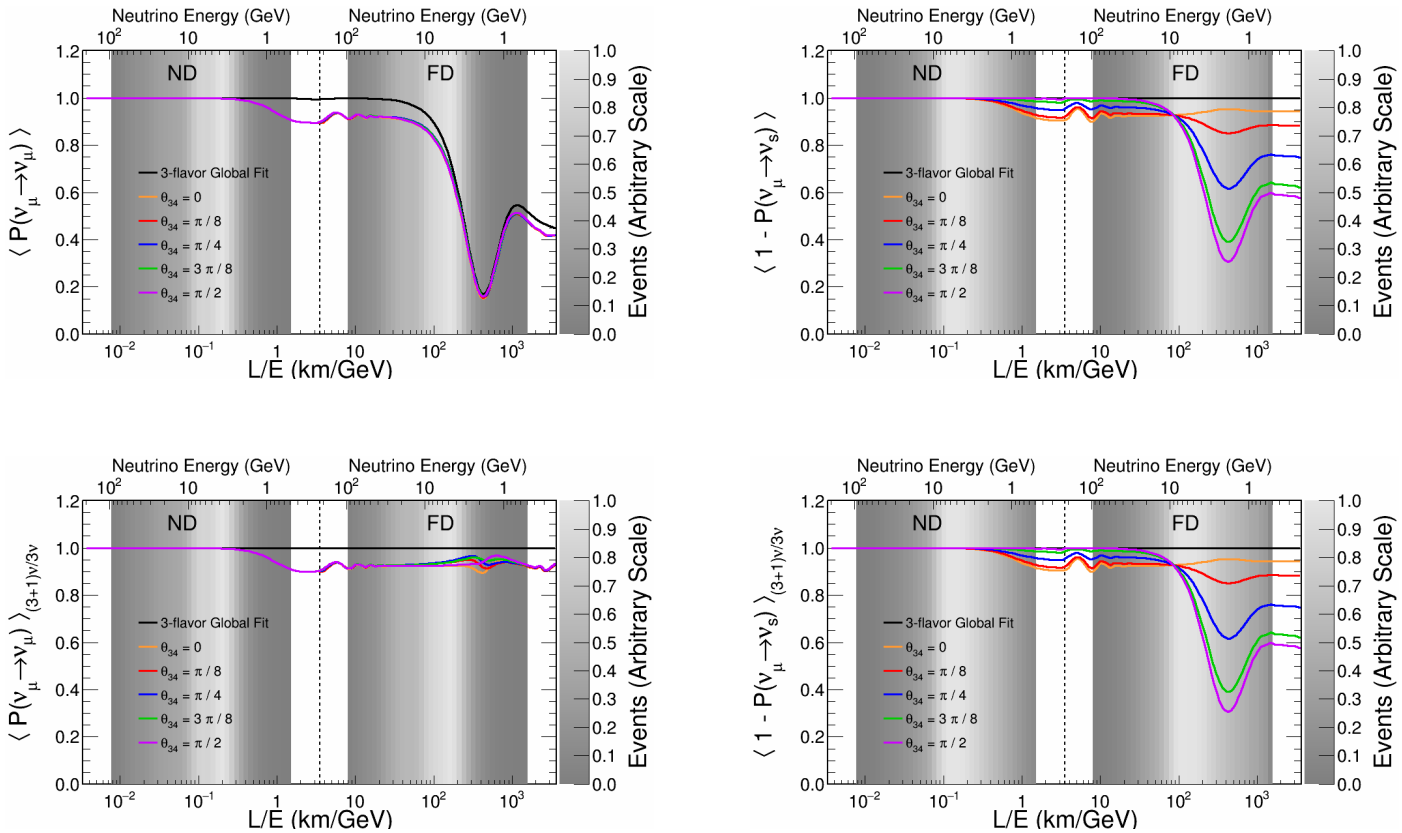

Figure 6.6: Plotted are oscillation probabilities as a function of L/E showing the effect of the mixing angle θ_{34} (top row) and the ratios of the probabilities with respect to the three-flavor global fit (bottom row) for ν_μ-CC disappearance (left column) and NC disappearance (right column). The θ_{34} mixing angle is a free parameter in the fit described in this analysis. The black line gives the probabilities associated with the global best fit parameters in Figure 1.6. For the color lines, parameters not explicitly stated are fixed to the values shown in Table 6.1.

The magnitude of the sterile mediated oscillations in NC disappearance is also determined by θ_{34} through the second term in Eq. 6.5. It is straightforward to note a parallel relationship between this term and the modification of atmospheric neutrino oscillations by θ_{24} by defining the effective mixing angle

$$\sin^2(2\theta_{24}^{\text{eff}}) = \sin^2(2\theta_{24})\cos^2(\theta_{34}), \tag{6.7}$$

which has a similar functional form to the definition of θ_{23}^{eff} in Eq. 6.6. We can observe from this effective mixing angle that for increasing θ_{34}, the magnitude of the oscillations is reduced even for near-maximal mixing from θ_{24}. This property is readily seen in Figure 6.6 as the sterile mixing feature occuring between the detectors for small θ_{34} is entirely removed when $\theta_{34} = \pi/2$, which is opposite to the maximal mixing at the atmospheric frequency for this value of the mixing angle.

6.2 Motivation for a Two-Detector Fit

The three-flavor standard oscillations analyses in MINOS and MINOS+ searched for muon neutrino disappearance in the FD as predicted by the observation of the neutrino data spectrum in the ND [238]. In the case of standard oscillations, oscillations do not occur in the ND, so any discrepancy between data and simulation can be attributed to some form of mismodeling either in the detector or in the neutrino beam. A beam fit mechanism was employed in the three-flavor analyses in order to alter the underlying phase space of the MC prediction in such a manner that the data/MC agreement in the energy spectrum was improved [92]. The systematic shifts determined by this beam fit are

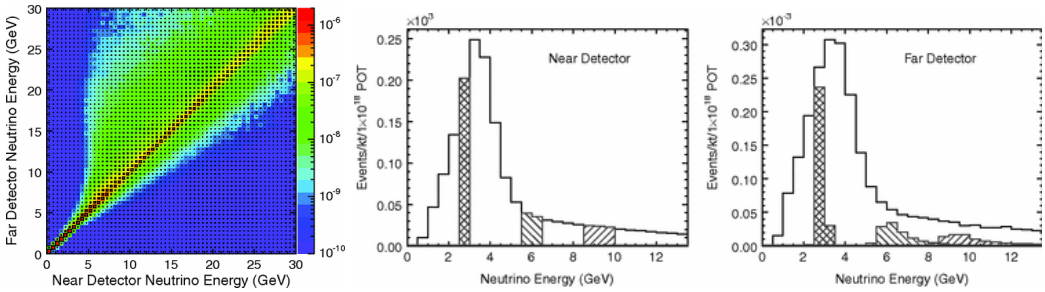

Figure 6.7: The beam matrix used in the extrapolation of the FD reconstructed energy spectrum for the standard oscillations analysis (left) together with the simulated ND and FD reconstructed energy spectra (right). The transformation of the hatched regions between the FD and ND spectra demonstrates the effect of applying the beam matrix. Figures are reproduced from Reference [92].

propagated to the FD by use of the beam matrix method, which accounts for differing detector purity, background, energy resolution, and solid-angle acceptance using a multi-stage procedure. However, this analysis is not suitable in the search for sterile neutrino oscillations as it is based on the assumption that any data/MC disagreement in the ND can be attributed to systematic fluctuations and not sterile neutrino oscillations. It was demonstrated in Section 6.1 that this assumption is invalid for $\Delta m^2_{41} > 1$ eV^2.

The previous MINOS sterile analysis [155] used a Far-over-Near ratio fit method wherein MINOS FD spectrum was divided binwise by the MINOS ND spectrum for both CC and NC selected events in order to search for modulations caused by sterile neutrino mediated oscillations. The Far-over-Near ratio method benefits from the straightforward reduction or possible cancellation of systematic uncertainties that share similar relative effects in both

detectors such as cross sections with the detector components and beam optics effects that are readily propagated forward from the ND to the FD. The ratio of spectra shifted by equivalent relative amounts clearly would not suffer from any reduction in sensitivity due to such a systematic effect. While the reduction of systematic effects is a benefit of the Far-over-Near method, this property also serves as a demonstration that such a method eliminates valuable information arising from the observation of neutrino spectra in the two detectors. For instance, a shift in the energy spectra at a particular energy in both detectors is not necessarily attributable to systematic effects. The presence of sterile neutrino oscillations with shared effects at similar energies in the two detectors can allow for the introduction of undesirable ambiguity and degeneracy.

For the analysis presented in this thesis, I have developed a two-detector fit method which simultaneously searches both detectors for the effects of sterile neutrinos. In this method, the systematic uncertainties are incorporated through the construction of a covariance matrix which includes the correlation of systematics both within each detector and between the energy spectra of the two detectors, as will be discussed in detail in subsequent sections. The new method allows for the mitigation of the effects of systematic uncertainty without the destruction of information that occurs in a ratio method. The preservation of information from both detectors becomes critical to achieving the maximal possible sensitivity of the search when considering the wide range of possible oscillations that may be observed.

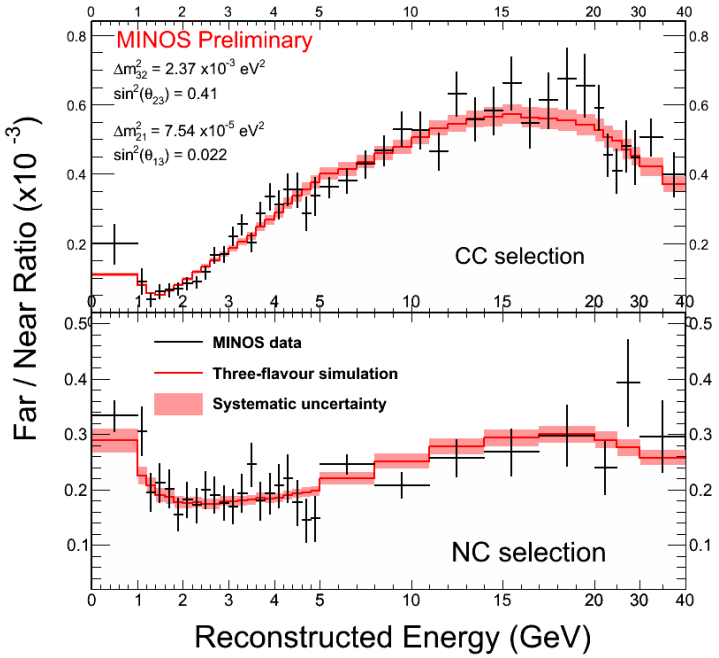

Figure 6.8: The Far-over-Near ratios for MINOS data (black points) plotted with the three-flavor simulation (red line) for the parameters listed on the plot with the uncorrelated systematic uncertainty given by the red shaded band. Events selected by the CC selector are shown in the upper plot while events selected by the NC selector are shown in the lower plot. The data and three-flavor prediction shown in this plot are reproduced from the similar figure in Reference [155].

In MINOS and MINOS+, oscillations arising from mixing with a sterile neutrino state may occur at baselines ranging from before the ND to beyond the FD, as illustrated in Section 6.1. Given that the three-flavor neutrino oscillations paradigm has been well-measured, further searches for oscillations phenomenon depend on the observation of variations on the three-flavor probability. The modulations on the standard three-flavor probability are shown in the lower panels of Figs. 6.4, 6.5, and 6.6 by taking the ratio of the (3+1)-flavor probability function with respect to the three-flavor expectation. Studying these probability curves leads to several general conclusions. First, the first oscillation maximum shifts to smaller values of L/E, which corresponds to higher energy in each detector given the fixed baselines, as the mass-splitting scale becomes larger. Second, if a first oscillation maximum occurs in the FD, the ND spectrum remains largely unchanged, whereas if the first oscillation maximum occurs in the ND, the FD spectrum observes a net normalization offset due to smeared rapid oscillations. Third, if the oscillations maximum occurs in the high-energy regime of the ND, then both detectors observe a net normalization deficit with respect to the three-flavor oscillation case. Finally, if both detectors fall within the regime of rapid oscillations for the sterile mass-splitting, variations are still present in the magnitude of the atmospheric oscillations.

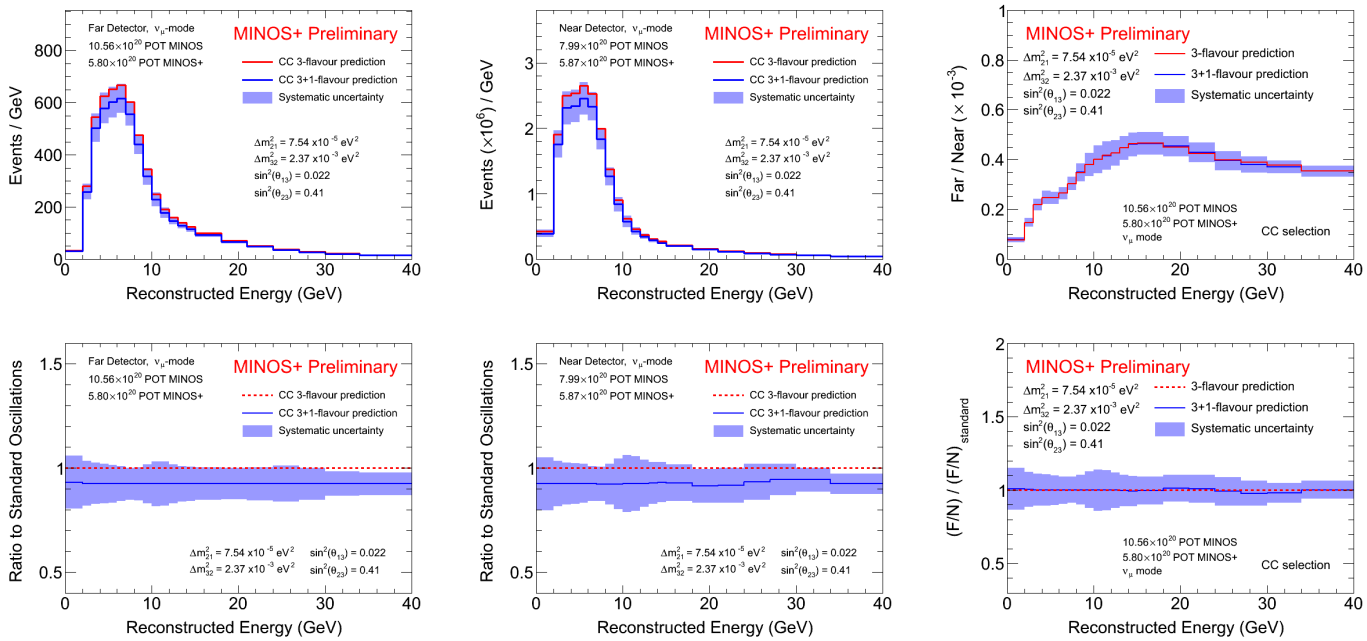

Figure 6.9: MC simulation of predicted reconstructed energy spectra and Far-over-Near ratio for three-flavor oscillations and (3+1)-flavor oscillations at a test point in parameter space where $\theta_{24} = 0.2$ and $\Delta m^2_{41} = 80.0\ eV^2$. The FD (upper left) and ND (upper center) simulated reconstructed energy spectra are plotted. Using these plots as input, the ratios of the (3+1)-flavor prediction with respect to the standard three flavor prediction are plotted for the FD (lower left) and ND (lower center) as well as the simulated Far-over-Near ratio for 3- and (3+1)-flavor oscillations (upper right). Using the Far-over-Near ratio results, the double Far-over-Near ratios of the simulated spectra with respect to three-flavor oscillations are plotted (lower right).

A comparison of the Far-over-Near ratio and simultaneous two-detector fits methods is possible taking into account the probability signals that may be observed. When oscillations are confined to the L/E regime corresponding to greater than or equal to the FD, there is no significant difference between methods as the ND serves only to establish the spectrum for a probability of unity, either as the denominator of a ratio or through cancellations within a covariance matrix. The power of the two-detector method is made apparent when considering oscillations occurring at baselines less than or equal to the ND. In a Far-over-Near ratio fit, the ratio spectrum is always subject to the statistical uncertainties associated with the predicted event rate in the FD. For MINOS and MINOS+, the relative statistical uncertainties in the FD are on the order of 15%, as compared to the $< 0.1\%$ relative statistical uncertainty in the ND. Thus, even though modulations on the three-flavor paradigm in the ND can ideally be observed in a Far-over-Near ratio fit, the sensitivity of the analysis is limited by the statistical errors in the FD. In fact, it would be reasonable to expect a better measurement from a ND-only fit as compared to a Far-over-Near ratio fit when considering these short-baseline oscillations. A simultaneous two-detector fit permits a synergistic combination of the strengths of each detector without unduly penalizing the other.

A demonstration of the improvement in experimental sensitivity using a two-detector fit is illustrated in Figure 6.9. Consider the predicted reconstructed neutrino energy spectrum in both the FD and ND for the case where a sterile neutrino exists with $\Delta m^2_{41} = 80.0$ eV^2 and $\theta_{24} = 0.2$. At this point

in the parameter space, the Far-over-Near ratio contains only minimal oscillatory behavior, which could not be disentangled from statistical or systematic uncertainties. However, when using a two-detector fit both the FD and ND observe a depletion in predicted event rate for the full range of reconstructed neutrino energies with a small oscillatory modulation in the high energy tail of the ND. Any oscillation signal with similar behavior becomes ambiguous in a Far-over-Near ratio fit but is readily detectable when utilizing the combined sensitivity of both detectors.

6.3 Simultaneous Two-Detector Fit

As discussed in the previous section, the 2016 MINOS sterile analysis was based on a fit to the Far-to-Near ratio which had the benefit of canceling many systematic uncertainties directly at the expense of removal of any effects that occur at similar energies in both detectors, regardless of whether these effects may in fact be due to oscillations. The simultaneous two-detector fit presented here uses a covariance matrix in order to encode information about both correlated and uncorrelated systematic effects between bins of reconstructed energy in both the ND and FD. The covariance matrix construction still permits the mitigation of the effects of correlated systematic uncertainties through the behavior of large off-diagonal elements in the covariance matrices.

It can be demonstrated that the covariance matrix approach is mathematically equivalent to the fitting of systematic uncertainties using estimated systematic template spectra with scaling determined by nuisance parame-

ters [187]. However, such a systematic parameter based fit is subject to increased computational demands due to a large number of potentially degenerate nuisance parameters, which can be avoided by the use of a covariance matrix. We will also see in the next section that it is possible to extract systematic information in post-fit analysis, reproducing the results determined by a nuisance parameter fit while avoiding known weaknesses of that method and demonstrating the superiority of a covariance matrix approach.

6.3.1 Fit Strategy

In this analysis we search simultaneously in both detectors for modulations on the standard oscillations due to sterile neutrinos by minimizing

$$\chi^2_{CC,NC} = \sum_{i=1}^{N}\sum_{j=1}^{N}(x_i - \mu_i)[\mathbf{V}^{-1}]_{ij}(x_j - \mu_j), \tag{6.8}$$

where the number of events observed in data and the MC prediction are denoted by x_i and μ_i, respectively. The index $i = 1, ..., N$ labels the reconstructed energy bins from 0 to 40 GeV in each detector with N being the sum of ND and FD bins. The predicted number of events μ_i is varied using a MC simulation with exact forms of all oscillation probabilities in vacuum and includes all other experimental effects. The V^{-1} matrix is defined as the inverse of the $N \times N$ covariance matrix, which incorporates the sum of the statistical and systematic uncertainties. The total χ^2 expression has the form

$$\chi^2 = \chi^2_{CC} + \chi^2_{NC} + \frac{(|\Delta m^2_{32}| - \Delta m^2_{gf})^2}{\sigma^2_{\Delta m^2_{gf}}}, \tag{6.9}$$

Parameter	Fit Status	Constraints
Δm^2_{21}	Fixed	7.40×10^{-5} eV^2
θ_{12}	Fixed	0.587
θ_{13}	Fixed	0.149
Δm^2_{32}	Free	penalty (see Eq. 6.9)
θ_{23}	Free	$\in [0, \pi/2]$
Δm^2_{41}	Free	$\in [10^{-4}, 10^2]$ eV^2
θ_{24}	Free	$\in [0.01, \pi/2]$
θ_{34}	Free	$\in [0, \pi/2]$
$\{\theta_{14}, \delta_{13}, \delta_{14}, \delta_{24}\}$	Fixed	0

Table 6.2: The parameters for the (3+1)-flavor oscillation model analyzed in the simultaneous two-detector fit listed with fit status, either free or fixed, along with the constraints used in the fit.

where the last term constrains the atmospheric mass-splitting to the confidence interval preferred by the global best fit [114] in order to prevent the fit from reversing the roles of the atmospheric and sterile-mediated oscillation frequencies. The status in the fit framework of all neutrino oscillations parameters in the (3+1)-flavor model are listed in Table 6.2. The χ^2 statistic is minimized with respect to the free atmospheric oscillation paramters Δm^2_{32} and θ_{23}, profiling over both mass orderings and mixing angle octants, as well as the sterile mixing angle θ_{34} while searching grid points in the parameter space of (θ_{24}, Δm^2_{41}). All remaining oscillations parameters are irrelevant or subdominant in the analysis and are fixed either to global best fit values or to zero.

The covariance matrix V is a sum of the component statistical and systematic uncertainty covariance matrices following the form

$$V = V_{stat} + V_{scale} + V_{had} + V_{xsec} + V_{bkgd} + V_{other} \tag{6.10}$$

where each term accounts for a particular source of uncertainty as fully expounded in Chapter 5. The general structure of the covariance matrices is four quadrants corresponding to the FD covariance matrix, the ND covariance matrix, and cross-term matrices encoding the covariance between the detectors. The total covariance matrix has the structure

$$V = \begin{pmatrix} \delta(f)_1 & 0 & & \cdots & & 0 \\ 0 & \ddots & & & & \\ & & \delta(f)_k & & & \vdots \\ \vdots & & & \delta(n)_1 & & \\ & & & & \ddots & 0 \\ 0 & & \cdots & & 0 & \delta(n)_m \end{pmatrix} + \sum_{i=1}^{26} V_i \tag{6.11}$$

where the first matrix handles the statistical uncertainties for FD ($\delta(f)_k$) and ND ($\delta(n)_k$) bins and the second matrix is the sum of all systematics covariance matrices. Here the index k indicates the number of bins in the FD prediction while the index m indicates the number of bins in the ND prediction. The statistical uncertainties are the standard uncertainty for a Poisson process, namely $\sqrt{N}$, where N is the expected number of events in a given bin. The two-detector spectrum is generated for this fit by taking the FD and ND predictions and joining the final FD bin with the initial ND bin to form a single vector. This structure can be seen in the diagonal elements of the statistical

uncertainty matrix where the final (k^{th}) element of the FD spectrum is followed by the first element of the ND spectrum. As opposed to the extrapolation technique, this method treats the ND and FD on equal footing in order to properly disambiguate shape variations arising from systematic uncertainties from those due to sterile-mediated oscillations.

6.3.2 Near Detector Oscillations

Sterile neutrino mediated oscillations can occur in the ND for sufficiently large mass-splitting Δm^2_{41}. For the purposes of a standard oscillations analysis, where the baseline for the first oscillation maximum is on the order of the 735 km distance to the FD, the variations in the true baseline for detected neutrinos arising from decay within the 675 m decay pipe is of the order $\sim 10^{-3}$, which is negligible. In order to measure the ND oscillations, it is critical to properly account for the baseline traversed by the neutrinos, as the effects of baseline variation rapidly become non-perturbative with increasing Δm^2_{41}. While it is not possible to detect the point of creation of a given neutrino, and to therefore have perfect knowledge of the traversed baseline, we model the relative quantities of neutrinos being produced by hadron decay along the length of the decay pipe. The mapping of this distance traveled by simulated neutrinos prior to interaction in the ND is shown in Figure 6.10. In order to properly compute the oscillation probabilities, we generate a matrix for conversion of simulated neutrino L/E to reconstructed energy, which is utilized in the generation of both ND and FD predictions. This method provides

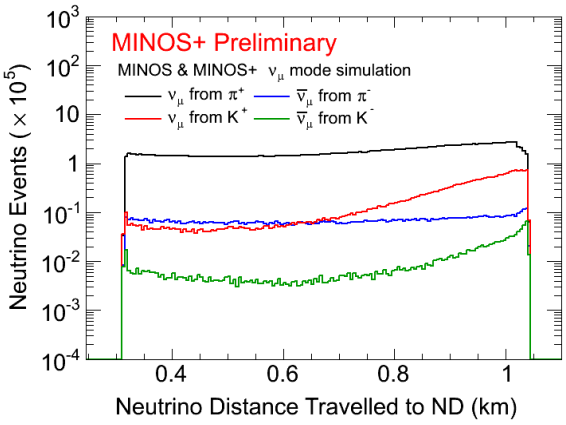

Figure 6.10: Plotted are the number of ν_μ produced from the decay of π^+ (black) or K^+ (red) and the number of $\bar{\nu_\mu}$ produced from the decay of π^- (blue) or K^- (green) as a function of the distance traveled by the neutrino prior to detection in the ND. The baseline information of the simulated neutrinos is preserved by the generation of L/E versus reconstructed energy matrices which are used to generate oscillated predictions for ND and FD reconstructed energy.

sufficient resolution to detect neutrino oscillations due to $\Delta m^2_{41} < 1000$ eV^2, which would not be possible under the assumption of a single fixed baseline for each detector.

6.3.3 Conditional Multivariate Gaussian Distributions

Performing a fit with a covariance matrix-based χ^2 function implies that the energy bins are distributed according to a multivariate Gaussian distribution. A multivariate Gaussian distribution is a generalization of the univariate Gaussian distribution, which consists of a set of normally-distributed random variables that may or may not be correlated. In the event that the multivari-

ate Gaussian is correlated, and thus covariances exist between the variables, one can compute the conditional distribution of a subset of the variables given the observation of the remaining subset. The condition of strong correlations between energy bins yields significant power in detecting oscillatory behavior that is not expected from known sources of systematic uncertainty as each observed energy bin serves as a constraint on the expected observation in correlated energy bins.

Visualization techniques used to display relative uncertainties in the form of uncorrelated error bands can be highly misleading in the case of strongly correlated uncertainties. Typically, an uncorrelated error band approximating the general shape and magnitude of systematic uncertainties can be extracted from the diagonal elements of the covariance matrix, which are the bin-by-bin variances. This method is sufficient in the case of a single source of systematic uncertainty, or in the case of a weakly correlated ensemble of uncertainties. As correlations increase, it is substantially more likely that variations outside of those predicted by the uncorrelated error band could arise that would not contribute significantly to a measurement of χ^2. Further, in displaying data/MC agreement in the context of a covariance matrix fit, large deviations may be observed that correspond to known systematic fluctuations. In a fit with template sytematics and nuisance parameters, these systematic variations would be directly corrected out of the MC simulation but such corrections are not naturally applied in the covariance matrix technique.

In order to address the need to visualize the internal functioning of the

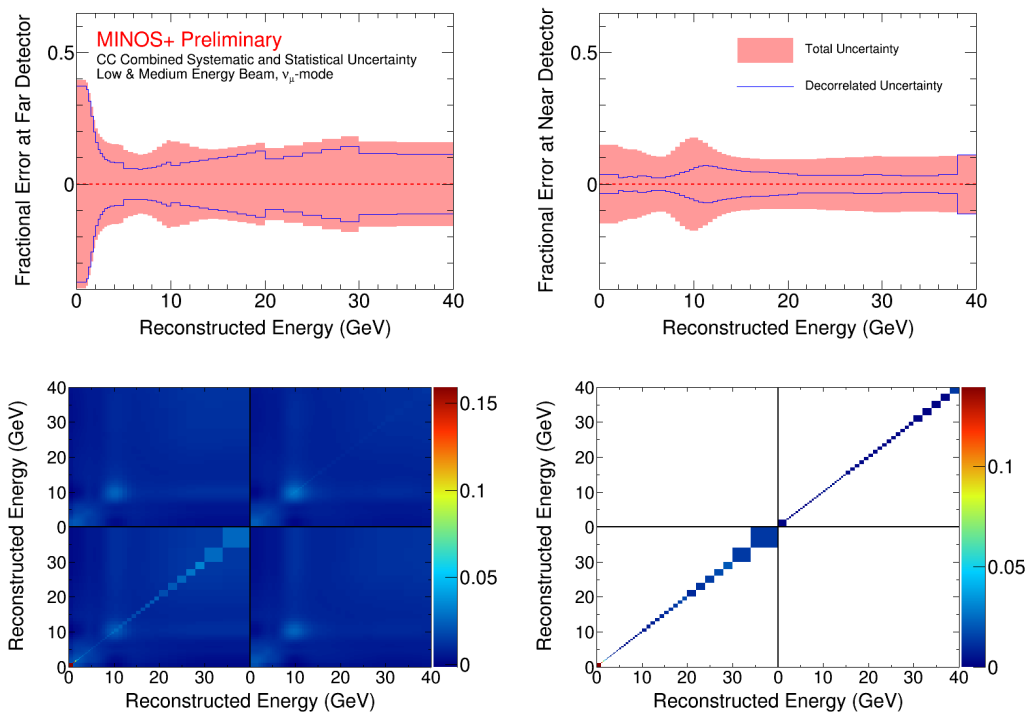

Figure 6.11: The combined total of systematic and statistical fractional uncertainty for the ν_μ-CC sample is plotted as a function of the reconstructed energy for at the FD (upper left) and ND (upper right). The fractional uncertainty bands are computed from the square roots of the diagonal elements of the summed statistical and systematic matrices. The red band corresponds to the diagonal of the covariance matrix before the decorrelation procedure (lower left), and the blue line corresponds to the diagonal after the decorrelation procedure (lower right)

covariance matrix method, we introduce here a decorrelation procedure, which can be used to produce a post-fit data/MC spectrum that shows the differences between observation and simulation after accounting for all the effects of correlated uncertainties. Additionally, this method produces an uncorrelated error band, which shows the irreducible level of uncertainty in each energy bin given the known sources of systematic uncertainty. The decorrelation procedure has a similar purpose to more traditional extrapolation methods in which one detector observation is propagated to correct the prediction in a second detector, though it should be noted that this is in fact occuring beneath the surface in the mechanism of the covariance matrix fit. The decorrelation method exploits the aforementioned properties of multivariate Gaussian distributions by iteratively conditioning each bin of reconstructed energy upon the observations of events in all other energy bins.

Consider the multivariate Gaussian distribution, $\mathbf{x} \sim N(\boldsymbol{\mu}, \boldsymbol{\Sigma})$ where $\mathbf{x}$ contains N random variables representing histogram bins, $\boldsymbol{\mu}$ is the nominal prediction, and $\boldsymbol{\Sigma}$ is the positive semi-definite symmetric matrix describing the covariances between bins. The N bins can be partitioned into two group $\mathbf{x_1}$ and $\mathbf{x_2}$, which could represent the FD bins and ND bins, such that

$$\mathbf{x} = \begin{bmatrix} \mathbf{x_1} \\ \mathbf{x_2} \end{bmatrix} \text{ with sizes } \begin{bmatrix} q \times 1 \\ (N-q) \times 1 \end{bmatrix}, \tag{6.12}$$

with the mean vector given by

$$\boldsymbol{\mu} = \begin{bmatrix} \boldsymbol{\mu_1} \\ \boldsymbol{\mu_2} \end{bmatrix} \text{ with sizes } \begin{bmatrix} q \times 1 \\ (N-q) \times 1 \end{bmatrix}, \tag{6.13}$$

and the covariance matrix taking the form

$$\boldsymbol{\Sigma} = \begin{bmatrix} \boldsymbol{\Sigma_{11}} & \boldsymbol{\Sigma_{12}} \\ \boldsymbol{\Sigma_{21}} & \boldsymbol{\Sigma_{22}} \end{bmatrix} \text{with sizes} \begin{bmatrix} q \times q & q \times (N-q) \\ (N-q) \times q & (N-q) \times (N-q) \end{bmatrix}. \tag{6.14}$$

Using the FD and ND example, $\boldsymbol{\mu_1}$ is the nominal FD prediction and $\boldsymbol{\mu_2}$ is the nominal ND prediction. Similarly $\boldsymbol{\Sigma_{11}}$ is the FD covariance matrix, $\boldsymbol{\Sigma_{22}}$ is the ND covariance matrix, and $\boldsymbol{\Sigma_{12}}$ and $\boldsymbol{\Sigma_{21}}$ contain covariances between the detectors.

Now consider an observation (measurement) of $\mathbf{x_2}$ such that $\mathbf{x_2} = \boldsymbol{\alpha}$. One can calculate the conditional distribution of $\mathbf{x_1}$ after accounting for the correlations encoded in the covariance matrix. Calculating the FD distribution conditional on the ND is effectively an extrapolation procedure.

The conditional distribution is defined by $\mathbf{x_1} \sim N(\bar{\boldsymbol{\mu}}, \bar{\boldsymbol{\Sigma}})$ [239] where

$$\bar{\boldsymbol{\mu}} = \boldsymbol{\mu_1} + \boldsymbol{\Sigma_{12}}\boldsymbol{\Sigma_{22}^{-1}}(\boldsymbol{\alpha} - \boldsymbol{\mu_2}), \tag{6.15}$$

with variance

$$\bar{\boldsymbol{\Sigma}} = \boldsymbol{\Sigma_{11}} - \boldsymbol{\Sigma_{12}}\boldsymbol{\Sigma_{22}^{-1}}\boldsymbol{\Sigma_{21}}. \tag{6.16}$$

In a simple two-bin example, after computing the conditional distribution of $\mathbf{x_1}$, $\mathbf{x_1}$ and $\mathbf{x_2}$ are no longer correlated. In addition, μ_2 is corrected according to the difference between $\boldsymbol{\alpha}$ and $\boldsymbol{\mu_2}$. For more than two-bin fits, this decorrelation procedure can be performed recursively, correcting $N-1$ based on observed data. This procedure is not used directly in the analysis, but it is

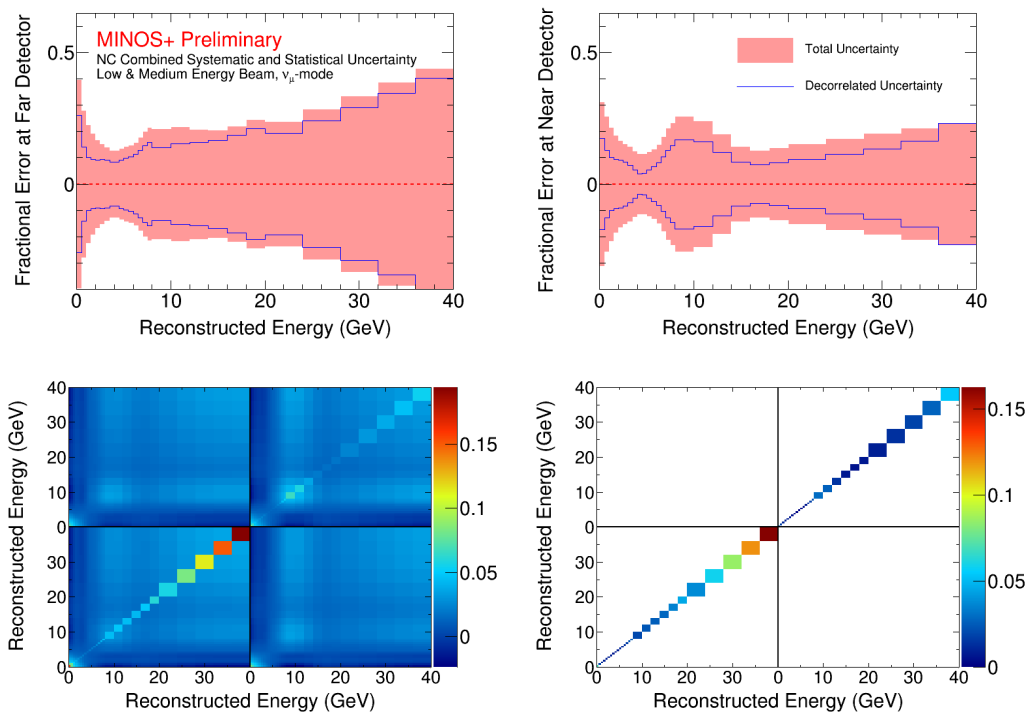

Figure 6.12: The combined total of systematic and statistical fractional uncertainty for the NC sample is plotted as a function of the reconstructed energy for at the FD (upper left) and ND (upper right). The fractional uncertainty bands are computed from the square roots of the diagonal elements of the summed statistical and systematic matrices. The red band corresponds to the diagonal of the covariance matrix before the decorrelation procedure (lower left), and the blue line corresponds to the diagonal after the decorrelation procedure (lower right)

useful for visualizing the true data/MC agreement within the expected systematic uncertainties. The results of the decorrelation procedure outlined in this section are shown for the combined total covariance matrices, including both statistical and systematic uncertainties, are shown in Figs. 6.11 and 6.12.

6.4 Asimov Sensitivities

In order to quantify the improved sensitivity of the two-detector fit method, we compute the confidence interval in the sterile mixing parameter space $(\sin^2(\theta_{24}), \Delta m^2_{41})$ as determined by fitting an Asimov experiment. The Asimov experiment in the case of this analysis is defined as a high-statistics pseudodata generated using the three-flavor neutrino oscillations paradigm with all systematic parameters set to the nominal values. The Asimov experiment defines the expected median spectrum of the population of all possible spectra arising from the estimated statistical and systematic variations [240].

Contours showing the 90% C.L. Asimov sensitivities for the Far-over-Near and simultaneous two-detector fit methods are presented in Figure 6.13. A comparison of the plotted contours demonstrates the increased sensitivity for all mass-splitting scales, though the most significant improvement is seen for $\Delta m^2_{41} > 10$ eV^2. The source of this dramatic increase in sensitivity is the utilization of the full statistical power of the ND spectrum as was previously discussed, in addition to the more precise cancellation of only systematic effects between the FD and ND. The contributions to the Asimov sensitivity resulting from the component ν_μ-CC and NC samples is plotted in Figure 6.14. These

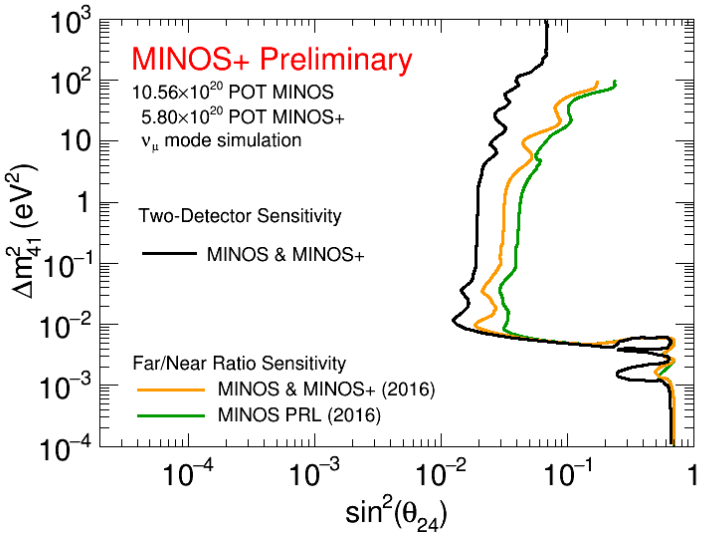

Figure 6.13: Comparison of the Asimov sensitivities computed using the simultaneous Two-Detector fit method for MINOS and MINOS+ simulation (black) with the Far-over-Near ratio method for the MINOS only analysis (green) and the combined MINOS and MINOS+ analysis (orange). The two-detector method has significantly higher sensitivity for all Δm^2_{41} with the greatest improvement at large mass-splitting.

contours demonstrate the dominance of the ν_μ-CC sample in terms of sensitivity to sterile oscillation parameters for all regions of the $(\sin^2(\theta_{24}), \Delta m^2_{41})$ parameter space due to significantly lower estimated systematic uncertainties. The NC events provide some excess sensitivity in the rapid oscillations region ($\Delta m^2_{41} > 500$ eV^2) and in the vicinity of the degeneracies associated with the atmospheric mixing parameters discussed in detail in Chapter 7.

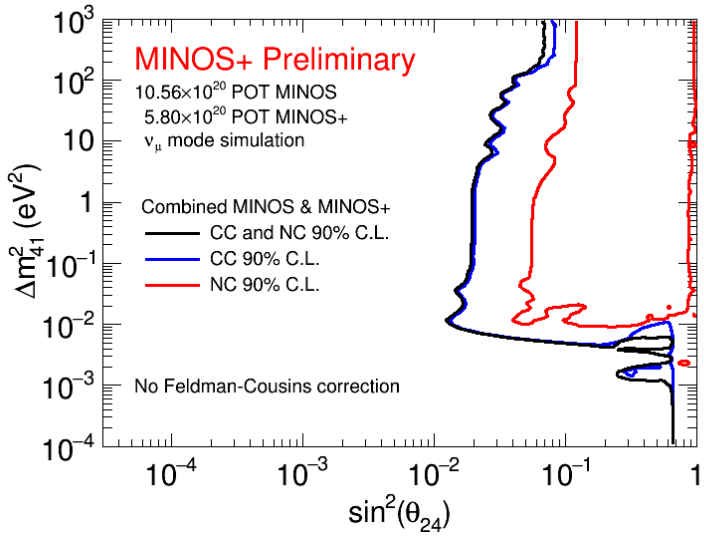

Figure 6.14: The 90% C.L. Asimov sensitivities computed in the simultaneous Two-Detector fit framework for the isolated ν_μ-CC sample (blue), the isolated NC sample (red), and the joint ν_μ-CC and NC fit (black). The ν_μ-CC sample provides the dominant sensitivity for all regions of the parameter space. The NC sample provides additional sensitivity at very high mass-splitting and in the region surrounding the atmospheric oscillations degeneracy discussed in Chapter 7.

The contributions to the Asimov sensitivity from independent fits to the ND and FD are compared with the simultaneous Two-Detector fit method

in Figure 6.15. The transition between the FD and ND dominance of the sensitivity takes place at $\Delta m^2_{41} \sim 1$ eV^2. The individual and joint detector contributions are also shown for the isolated CC and NC samples. The similarity between the CC sample contributions and the overall CC and NC Asimov sensitivity demonstrates again that the CC sample is the dominant source of sensitivity over the entire search range, though the NC events provide a cross-check on the observation of large mixing angles. The comparison of the individual FD Asimov sensitivity to that for the Two-Detector demonstrates the role of the ND in strong cancellation of correlated sources of systematic uncertainty. Further, the magnitude of the systematic and statistical uncertainties in each detector are such that the detectors coincidentally contribute in nearly equal proportion to the Asimov sensitivity for high Δm^2_{41}.

6.4.1 Shape vs. Normalization

Decorrelation of the covariance matrix and the resulting modifications both to the band of uncertainty and the spectral prediction makes manifest the complex interplay between the aspects of shape and normalization of the energy spectra. In this context, shape refers to fluctuation behavior that does not result in a net change in event rate over the energy spectrum, whereas normalization refers to the obverse. It has been shown in previous sections that the measurement of a normalization deficit is necessary in this analysis for detecting sterile neutrino mediated oscillations that may occur at shorter baselines than the distance to the ND. In a covariance matrix fit, it is non-trivial to

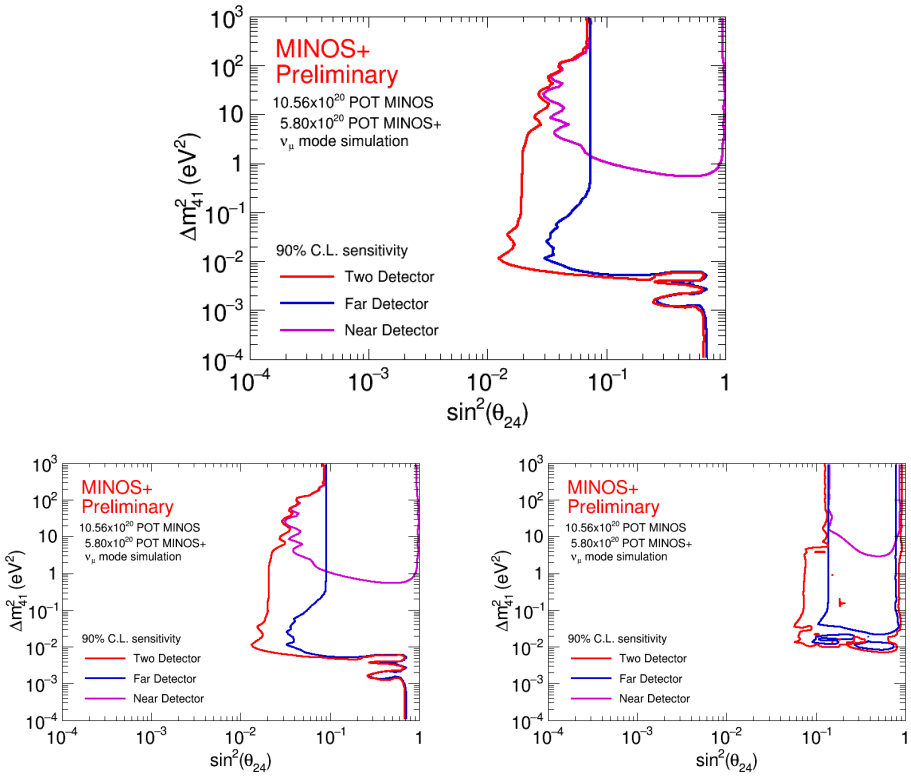

Figure 6.15: Asimov sensitivities for the simultaneous Two-Detector fit method compared with the independent fits to the ND and FD. The detector contributions are plotted for fits to the isolated ν_μ-CC sample (bottom left), the isolated NC sample (bottom right), and the joint ν_μ-CC and NC fit (top).

declare a single value which captures the level of uncertainty associated with normalization. An effective normalization uncertainty can be determined by sampling the χ^2 function over a range of overall normalization shifts and determining the magnitude of the displacement which varies the χ^2 by one unit. This procedure is demonstrated in Figure 6.16 for the MINOS and MINOS+ simultaneous Two-Detector fit, and the effective 1σ normalization uncertainty is found to be 8.3% for the $\nu_\mu - CC$ sample and 9.6% in the case of the NC sample. Using these measured effective normalization parameters, we use a post-fit minimization procedure to determine the magnitude of the systematic contribution from the normalization that was favored by the covariance matrix fit, which is an equivalent result to a fit using a normalization systematic correction scaled by nuisance parameter.

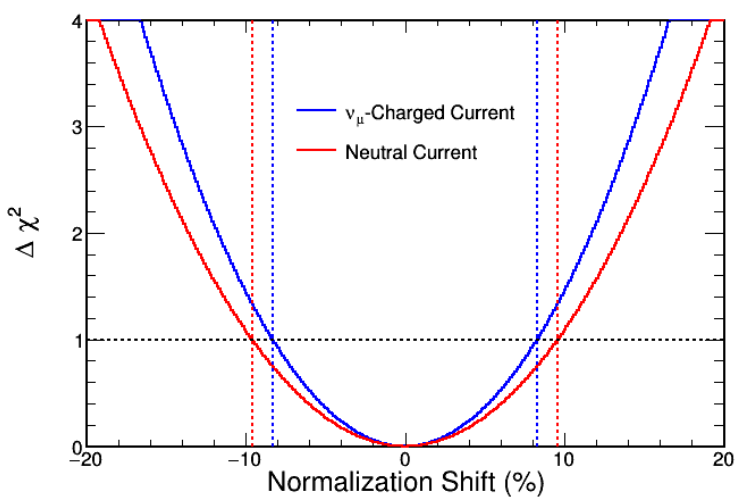

Figure 6.16: The χ^2 function for three flavor fake data scaled by a normalization factor. This implies that the effective normalization systematic is ∼3%.

The contributions to the Asimov sensitivity by the shape and normalization effects is shown in Figure 6.17. For all $\Delta m^2_{41} < 10\, eV^2$ the contributions from shape modulations are the dominant source of sensitivity. It is important to note that for the purposes of the two-detector analysis a relative normalization difference between the FD and ND is a shape effect since it affects some bins of reconstructed energy at the exclusion of others. Thus, an exclusive normalization component of the sensitivity can only emerge when an absolute normalization offset is observed in both detectors. As has been discussed in previous sections, a net normalization offset can only be observed in both detectors when the first oscillation maximum precedes sampling by the ND, which corresponds to a large value of Δm^2_{41}. This is the reason that the dominant contribution to the experimental sensitivity transitions from shape-driven to normalization-driven effects with increasing mass-splitting.

Although perhaps intuitively unexpected, there exist contributions to the sensitivity due to shape effects at $\Delta m^2_{41} = 1$ keV^2. For sterile neutrino mediated oscillations with $\Delta m^2_{41} \geq 1$ keV^2, the first oscillation maximum occurs at shorter baselines than the distance to the ND, and thus the oscillations may be entirely smeared by energy resolution limitations such that both detectors observe a net normalization offset. In this case, the contribution due to shape arises from variations in the atmospheric oscillations maximum observed in both the CC and NC samples as was discussed in the phenomenology section and plotted in Figure 6.4. The shape contribution contour plotted in Figure 6.17 indicates the minimum constraint in the (3+1)-flavor parameter

space arising due to the observation in three-flavor neutrino oscillations of near-maximal atmospheric mixing.

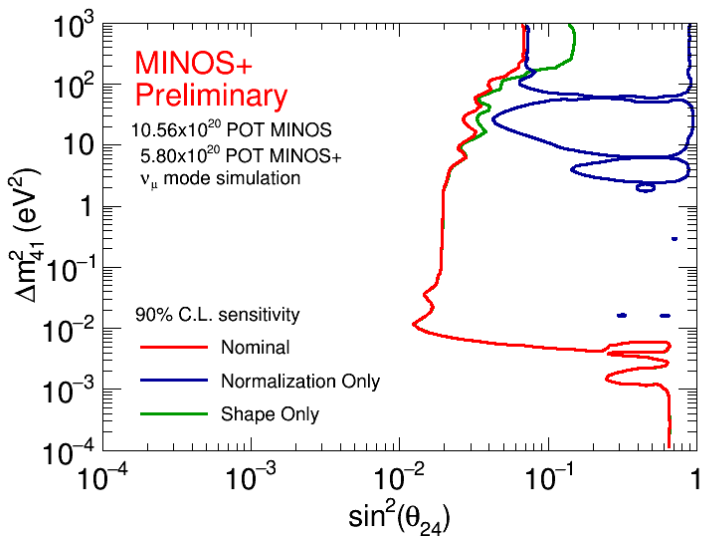

Figure 6.17: Comparison of the simultaneous Two-Detector Asimov sensitivity (red) to the contributions from the spectral shape variations (green) and the normalization systematic uncertainty (blue) as extracted in post-fit analysis. The normalization component dominates the sensitivity for $\Delta m^2_{41} > 100$ eV^2 while shape information dominates the sensitivity for the remainder of the parameter space.

6.4.2 Insufficiency of Asimov Sensitivity

The effectiveness of the Asimov sensitivity for determining the relative contributions from the various fit components and simulated data samples has been demonstrated. However, the Asimov experiment represents an idealized case for the experimental results and is inadequate in determining the expected median experimental sensitivity in the $(\sin^2(\theta_{24}), \Delta m^2_{41})$ parameter

space. In order to understand why this is true, we first note that the Asimov experiment spectrum can only correspond to the expected median sensitivity if systematic and statistical fluctuations that are symmetric with respect to the Asimov result in symmetric variations in the resultant sensitivity. This criteria can be tested empirically by applying symmetric shifts to the Asimov experiment and observing the effect on the sensitivity. It can be demonstrated to very high precision, as shown in Figure 6.19, that normalization-only shifts in the Asimov experiment result in symmetric shifts in the expected sensitivity. In this case, the median sensitivity of an ensemble of fluctuated pseudoexperiments coincides with the Asimov sensitivity. In contrast, as is shown in Figure 6.18, symmetric shifts with respect to the Asimov sensitivity that include shape information derived from known systematic uncertainties do not result in symmetric variations in the fluctuated sensitivities with respect to the Asimov sensitivity. Thus, the Asimov sensitivity is not generally an adequate approximation for the median experimental sensitivity.

In order to understand the differing behaviors for normalization-only and shapeful shifts with respect to the Asimov experiment, we note that a normalization shift with respect to the Asimov experiment approximates a possible sterile neutrino oscillation signal for high mass-splitting. The covariance matrix fit is highly sensitive to the detection of spectral variations that have the appearance of sterile oscillations, while strongly disfavoring a sterile neutrino interpretation of an expected systematic shape fluctuation. Any systematic variation which introduces spectral shape variations inconsistent

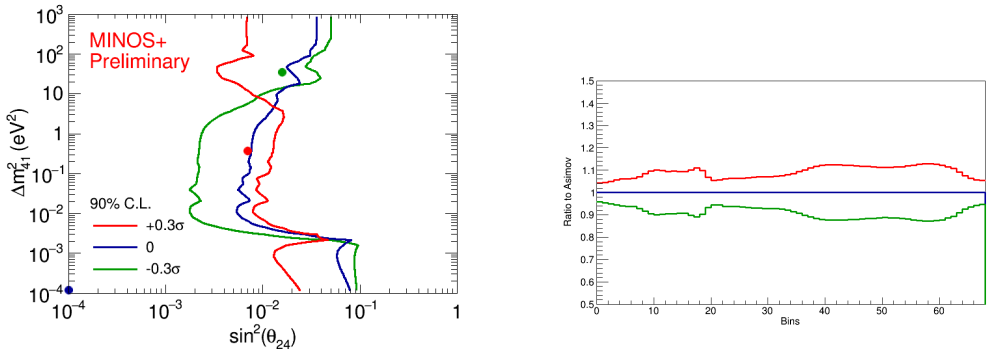

Figure 6.18: Ratios of pseudodata samples with symmetrically varied systematics parameters to the Asimov spectrum (right) and the resulting Asimov and fluctuated sensitivities in the sterile parameter space (left). The symmetry observed in the comparison of fluctuated and Asimov spectra is not translated to a symmetric response in the sensitivities.

with a sterile signature will necessarily increase the χ^2 and therefore tend to increase the sensitivity constraint, particularly for large Δm^2_{41}.

The asymmetric systematic fluctuations effected can be demonstrated by studying an ensemble of flucutated senstivities with full systematic variations, which do not necessarily mimic a sterile signal in the manner of an absolute normalization shift. The results of such a study are shown in Figure 6.20 where the FD has been removed from the sensitivities for simplicity. In the case of purely statistical fluctuations, we see a lack of agreement between the Asimov sensitivity and median of the fluctuated sensitivities due to the discord between the randomness of statistical fluctuations and the smoothly varying modulations that are observed for sterile signals. Reduction in the size of the data sample, which necessarily increases the relative statistical errors, results in a larger disagreement between Asimov and median sensitivity,

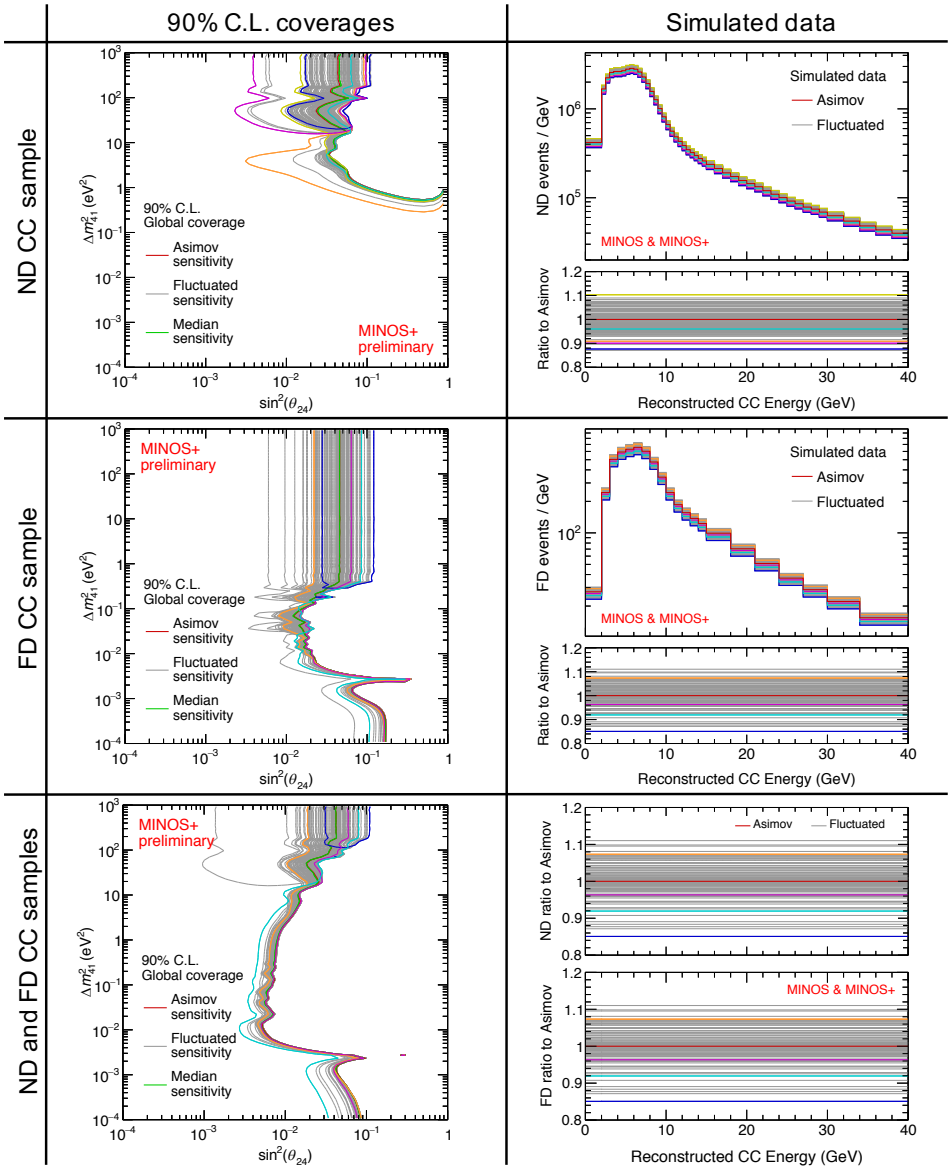

Figure 6.19: Demonstration of the effects on the Asimov sensitivity for normalization-only variations to the spectrum. The simulated data samples with normalization shifts .

though the relative size is preserved. The most dramatic difference between the Asimov and median sensitivities is seen for the highly-correlated systematics variations as this results in the strongest difference between possible sterile signals and expected systematic variations. As a result of these observations, Asimov experiments and the corresponding sensitivities are useful only for the rapid validation of the mechanism of the covariance fit method and should not be considered as a reliable determination of the expected experimental senstivity.

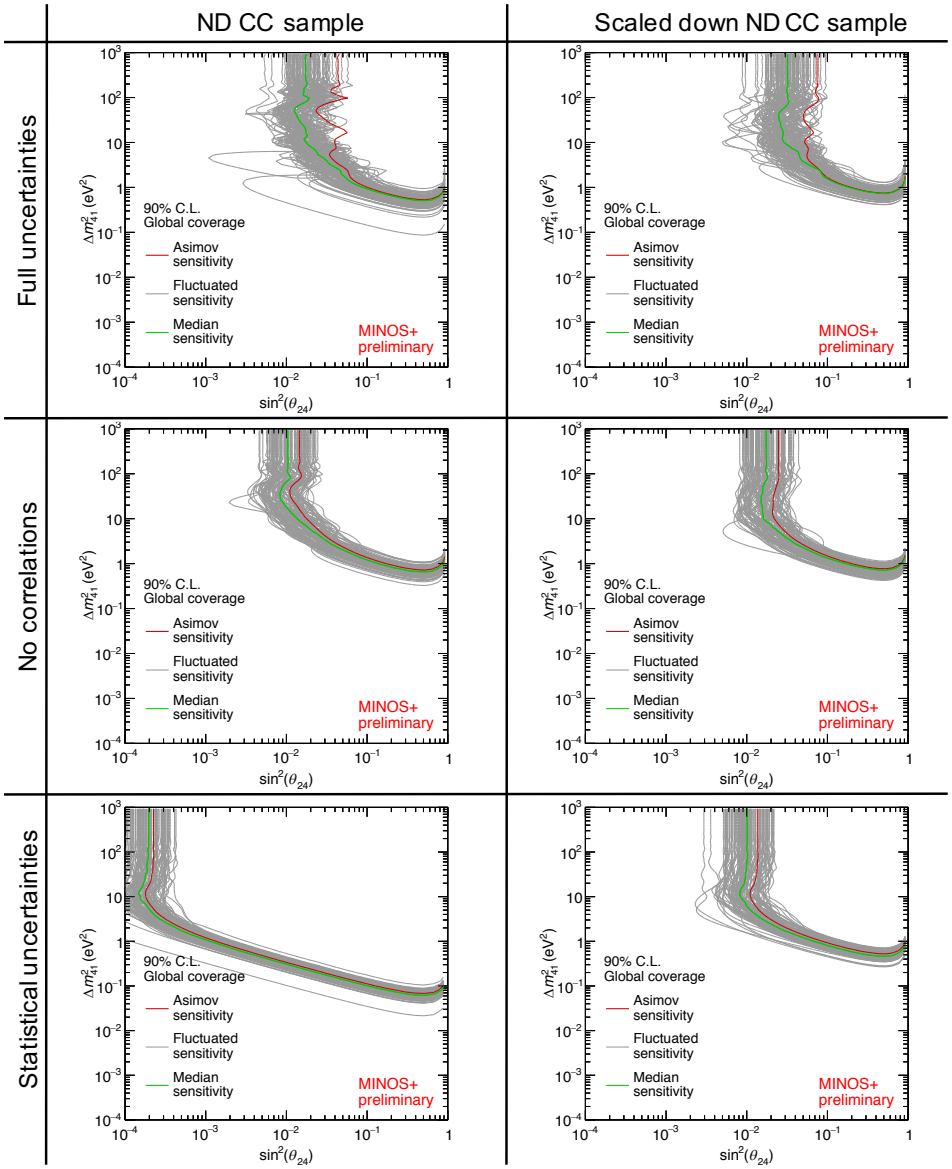

Figure 6.20: A simulated ν_μ-CC data study of the differences between the Asimov senstivity and median sensitvity of an ensemble of pseudoexperiments for the standard covariance matrix (top row), the covariance matrix with correlations removed (center row), and statistical uncertainty only (bottom row). The left column is generated using the full simulated ND CC sample, while the right column is produced with a scaled down ND CC sample in order to increase the significance of statistical uncertainties.

Chapter 7

Results of the Sterile Neutrino Oscillations Search

In this chapter, we present the results of the simultaneous Two-Detector search for sterile neutrino mediated oscillations. We begin by presenting the data spectra for the combined MINOS and MINOS+ samples, and by performing initial measurements of consistency with the standard three-flavor oscillations paradigm. The χ^2 surfaces resulting from the fit to the data are then presented along with the data spectra compared to the best-fit (3+1)-flavor spectral predictions. We then discuss the properties of the fit result including properties of the χ^2 surface and decomposition of the fit components. Further, we discuss the statistical interpretation of the fit results using two distinct methods to validate the setting of proper frequentist confidence intervals. Finally, we discuss an experimental combination with reactor neutrino experiments Daya Bay and Bugey-3 in order to frame the results in the electron neutrino appearance parameter space directly probed by LSND and MiniBooNE.

7.1 Reconstructed Energy Data Spectra

The sum of data collected by the MINOS experiment in neutrino (ν_μ) mode, which accumulated an integrated proton exposure of 10.56×10^{20} POT, and the MINOS+ experiment, which accumulated an integrated proton exposure of 5.80×10^{20} POT in the first two years of running, is shown in Figs. 7.1 and 7.2 for the ν_μ-CC selected and NC selected events, respectively. The reconstructed energy spectrum of the data demonstrate the substantial number of events MINOS and MINOS+ have collected over a broad range of energies, and the data is observed to be consistent with a three-flavor oscillations hypothesis, as expected from the standard oscillations result. The energy window used in this analysis ranges from $0 - 40$ GeV in both detectors, which ensures that data is collected and analyzed both from the strongly focused peak regions as well as the high-energy tail which is dominated by an unfocused, highly-forward parent hadron flux. The estimated backgrounds are also shown in the data energy spectra with the CC selection containing a minimal NC background component and the NC selection containing a substantially larger quantity of focused background CC events. The background CC events in the NC sample undergo three-flavor oscillations, as evidenced by the variation in the background flavor composition from the ND to the FD.

7.1.1 Consistency with Standard Oscillations

Visual inspection of the reconstructed energy data spectra in Figs. 7.1 and 7.2 shows apparent agreement with the standard three-flavor oscillations

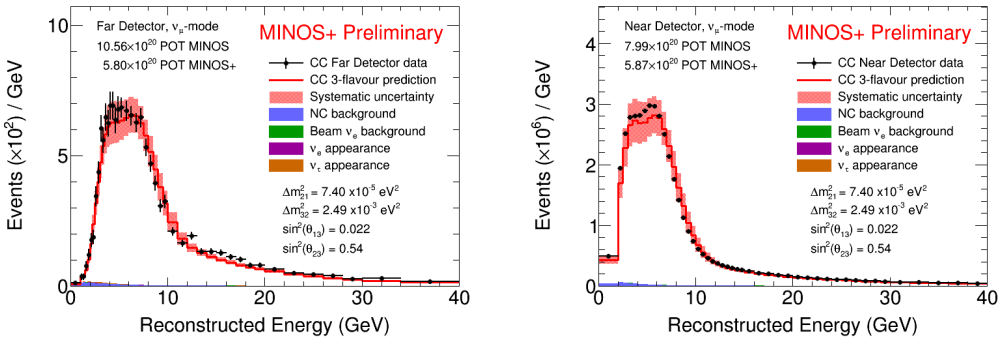

Figure 7.1: The FD CC-selected (left) and ND CC-selected (right) reconstructed energy data sample (black points) compared to the simulated prediction for standard three-flavor oscillations (red) displayed with the uncorrelated systematic uncertainty (red shading). The background events are also plotted in stacked histograms, with the NC events representing the dominant background component.

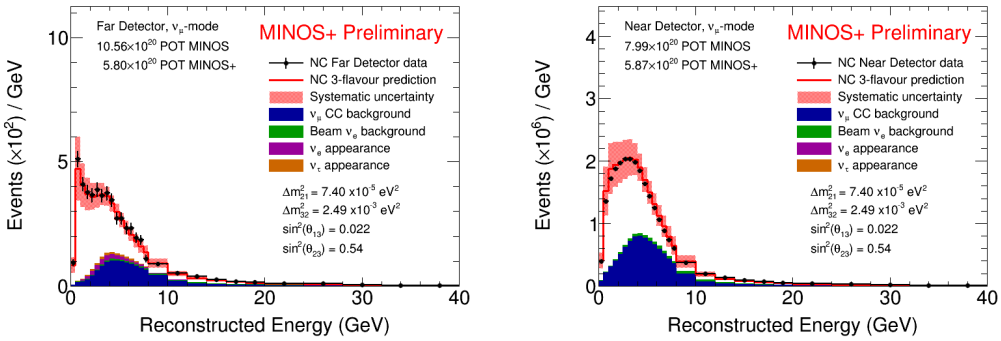

Figure 7.2: The FD NC-selected (left) and ND NC-selected (right) reconstructed energy data sample (black points) compared to the simulated prediction for standard three-flavor oscillations (red) displayed with the uncorrelated systematic uncertainty (red shading). The background events are also plotted in stacked histograms, with the ν_μ-CC events representing the dominant background component. The variations in the relative composition of the background events is due to the effects of three-flavor oscillations.

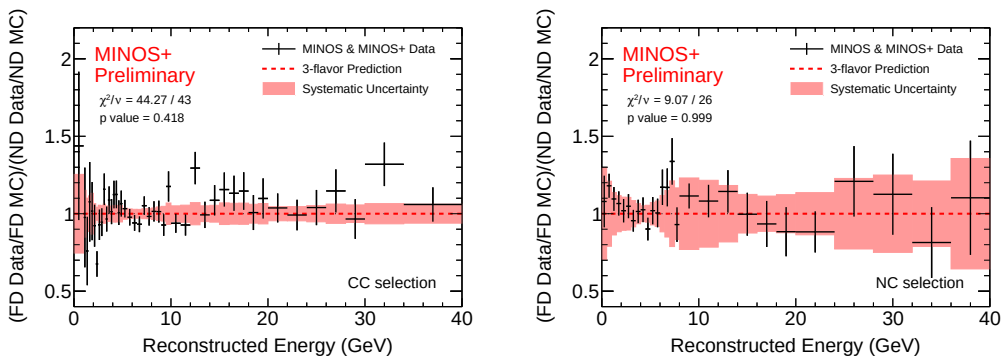

Figure 7.3: The double ratio of the Far-over-Near ratio in data (black) to the Far-over-Near ratio for the standard three-flavor prediction (dashed red) for the CC-selected sample (left) and the NC-selected sample (right). Relative statistical uncertainties are represented by the black error bars, while the relative decorrelated systematic uncertainties are shown by the red shaded bands. The χ^2 per degree of freedom and p-values are computed using the standard Pearson's χ^2 test [241] and are insufficient to reject the null three-flavor oscillations hypothesis at a reasonable level of confidence.

paradigm. In order to make an initial quantitative statement with respect to the level of this agreement, we construct double-ratio spectra separately for the ν_μ-CC and NC spectra where the ith bin is given by

$$\mathscr{R}_{3\nu} = \frac{\mathrm{FD}_{\mathrm{pred},3\nu}/\mathrm{FD}_{\mathrm{data}}}{\mathrm{ND}_{\mathrm{pred},3\nu}/\mathrm{ND}_{\mathrm{data}}}. \tag{7.1}$$

In Eq. 7.1, $\mathrm{FD}_{\mathrm{MC},3\nu}$ and $\mathrm{ND}_{\mathrm{MC},3\nu}$ are the MC reconstructed energy spectra simulations assuming three-flavor oscillations and FD_{D} and ND_{D} are the data spectra. In the case of an Asimov experiment, which is defined by the expected median spectrum under the three-flavor oscillations hypothesis, this ratio would be uniformly unity. The data $\mathscr{R}_{3\nu}$ spectra are plotted in Fig. compared to the prediction from standard three-flavor oscillations with the

systematic uncertainty band displayed after decorrelating the covariance matrix as described in Chapter 6. We compute a χ^2 statistic using Pearson's χ^2 test [241], which results in $\chi^2/dof = 44.27/43$ and $\chi^2/dof = 9.07/26$ for the CC- and NC-selected samples, respectively. The p-value associated with the observed χ^2, which is the probability of finding a distribution at least as discrepant as we observe, conditional on a true standard oscillations hypothesis, is 0.418 in the case of the CC sample and 0.999 in the case of the NC sample.

The initial assessment of the double ratio $\mathscr{R}_{3\nu}$ permits two general conclusions. First, the variations between the observed data spectra and the three-flavor oscillations predictions are not statistically significant. In order for a result to permit rejection of the null hypothesis, which in this case is the three-flavor paradigm, a p-value threshold is usually set at a value less than 0.05, which would represent a greater than 2σ deviation from the expected result. Neither the ν_μ-CC- nor NC-selected samples give a large enough χ^2 value to rise to such a threshold. The second conclusion is that the p-values are indicative of a greater overall disagreement between data and MC in the CC sample as opposed to the NC sample under the assumption of three-flavor oscillations. This result is attributable at least in part to both a lower overall event rate in the NC selected sample and larger residual systematic uncertainties in this sample after accounting for correlated effects. It is important to note that this initial evaluation of the data suffers the weaknesses associated with the Far-over-Near ratio method discussed in Chapter 6, whereas statements of greater significance can be achieved through an analysis using the

simultaneous Two-Detector fit, as discussed in the following sections.

7.2 The χ^2 Surfaces

Using the simultaneous Two-Detector fit method, we minimize the χ^2 test statistic as described in Section 6.3.1 using the MINUIT package [242] within the ROOT data analysis framework. The best-fit (minimum) χ^2 at each fixed point of a logarithmically-spaced grid in the parameter space $(\sin^2(\theta_{24}), \Delta m^2_{41})$ is shown in Fig. 7.4 with the identically computed surface for the Asimov spectrum also shown for comparison. The plotted surfaces are truncated such that the color scale represents the range $\Delta\chi^2 \in [0, 20]$. The Asimov and data fit χ^2 surfaces have similar structures, particularly in the region of 10^{-2} eV$^2 < \Delta m^2_{41} < 10^3$ eV^2 where the χ^2 values increase uniformly across the range of mass-splitting at an approximately quadratic rate. Both surfaces also show clear signs of the degenerate regions in the area where $\Delta m^2_{41} < 5 \times 10^{-2}$ eV^2 and $\sin^2(\theta_{24}) > 0.01$, which is discussed in detail in Section 7.2.2.

The global best-fit points are indicated on the χ^2 surfaces by the yellow circles, and the parameters associated with the global best fit to the combined MINOS and MINOS+ data are listed in Table 7.2. The global best-fit to the data is degenerate with the standard three-flavor oscillations solution as will be discussed in the next section. At the joint best-fit point, $\chi^2/ = 99.3085/140$, which corresponds to significantly less than one unit of χ^2 per degree of freedom and is indicative of conservative error estimation. While the difference

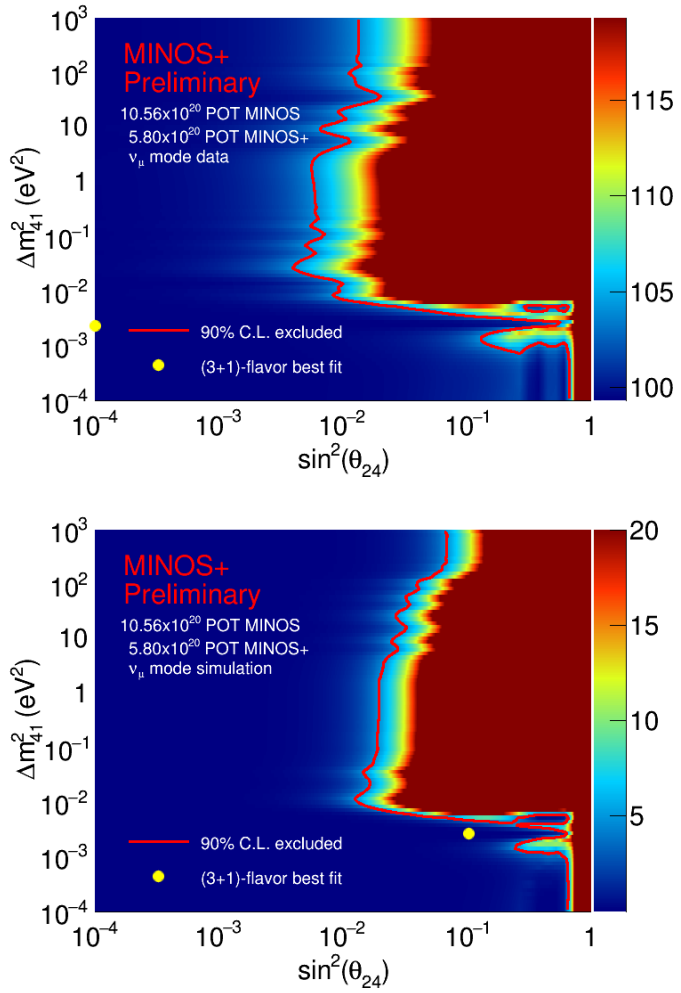

Figure 7.4: The χ^2 surfaces in the $(\sin^2(\theta_{24}), \Delta m^2_{41})$ parameter space resulting from the simultaneous Two-Detector fit to data (upper) and to the Asimov spectrum (lower). The contour at the nominal $\Delta\chi^2_{2,0.9} = 4.61$ value for the 90% C.L. is drawn (red) without correction by the FC method.

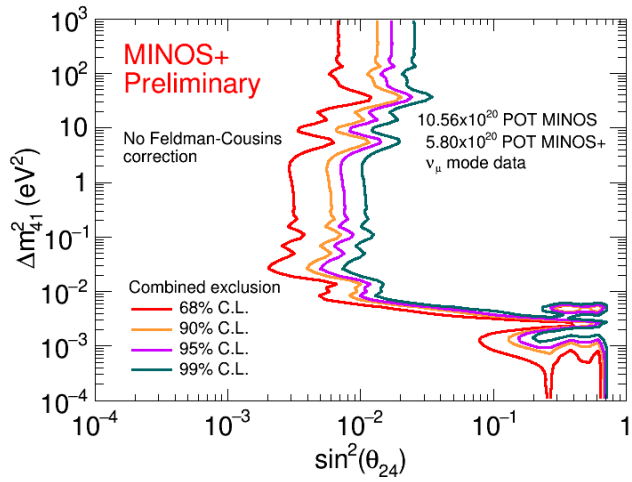

Figure 7.5: Contours of constant $\Delta\chi^2$ resulting from the (3+1)-flavor model Two-Detector Fit to MINOS and MINOS+ data are plotted in the parameter space $(\sin^2(\theta_{24}), \Delta m^2_{41})$. The plotted contours are the raw output of the fit framework and have not been corrected by the FC method.

between the Asimov and data best-fit points is large in the context of the available parameter space, it must be emphasized that both of these solutions are indistinguishable from the standard oscillations case. The $\Delta\chi^2$ with respect to the standard three-flavor oscillations prediction is 0.0002, which is negligible.

Given that we minimize the χ^2 statistic with respect to all free neutrino oscillation parameters, the number of degrees of freedom of the distribution for the difference of χ^2 given by

$$\Delta\chi^2 = \chi^2_{profile} - \chi^2_{best}, \tag{7.2}$$

where $\chi^2_{profile}$ is the minimum χ^2 at a given $(\sin^2(\theta_{24}), \Delta m^2_{41})$ grid point, and χ^2_{best} is the global minimum χ^2, is reduced to the dimensionality of the parameter space under the assumption of Gaussian-distributed uncertainties and an

χ^2_k	Confidence Level			
k	68%	90%	95%	99%
1	1.00	2.71	3.84	6.63
2	2.28	4.61	5.99	9.21

Table 7.1: Critical values defining the tail probability (Confidence Level) of the χ^2_k distribution where k is the number of degrees of freedom.

absence of physical boundaries. These assumptions are discussed further in Section 7.3. The critical values of the χ^2 distribution, which delimit particular confidence levels (C.L.s), defined by the p-value or tail proability, are given in Table 7.1 for both one and two degrees of freedom. The contours of $\Delta\chi^2$ with respect to the global minimum for the data fit corresponding to the relevant confidence levels in Table 7.1 are plotted in Fig. 7.5, and the 90% C.L. contour alone is also plotted superimposed on the χ^2 surface plot in Fig. 7.4. The C.L. contours demonstrate the nearly uniform decrease with respect to Δm^2_{41} in the overall data constraint as the confidence level is increased.

7.2.1 Best Fit Reconstructed Energy Spectra

The ν_μ-CC- and NC-selected data as a function of reconstructed energy compared to the standard three-flavor prediction and the (3+1)-flavor best-fit before and after application of the decorrelation procedure (see Section 6.3.3) are shown in Figs. 7.6 and 7.7, respectively. Fluctuations are observed between data and raw three-flavor predictions which are consistent with those expected from statistical and systematic uncertainties, and the effect of decorrelation is

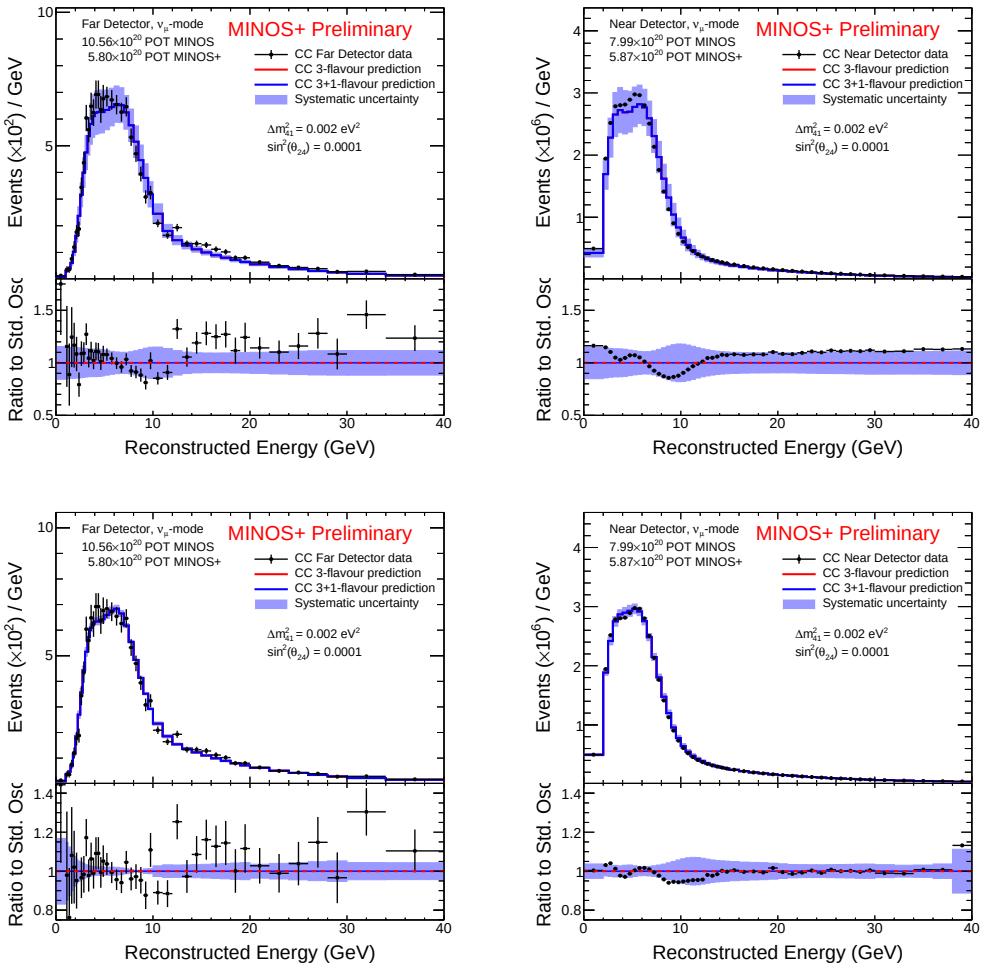

Figure 7.6: The FD CC-selected (left column) and the ND CC-selected (right column) reconstructed energy data sample (black points) compared to the standard three-flavor oscillations prediction (red) and the best-fit 3+1-flavor predictions (blue). The upper plots show the raw spectra and uncorrelated systematic uncertainties while the lower plots show the spectra and residual uncertainties after the application of the decorrelation procedure to both the three-flavor predictions and the (3+1)-flavor best-fit predictions.

Parameter	best fit	preferred values	
	CC+NC	CC	NC
Δm^2_{32} (eV^2)	2.430×10^{-3}	2.430×10^{-3}	2.636×10^{-3}
Δm^2_{41} (eV^2)	2.325×10^{-3}	2.325×10^{-3}	9.256×10^{2}
$\sin^2(\theta_{23})$	0.6413	0.6413	0.5103
$\sin^2(\theta_{24})$	0.0001	0.0001	0.9526
$\sin^2(\theta_{34})$	< 0.0001	< 0.0001	1.0000

Table 7.2: Best-fit parameter values in the (3+1)-flavor model from the simultaneous Two-Detector fit to the combined MINOS and MINOS+ ν_μ-CC and NC disappearance samples. The preferred parameter values for the CC and NC component contributions to the joint fit are shown for comparison.

discussed in the context of systematic effects in Section 7.2.3. A comparison of the data spectra with the three-flavor prediction spectra shows no significant modulations consistent with a (3+1)-flavor model such as significant rate depletion with oscillatory effects, which would be most clearly visible when comparing the ratio of the data specta to the standard oscillations prediction. As stated in the previous section, the (3+1)-flavor best fit is approximately degenerate with the three-flavor solution as evidenced by the complete overlap of the red and blue spectra and ratios. The NC spectra retain larger residual deviations from the standard oscillations prediction than the CC spectra, however this corresponds well with the similarly larger residual uncertainties presnt in the NC sample, which tends to negate a sterile neutrino interpretation of these features given the present state of uncertainty.

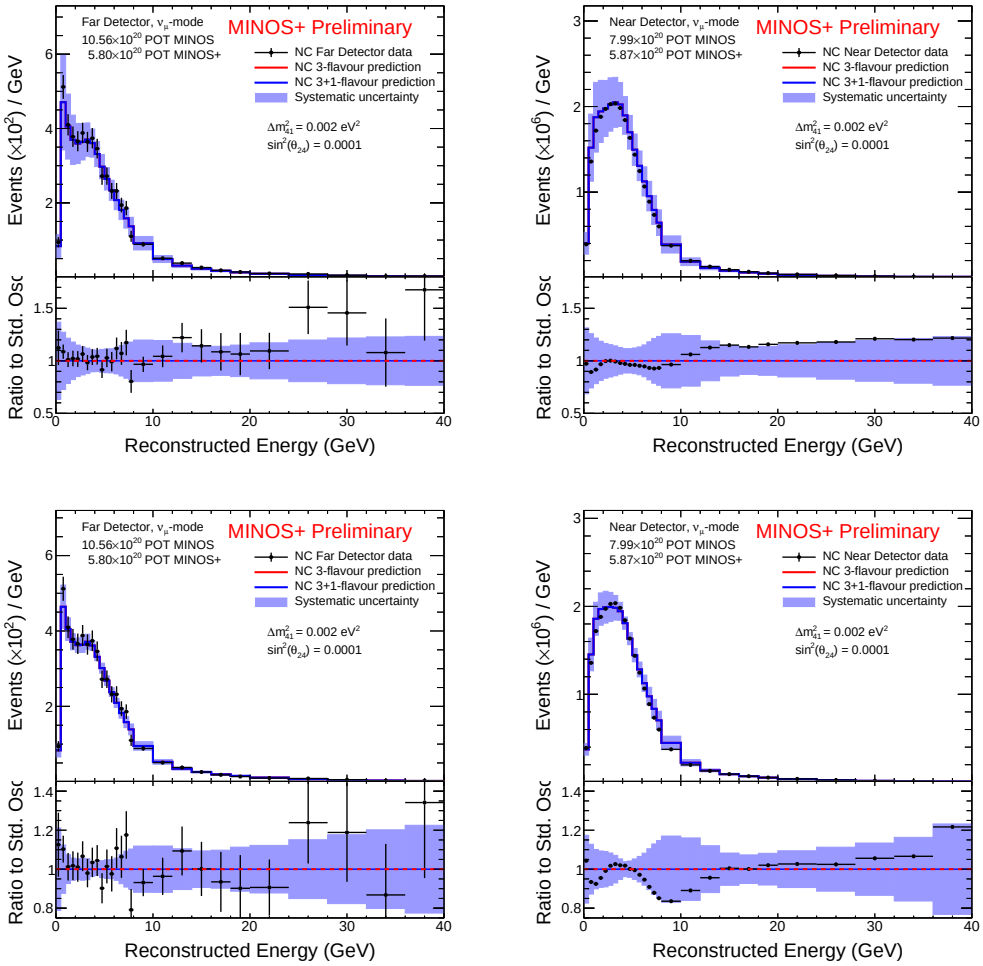

Figure 7.7: The FD NC-selected (left column) and the ND NC-selected (right column) reconstructed energy data sample (black points) compared to the standard three-flavor oscillations predictions (red) and the best-fit 3+1-flavor predictions (blue). The upper plots show the raw spectra and uncorrelated systematic uncertainties while the lower plots show the spectra and residual uncertainties after the application of the decorrelation procedure to both the three-flavor predictions and the (3+1)-flavor best-fit predictions.

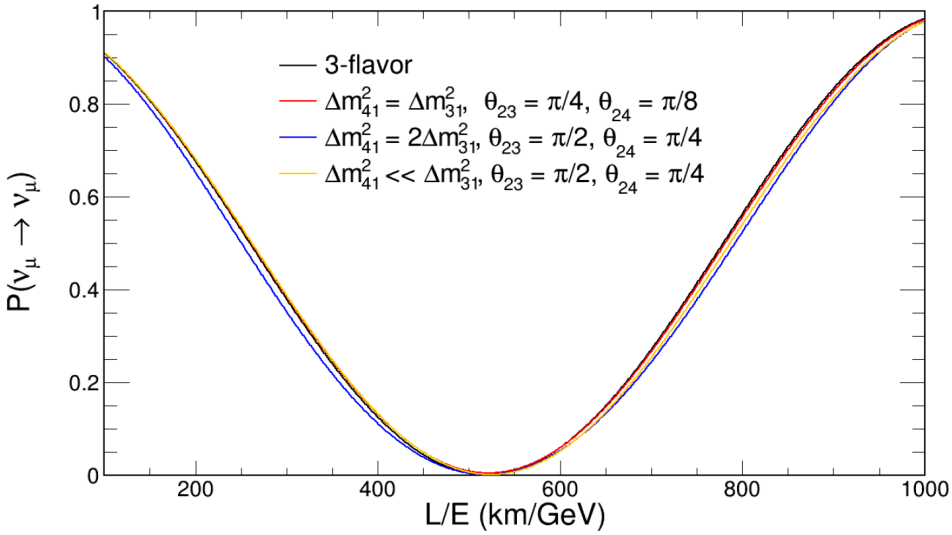

Figure 7.8: Oscillation probability curves plotted for sets of (3+1)-flavor parameters which result in approximately degenerate solutions to the standard three-flavor oscillations case. The analysis presented here does not strongly distinguish between these approximate degeneracies.

7.2.2 Degeneracies

In each of the χ^2 surface plots presented, a rapid loss of sensitivity begins to occur in the region of $\Delta m^2_{41} < 5 \times 10^{-2}$ eV^2, with an additional distinct island of allowed parameter space for $\Delta m^2_{41} \approx 5 \times 10^{-2}$ eV^2 and $\theta_{24} \approx \pi/4$. These features can be attributed to the possibility of emergent degeneracy between the probabilities for ν_μ-CC disappearance and NC disappearance in the standard three-flavor and (3+1)-flavor models. The (3+1)-flavor oscillations probability becomes approximately degenerate with the standard three-flavor oscillations probability in three cases:

1. $\Delta m^2_{41} \ll \Delta m^2_{31}$. In this case, $\Delta m^2_{41} \approx 0$ and $\Delta m^2_{43} \approx \Delta m^2_{31}$. The convergence of the oscillation frequencies reduces the dependence of the probability function to the single dominant atmospheric oscillations frequency. The fit can then mimic the standard oscillations probability by taking $\theta_{24} \approx \pi/4$ and $\{\theta_{23}, \theta_{34}\} \approx \pi/2$.

2. $\Delta m^2_{41} \approx \Delta m^2_{31}$. As in the first case, the oscillation frequencies here converge on the single atmospheric oscillation frequency, since $\Delta m^2_{43} \approx 0$. This results in a multivalued functional form for the magnitude of the observed atmospheric oscillation maximum, whereby the fit may mimic standard oscillations by pairs of mixing angles θ_{23} and θ_{24} less than the upper-octant constraint from a three-flavor fit to the effective θ_{23} mixing angle. An example pairing of the mixing angles resulting in approximate degeneracy is $(\theta_{23}, \theta_{24}) = (\pi/4, \pi/8)$

3. $\Delta m^2_{41} \approx 2\Delta m^2_{31}$. In this final case, since the sterile mass-splitting is twice as large as the atmospheric, $\Delta m^2_{43} = \Delta m^2_{31}$ which again reduces to a single overall oscillation frequency approximately consistent with the observed atmospheric oscillations. The fit can then mimic standard three-flavor oscillations by taking $\theta_{24} \approx \pi/4$ and $\{\theta_{23}, \theta_{34}\} \approx \pi/2$. This results in allowed regions in the sterile parameter space of similar shape with allowed regions from the standard oscllations analysis.

In each of the scenarios the fit is free to minimize the χ^2 to a value consistent with standard three-flavor oscillations. Given that both the Asimov spectrum and the observed data spectrum are consistent with the expectation from standard three-flavor oscillations, we are prevented from excluding these regions from the allowed parameter space.

7.2.3 Systematic effects

The disagreement between the data and three-flavor oscillations prediction shown in the upper panels of Figs. 7.6 and 7.7, particularly for reconstructed energies larger than 12 GeV, has the clear appearance of a systematic effect. This attribution is due to the observation of similar fluctuations at similar energies observed in both detectors and due to the fluctuations being observed in a large number of consecutive bins. Further, the fact that in nearly all cases the observed fluctuations are consistent with an excess number of events as opposed to a rate depletion leads to the conclusion that an explanation due to oscillation phenomena is unlikely.

Having made these observations, it is critical to restate that the power of the covariance matrix mechanism within the Two-Detector fit framework is to minimize the impact of known systematic uncertainties at the level achieved by a standard extrapolation method, while preserving strong sensitivity to oscillations phenomena. For illustration purposes, one can imagine that the covariance matrix method achieves these coequal aims by "selecting" from amongst a series of embedded correlated systematic shapes, "extracting" the given shape from the covariance matrix, and "scaling" a corrected MC prediction according to those shapes with iterative repetition until irreducible uncorrelated uncertainties are all that remains. The actions in this illustration are not to be taken literally, as the matrix accomplishes the net effect by a single calculation, which can only be decomposed in the described manner through the decorrelation procedure.

The output of the decorrelation procedure is the irreducible, uncorrelated systematic uncertainty and the systematically-corrected MC prediction. We can demonstrate the proper functioning of the covariance matrix method by observing the results of the decorrelation method shown in the lower panels of the same Figs. 7.6 and 7.7. In the CC selected sample, it is readily apparent that the differences between data and the uncorrected MC prediction are readily attributable to the various correlated systematic uncertainties contained in the covariance matrix given the decorrelated agreement.

In the case of the NC sample, the discrepancy between data and the three-flavor prediction in the ND appears to retain residual correlated shape

Uncertainty	Sensitivity to $\sin^2\theta_{24}$ at:	
	$\Delta m^2_{41} = 1\,\mathrm{eV}^2$	$\Delta m^2_{41} = 1000\,\mathrm{eV}^2$
Statistics only	0.0008	0.0002
+Energy scale	0.0054	0.0003
+Hadron production	0.0131	0.0063
+Cross section	0.0138	0.0103
+Background	0.0141	0.0112
+Beam	0.0143	0.0128
+Other	0.0153	0.0165

Table 7.3: The cumulative reduction of the experimental sensitivity as determined from the median of fluctuated pseudoexperiments to the oscillations parameter $\sin^2\theta_{24}$ due to the effects of systematic uncertainties for selected values of Δm^2_{41}. The sources of systematic uncertainty given in this table are described in detail in Chapter 5.

effects, implying that a source of systematic uncertainty was suboptimally treated as uncorrelated in the construction of the covariance matrix. In particular, it may be noted that the shape of the irreducible uncorrelated uncertainty and the residual data/MC discrepancy are highly similar and share common features with the uncertainty due to hadronic shower energy modeling errors given in Fig. 5.7. A subsequent analysis of this data sample could potentially achieve a more constraining overall result if hadronic shower energy modeling could be reevaluated in a manner consistent with bin-to-bin correlations, resulting in both greater error reduction and signficantly better post-fit agreement between data and simulation. For the purposes of this analysis, we note that since the overall magnitude of the residual data/MC discrepancy is

well contained within one standard deviation of the uncorrelated uncertainty for all energies, the limits computed in this analysis are a conservative (i.e. minimally constraining) given the observed data.

The estimated cumulative effects on the experimental sensitivity to $\sin^2(\theta_{24})$ are listed in Table 7.3. The largest single degradation in sensitivity is due to the hadron production systematic, which is attributable to the large uncertainty over a broad range of energies as well as the loss of strong correlation as a function of bin-to-bin energy difference. The degradation in sensitivity in the inter-detector region ($\Delta m^2_{41} \approx 1$ eV^2) is initially signficant with reduced impact as a large number of systematic effects are absorbed. The high mass-splitting region shows a more incremental response to the addition of systematic sources, which is attributable to the increased importance of correlated, shapeful systematic uncertainties given the negligible ND statistical uncertainty.

7.2.4 Decomposition of the χ^2 Contributions

The modular structure of the simultaneous Two-Detector fit framework allows for the decomposition of various subcomponents, which contribute to the joint χ^2 fit surface. In decomposing the results of a multi-input joint fit, it must be noted that only the dominant contributions in any given decomposition can be interpreted in the context of physical phenomena. If a single component contribution to the overall χ^2 is much larger than others, the subdominant components may be allowed to experience pathological behaviors

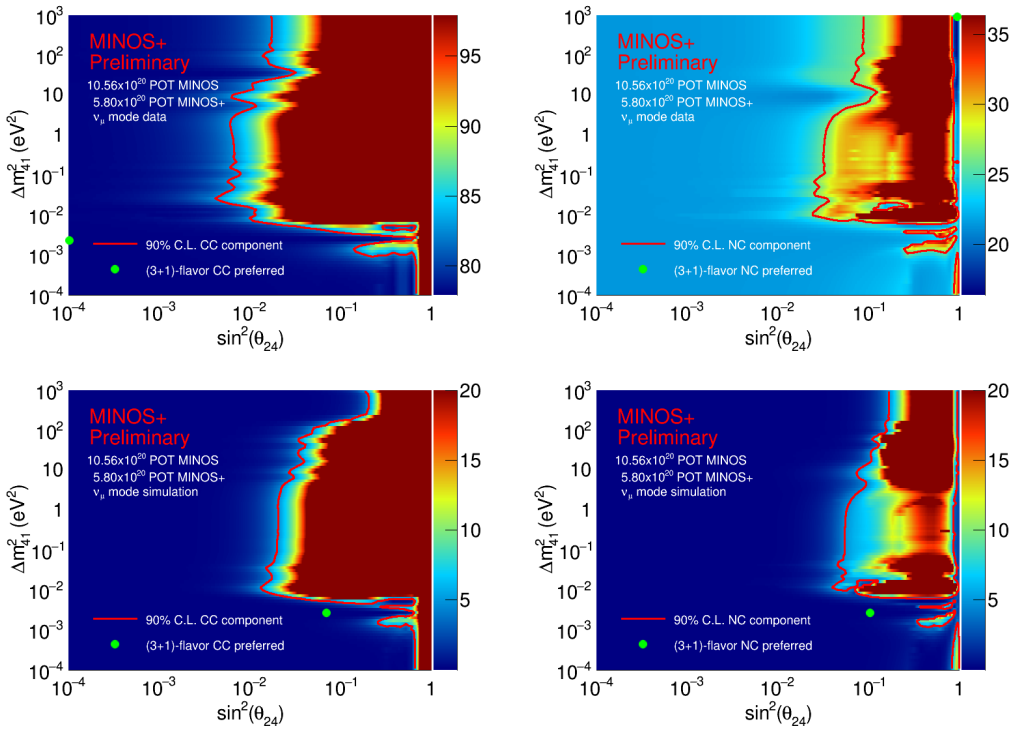

Figure 7.9: The χ^2 surfaces in the $(\sin^2(\theta_{24}), \Delta m^2_{41})$ parameter space for the CC (left) and NC (right) component samples resulting from the simultaneous Two-Detector fit to data (upper) and to the Asimov spectrum (lower). The contours at the nominal $\Delta\chi^2_{2,0.9} = 4.61$ value for the 90% C.L. are drawn (red) with respect to the best-fit point for the joint fit and without correction by the FC method. The minimum χ^2 point in each component plot is indicated by the green point.

Component	χ^2
CC sample	77.9479
NC sample	21.3408
Δm^2_{32} penalty	0.0196
$\chi^2_{4\nu}$ best fit	99.3083
$\chi^2_{3\nu}$ best fit	99.3085
$\Delta\chi^2$	0.0002

Table 7.4: The contributions to the χ^2 test statistic at the (3+1)-flavor best fit to MINOS and MINOS+ ν_μ-CC and NC data. The best-fit χ^2 to the three-flavor hypothesis and the $\Delta\chi^2$ differentiating (3+1)- and three-flavor hypotheses are also given.

without having an observable effect on the overall results.

Perhaps the most obvious decomposition is the separation of contributions from the ν_μ-CC- and NC-selected samples. The χ^2 surfaces extracted from the joint fit result for the CC and NC samples, both in the case of the Asimov spectra and data, are shown in Fig. 7.9. Here the same trunctation has been used as in the overall fit surface such that the color scale represents the range such that $\Delta\chi^2 \in [0, 20]$.

We can immediately see significant similarities in overall structure between the data and Asimov cases, with the exception being that the χ^2 increases at a slightly larger rate as a function of $\sin^2(\theta_{24})$ in the data surface as opposed to the Asimov sensitivity. The 90% C.L. limits drawn in Fig. 7.9 use the $\Delta\chi^2$ critical value indicated by Table 7.1 as computed from the best-fit point of the joint fit, which does not necessarily coincide with the preferred

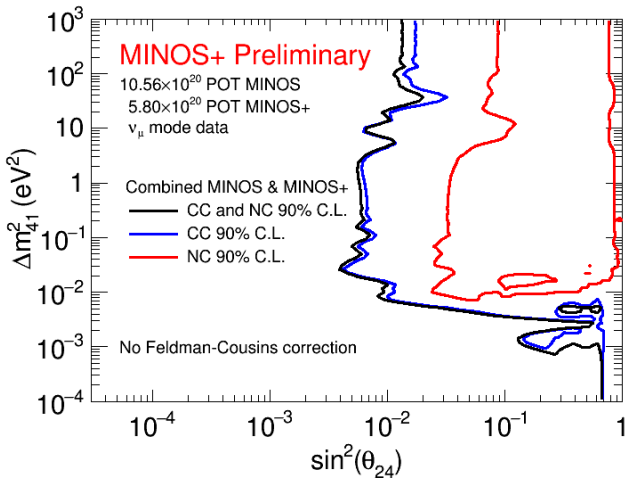

Figure 7.10: The upper limit contour at 90% C.L. in the parameter space $(\sin^2(\theta_{24}), \Delta m^2_{41})$ resulting from the (3+1)-flavor model Two-Detector Fit to the combined ν_μ-CC and NC samples (black) in comparison to the limits computed from the CC (blue) and NC (red) component surfaces in the joint fit. All contours are constructed by considering the $\Delta\chi^2$ with respect to the joint best-fit point. The plotted contours are the raw output of the fit framework and have not been corrected by the FC method.

parameters indicated by the minimum χ^2 in the surface for each sample. A comparison of the joint best-fit parameters to the preferred values in each of the component samples is given in Table 7.2. The parameters preferred by the CC sample are degenerate with those preferred by the joint fit. The values preferred by the NC surface are an artifact of the joint fit procedure and should not be attributed to oscillations phenomena given that the point is in region where there is not expected to be NC sensitivity and where the CC χ^2 contribution is extremely high, which can allow for the aforementioned pathologies.

The contributions of the CC and NC samples to the total χ^2 at the joint best-fit point are given in Table 7.4. The CC component is the dominant contributor to the total χ^2 with the NC sample contributing around one-third of the value and the Δm^2_{32} penalty term discussed in Section 6.3.1 making a negligible contribution. The dominance of the CC sample for the entire range of Δm^2_{41} at the 90% C.L. can be seen in Fig. 7.10, where the CC and NC component contours have been drawn for comparison with the combined fit. Given the observed data in MINOS and MINOS+, the NC sample provides only a minor increase in the overall exclusion region, which is very nearly uniform across the entire range of the parameter space and is consistent with the expectation for standard three-flavor oscillations as demonstrated in the Asimov study in Fig. 6.14.

A second important decomposition of the joint fit result is the separation of exclusion power from isolated normalization and shape effects, corre-

sponding to the same study performed on the Asimov sensitivity in Fig. 6.17. The separate exclusion limits from normalization and shape components constructed using the $\Delta\chi^2$ with respect to the joint best fit is plotted in Fig. 7.11. In contrast to the Asimov spectrum, the observed data spectrum contains systematic and statistical fluctuations, as would be expected in the case of any experimental result. These fluctuations introduce excess shape information beyond that which would be expected by an Asimov experiment, and this results in the shape contribution to the joint limit overwhelming normalization-only contributions for the vast majority of the range of Δm^2_{41}. This is the opposite behavior of what is observed in the case of the Asimov sensitivity for large sterile mass-splitting. For this reason, it is not possible to determine the effective normalization systematic constraint used in the fit directly from the data fit.

At high Δm^2_{41}, the 90% CL limit on $\sin^2\theta_{24}$ in the Asimov case (Fig. 6.17) is due almost entirely to normalization effects since for sufficiently small θ_{24} the probability difference is an energy-independent net deficit. In such a case, the effect of having a large number of bins in the fit to measure shape information is rendered ineffective, and the measurement is equivalent to a counting experiment. These conditions, which are satisfied by our Asimov spectrum would allow the computation of the relative size of the one standard deviation normalization constraint, $\frac{\sigma_N}{N}$ using the expression

$$\left(\frac{N - (1 - \frac{1}{2}\sin^2(2\theta_{24}))N}{\sigma_N}\right)^2 < 2.71 \tag{7.3}$$

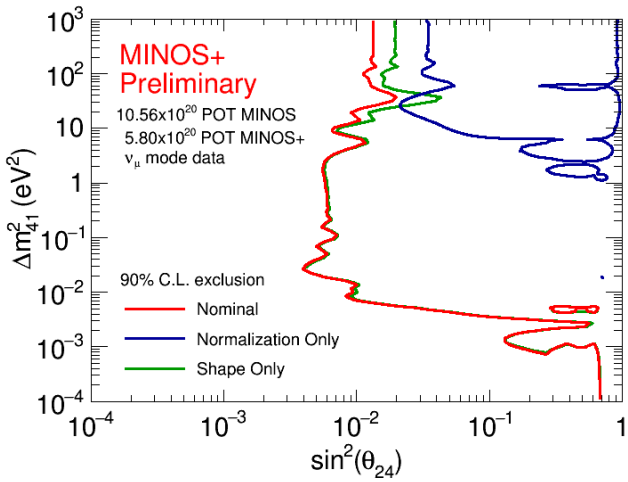

Figure 7.11: Comparison of the simultaneous Two-Detector data fit upper limit at 90% C.L. (red) to the contributions from the spectral shape variations (green) and the normalization systematic uncertainty (blue) as extracted in post-fit analysis. The shape component is the dominant contribution to the total limit for very nearly the entire range of mass-splittings with the normalization constraint providing additional exclusion for $\Delta m^2_{41} > 10$ eV^2. The contours plotted in this figure follow the structure established in Fig. 6.17.

which can be rearranged to yield

$$\frac{1}{2}\sin^2(2\theta_{24}) < \sqrt{2.71}\frac{\sigma_N}{N}, \tag{7.4}$$

where the factor of 2.71 comes from the conversion of a 90% C.L. limit to a 68% C.L. (1σ) limit. In the case of the Asimov sensitivity, the observed high Δm^2_{41} limit is $\sin^2(2\theta_{24}) \approx 0.07$, which when substituted into Eq. 7.4 yields an estimated relative normalization constraint of $\sim 8\%$ with respect to three-flavor oscillations, which is fully consistent with the dominant CC normalization constraint shown in Fig. 6.16. Performing a similar procedure for the normalization-only component of the fit to data, we observe a high Δm^2_{41} limit of $\sin^2(2\theta_{24}) \approx 0.034$, which when substituted into Eq. 7.4 corresponds to an estimated relative normalization constraint of $\sim 4.3\%$ with respect to three-flavor oscillations. The apparent decrease in this normalization constraint with respect to the Asimov arises from the fact that in both the CC and NC samples in the FD, MINOS and MINOS+ observed an overall event rate $\sim 4\%$ in excess of the prediction from three-flavor oscillations. Therefore, a one standard deviation constraint of $\sim 8\%$ with respect to an observed data/MC of ~ 1.04 translates to a lower ratio bound of 0.957, which rather accurately corresponds to the $\sim 4.3\%$ upper bound placed on the normalization-only, high Δm^2_{41} mixing from the decomposed limit. The entire discussion rendered here would not apply in the case of a shape-only fit, yet the observed limit in this case, as shown in Fig. 6.17 is still $\sin^2(\theta_{24}) < 0.01$ for arbitrarily large mass-splitting.

7.3 Statistical Interpretation

Under the assumptions that a given parameter space has no relevant physical boundaries, all uncertainties are normally-distributed, and that signals are non-degenerate, all results presented to this point are completely valid. We know however, that in the case of a neutrino oscillations analysis, at least the third assumption is invalid, and potentially the first two as well. In order to form proper frequentist confidence intervals, we perform three distinct brute force procedures, the Feldman-Cousins Unified Approach, the generation of sensitivity confidence bands, and the CL_s method, each of which serve as a tool for correction of the statistical interpretation of the analysis.

7.3.1 Fluctuated Data

In all the statistical methods, the brute force approach equires the simulation of large samples of pseudoexperiments. A pseudoexperiment is defined as the simulation of a randomly fluctuated pseudodata sample consistent with a mean spectrum defined as the predicted spectrum for a given set of oscillations parameters and induced spectral flucutations consistent with the estimated statistical and systematic uncertainties. In each pseudoexperiment, the fluctuated pseudodata is treated by the analysis framework in the same manner as the real MINOS and MINOS+ data samples. The generation of prediction spectra consistent with a given set of oscillatons parameters is a native function of the fit mechanism and is accomplished by the application of the oscillation probabilities to the migration matrices connecting true neutrino

L/E to reconstructed neutrino energy for both signal and background events. An example of one such prediction spectrum is the well-expounded Asimov spectrum, the spectrum for the case of standard three-flavor oscillations.

In order to replicate fluctuations in the prediction spectra, which could be reasonably expected from the estimated statistical and systematic uncertainties, we again make use of a covariance matrix method. By construction, the covariance matrix, V, contains all of the estimated sources of systematic uncertainty, including the relative shape information and the expected bin-to-bin correlations. The covariance matrix is also by definition Hermitian and positive semi-definite, which permits Cholesky Decomposition [243] of the matrix into a product of upper and lower triangular component matrices, as in:

$$V = L^T L \tag{7.5}$$

where L is the lower triangular matrix. The Cholesky decomposition is akin to calculating the square-root of the covariance matrix. As discussed previously, the fit mechanism is capable of generating a high-statistics spectral prediction consistent with a set of oscillation parameters, which for convenience we will call $\boldsymbol{S}$. We then generate a random vector of independent, uncorrelated numbers $\boldsymbol{y}$, such that $\boldsymbol{y}$ has the same number of elements as the spectral vector $\boldsymbol{S}$ and $y_i \sim N(0,1)$. In order to transform the set of uncorrelated random numbers in $\boldsymbol{y}$ into a correlated vector corresponding to the expected shape information in covriance matrix, we use the lower triangular matrix to produce

$$\boldsymbol{S}_{fluc} = \boldsymbol{S} + L\boldsymbol{y} \tag{7.6}$$

where $\boldsymbol{S}_{fluc}$ is the sysetmatically and statistically fluctuated pseudodata sample required for generating pseudoexperiments [244]. After the initial spectrum $\boldsymbol{S}$ and the lower triangular matrix L have been computed, an arbitrary number of pseudodata samples can be produced by the regeneration of differing random $\boldsymbol{y}$ vectors. An example of a statistically and systematically fluctuated pseudodata sample compared with the Asimov spectrum from which it was generated is shown in Fig. 7.16. Computation of the covariance of a sufficiently large number of pseudodata spectra reproduces the initial input covariance matrix, which serves as a convenient method for validation of the computational procedure.

7.3.2 Feldman-Cousins Unified Approach

The Unified Approach proposed by Feldman and Cousins [245], hereafter referred to as the FC method or correction, is a mechanism for determing the proper frequentist confidence interval for given set of parameters in a scenario where one or more of the assumptions listed at the beginning of this section is suspected to lead to either too broad or too narrow an accepted interval. In the frequentist perspective, which generally uses the Neyman construction [246], no prior knowledge of model parameters is assumed and a classical confidence interval $[\theta_1, \theta_2]$ is a member of a set of similar intervals such that the set satisfies

$$P(\theta \in [\theta_1, \theta_2]) = \alpha, \tag{7.7}$$

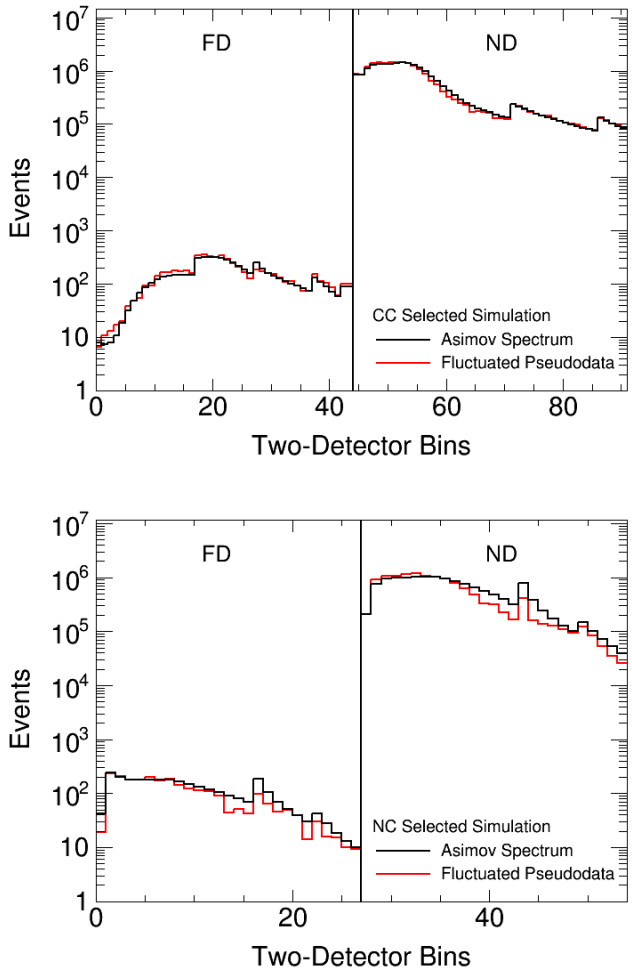

Figure 7.12: Example simulated spectra for the Asimov experiment (black) and statistically and systematically fluctuated pseudodata used for statistical analysis of the Two-Detector fit. Fluctuated pseudodata are used in the FC correction method (see Figs. 7.13 and 7.14), in the generation of the fluctuated sensitivity band (see Fig. 7.16), and in the CL_s method (see Figs. 7.17 and 7.18).

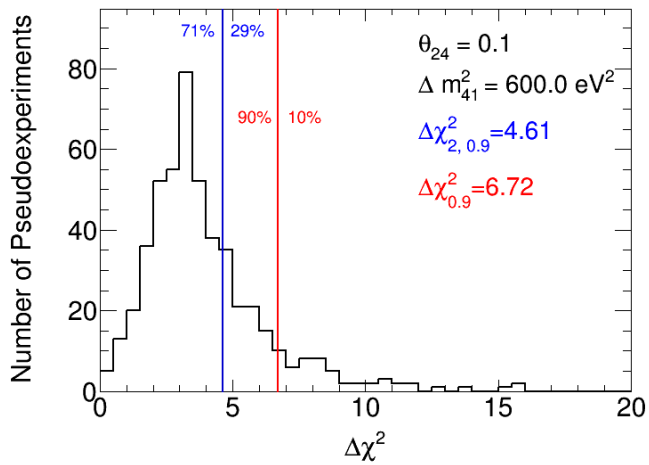

Figure 7.13: The $\Delta\chi^2$ distribution at a sample point in the $(\sin^2(\theta_{24}), \Delta m^2_{41})$ parameter space used for the determination of the FC correction. Using the standard 90% C.L. critical value $\Delta\chi^2 = 4.61$ results in the exclusion of this point by 29% of pseudoexperiments. The ensemble of pseudoexperiments indicate that for a true confidence level of 90%, a $\Delta\chi^2_{critical} = 6.72$ must be observed in order to ensure the proper frequentist coverage.

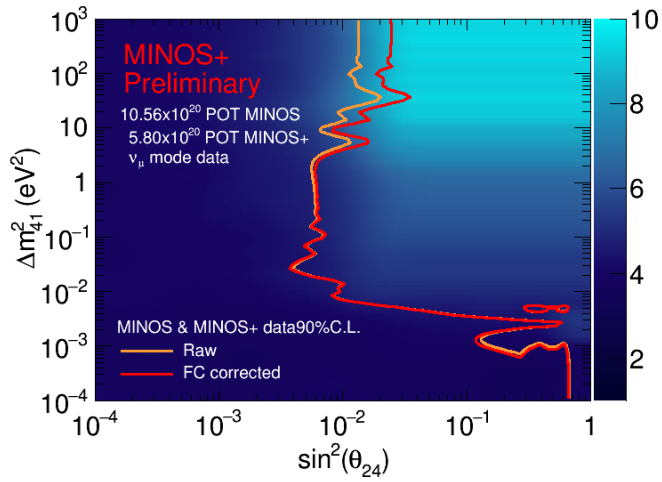

Figure 7.14: The FC correction surface as computed for the Two-Detector fit. Corrected $\Delta\chi^2$ critical values are indicated by the shaded scale. The raw data exclusion contour at 90% C.L. (orange) is compared with the exclusion contour at 90% C.L. after the application of the FC correction (red).

where θ is the true parameter value, α is the confidence level, and θ_1, θ_2 are functions of the experimentally observable quantities. A common interpreatation of this probability statement in the frequentist approach is that for a large number of hypothetical repetitions of the identical experiment, the fraction of computed confidence intervals $[\theta_1, \theta_2]$ containing the true value θ converges to α. It is therefore true to claim that for a given future experiment, the probability that the computed confidence interval will contain the true parameter value is equivalent to the confidence level. Once an experiment is performed and a confidence level is established, however, the probability collapses to either 0 or 1 as the true value is definitively either contained in the interval or it is not.

In this analysis, we seek to set an interval in the $(\sin^2(\theta_{24}), \Delta m^2_{41})$ parameter space at the 90% C.L. As was argued previously, the naive expectation in this case is that the $\Delta\chi^2$ critical value of 4.61 for two degrees of freedom should be the proper threshold for establishing such a confidence interval. The FC method is a test of this assumption through the simulation of pseudoexperiments at relevant points in the parameter space, which are generally those in the region near the raw data limit. In MINOS and MINOS+, we implement the FC method by simulating statistically and systematically fluctuated pseudoexperiments with true (3+1)-flavor oscillation parameters. For each pseudoexperiment, the $\Delta\chi^2$ is computed in the same manner as for the data, the form of which is given in Eq. 7.2. An example distribution of $\Delta\chi^2$ computed for true parameter values $\sin^2(\theta_{24}), \Delta m^2_{41}) = (0.01,\ 600\ \mathrm{eV}^2)$ is shown. For these parameters, the pseudoexperiment distribution shows that a threshold set at $\Delta\chi^2 = 4.61$ would result in 29% of experiments rejecting the true parameter values, whereas at the 90% C.L. only 10% of experiments would be expected to exclude the truth. In order to correct for this overcoverage effect, we determine a threshold of $\Delta\chi^2_{critical} = 6.72$ corresponding to 10% of the simulated pseudoexperiments rejecting the true parameters. FC correction refers to the requirement for the data to reach the computationally determined $\Delta\chi^2$ thresholds in order to reject regions of parameter space instead of the initial assumption of a flat $\Delta\chi^2 = 4.61$ critical value.

The results of the FC correction are shown in Fig. 7.14, with the threshold $\Delta\chi^2$ values given by the blue-scale shading. The most significant correction

is observed in the ND dominated, high Δm^2_{41} region, which is susceptible to signicant overcoverage due to the tendency of the fit to find local minima in the degenerate region given these true parameters. As a result of this tendency toward overcoverage, the 90% C.L. exclusion region is reduced by approximately a factor of two in the high Δm^2_{41} region. The FC-corrected contour is the proper frequentist upper bound presented as the data limit in all subsequent plots.

The FC-corrected data limit is shown in Fig. 7.15 in order to compare the new result with previously published experiment results constraining this parameter space. MINOS and MINOS+ set a signficant upper bound on sterile neutrino mediated oscillations over seven orders of magnitude in Δm^2_{41}. Over significant ranges of the mass-splitting, MINOS and MINOS+ now set the most constraining limits to date. The new MINOS and MINOS+ result improves upon the previously published MINOS-only Far-over-Near ratio analysis shown in the figure. This improvement can be attributed to the increase in the data sample, including the new energy range detailed by MINOS+, the new simultaneous Two-Detector fit method, and improved mapping of the atmospheric oscillations maximum due to a finer binning structure. The result is also in clear tension with global best-fit results for sterile neutrino mediated oscillations in a (3+1)-model, as evidenced by the clear exclusion of a best-fit result from Gariazzo et al. [142] shown in Fig. 7.15.

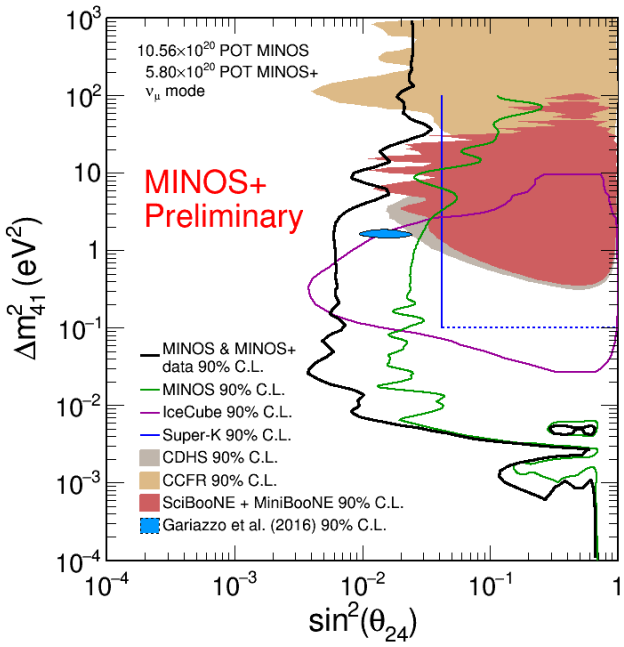

Figure 7.15: Comparison of the simultaneous Two-Detector data fit upper limit at 90% C.L. with previous results from IceCube [156], Super-K [247], CDHS [248], CCFR [230], and SciBooNE/MiniBooNE [131] constraining this parameter space. The Gariazzo et al. region is the result of a fit using a (3+1)-flavor model to global neutrino oscillation data [142].

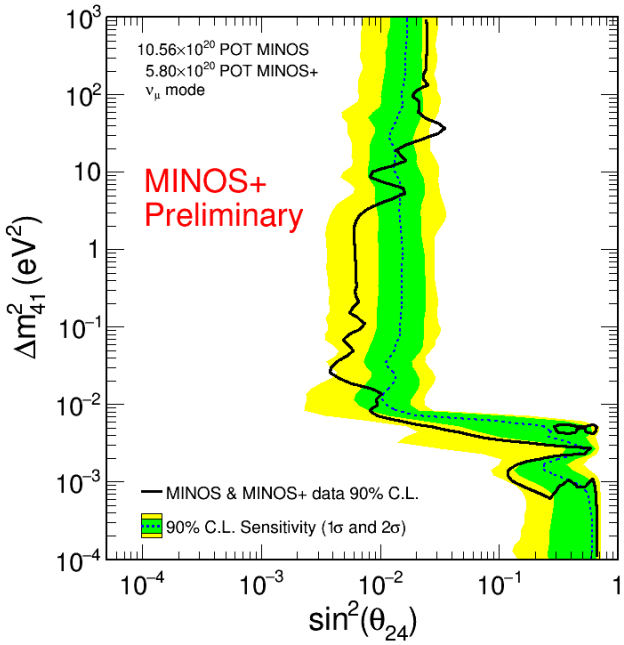

Figure 7.16: Plotted are the MINOS and MINOS+ data upper limit (black) and median fluctuated sensitivity (blue dashed) at 90% C.L. in the $(\sin^2(\theta_{24}), \Delta m^2_{41})$ parameter space resulting from the simultaneous Two-Detector fit after the FC correction. The bands surrounding the median sensitivity indicate the regions containing 68% (green) and 90% (yellow) of the 90% C.L. sensitivity contours resulting from statistically and systematically varied pseudoexperiments.

7.3.3 Fluctuated Sensitivity Band

In order to determine how unusual our observed data limit is with respect to the expected experimental sensitivity, we draw systematically and statistically fluctuated pseudoexperiments using the aforementioned method with the oscillation parameters set to standard three-flavor values. For each pseudoexperiment we construct a 90% CL sensitivity and apply the FC correction. As was discussed in Section 6.4.2, the median sensitivity of fluctuated pseudoexperiments is expected to be significantly more constraining than the Asimov sensitivity in the case of our systematically dominated, highly correlated covariance matrix fit.

Given that the data is expected to have fluctuations of the type applied to the pseudoexperiments, the median sensitivity provides the relevant benchmark for comparison with the data result. The large number of pseudoexperiment contours are summarized by the construction of bands which contain 68% and 95% of the contours. The fluctuated sensitivity bands are shown with the FC-corrected data limit in Fig. 7.16. In the FD region, where $\Delta m^2_{41} \leq 3\ eV^2$, the data contour broadly excludes more parameter space at 90% C.L. than the expected median sensitivity. This limit is attributable to upward fluctuations in the event rate observed in the FD spectrum as can be seen in Fig. 7.6. As stated previously, these fluctuations are consistent with expected and reasonably likely statistical and systematic fluctuations, and this is further demonstrated by the fact that the exclusion contour falls largely within the 1σ fluctuated sensitivity band.

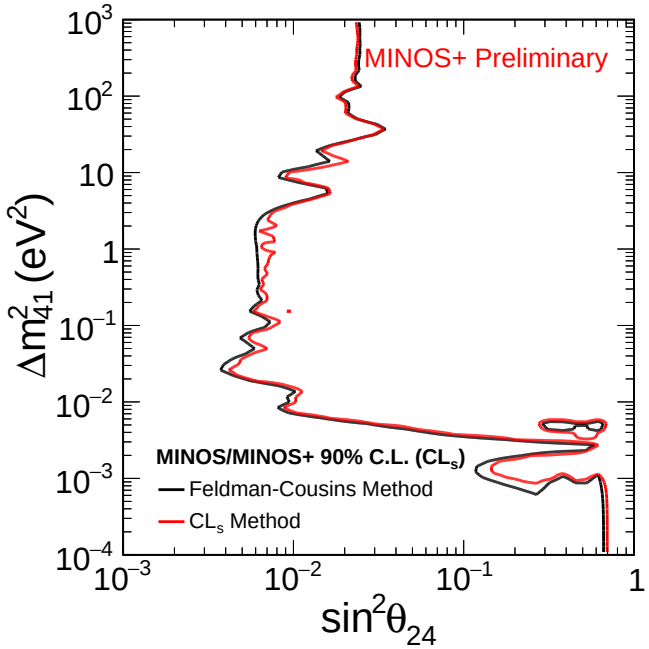

Figure 7.17: Comparison of the upper limits derived from the data fit using the FC method and the CL_s method. The limits are mutually consistent within the variations caused by statistical fluctuations in the samples of pseudoexperiments produced in both methods.

7.3.4 CL_s Method

The CL_s method is a statistical computation using a frequentist approach to set upper limits or define exclusion regions in a parameter space. The method reiles on defining the probabilities

$$\begin{aligned} CL_b &= P(\Delta\chi^2 \geq \Delta\chi^2 | 3\nu) \\ CL_{s+b} &= P(\Delta\chi^2 \geq \Delta\chi^2 | 4\nu), \end{aligned} \tag{7.8}$$

where $(1 - CL_b)$ is the ordinary discovery p-value, which is the probability of finding an experimental result at least as extreme as the observed result under

the condition that the null hypothesis (3ν) is true, and CL_{s+b} is similarly the p-value under the assumption that the alternate hypothesis (4ν) is true. We can then define the test statistic CL_s given by the ratio

$$CL_s = \frac{CL_{s+b}}{CL_b} \tag{7.9}$$

where the level of exclusion is determined by $(1 - CL_s) \times 100\%$.

In order to compute the relevant probability distributions of $\Delta\chi^2$ required for the CL_s method, two alternative procedures may be employed. The first method, called the Gaussian method in literature [249], involves the computation of the central values of the null and alternative hypothesis distributions from the Asimov experiment. For this method, the assumption is made that the $\Delta\chi^2$ are normally-distributed such that the mean, $\Delta\bar{\chi}^2$, is given by the Asimov experiment and the width may be computed analytically according to $2\sqrt{|\Delta\bar{\chi}^2|}$. The second method, which is employed for MINOS and MINOS+, involves computing the $\Delta\chi^2_{3\nu}$ and $\Delta\chi^2_{4\nu}$ through the simulation of pseudoexperiments under the assumption of standard three-flavor oscillations and (3+1)-flavor oscillations, respectively. The empirical calculation of the distributions requires no assumptions about the shape of the distributions and is therefore robust to deviations from normally-distributed test statistics, examples of which were already hinted at by the discussions in Sections 7.3.2 and 6.4.2.

The result of the CL_s method using the MINOS and MINOS+ combined data sample is shown in Fig. 7.18 compared with the contour construced

using the FC correction. Due to present computational constraints, the CL_s contour presented in this section was confined to 500 pseudoexperiments per grid point, which can result in variations in the limit due entirely to statistical effects. Even under this constraint, broad agreement is found between these two methods which points to the efficacy of both methods in determining properly covering frequentist intervals.

7.4 MINOS/MINOS+ and Daya Bay/Bugey-3

Using a similar method to that given in Section 1.4.2 for computing oscillation probabilities in a (3+1)-flavor oscillation model, the probability for the appearance of electron neutrinos from a muon neutrino source can be written:

$$P(\nu_\mu \to \nu_e) \approx 4|U_{\mu 4}|^2|U_{e4}|^2 \sin^2 \Delta_{41}, \tag{7.10}$$

where we have assumed large sterile mass-splitting such that $\Delta m^2_{41} \approx \Delta m^2_{42} \approx \Delta m^2_{43}$ and $\Delta m^2_{41} \gg \Delta m^2_{32}, \Delta m^2_{21}$. It is convenient to define an effective mixing angle such that

$$P(\nu_\mu \to \nu_e) \approx \sin^2(2\theta_{\mu e} \sin^2 \Delta_{41}, \tag{7.11}$$

where

$$\sin^2(2\theta_{\mu e}) = 4|U_{\mu 4}|^2|U_{e4}|^2, \tag{7.12}$$

In the standard parameterization of the (3+1)-flavor model, the absolute square of the matrix elements $U_{\mu 4}$ and U_{e4} are given by

$$\begin{aligned} |U_{e4}|^2 &= \sin^2(\theta_{14}) \\ |U_{\mu 4}|^2 &= \sin^2(\theta_{24}) \cos^2(\theta_{14}), \end{aligned} \tag{7.13}$$

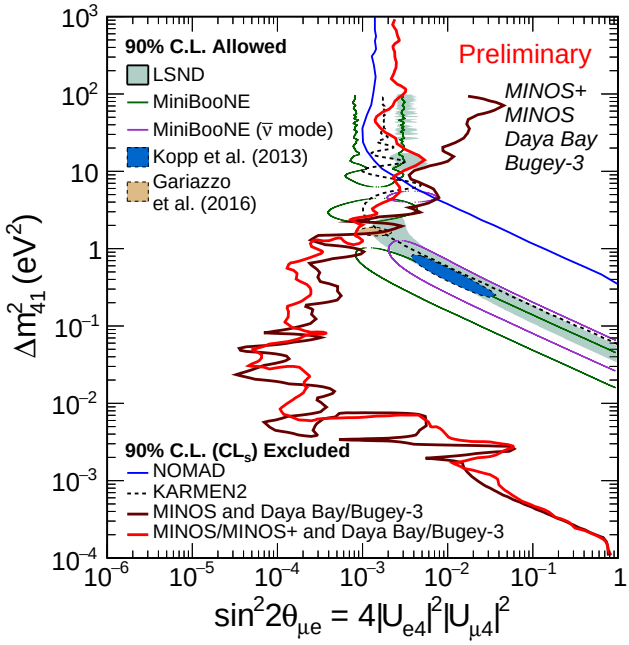

Figure 7.18: The joint exclusion contour at 90% CL_s for the MINOS/MINOS+ and Daya Bay/Bugey-3 combination in the parameter space ($\sin^2 2\theta_{\mu e}, \Delta m^2_{41}$). Previous exclusion results from the MINOS and Daya Bay/Bugey-3 combination [249], KARMEN2 [148], and NOMAD [149] are plotted in addition to allowed regions from short-basline ν_e ($\bar{\nu}_e$) appearance experiments LSND [120] and MiniBooNE [250] for comparison.

which implies that the effecting mixing angle is expressed in terms of mixing angles θ_{14} and θ_{24} through the relation

$$\sin^2(2\theta_{\mu e}) = \sin^2(2\theta_{14})\sin^2(\theta_{24}). \tag{7.14}$$

By construction, this effective mixing angle is the amplitude for the anomalous electron neutrino and antineutrino appearance observed by LSND [120] and MiniBooNE [250].

We can indirectly probe the effective mixing angle for electron neutrino appearance by the combination of experiment results. MINOS and MINOS+ place strong constraints on the mixing angle θ_{24} as presented throughout this chapter. Reactor neutrino searches for sterile neutrino oscillations, such as that produced by Daya Bay in combination with data from Bugey-3 [237], constrain the mixing angle θ_{14} through the null observation of electron antineutrino disappearance.

In order to combine the experiment results, MINOS/MINOS+ and Daya Bay/Bugey-3 have used the previously discussed CL_s method in close collaboration, which is discussed in detail in Ref. [249]. Briefly, each experiment produces the CL_b and CL_{s+b} distributions associated with its data independently, with Daya Bay employing the Gaussian method for determining the distributions and MINOS/MINOS+ using the brute force MC simulation method. The CL_b and CL_{s+b} distributions are summed in order to create combined distributions from which CL_s can be calculated. For each row of Δm^2_{41} in the $[\sin^2(2\theta_{\mu e}), \Delta m^2_{41}]$ parameter space the effective mixing angle $\theta_{\mu e}$ is a

multivalued function of θ_{14} and θ_{24}. The CL_s is computed for all values of θ_{14} and θ_{24}, and the largest (most conservative) value of CL_s for each $\sin^2(2\theta_{\mu e})$ is taken as the combination value to form the CL_s surface.

The MINOS/MINOS+ and Daya Bay/Bugey-3 combination contour at the 90% CL_s, which is given by the threshold value $CL_s = 0.1$, is plotted in Fig. 7.18. In comparison to the previously published combination result [249], which used the MINOS Far-over-Near sterile neutrino analysis as input, the new combination is more constraining for nearly all choices of the mass-splitting Δm^2_{41}. The greatest improvement is seen in the high Δm^2_{41} region due to the effects of the Two-Detector fit framework, as should be expected given the results presented in previous sections. The new MINOS/MINOS+ and Daya Bay/Bugey-3 combination increases the already strong tension with observations of $\nu_e/\bar{\nu}_e$ appearance at LSND and MiniBooNE, and excludes the current global best-fit allowed regions at 90% CL_s. Further efforts are in progress to include a larger Daya Bay data set representing an accumulation of 1230 days of data, which may result in a stronger constraint than that shown here.

7.5 Projection to Probability Space

In the vast majority of published neutrino oscillation studies, the results are displayed in terms of allowed or excluded regions of parameter space, as has been the case for this analysis to this point. It is important to remember that these parameter space points each define unique oscillatory functions of

probability which exist in a completely distinct space that is entirely model-independent. If the exclusion or allowed regions of parameter space can be effectively mapped into the probability space, the comparison of a variety of oscillation models could be made without specific concern for the particulars of the parameters describing the probability calculation.

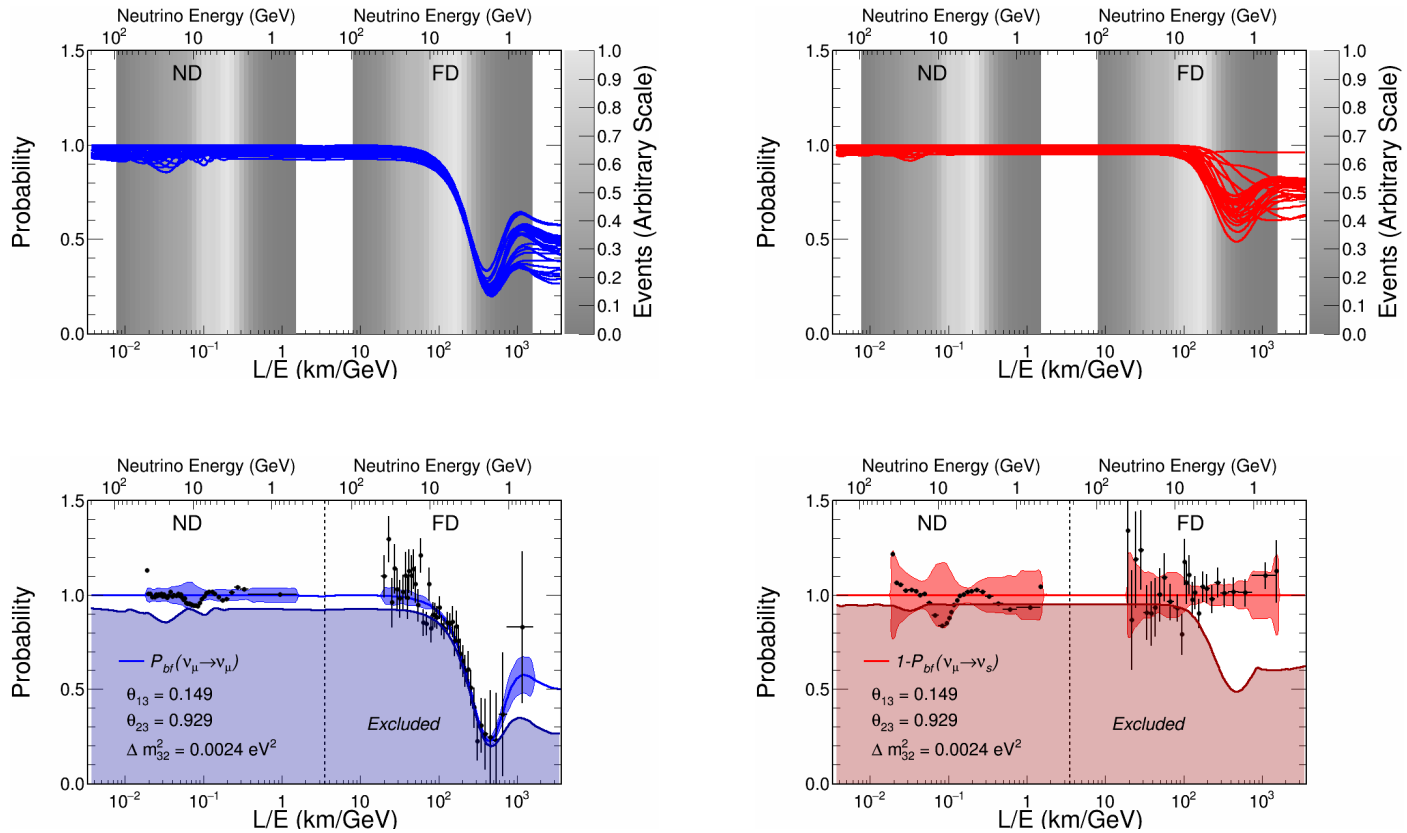

Figure 7.19: Projection of the (3+1)-flavor model 90% C.L. exclusion contour into the space of oscillation probabilities. Upper row: The probability curves associated with the best-fit (3+1)-flavor model parameters at points forming the exclusion contour are plotted for ν_μ-CC disappearance (left) and NC disappearance (right). Lower row: Taking the minimum probability as the conservative (largest) estimate of the oscillation magnitude at each value of L/E in the upper plots results in the excluded regions (dark shading) in probability space. For comparison, the MINOS and MINOS+ data ratio to the null-oscillations hypothesis (black points), estimated residual uncertainty bands (light shading bands), and (3+1)-flavor model best-fit probability curves are plotted for comparison to the excluded region.

In order to attempt to describe in a model independent way the MINOS and MINOS+ exlcusion result, which in point of fact is calculated in a (3+1)-flavor model space, we first scan along each row of Δm^2_{41} in our FC-corrected exclusion plot (see Fig. 7.16) until the limiting contour is reached. For each point along the limit contour, the oscillation probablility is plotted for both the CC ($P(\nu_\mu \to \nu_\mu)$) and NC ($1 - P(\nu_\mu \to \nu_s)$) events, the results of which are shown in the top panels of Fig. 7.19. Since we are considering a disappearance analysis from MINOS and MINOS+ in this exercise, we take the largest allowed oscillations from the ensemble of plotted probability curves at each value of L/E as the conservative exclusion limit. The result of plotting this lower bound on oscillations probability variations is shown in the lower panels of Fig. 7.19. The MINOS and MINOS+ decorrelated data spectra, relative uncertainties, and the best-fit oscillations probabilities are also plotted for comparison with the exclusion region. The probability exclusion plots appear to be dominated by the CC sample given the large allowed deviations in the NC sample, which is expected from the observations of the χ^2 surfaces. While this projection method is novel and not yet well-studied, it may represent a useful proof-of-concept for transition to model independent comparisons of the allowed probability effects in future study of neutrino oscillations.

Chapter 8

Summary and Future Work

We have conducted an extensive search for sterile neutrino mediated oscillations within a (3+1)-flavor model using MINOS and MINOS+ neutrino mode data. The search employed the new Two-Detector fit technique, which treats the observations in both detectors as coequal measurements via the use of a covariance matrix. We find no significant evidence for oscillations driven by the existence of sterile neutrinos. We set a leading upper limit on the magnitude of oscillations governed by $\sin^2(\theta_{24})$ over approximately seven orders of magnitude in Δm^2_{41}. With the exception of regions in the parameter space where experiments are uniquely positioned to observe very strong constraints (e.g. IceCube), MINOS and MINOS+ set the most constraining limit to date on sterile mixing-driven ν_μ-CC- and NC-disappearance.

The covariance matrix method for fitting neutrino oscillations in two detectors over a long-baseline has been demonstrated to be both effective and efficient in this analysis. We believe that the covariance matrix fit technique should become the standard method for neturino oscillations analyses. This method has been demonstrated to be uniquely effective in the detection of neutrino oscillations signals while simultaneously enabling extensive cancella-

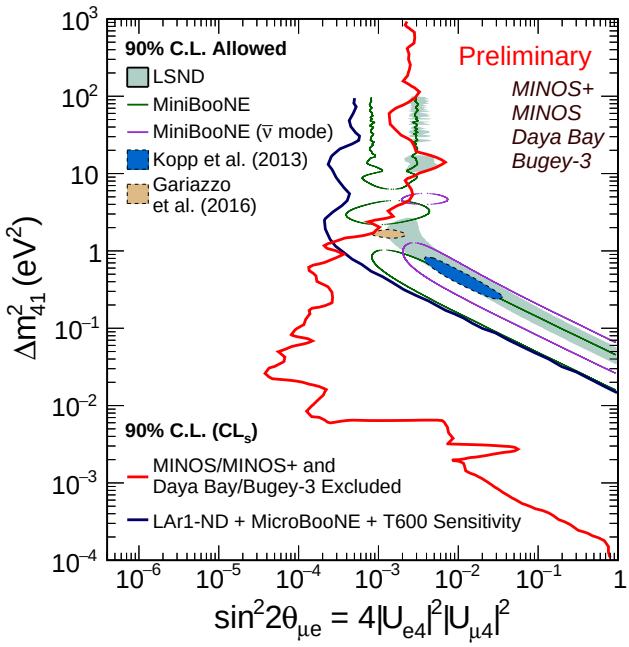

Figure 8.1: The expected senstivity of the Fermilab SBN program in a three-detector analysis with the listed POT accumulations in Ref. [157] used for scaling the data sample. The LSND, MiniBooNE and global fit allowed regions, and several exclusion limits corresponding to those shown in Fig. 7.18 are also plotted for comparison.

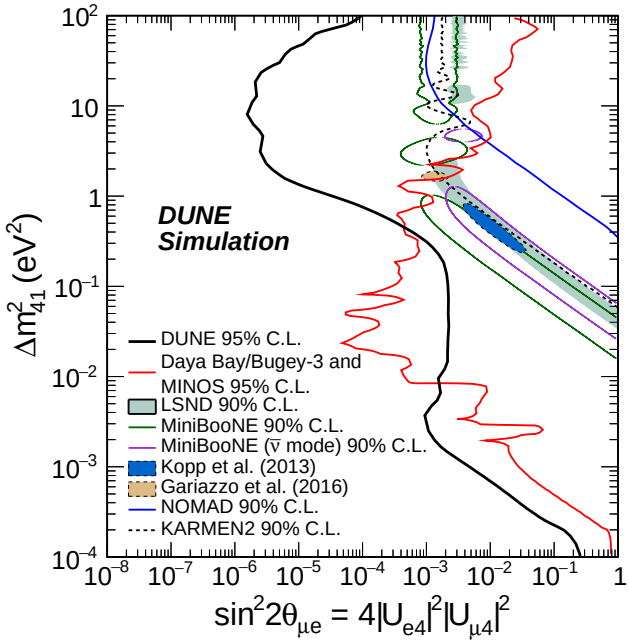

Figure 8.2: The simulated senstivity of DUNE for 3.5 years each of running in neutrino and antineutrino mode assuming a 40-kt fiducial mass far detector in an 80-GeV, 1.07 MW beam. The LSND, MiniBooNE and global fit allowed regions, and several exclusion limits corresponding to those shown in Fig. 7.18 are also plotted for comparison. Figure taken from Reference [251].

tion of highly correlated systematic uncertainties. The decorrelation method we introduce in this thesis further allows for the post-fit extraction of all information described in other forms of analysis. We have illustrated that the internal mechanism of the covariance matrix fit is able to accomplish the same goals of all other existing fitting frameworks, while providing the additional benefit of a holistic treatment of the correlations of all sources of systematic and statistical uncertainty.

Future searches for sterile neutrinos in MINOS and MINOS+ will in-

volve new contributions to the overall data sample including data collected during MINOS $\bar{\nu}_\mu$ mode running, the final year of MINOS+ ν_μ mode data (a $\sim$ 50% increase in MINOS+ statistics), and the unfocused $\bar{\nu}_\mu$ and ν_μ samples from both MINOS and MINOS+ eras. Each of these samples offer new windows on the parameter space of sterile mediated neutrino oscillations in addition to providing the opportunity for the reevaluation of systematic uncertainties, which are treated with clear conservatism in the context of the present analysis. Additionally, the analysis presented here could be significantly improved by the treatment of all samples in a single joint covariance matrix, permitting the further extraction of all correlated information from a collection of systematically disparate samples.

In the general field of sterile neutrino searches, a collection of ongoing experimental efforts provide hope for continually increasing sensitivity and clarification of the disappearance and appearance tension observed in global data, two of which we will highlight briefly. In the ν_e appearance channel, the Short Baseline Neutrino (SBN) program at Fermilab will use three separate detectors to yield a definitive answer to the LSND/MiniBooNE anomaly [157]. The expected sensitivity from the full SBN program is shown in Fig. 8.1. The first of these detectors to be constructed, MicroBooNE, has done pioneering work in the understanding of state-of-the-art Liquid Argon Time Projection Chamber (LArTPC) technology since it began data collection in 2015. The SBN program has set a target of 2020 for full three-detector operations.

Finally, perhaps the largest and most sensitive of planned neutrino ex-

periments to date, the Deep Underground Neutrino Experiment (DUNE) will probe not only the existence of leptonic CP violation and potentially make a first measurement of δ_{CP}, as well as the question of the ordering of neutrino mass eigenstates, but also continue the hunt for sterile neutrinos. Early estimates of the potential sensitivity to (3+1)-flavor mixing are very strong, an example of which is show in Fig. 8.2. DUNE will combine the LArTPC technology with a high-energy, high-intensity beam over a very long baseline, permitting precision measurements of all forms of oscillations phenomena.

The future is bright.

Bibliography

[1] J. Chadwick. The intensity distribution in the magnetic spectrum of beta particles from radium (B + C). *Verh. Phys. Gesell.*, **16**:383–391, 1914.

[2] Michael L'Annunziata, editor. *Handbook of Radioactivity Analysis, 3rd Edition*. Elsevier, Amsterdam, Netherlands, 2012.

[3] A H Bcquerel. Sur la transparence de l'aluminium pour la rayonnement du radium. *C. R. Acad. Sci. Paris*, **130**:1154, 1900.

[4] James Chadwick and Charles D Ellis. A Preliminary Investigation of the Intensity Distribution in the β-Ray Spectra of Radium B and C. In *Proceedings of the Cambridge Philosophical Society*, volume 21, pages 274–280, 1922.

[5] C. D. Ellis and W. A. Wooster. The average energy of disintegration of radium E. *Proceedings of the Royal Society of London A: Mathematical, Physical and Engineering Sciences*, **117**(776):109–123, 1927.

[6] Lise Meitner and Wilhelm Orthmann. Über eine absolute Bestimmung der Energie der primären β-Strahlen von Radium E. *Zeitschrift für Physik*, **60**(3-4):143–155, 1930.

[7] Laurie M Brown. The idea of the neutrino. *Physics Today*, **31**(9):23, 1978.

[8] James Chadwick. The existence of a neutron. *Proceedings of the Royal Society of London. Series A*, **136**(830):692–708, 1932.

[9] Erasmo Recami. Majorana, the Neutron, and the Neutrino: Some elementary historical remarks. *Hadronic J.*, **40**:149–185, 2017.

[10] E Fermi. Versuch einer Theorie des ß-Zerfalls. *Z. Physik*, **88**:161, 1934.

[11] Fred L Wilson. Fermi's theory of beta decay. *American Journal of Physics*, **36**(12):1150–1160, 1968.

[12] CL Cowan Jr, F Reines, FB Harrison, EC Anderson, and FN Hayes. Large liquid scintillation detectors. *Physical Review*, **90**(3):493, 1953.

[13] F. Reines and C. L. Cowan. A Proposed Experiment to Detect the Free Neutrino. *Phys. Rev.*, **90**:492–493, May 1953.

[14] F. Reines and C. L. Cowan. Detection of the Free Neutrino. *Phys. Rev.*, **92**:830–831, Nov 1953.

[15] Clyde L Cowan Jr, Frederick Reines, FB Harrison, HW Kruse, and AD McGuire. Detection of the free neutrino: a confirmation. In *Neutrinos And Other Matters: Selected Works of Frederick Reines*, pages 57–58. World Scientific, 1991.

[16] Hans Bethe and Rudolph Peierls. The neutrino. *Nature*, **133**(3362):532, 1934.

[17] Carl D. Anderson and Seth H. Neddermeyer. Cloud Chamber Observations of Cosmic Rays at 4300 Meters Elevation and Near Sea-Level. *Phys. Rev.*, **50**:263–271, 1936.

[18] Seth H Neddermeyer and Carl D Anderson. Note on the nature of cosmic-ray particles. *Physical Review*, **51**(10):884, 1937.

[19] B. Pontecorvo. Electron and Muon Neutrinos. *Sov. Phys. JETP*, **10**:1236–1240, 1960. [Zh. Eksp. Teor. Fiz.37,1751(1959)].

[20] G. Danby, J. M. Gaillard, Konstantin A. Goulianos, L. M. Lederman, Nari B. Mistry, M. Schwartz, and J. Steinberger. Observation of High-Energy Neutrino Reactions and the Existence of Two Kinds of Neutrinos. *Phys. Rev. Lett.*, **9**:36–44, 1962.

[21] Yung-Su Tsai. Decay Correlations of Heavy Leptons in e++ e- l++ l-. *Physical Review D*, **4**(9):2821, 1971.

[22] Martin L Perl, GS Abrams, AM Boyarski, Martin Breidenbach, DD Briggs, F Bulos, William Chinowsky, JT Dakin, GJ Feldman, CE Friedberg, et al. Evidence for anomalous lepton production in e+- e- annihilation. *Physical Review Letters*, **35**(22):1489, 1975.

[23] Martin L Perl, GL Feldman, GS Abrams, MS Alam, AM Boyarski, Martin Breidenbach, J Dorfan, William Chinowsky, G Goldhaber, G Hanson,

et al. Properties of the proposed τ charged lepton. *Physics Letters B*, **70**(4):487–490, 1977.

[24] Martin L Perl. Evidence for, and properties of, the new charged heavy lepton. Technical report, 1977.

[25] K. Kodama et al. Observation of tau neutrino interactions. *Phys. Lett.*, **B504**:218–224, 2001.

[26] K. Kodama et al. Final tau-neutrino results from the DONuT experiment. *Phys. Rev.*, **D78**:052002, 2008.

[27] John Ellis and Keith A Olive. Constraints on light particles from Supernova SN 1987A. *Physics Letters B*, **193**(4):525–530, 1987.

[28] P James E Peebles. Primordial helium abundance and the primordial fireball. II. *The Astrophysical Journal*, **146**:542, 1966.

[29] Aleph Collaboration, Delphi Collaboration, L3 Collaboration, Opal Collaboration, SLD collaboration, LEP Electroweak Working Group, et al. Precision electroweak measurements on the Z resonance. *Physics Reports*, **427**(5-6):257–454, 2006.

[30] C. Patrignani et al. Review of Particle Physics. *Chin. Phys.*, **C40**(10):100001, 2016.

[31] Tsung-Dao Lee and Chen-Ning Yang. Question of parity conservation in weak interactions. *Physical Review*, **104**(1):254, 1956.

[32] Chien-Shiung Wu, Ernest Ambler, RW Hayward, DD Hoppes, and R Pl Hudson. Experimental test of parity conservation in beta decay. *Physical review*, **105**(4):1413, 1957.

[33] Eo CG Sudarshan and RE Marshak. Chirality invariance and the universal Fermi interaction. *Physical Review*, **109**(5):1860, 1958.

[34] R. P. Feynman and M. Gell-Mann. Theory of the Fermi Interaction. *Phys. Rev.*, **109**:193–198, Jan 1958.

[35] M. Goldhaber, L. Grodzins, and A. W. Sunyar. Helicity of Neutrinos. *Phys. Rev.*, **109**:1015–1017, Feb 1958.

[36] Raymond Davis, Don S. Harmer, and Kenneth C. Hoffman. Search for Neutrinos from the Sun. *Phys. Rev. Lett.*, **20**:1205–1209, May 1968.

[37] John N Bahcall. *Neutrino astrophysics.* Cambridge University Press, 1989.

[38] K. S. Hirata et al. Observation of ^{8}B solar neutrinos in the Kamiokande-II detector. *Phys. Rev. Lett.*, **63**:16–19, Jul 1989.

[39] K. S. Hirata et al. Real-time, directional measurement of ^{8}B solar neutrinos in the Kamiokande II detector. *Phys. Rev. D*, **44**:2241–2260, Oct 1991.

[40] S Turck-Chieze. S. Turck-Chieze et al., Astrophys. J. 335, 415 (1988). *Astrophys. J.*, **335**:415, 1988.

[41] Y. Fukuda et al. Solar Neutrino Data Covering Solar Cycle 22. *Phys. Rev. Lett.*, **77**:1683–1686, Aug 1996.

[42] JN Abdurashitov, EL Faizov, VN Gavrin, AO Gusev, AV Kalikhov, TV Knodel, II Knyshenko, VN Kornoukhov, IN Mirmov, AM Pshukov, et al. Results from SAGE (The Russian-American gallium solar neutrino experiment). *Physics Letters B*, **328**(1-2):234–248, 1994.

[43] P Anselmann, W Hampel, G Heusser, J Kiko, T Kirsten, E Pernicka, R Plaga, U Rönn, M Sann, C Schlosser, et al. Solar neutrinos observed by GALLEX at Gran Sasso. *Physics Letters B*, **285**(4):376–389, 1992.

[44] John N. Bahcall and Roger K. Ulrich. Solar models, neutrino experiments, and helioseismology. *Rev. Mod. Phys.*, **60**:297–372, Apr 1988.

[45] J. N. Abdurashitov et al. Measurement of the solar neutrino capture rate with gallium metal. III: Results for the 2002–2007 data-taking period. *Phys. Rev.*, **C80**:015807, 2009.

[46] Wolfgang Hampel, J Handt, G Heusser, J Kiko, T Kirsten, M Laubenstein, E Pernicka, W Rau, M Wojcik, Yu Zakharov, et al. GALLEX solar neutrino observations: Results for GALLEX IV. *Physics Letters B*, **447**(1-2):127–133, 1999.

[47] M. Altmann et al. Complete results for five years of GNO solar neutrino observations. *Phys. Lett.*, **B616**:174–190, 2005.

[48] John N. Bahcall, Aldo M. Serenelli, and Sarbani Basu. New solar opacities, abundances, helioseismology, and neutrino fluxes. *Astrophys. J.*, **621**:L85–L88, 2005.

[49] Yoichiro Suzuki. Solar Neutrinos. *International Journal of Modern Physics A*, **15**(supp01a):201–228, 2000.

[50] Eric G Adelberger, Sam M Austin, John N Bahcall, AB Balantekin, Gilles Bogaert, Lowell S Brown, Lothar Buchmann, F Edward Cecil, Arthur E Champagne, Ludwig De Braeckeleer, et al. Solar fusion cross sections. *Reviews of Modern Physics*, **70**(4):1265, 1998.

[51] John N. Bahcall, Neta A. Bahcall, and Giora Shaviv. Present Status of the Theoretical Predictions for the ^{37}Cl Solar-Neutrino Experiment. *Phys. Rev. Lett.*, **20**:1209–1212, May 1968.

[52] John N. Bahcall and M. H. Pinsonneault. What Do We (Not) Know Theoretically about Solar Neutrino Fluxes? *Phys. Rev. Lett.*, **92**:121301, Mar 2004.

[53] John N Bahcall, Aldo M Serenelli, and Sarbani Basu. New solar opacities, abundances, helioseismology, and neutrino fluxes. *The Astrophysical Journal Letters*, **621**(1):L85, 2005.

[54] Masayuki Nakahata et al. Atmospheric neutrino background and pion nuclear effect for Kamioka nucleon decay experiment. *J. Phys. Soc. Jap.*, **55**:3786, 1986.

[55] K. S. Hirata et al. Experimental study of the atmospheric neutrino flux. *Phys. Lett.*, **B205**:416, 1988.

[56] Takaaki Kajita. Atmospheric neutrinos and discovery of neutrino oscillations. *Proceedings of the Japan Academy, Series B*, **86**(4):303–321, 2010.

[57] KS Hirata, T Kajita, M Koshiba, M Nakahata, S Ohara, Y Oyama, N Sato, A Suzuki, M Takita, Y Totsuka, et al. Experimental study of the atmospheric neutrino flux. *Physics Letters B*, **205**(2-3):416–420, 1988.

[58] R. M. Bionta et al. Search for Proton Decay into $e^+\pi^0$. *Phys. Rev. Lett.*, **51**:27–30, Jul 1983.

[59] R. Becker-Szendy, C. B. Bratton, D. Casper, S. T. Dye, W. Gajewski, M. Goldhaber, T. J. Haines, P. G. Halverson, D. Kielczewska, W. R. Kropp, J. G. Learned, J. M. LoSecco, S. Matsuno, G. McGrath, C. McGrew, R. Miller, L. R. Price, F. Reines, J. Schultz, H. W. Sobel, J. L. Stone, L. R. Sulak, and R. Svoboda. Electron- and muon-neutrino content of the atmospheric flux. *Phys. Rev. D*, **46**:3720–3724, Nov 1992.

[60] WWM Allison, GJ Alner, DS Ayres, WL Barrett, C Bode, PM Border, CB Brooks, JH Cobb, DJA Cockerill, RJ Cotton, et al. Measurement of the atmospheric neutrino flavour composition in Soudan 2. *Physics Letters B*, **391**(3-4):491–500, 1997.

[61] P Lipari. The atmospheric neutrino problem. In *Ital. Phys. Soc. Conf. Ser. 57: Frontier Objects in Astrophysics and Particle Physics*, page 467, 1997.

[62] V Gribov and B Pontecorvo. Neutrino astronomy and lepton charge. *Physics Letters B*, **28**(7):493–496, 1969.

[63] Evgeny Kh. Akhmedov and Alexei Yu. Smirnov. Paradoxes of neutrino oscillations. *Phys. Atom. Nucl.*, **72**:1363–1381, 2009.

[64] SP Mikheev and A Yu Smirnov. Resonance amplification of oscillations in matter and spectroscopy of solar neutrinos. *Yadernaya Fizika*, **42**(6):1441–1448, 1985.

[65] Lincoln Wolfenstein. Neutrino oscillations in matter. *Physical Review D*, **17**(9):2369, 1978.

[66] John N Bahcall, PI Krastev, and A Yu Smirnov. Is a large mixing angle MSW effect the solution of the solar neutrino problems? *Physical Review D*, **60**(9):093001, 1999.

[67] A Yu Smirnov. The MSW effect and matter effects in neutrino oscillations. *Physica Scripta*, **2005**(T121):57, 2005.

[68] Herbert H. Chen. Direct Approach to Resolve the Solar-Neutrino Problem. *Phys. Rev. Lett.*, **55**:1534–1536, Sep 1985.

[69] J. Boger et al. The Sudbury neutrino observatory. *Nucl. Instrum. Meth.*, **A449**:172–207, 2000.

[70] Q. R. Ahmad et al. Measurement of the Rate of $\nu_e + d \rightarrow p + p + e^-$ Interactions Produced by ^{8}B Solar Neutrinos at the Sudbury Neutrino Observatory. *Phys. Rev. Lett.*, **87**:071301, 2001.

[71] B. Aharmim et al. Electron Energy Spectra, Fluxes, and Day-Night Asymmetries of ^{8}B Solar Neutrinos from the 391-Day Salt Phase SNO Data Set. *Phys. Rev.*, **C72**:055502, 2005.

[72] B. Aharmim et al. An Independent Measurement of the Total Active 8B Solar Neutrino Flux Using an Array of 3He Proportional Counters at the Sudbury Neutrino Observatory. *Phys. Rev. Lett.*, **101**:111301, 2008.

[73] S. Fukuda et al. Determination of solar neutrino oscillation parameters using 1496 days of Super-Kamiokande I data. *Phys. Lett.*, **B539**:179–187, 2002.

[74] Y. Fukuda et al. Measurement of a small atmospheric muon-neutrino / electron-neutrino ratio. *Phys. Lett.*, **B433**:9–18, 1998.

[75] M. Shiozawa. Reconstruction algorithms in the Super-Kamiokande large water Cherenkov detector. *Nucl. Instrum. Meth.*, **A433**:240–246, 1999.

[76] Y. Fukuda et al. Measurement of the flux and zenith-angle distribution of upward through-going muons by Super-Kamiokande. *Phys. Rev. Lett.*, **82**:2644–2648, 1999.

[77] T. Futagami et al. Observation of the east-west anisotropy of the atmospheric neutrino flux. *Phys. Rev. Lett.*, **82**:5194–5197, 1999.

[78] Y. Fukuda et al. Neutrino-induced upward stopping muons in Super-Kamiokande. *Phys. Lett.*, **B467**:185–193, 1999.

[79] Y. Ashie et al. Evidence for an oscillatory signature in atmospheric neutrino oscillation. *Phys. Rev. Lett.*, **93**:101801, 2004.

[80] B. Aharmim et al. Combined Analysis of all Three Phases of Solar Neutrino Data from the Sudbury Neutrino Observatory. *Phys. Rev.*, **C88**:025501, 2013.

[81] The Nobel Prize in Physics 2015, 2015.

[82] K. Eguchi et al. First Results from KamLAND: Evidence for Reactor Anti-Neutrino Disappearance. *Phys. Rev. Lett.*, **90**:021802, 2003.

[83] T. Araki et al. Measurement of Neutrino Oscillation with KamLAND: Evidence of Spectral Distortion. *Phys. Rev. Lett.*, **94**:081801, 2005.

[84] S. Abe et al. Precision Measurement of Neutrino Oscillation Parameters with KamLAND. *Phys. Rev. Lett.*, **100**:221803, 2008.

[85] S. H. Ahn et al. Detection of accelerator produced neutrinos at a distance of 250-km. *Phys. Lett.*, **B511**:178–184, 2001.

[86] M. H. Ahn et al. Indications of Neutrino Oscillation in a 250 km Long-baseline Experiment. *Phys. Rev. Lett.*, **90**:041801, 2003.

[87] Ludovica Sartini, F Simeone, P Pani, N Lo Bue, G Marinaro, A Grubich, A Lobko, G Etiope, A Capone, P Favali, et al. Nuclear instruments and methods in physics research section a: Accelerators, spectrometers, detectors and associated equipment. *Nuclear Instruments and Methods in Physics Research A*, 2010.

[88] K. Abe et al. Indication of Electron Neutrino Appearance from an Accelerator-produced Off-axis Muon Neutrino Beam. *Phys. Rev. Lett.*, **107**:041801, 2011.

[89] K. Abe et al. First Muon-Neutrino Disappearance Study with an Off-Axis Beam. *Phys. Rev.*, **D85**:031103, 2012.

[90] M.G. Catanesi. T2K & beyond. *Adv.High Energy Phys.*, **2016**:5496103, 2016.

[91] K. Abe et al. Measurement of neutrino and antineutrino oscillations by the T2K experiment including a new additional sample of ν_e interactions at the far detector. *Phys.Rev.*, **D96**:092006, 2017.

[92] D.G. Michael et al. Observation of muon neutrino disappearance with the MINOS detectors and the NuMI neutrino beam. *Phys. Rev. Lett.*, **97**:191801, 2006.

[93] P. Adamson et al. A Study of Muon Neutrino Disappearance Using the Fermilab Main Injector Neutrino Beam. *Phys. Rev.*, **D77**:072002, 2008.

[94] P. Adamson et al. First measurement of electron neutrino appearance in NOvA. *Phys. Rev. Lett.*, **116**:151806, 2016.

[95] M. A. Acero et al. New constraints on oscillation parameters from ν_e appearance and ν_μ disappearance in the NOvA experiment. 2018.

[96] R. Acquafredda et al. First events from the CNGS neutrino beam detected in the OPERA experiment. *New J. Phys.*, **8**:303, 2006.

[97] Donato Di Ferdinando. Nuclear emulsions in the OPERA experiment. *Radiat. Meas.*, **44**:840–845, 2009.

[98] N. Agafonova et al. The Angular Matching Method for the Muon Charge Sign Measurement in the OPERA Experiment. *JINST*, **11**:P07022, 2016.

[99] N. Agafonova et al. Observation of a first ν_τ candidate in the OPERA experiment in the CNGS beam. *Phys. Lett.*, **B691**:138–145, 2012.

[100] N. Agafonova et al. Final results of the OPERA experiment on ν_τ appearance in the CNGS beam. *Phys.Rev.Lett.*, **120**:211801, 2018.

[101] M. Apollonio et al. Search for neutrino oscillations on a long base-line at the CHOOZ nuclear power station. *Eur. Phys. J.*, **C27**:331, 2003.

[102] Catherine I Low and Raymond R Volkas. Tribimaximal mixing, discrete family symmetries, and a conjecture connecting the quark and lepton mixing matrices. *Physical Review D*, **68**(3):033007, 2003.

[103] Naoyuki Haba, Atsushi Watanabe, and Koichi Yoshioka. Twisted flavors and tribimaximal neutrino mixing. *Physical review letters*, **97**(4):041601, 2006.

[104] Ernest Ma. Tribimaximal neutrino mixing from a supersymmetric model with A 4 family symmetry. *Physical Review D*, **73**(5):057304, 2006.

[105] F. P. An et al. Observation of electron-antineutrino disappearance at Daya Bay. *Phys. Rev. Lett.*, **108**:171803, 2012.

[106] Soo-Bong Kim et al. Observation of Reactor Electron Antineutrino Disappearance in the RENO Experiment. *Phys. Rev. Lett.*, **108**:191802, 2012.

[107] Y. Abe et al. Indication for the disappearance of reactor electron antineutrinos in the Double Chooz experiment. *Phys. Rev. Lett.*, **108**:131801, 2012.

[108] F. Ardellier et al. Double Chooz: A search for the neutrino mixing angle θ_{13}. 2006.

[109] X. Guo et al. A precision measurement of the neutrino mixing angle θ_{13} using reactor antineutrinos at Daya Bay. 2007. Proposal to DOE.

[110] Soo-Bong Kim and Reno Collaboration. RENO: Reactor experiment for neutrino oscillation at Yonggwang. In *AIP Conference Proceedings*, volume 981, pages 205–207. AIP, 2008.

[111] F. P. An et al. Measurement of electron antineutrino oscillation based on 1230 days of operation of the Daya Bay experiment. *Phys.Rev.*, **D95**:072006, 2017.

[112] G. Bak et al. Measurement of Reactor Antineutrino Oscillation Amplitude and Frequency at RENO. 2018.

[113] Y. Abe et al. Measurement of θ_{13} in Double Chooz using neutron captures on hydrogen with novel background rejection techniques. *JHEP*, **01**:163, 2016.

[114] v3.2: Three-neutrino fit based on data available in January 2018, 2018.

[115] PF de Salas, DV Forero, CA Ternes, M Tortola, and JWF Valle. Status of neutrino oscillations 2017. *arXiv preprint arXiv:1708.01186*, 2017.

[116] Ivan Esteban, MC Gonzalez-Garcia, Michele Maltoni, Ivan Martinez-Soler, and Thomas Schwetz. Updated fit to three neutrino mixing: exploring the accelerator-reactor complementarity. *Journal of High Energy Physics*, **2017**(1):87, 2017.

[117] S Gariazzo, M Archidiacono, PF de Salas, O Mena, CA Ternes, and M Tórtola. Neutrino masses and their ordering: Global Data, Priors and Models. *arXiv preprint arXiv:1801.04946*, 2018.

[118] F Capozzi, E Lisi, A Marrone, D Montanino, and A Palazzo. Status and prospects of global analyses of neutrino mass-mixing parameters. In *Journal of Physics: Conference Series*, volume 888, page 012037. IOP Publishing, 2017.

[119] M. Tanabashi, Particle Data Group, et al. The Review of Particle Physics. *Phys. Rev. D*, **98**:030001, 2018.

[120] A. Aguilar et al. Evidence for neutrino oscillations from the observation of $\bar{\nu}_e$ appearance in a $\bar{\nu}_\mu$ beam. *Phys. Rev.*, **D64**:112007, 2001.

[121] C. Athanassopoulos et al. Evidence for anti-muon-neutrino —¿ anti-electron-neutrino oscillations from the LSND experiment at LAMPF. *Phys. Rev. Lett.*, **77**:3082–3085, 1996.

[122] C. Athanassopoulos et al. Candidate events in a search for $\bar{\nu}_\mu \to \bar{\nu}_e$ oscillations. *Phys. Rev. Lett.*, **75**:2650–2653, 1995.

[123] C. Athanassopoulos et al. Evidence for neutrino oscillations from muon decay at rest. *Phys. Rev.*, **C54**:2685–2708, 1996.

[124] C. Athanassopoulos et al. Evidence for $\nu_\mu \to \nu_e$ neutrino oscillations from LSND. *Phys. Rev. Lett.*, **81**:1774–1777, 1998.

[125] A. A. Aguilar-Arevalo et al. Improved Search for $\bar{\nu}_\mu \to \bar{\nu}_e$ Oscillations in the MiniBooNE Experiment. *Phys. Rev. Lett.*, **110**:161801, 2013.

[126] A. A. Aguilar-Arevalo et al. The MiniBooNE Detector. *Nucl. Instrum. Meth.*, **A599**:28–46, 2009.

[127] A. A. Aguilar-Arevalo et al. A Search for Electron Neutrino Appearance at the $\Delta m^2 \sim 1\,\mathrm{eV}^2$ Scale. *Phys. Rev. Lett.*, **98**:231801, 2007.

[128] A. A. Aguilar-Arevalo et al. Unexplained Excess of Electron-Like Events From a 1-GeV Neutrino Beam. *Phys. Rev. Lett.*, **102**:101802, 2009.

[129] A. A. Aguilar-Arevalo et al. A search for muon neutrino and antineutrino disappearance in MiniBooNE. *Phys. Rev. Lett.*, **103**:061802, 2009.

[130] A. A. Aguilar-Arevalo et al. Bringing the SciBar Detector to the Booster Neutrino Beam. 2006.

[131] K. B. M. Mahn et al. Dual baseline search for muon neutrino disappearance at $0.5 < \Delta m^2 < 40\,\mathrm{eV}^2$. *Phys. Rev.*, **D85**:032007, 2012.

[132] G. Cheng et al. Dual baseline search for muon antineutrino disappearance at $0.1\mathrm{eV}^2 < \Delta m^2 < 100\mathrm{eV}^2$. *Phys. Rev.*, **D86**:052009, 2012.

[133] A. A. Aguilar-Arevalo et al. Observation of a Significant Excess of Electron-Like Events in the MiniBooNE Short-Baseline Neutrino Experiment. 2018.

[134] G. Mention, M. Fechner, Th. Lasserre, Th. A. Mueller, D. Lhuillier, M. Cribier, and A. Letourneau. Reactor antineutrino anomaly. *Phys. Rev. D*, **83**:073006, Apr 2011.

[135] Patrick Huber. Determination of antineutrino spectra from nuclear reactors. *Phys. Rev. C*, **84**:024617, Aug 2011.

[136] Th. A. Mueller, D. Lhuillier, M. Fallot, A. Letourneau, S. Cormon, M. Fechner, L. Giot, T. Lasserre, J. Martino, G. Mention, A. Porta, and F. Yermia. Improved predictions of reactor antineutrino spectra. *Phys. Rev. C*, **83**:054615, May 2011.

[137] S. Gariazzo, C. Giunti, M. Laveder, and Y. F. Li. Updated Global 3+1 Analysis of Short-BaseLine Neutrino Oscillations. *JHEP*, **06**:135, 2017.

[138] Carlo Giunti and Marco Laveder. Statistical Significance of the Gallium Anomaly. *Phys. Rev.*, **C83**:065504, 2011.

[139] P. Anselmann et al. First results from the Cr-51 neutrino source experiment with the GALLEX detector. *Phys. Lett.*, **B342**:440–450, 1995.

[140] W. Hampel et al. Final results of the Cr-51 neutrino source experiments in GALLEX. *Phys. Lett.*, **B420**:114–126, 1998.

[141] J. N. Abdurashitov et al. Measurement of the response of the Russian-American gallium experiment to neutrinos from a Cr-51 source. *Phys. Rev.*, **C59**:2246–2263, 1999.

[142] S. Gariazzo, C. Giunti, M. Laveder, Y. F. Li, and E. M. Zavanin. Light sterile neutrinos. *J. Phys.*, **G43**:033001, 2016.

[143] J. N. Abdurashitov et al. Measurement of the response of a Ga solar neutrino experiment to neutrinos from an Ar-37 source. *Phys. Rev.*, **C73**:045805, 2006.

[144] Florian Kaether, Wolfgang Hampel, Gerd Heusser, Juergen Kiko, and Till Kirsten. Reanalysis of the GALLEX solar neutrino flux and source experiments. *Physics Letters B*, **685**(1):47–54, 2010.

[145] B. Bodmann et al. Results from the KARMEN neutrino experiment. *Nucl. Phys.*, **A553**:831c–834c, 1993.

[146] J. Altegoer et al. A search for $\nu_\mu \to \nu_\tau$ oscillations using the NOMAD detector. *Phys. Lett.*, **B431**:219–236, 1998.

[147] Y. Declais et al. Study of reactor anti-neutrino interaction with proton at Bugey nuclear power plant. *Phys. Lett.*, **B338**:383–389, 1994.

[148] B. Armbruster et al. Upper limits for neutrino oscillations $\bar{\nu}_\mu \to \bar{\nu}_e$ from muon decay at rest. *Phys. Rev.*, **D65**:112001, 2002.

[149] P. Astier et al. Search for $\nu_\mu \to \nu_e$ Oscillations in the NOMAD Experiment. *Phys. Lett.*, **B570**:19–31, 2003.

[150] N. Agafonova et al. Final results of the search for $\nu_\mu \to \nu_e$ oscillations with the OPERA detector in the CNGS beam. 2018.

[151] B Achkar, R Aleksan, M Avenier, G Bagieu, J Bouchez, R Brissot, J-F Cavaignac, J Collot, MC Cousinou, Jean-Pierre Cussonneau, et al. Search for neutrino oscillations at 15, 40 and 95 meters from a nuclear power reactor at Bugey. *Nuclear Physics B*, **434**(3):503–532, 1995.

[152] F. P. An et al. Evolution of the Reactor Antineutrino Flux and Spectrum at Daya Bay. *Phys. Rev. Lett.*, **118**(25):251801, 2017.

[153] P. A. R. Ade et al. Planck 2013 results. I. Overview of products and scientific results. *Astron. Astrophys.*, **571**:A1, 2014.

[154] Sarah Bridle, Jack Elvin-Poole, Justin Evans, Susana Fernandez, Pawel Guzowski, and Stefan Soldner-Rembold. A Combined View of Sterile-Neutrino Constraints from CMB and Neutrino Oscillation Measurements. *Phys. Lett.*, **B764**:322–327, 2017.

[155] P. Adamson et al. Search for Sterile Neutrinos Mixing with Muon Neutrinos in MINOS. *Phys. Rev. Lett.*, **117**(15):151803, 2016.

[156] M. G. Aartsen et al. Searches for Sterile Neutrinos with the IceCube Detector. *Phys. Rev. Lett.*, **117**(7):071801, 2016.

[157] M. Antonello et al. A Proposal for a Three Detector Short-Baseline Neutrino Oscillation Program in the Fermilab Booster Neutrino Beam. 2015.

[158] P. Adamson et al. Search for active-sterile neutrino mixing using neutral-current interactions in NOvA. *Phys. Rev.*, **D96**(7):072006, 2017.

[159] Debra Dewhurst. Searches for Sterile Neutrinos Using the T2K Off-Axis Near Detector. In *Proceedings, Topical Research Meeting on Prospects in Neutrino Physics (NuPhys2014): London, UK, December 15-17, 2014*, 2015.

[160] Marco Drewes. The Phenomenology of Right Handed Neutrinos. *Int. J. Mod. Phys.*, **E22**:1330019, 2013.

[161] Scott Dodelson and Lawrence M Widrow. Sterile neutrinos as dark matter. *Physical Review Letters*, **72**(1):17, 1994.

[162] K. N. Abazajian et al. Light Sterile Neutrinos: A White Paper. 2012.

[163] E. Ables et al. P-875: A Long baseline neutrino oscillation experiment at Fermilab. 1995.

[164] Stephen J. Parke. Overview of accelerator long baseline neutrino oscillation experiments. In *Perspectives in neutrinos, atomic physics and gravitation. Proceedings, 28th Rencontres de Moriond, 13th Moriond Workshop, Villars sur Ollon, Switzerland, January 30 - February 6, 1993*, pages 229–236, 1993.

[165] P. Adamson et al. The NuMI Neutrino Beam. *Nucl. Instrum. Meth.*, **A806**:279–306, 2016.

[166] Jessica Sarah Mitchell. Measuring ν_μ Disappearance with the MINOS Experiment. 2011.

[167] Adam Aurisano. Recent Results from MINOS and MINOS+, June 2018.

[168] P. Adamson et al. Measurements of atmospheric neutrinos and antineutrinos in the MINOS Far Detector. *Phys. Rev.*, **D86**:052007, 2012.

[169] Alexandre B. Sousa. First MINOS+ Data and New Results from MINOS. *AIP Conf. Proc.*, **1666**:110004, 2015.

[170] G. Tzanankos et al. MINOS+: a Proposal to FNAL to run MINOS with the medium energy NuMI beam. 2011.

[171] Justin Evans. The MINOS experiment: results and prospects. *Adv. High Energy Phys.*, **2013**:182537, 2013.

[172] A. Blake. Far Detector PoT Integration for MINOS Physics Analyses, MINOS Document 9093, May 2012.

[173] A. Blake. Far Detector PoT Integration for MINOS Physics Analyses, MINOS Document 9093, September 2016.

[174] Simon van der Meer. A directive device for charged particles and its use in an enhanced neutrino beam. Technical report, Cern, 1961.

[175] Ashley Michael Timmons. *Search for Sterile Neutrinos with the MINOS Long-Baseline Experiment*. PhD thesis, Manchester U., 2016.

[176] Alexander Radovic. *Measuring the Disappearance of Muon Neutrinos with the MINOS Detector.* PhD thesis, U. Coll. London, 2013.

[177] D. G. Michael et al. The Magnetized steel and scintillator calorimeters of the MINOS experiment. *Nucl. Instrum. Meth.*, **A596**:190–228, 2008.

[178] T. Cundiff et al. The MINOS near detector front end electronics. *IEEE Trans. Nucl. Sci.*, **53**:1347–1355, 2006.

[179] J. Oliver, N. Felt, G. Feldman, A. Lebedev, and R. Lee. Design and performance of the readout system of the MINOS Far Detector. *IEEE Trans. Nucl. Sci.*, **51**:2193–2195, 2004.

[180] P. Adamson et al. The MINOS calibration detector. *Nucl. Instrum. Meth.*, **A556**:119–133, 2006.

[181] J. A. Formaggio and G. P. Zeller. From eV to EeV: Neutrino Cross Sections Across Energy Scales. *Rev. Mod. Phys.*, **84**:1307–1341, 2012.

[182] R. Devenish and A. Cooper-Sarkar. *Deep Inelastic Scattering.* Oxford University Press, 2004.

[183] J. Coelho. Results and prospects from MINOS and MINOS+. NuFact 2013.

[184] J. DeJong et al. 2009 Position Paper on Calibration of Runs I-II-III, MINOS Document 6717, December 2009.

[185] S. DeRijck. MINOS+ Collaboration Meeting: Calibration Paper Status, MINOS Document 12556, Oct 2017.

[186] Jeffrey John Hartnell. *Measurement of the Calorimetric Energy Scale in MINOS*. PhD thesis, Oxford U., 2005.

[187] Junting Huang. *Sterile Neutrino Searches in MINOS/MINOS+ Experiment*. PhD thesis, U. Texas, Austin, 2015.

[188] Michael Alan Kordosky. *Hadronic interactions in the MINOS detectors*. PhD thesis, Texas U., 2004.

[189] Patricia LaVern Vahle. *Electromagnetic interactions in the MINOS detectors*. PhD thesis, Texas U., 2004.

[190] Zarko Pavlovic. *Observation of Disappearance of Muon Neutrinos in the NuMI Beam*. PhD thesis, Texas U., 2008.

[191] Leonidas Aliaga Soplin. *Neutrino Flux Prediction for the NuMI Beamline*. PhD thesis, William-Mary Coll., 2016.

[192] H. Gallagher. The NEUGEN neutrino event generator. *Nucl. Phys. Proc. Suppl.*, **112**:188–194, 2002.

[193] C. H. Llewellyn Smith. Neutrino Reactions at Accelerator Energies. *Phys. Rept.*, **3**:261–379, 1972.

[194] D. Rein and L. M. Sehgal. Coherent Production of Photons by Neutrinos. *Phys. Lett.*, **104B**:394–398, 1981. [Erratum: Phys. Lett.106B,513(1981)].

[195] Dieter Rein and Lakshita Sehgal. Neutrino-excitation of baryon resonances and single pion production. **133**:79–153, 04 1981.

[196] A. Bodek and U. K. Yang. Modeling deep inelastic cross-sections in the few GeV region. *Nucl. Phys. Proc. Suppl.*, **112**:70–76, 2002. [,70(2002)].

[197] Torbjorn Sjostrand, Stephen Mrenna, and Peter Z. Skands. PYTHIA 6.4 Physics and Manual. *JHEP*, **05**:026, 2006.

[198] Z. Koba, Holger Bech Nielsen, and P. Olesen. Scaling of multiplicity distributions in high-energy hadron collisions. *Nucl. Phys.*, **B40**:317–334, 1972.

[199] T. Yang, C. Andreopoulos, H. Gallagher, K. Hoffmann, and P. Kehayias. A Hadronization Model for Few-GeV Neutrino Interactions. *Eur. Phys. J.*, **C63**:1–10, 2009.

[200] R Merenyi, WA Mann, T Kafka, W Leeson, Biagio Saitta, J Schneps, M Derrick, and B Musgrave. Determination of pion intranuclear rescattering rates in ν μ- N e versus ν μ- D interactions for the atmospheric ν flux. *Physical Review D*, **45**(3):743, 1992.

[201] R. Hatcher and S. Kasahara. The (Attempt at a Semi-) Definitive Guide to MINOS Geometry, MINOS Document 7828, Jan 2011.

[202] C. Zeitnitz and T. A. Gabriel. The GEANT - CALOR interface and benchmark calculations of ZEUS test calorimeters. *Nucl. Instrum. Meth.*, **A349**:106–111, 1994.

[203] J. Boehm. Detector Simulation effects, MINOS Document 4364, Mar 2008.

[204] Justin John Evans. Measuring Antineutrino Oscillations with the MINOS Experiment. 2008.

[205] Christopher James Backhouse. *Measuring neutrino oscillation parameters using ν_μ disappearance in MINOS*. PhD thesis, Oxford U., 2011.

[206] P. Litchfield. Far Detector event preselection (data cleaning) for NC analysis. *MINOS Document*, **3377**.

[207] Rustem Ospanov. *A measurement of muon neutrino disappearance with the MINOS detectors and NuMI beam*. PhD thesis, Texas U., 2008.

[208] Jasmine Star Ratchford. *Identifying Muons for Neutrino Oscillation and Cross Section Experiments*. PhD thesis, Texas U., ARL, 2012.

[209] T. Carroll. Standard Oscillations 05/04/2017: MINOS+ CC Selection kNN, MINOS Document 12057, May 2017.

[210] A. Aurisano et al. Sterile Neutrino Systematic Correlations, MINOS Document 11710, December 2016.

[211] A. Aurisano. A Position Paper on Constructing Systematic Covariance Matrices for the 2014 Sterile Analysis, MINOS Document 10581, April 2014.

[212] J. Evans, K. Lang, and R. Nichol. Position paper on the 2010 analysis of charged current events from runs I, II and III, MINOS Document 7218, April 2010.

[213] P. Adamson et al. Search for sterile neutrino mixing in the MINOS long baseline experiment. *Phys.Rev.*, **D81**:052004, 2010.

[214] J. Musser et al. Range Curvature Task Force Position Paper, MINOS Document 3134, June 2007.

[215] R. Nichol et al. January 2008 Position Paper on Calibration of the Pre-Shutdown Data, MINOS Document 3941, January 2008.

[216] S. Dytman, H. Gallagher, and M. Kordosky. Hadronic Shower Energy Scale Uncertainties in the MINOS Experiment. *arXiv:0806.2119*, 2008.

[217] S. Dytman et al. Shower Energy Scale Uncertainty For the Run I+II CC Analysis, MINOS Document 4287, March 2008.

[218] J. Evans. Absolute (calorimetric) shower energy uncertainty, MINOS Document 7173, April 2010.

[219] Andrey V. Lebedev. *Ratio of pion kaon production in proton carbon interactions*. PhD thesis, Harvard U., 2007.

[220] A. Holin. MINOS Lessons for the NUMI Beam Flux. proceedings submitted.

[221] L. Aliaga et al. Neutrino Flux Predictions for the NuMI Beam. *Phys. Rev.*, **D94**(9):092005, 2016. [Addendum: Phys. Rev.D95,no.3,039903(2017)].

[222] C. E. Patrick et al. Measurement of the Muon Antineutrino Double-Differential Cross Section for Quasielastic-like Scattering on Hydrocarbon at $E_\nu \sim 3.5$GeV. *Phys. Rev.*, **D97**(5):052002, 2018.

[223] Svante Wold, Kim Esbensen, and Paul Geladi. Principal component analysis. *Chemometrics and Intelligent Laboratory Systems*, **2**(1):37 – 52, 1987. Proceedings of the Multivariate Statistical Workshop for Geologists and Geochemists.

[224] S. Kopp et al. Systematic Uncertainties in the NuMI Beam Flux, MINOS Document 1283, November 2005.

[225] John David Jackson. *Classical electrodynamics*. Wiley, New York, NY, 3rd ed. edition, 1999.

[226] David Bohm and David Pines. A Collective Description of Electron Interactions: 3. Coulomb Interactions in a Degenerate Electron Gas. *Phys. Rev.*, **92**:609–625, 1953.

[227] R. Gran, J. Nieves, F. Sanchez, and M. J. Vicente Vacas. Neutrino-nucleus quasi-elastic and 2p2h interactions up to 10 GeV. *Phys. Rev.*, **D88**(11):113007, 2013.

[228] J. Evans. Systematic uncertainties for the 2010 CC analysis, MINOS Document 7145, April 2010.

[229] P. S. Auchincloss et al. Measurement of the inclusive charged-current cross section for neutrino and antineutrino scattering on isoscalar nucleons. *Z Phys C*, **48**:411–431, 1990.

[230] I. E. Stockdale et al. Limits on Muon Neutrino Oscillations in the Mass Range $55\text{eV}^2 < \Delta m^2 < 800\text{eV}^2$. *Phys. Rev. Lett.*, **52**:1384, 1984.

[231] J. Ling. Prediction of NC/CC as a Function of Ehad for MINOS-LE using NOMAD Measurement, MINOS Document 3959, January 2008.

[232] P. Rodrigues. Notes on the Normalization Systematic, MINOS Document 6636, January 2009.

[233] Paley:2009. Hand-scan Estimation of the Reconstruction-Related Systematic Uncertainty in the Near/Far Normalization of the MINOS CC Analysis, MINOS Document 5613, January 2009.

[234] P. Rodrigues. Constraining the NC normalization uncertainty using MRCC events, MINOS Document 6841, January 2010.

[235] J. DeJong. Position Paper for the Runs I-III FD NC Cleaning, MINOS Document 7165, April 2010.

[236] Alena v. Devan. *Sterile Neutrino Search with MINOS*. PhD thesis, Coll. William and Mary, 2015.

[237] F.P. An et al. Improved Search for a Light Sterile Neutrino with the Full Configuration of the Daya Bay Experiment. *Phys. Rev. Lett.*, **117**:151802, 2016.

[238] P. Adamson et al. Combined analysis of ν_μ disappearance and $\nu_\mu \to \nu_e$ appearance in MINOS using accelerator and atmospheric neutrinos. *Phys. Rev. Lett.*, **112**:191801, 2014.

[239] Morris L. Eaton. *Multivariate Statistics: a Vector Space Approach.* John Wiley and Sons, 1983.

[240] Glen Cowan, Kyle Cranmer, Eilam Gross, and Ofer Vitells. Asymptotic formulae for likelihood-based tests of new physics. *Eur. Phys. J.*, **C71**:1554, 2011. [Erratum: Eur. Phys. J.C73,2501(2013)].

[241] Alan Agresti. Logistic regression. *An Introduction to Categorical Data Analysis, Second Edition*, pages 99–136, 2007.

[242] F. James and M. Roos. Minuit - a system for function minimization and analysis of the parameter errors and correlations. *Computer Physics Communications*, **10**(6):343 – 367, 1975.

[243] Roger A Horn and Charles R Johnson. Matrix analysis cambridge university press. *New York*, **37**, 1985.

[244] Rüdiger Seydel. *Generating Random Numbers with Specified Distributions*, pages 51–77. Springer Berlin Heidelberg, Berlin, Heidelberg, 2002.

[245] Gary J. Feldman and Robert D. Cousins. A Unified approach to the classical statistical analysis of small signals. *Phys. Rev.*, **D57**:3873–3889, 1998.

[246] Jerzy Neyman. XOutline of a Theory of Statistical Estimation Based on the Classical Theory of Probability. *Phil. Trans. R. Soc. Lond. A*, **236**(767):333–380, 1937.

[247] K. Abe et al. Limits on sterile neutrino mixing using atmospheric neutrinos in Super-Kamiokande. *Phys. Rev. D*, **91**:052019, 2015.

[248] F. Dydak et al. A Search for Muon-neutrino Oscillations in the Delta m**2 Range 0.3-eV**2 to 90-eV**2. *Phys. Lett.*, **B134**:281, 1984.

[249] P. Adamson et al. Limits on Active to Sterile Neutrino Oscillations from Disappearance Searches in the MINOS, Daya Bay, and Bugey-3 Experiments. *Phys. Rev. Lett.*, **117**:151801, Oct 2016.

[250] Aguilar-Arevalo et al. Improved Search for $\overline{\nu}_\mu \to \overline{\nu}_e$ Oscillations in the MiniBooNE Experiment. *Phys. Rev. Lett.*, **110**:161801, Apr 2013.

[251] Elizabeth Worcester. DUNE: Status and Science, June 2018.

Index

Abstract, ii
Acknowledgments, vi

Bibliography, 327

Dedication, v

Vita

Jacob Todd was born in Cincinnati, Ohio, United States of America on June 23, 1989, the son of Gary and Pamela Todd (née Gruber). He earned his Bachelor of Arts degree in Physics from the University of Cincinnati in 2011. He then earned a Master of Education degree from Xavier University in 2012 specializing in Secondary Education. He began the Ph.D. program at the University of Cincinnati in August 2012. He earned a Master of Science degree en route to Ph.D. at the University of Cincinnati in the spring of 2018.

Permanent address: University of Cincinnati
Department of Physics
400 Geology/Physics Building
PO Box 210011
Cincinnati, OH 45221-0011

This dissertation was typeset with LaTeX[†] by the author.

[†]LaTeX is a document preparation system developed by Leslie Lamport as a special version of Donald Knuth's TeX Program.